The 4th Japan – Greece Workshop

Seismic Design of Foundations, Innovations in Seismic Design, and Protection of Cultural Heritage

Special Issue: The 2011 East Japan Great Earthquake

October 6–7, 2011 Kobe, Japan

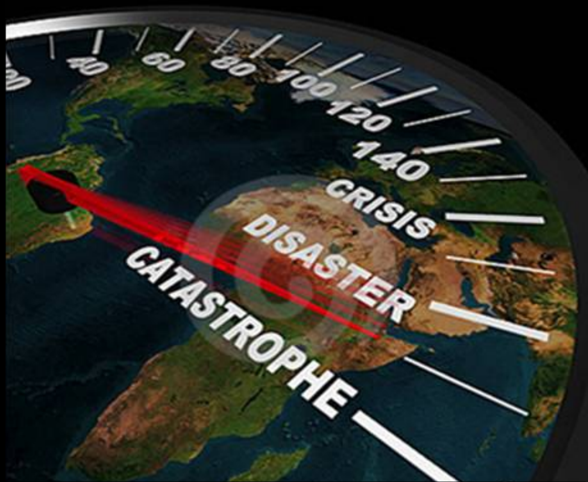

Volume 1

Edited by T. Tazoh and G. Gazetas

Co-chairperson: T. Okada
G. Gazetas

Secretariat General: T. Tazoh

Organizing Committee

Y. Goto	H. Kimata
K. Maebayashi	K. Horikoshi
T. Sato	M. Saitoh
K. Wakamatsu	N. Funaki
T. Kaneyoshi	P. Dakoulas
N. Yoshida	M. Panagiotou
T. Asano	N. Gerolymos
F. Miura	I. Anastasopoulos
A. Mikami	R. Kourkoulis

Organized by:

- Earthquake Engineering Committee of Japanese Society of Civil Engineers
- Kobe Gakuin University
- Hellenic Society for Earthquake Engineering, Technical Chamber of Greece
- Laboratory of Soil Mechanics of National Technological University of Athens
- Project DARE funded by ERC
- Project PERPETUATE funded by EC FP7

Supported financially by:

- Japan Society of Civil Engineers
- Kobe Gakuin University
- ATTIKES DIADROMES, ATTIKI ODOS, J&P AVAX, OMETE

Introduction and Objectives

Following the 1995 Kobe Earthquake a close scientific cooperation was initiated between the National Technical University of Athens (NTUA), Greece, and some Japanese institutes. As part of this cooperation a visit to Kobe of 25 graduating students from NTUA has taken place every year starting in 1999. In one of these visits an agreement was reached to organize this joint Japan-Greece Workshop. Starting in 2005, it was held successfully every two years.

The workshop serves as an international meeting at which specialists, governmental officials and professors in earthquake engineering and related fields may exchange ideas on the latest research results and technologies mainly on soil-foundation-structure interaction, seismic behavior of soft soil deposits, performance-based seismic design, lessons learned from recent earthquakes, innovations on seismic protection of structures, and seismic protection of monuments.

Researchers and engineers participated not only from Japan and Greece, but also from Algeria, China, France, USA, UK, India, Italy, and Germany.

The workshop strives to promote innovation, practice and safety in reducing the impact of earthquakes on our society and natural environment. We hope many participants will join this workshop to upgrade their knowledge and contribute tor the progress of seismic disaster mitigation.

Workshop Topics

- Seismic analysis of shallow, embedded, and deep foundations
- Seismic design of foundations against liquefaction
- Site response of soil deposits
- Soil liquefaction and liquefaction-induced flow
- Remedial measures, repair–retrofit, and health monitoring of foundation–structure systems
- Performance–based design in geotechnical and structural engineering
- Innovations in seismic protection of structures and foundations
- Seismic protection of cultural heritage
- Lessons learned from recent earthquakes

Contents

Volume 1

Invited papers

Submitted papers

Volume 2

Volume 3

The impact of the March 11th 2011
Great East Japan Earthquake

-- As a substitute for the welcome address --

by
Professor Kazuo Konagai

The impact of the March 11^{th} 2011 Great East Japan Earthquake
-- As a substitute for the welcome address --

The irony was that we saw tsunami debris has spread over Ishinomaki, Rikuzen-Takada, Otsuchi, all coastal cities, beyond signs saying "Tsunami would probably reach up here". Not a few numbers of tsunami/emergency shelters in inland beyond these signs were inundated and severely destroyed tragically bringing many deaths. Most profoundly affected will be nuclear power. We weren't predicting a large earthquake to strike the northeastern coast of Japan followed by a tsunami and failure of backup equipment. The situation at Fukushima is still developing, and for now it is unlikely that we have known the complete figure of the "Black Swan" accident. Controversy abounds that nuclear power plants should be shut down or not sometimes with no logical reasons but a vague feeling of anxiety.

This "Black swan" event has reminded us of the fact that we have opened several Pandora's boxes. As for nuclear power, it allowed people to phase out of coal which had been contributing to global warming through emissions and mining deaths. On the other hand, we have known for a long time that the consequences of partial or full meltdowns are extremely high. Tokyo suffered a serious tsunami due to not an earthquake but a typhoon in 1910. Tokyo bay areas were seriously engulfed with some ships sent inland as was described in the autobiographical novel "Wife of Mokugyo" by Shigure Hasegawa, a female novelist of the time. This tsunami had promoted a 17-years project of Arakawa Diversion Channel to let the water of Arakawa River flow around the east bound of Tokyo. In this project, it was planned that eastern side of the diversion channel would be a flood control reservoir. About eighty years after the completion of the project, the originally planned reservoir is now completely urbanized with houses for about 650,000 people, suffering from ground subsidence beneath the sea/river level caused by long-continued natural gas extraction and overuse of ground water. The areas under sea level in Tokyo reaches 124km^2 increasing the risk of the "Black swan" event in which inexhaustible amount of water can flow in through a narrow fray of walls.

We need to map out rational tactics to deal with the negative legacy from what we obtained from Pandora's boxes. Given that Japan gets 30% of its electricity from nuclear power, it is not practical to ban it all at once. We need to phase out of coal and more slowly nuclear power, as renewables can fill in the gaps. Slow and misleading disclosure of the full truth of the "Black swan" event would lead to tons of hasty activism which would wind up hurting our environment. The role of engineers is thus very important.

On behalf of the Earthquake Engineering Committee of the Japan Society of Civil Engineers, I would like to extend my hearty welcome to you all attending the 4th Japan Greece Workshop, Seismic Design of Foundations, Innovations in Seismic Design, and Protection of Cultural Heritage. The workshop is really timely to discuss our roles beyond the confines of our areas of expertise, given the impact from the March 11^{th} Earthquake. Be a part of defining the solutions and building a socially responsible and sustainable world.

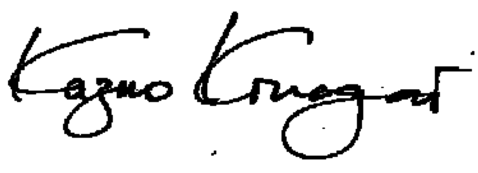

Kazuo KONAGAI
Chairman of the Earthquake Engineering Committee, JSCE

To our dear Japanese friends

by
Professor George Gazetas

To our dear Japanese friends

by

George Gazetas

Seven months have passed from 11–3–11, the day that the colossal magnitude 9 earthquake shook Japan, and the world, as it triggered an unprecedented bleak sequence of calamities, obliterating towns and small cities, and turning the lives of ordinary citizens upside down. We, as all people around the globe, watched speechless at the extent of the disaster, but with sympathy and astonishment at the stoic heroism, dignity, and altruism with which survivors confronted the devastating loss and the terrifying danger; and we marveled at the determination of the whole nation to help rebuilding with no delay.

We recalled the Kobe disaster in 1995, and the equally heroic efforts to rebuild, and even expand the city, in response to devastation — efforts that met unequivocal success. Our civil engineering profession, of which You are a part, was at the forefront of that feat. We have no doubt that You are again leading the effort in the aftermath of Japan's worst ever combination of earthquake and tsunami. I am sure you will succeed.

This Workshop, and the special session on the March 11 Earthquake that your society has organized, are a vivid testament to your determination to overcome the painful plight.

Along with my sincere condolences on behalf of the Greek participants and our Society, allow me to express my strong conviction that with your unselfish help Japan will emerge stronger from this disaster, as it has done so many times in the past.

Invited Speakers

Prof. M. Hamada (Japan) 

Prof. K. Kawashima (Japan) 

Prof. M. K. Yegian (USA) 

Prof. K. Pitilakis (Greece) 

Prof. S. Lagomarsino (Italy) 

Prof. E. Vintzileou (Greece) 

Invited Lectures

1. “Future Directions of Earthquake-Tsunami Disaster Reduction Based on the Lessons from the 2011 Great East Japan Earthquake“
   M. Hamada , N. Y. Yun (Japan)

2. “Effectiveness of Polypropylene Fiber Reinforced Cement Composite for Enhancing the Seismic Performance of Bridge Columns”
   K. Kawashima , R. Zafra, T. Sasaki, K. Kajiwara, M. Nakayama (Japan)

3. “Seismic Vulnerability Assessment and Retrofitting of the Historic Brooklyn Bridge”
   M. K. Yegian, S. G. Arzoumanidis (USA)

4. “The European Research Project SYNERG-G: Systemic Vulnerability and Risk Analysis for Lifelines and Infrastructures”
   K. Pitilakis (GR)

5. “PERPATUATE Project: Performance-based Assessment for Earthquake Protection of Cultural Heritage”
   S. Lagomarsino (Italy)

6. “Testing a Cross Vault and a 2-Storey Masonry Building on the Shaking Table”
   E. Vintzileou (GR)

Future Directions of Earthquake-Tsunami Disaster Reduction Based on the Lessons from the 2011 Great East Japan Earthquake

M. HAMADA & N.Y. YUN
Dept. of Civil and Environment Engineering, Waseda University, Tokyo, Japan

ABSTRACT: This paper briefly reviews the damage caused by the caused by the 2011 Great East Japan Earthquake of March 11, 2011 and introduces author's opinions on the causes of this disaster at the present time (about six months after the event). It also introduces the features of buildings and bridges which could survive against tsunami. Finally, future research issues might gain some insights from the lessons learned from the disaster.

1 INTRODUCTION

The East Japan earthquake and consequent tsunami caused disastrous damages in a vast area from the Tōhoku district until Kanto district of the main island of Japan. The number of loss of human lives reached over 15,000, and the missing over 4,000 according to an announcement by the National Police Agency (September 4th, 2011). The tsunami inundated a large area, and destroyed a huge number of houses, buildings and infrastructures such as railways, roads, bridges and quay walls. The tsunami also severely damaged various lifeline systems, water, sewer, electricity and telecommunication. The accident of the Fukushima No. 1 nuclear power plant caused by the earthquake and the tsunami is most serious damage, and the critical situation is still continuing. As many as 50,000 residents within 30km (19 miles) of the plant have been forced to move a long way off from the contaminated area, and the life in the refuge areas is supposed to continue for a long time.

The earthquake also caused severe liquefaction in extensive areas, artificial islands reclaimed from the Tokyo Bay and the low land areas along big rivers. Particularly, in Urayasu of Chiba Prefecture, about 8 thousands houses and buildings among the total 14 thousand largely subsided and were severely embedded.

The East Japan earthquake caused unprecedented damage to the people and the society of Japan. It will take a long time for the reconstruction of the damaged area and recovery of the life of the people. However, we have to find the future directions to create safer and more secure society against future earthquakes and tsunamis based on the lessons from this disaster.

2 FAILURE OF EARTHQUAKE AND TSUNAMI PREDICTION

Before the occurrence of the Great East Japan earthquake, the Central council of Japan for Disaster Prevention had been warning five big earthquakes which have a high probability of occurrence in near future and may cause a serious damage. Those are Tōkai (Magnitude:8.0), Tōnankai (Magnitude: 8.1), Nankai (Magnitude: 8.4) earthquakes along the Nankai Sea Trough in the Pacific Ocean, Northern-Tokyo Bay earthquake (Magnitude: 7.3), and Off-Miyagi Prefecture earthquake (Magnitude: 7.5).

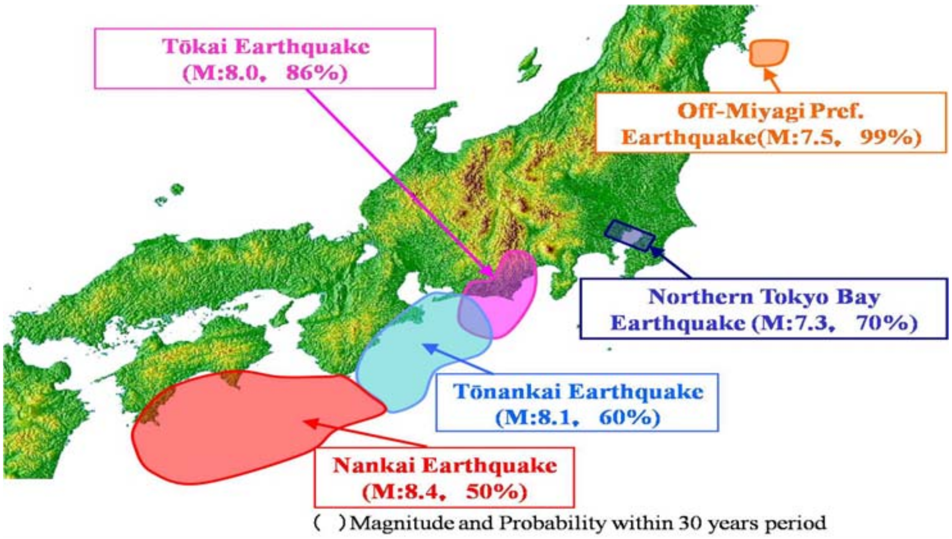

Figure 1. Earthquakes predicted before the 2011 Great East Japan occurred

Among these earthquakes, the attention of the seismologists and engineers had been focused on the continuous occurrence of the three earthquakes along the Nankai Trough in the Pacific Ocean. The magnitude of the earthquake Off-Miyagi Prefecture was estimated as a medium size earthquake of magnitude 7.5. However, the magnitude of the actually occurred event was 9.0, that is 180 times larger than the predicted earthquake. The irreparable mistake in the estimation of the earthquake's scale and of the tsunami's height in this area is the origin of the most tragic event in the last half century of Japan. We have to entirely examine the causes of this failure, and thoroughly check the organizations and systems and the researches for earthquake and tsunami prediction in the future. That will be the first step of the preparedness for the disaster reduction against future events.

3 PROMOTION OF ANTI-TSUNAMI ENGINEERING AND SCIENCE, AND MEASURES AGAINST FUTURE TSUNAMIS

As mentioned previously, a huge number of houses were swept out by the tsunami, and numerous bridges, quay walls and breakwaters were completely broken. However, some of buildings and concrete bridges which located in the tsunami inundated area survived from the tsunami attack as shown in Figure 2.

Figure 2. Survived a Five-story Concrete Building at Rikuzentakada, Iwate Prefecture in Japan(2011)

Figure 3. Survived the Baiturrahman Mosque, Banda Aceh in Indonesia (2004)

The concrete building shown in Figure 2 has a five-story, and the fifth floor was flooded. In other words, the water flew through the whole building. However, any structural damage to the super structure and concrete piles foundation was not found. Same thing was observed in Banda Ache of Indonesia during the 2004 Indian Ocean Tsunami. Figure 3 shows a survived mosque from the tsunami, which located along the shoreline. The examples of survived buildings shown in Figure 2 and Figure 3 suggest us a possibility of the construction of concrete buildings which can withstand tsunami attack. Then, when those kinds of characters apply to larger and taller building along the shoreline, the building can be a safe haven for evacuees from tsunami.

Moreover, lots of bridges survived the tsunami as shown Figure 4. This bridge was constructed by steel girders with concrete slab for a road. The tsunami exceeded the bridge's height, but no structural damage was observed. Same thing was reported from the Indonesia in 2004. A concrete bridge in Band Ache shown in figure 5 is also entirely survived from the tsunami.

Figure 4. Survived the Bridge in Japan (2011)

Figure 5. Survived the Concrete Bridge at Banda Aceh in Indonesia (2004)

This bridge has concrete shear keys to prevent lateral movements of the girder, which might resist tsunami force. The examples shown in Figure 4 and Figure 5 also give us some insights into the possibility of the construction of bridges against tsunami.

Based on the lessons from the tsunami damage caused by the 2011 disaster, the following measures and researcher should be strongly promoted.

1) Survey on traces of historical tsunamis in the world from geological view point
2) Establishment of information gathering and transfer system to grasp the situation of wide spread tsunami-hit areas
3) Research on tsunami resistant buildings and infrastructures
4) Town planning to strengthen the tsunami resistance (evacuation, construction tsunami resistant buildings, selection of residential areas, etc.)
5) Relief activity immediately after the disaster (evacuation warning, tsunami warning)
6) Enforcement of resistance of lifeline systems and quick recovery
7) Disaster education and training

4 FIRES OF INDUSTRIAL COMPLEXES AND SOIL LIQUAFACTION IN ARTIFICIAL ISLANDS

The 2011 Great East Japan Earthquake on March 11 triggered massive fires in the industrial complexes in Tokyo Bay and Sendai Port as shown Figure 6.Although the causes of these fires remain still unknown, they are thought to be affected by the tsunami in Sendai Port, and ground motion and liquefaction in Tokyo Bay, in addition to the quake which lasted for as long as a few minutes. In Sendai Port, heavy oil storage tanks were damaged and set ablaze, and the spilled oil traveled upstream in the river, surging into the residential areas because of the tsunami.

Figure 6. Fires in the Industrial Complexes (a: Tokyo Bay, b: Sendai Port)

Meanwhile, extensive liquefaction phenomena occurred in the reclaimed lands in Tokyo Bay, causing a large number of houses and buildings to sink and tilt, and causing lifeline pipelines to be damaged. This resulted in prolonged loss of city functions after the earthquake. One of the causes of the severe liquefaction phenomena could be the long duration of the earthquake.

Figure 7. Liquefaction of Reclaimed Land in Tokyo Bay

5 RISK OF COASTAL INDUTRIAL COMPLEXES AND MEASURES AGAINST FUTURE EARTHQUAKE

A vast expanse of land has been reclaimed along the coastal areas in Japan's large urban areas, Tokyo Bay, Ise Bay, and Osaka Bay. Amid the high-growth period of Japanese economy, heavy industrial and petrochemical industrial complexes were built on these reclaimed lands. Even now, in the petrochemical complex zone, a lot of petrochemical storage tanks and facilities to manufacture petroleum products still exist.

Figure 8. A Chemical Complex around the Tokyo Bay

As for these complexes build on the coastal reclaimed lands, there are two apprehensions over future earthquakes. One is large tank fires arising from so-called long period ground motions, and soil liquefaction-induced horizontal ground displacement by meters, so-called lateral ground flow, first causes tanks and pipes to be destroyed, and then it causes large amounts of dangerous materials such as heavy and crude oil as well as high-pressure gases to be discharged to marine waters. The incidence that is still a fresh memory is the two tanks that burst into flames in Tomakomai due to Tokachioki earthquake in 2003. These tanks were floating roof type tanks, where a lid was floating on the liquid in the tank. The long-period ground motion created a big wave of liquid in the tank, which caused the floating rid to jump out of the tank. The lid fell and crashed onto the side of the tank and caused fire.

At present, over 600 floating roof tanks have been built and are in operation in the reclaimed lands along Tokyo Bay. According to the assumption that the Tōkai Earthquake and the Tōnankai Earthquake whose epicenters are situated from Tōkaido to the area off Kii Peninsula occurred in series, long period ground motions in the Keiyo area and the Keihin area along Tokyo Bay were estimated, based on which the sloshing motions of the content liquid in the tanks were calculated. As a result, it turned out that the content liquid would leak out of 60 tanks, equivalent to approximately 10% of the total number of tanks. Most such content liquid may leak into marine waters. Table 1 shows the result of simulation on slashing of the oil tanks in Tokyo Bay.

Table 1. Prediction of Number of Overflowing Oil Tanks

Diameter of Tanks	Number of Tanks	Number of Overflowing Oil Tanks
~ 24 m	203	13 (6.4%)
24 m ~ 34 m	136	27 (19.9%)
34 m ~ 60 m	118	18 (15.3%)
60 m ~	159	6 (3.8%)
Total	616	64 (10.4%)

The other apprehension about the seismic adequacy of coastal reclaimed lands is soil liquefaction. Many of the reclaimed lands in Tokyo Bay have been developed since the early Showa era. Liquefaction phenomena were first recognized in the 1964 Niigata Earthquake.

In many cases, therefore, no anti-liquefaction measures had been implemented for embankments and soil in the reclaimed lands such as Tokyo Bay, Osaka Bay, and Ise Bay developed before the Niigata Earthquake.

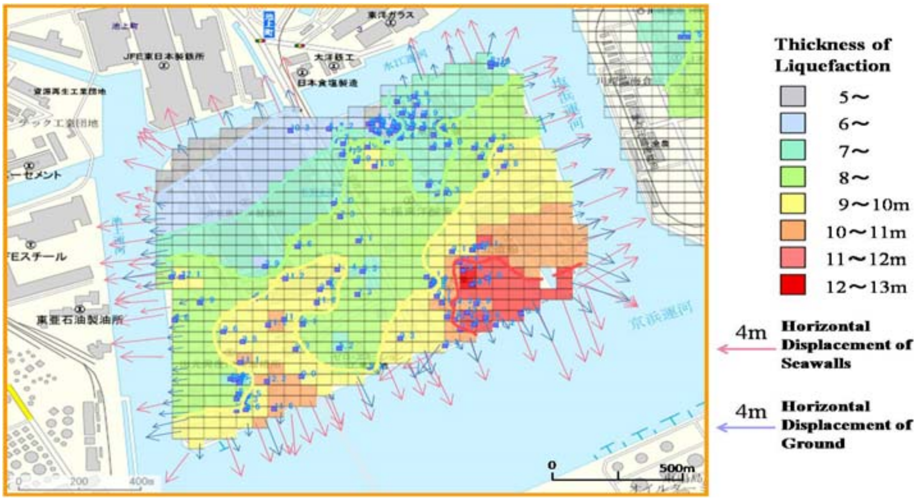

Figure 9. Displacement of Seawalls and Ground due to Liquefaction (Kawasaki City)

Figure 9 is one example for the movement of seawalls and ground surface displacements which were estimated for the Northern Tokyo Bay earthquake (M: 7.5) in the artificial island of Kawasaki city in the Tokyo Bay. The seawall was estimated to move up to 7 meters into sea. On this Island, many tanks and chemical complex facilities still exist. Liquefaction may flow into marine waters, causing a marine fire in the worst-case scenario.

6 CONCLUSIONS

We, the scientists and engineers in earthquake and tsunami disaster reduction field made an irreparable mistake for the earthquake and tsunami prediction to save human lives and properties against the disaster. For the huge disasters, it is clear that the different approach in necessary. Instead of protecting against any loss of live, trying to save as many lives as possible becomes the most important goal.

First thing which we have to do is to carefully grasp the whole aspect of the disaster and to deliver the exact information to the researchers in the seismological and earthquake engineering all over the world. It is important to communicate to the international community correct information on safety and security. Also, investigation reports of impacts of this catastrophic disaster will provide to people around world. Second thing is to investigate into study on the causes of the disaster. It is necessary to study what are the differences between the causes of the 2011 East Japan earthquake from the previous ones. Moreover, although tsunami warning was announced, many people who were in plains did not have time to evacuate to higher ground. There were also cases of people losing their lives due to failing to perform necessary evacuation behaviors. Moreover, third one is to promote the researches and measures against future earthquakes and tsunami under a close cooperation between the researches and practitioners in various fields such as science, engineering, social science, medical sector, etc. We have to strengthen our international collaboration to create safe and secure society in the world. Instead of relying on hardware approach such as improving and strengthening buildings, the disaster prevention puts emphasis on software approach such as improvements to warning systems and more thorough evacuation education.

REFERENCES

M. HAMADA. 2005. The Damage Unduced by Sumatra Earthquake and Associated Tsunami of December 26, 2004. *Japan Society of Civil Engineers*: August.

M. HAMADA. 2009. Global Increase of Natural Disasters and The Recommendations by the Science Council of Japan for the Creation of Safe and Secure Society. *3rd WFEO-JFES-JSCE Joint International Symposium Disaster Risk Management*: 1-6.

Effectiveness of Polypropylene Fiber Reinforced Cement Composite for Enhancing the Seismic Performance of Bridge Columns

K. Kawashima & R. Zafra
Department of Civil Engineering, Tokyo Institute of Technology, O-okayama, Meguro, Tokyo, Japan

T. Sasaki, K. Kajiwara & M. Nakayama
Hyogo Earthquake Engineering Research Center, National Research Institute for Earth Science and Disaster Prevention, Miki, Hyogo, Japan

ABSTRACT: This study investigates the effect of polypropylene fiber reinforced cement composite (PFRC) for enhancing the damage control and ductility capacity of a 7.5 m tall, 1.8 m by 1.8 m square bridge column subjected to 80% of the original intensity of the near-field ground motion recorded at the JR Takatori station during the 1995 Kobe, Japan earthquake using the E-Defense shake table. PFRC is a mixture of cement mortar and short discontinuous polypropylene fibers. Compared to the brittle failure of concrete in tension, PFRC exhibits ductile failure due to the formation of closely spaced micro cracks and the bridging action of fibers. The use of PFRC at the plastic hinge region mitigated cover and core concrete damage, local buckling of longitudinal bars and deformation of ties even after six times of repeated excitation. The damage sustained was much less than the normal damage of regular reinforced concrete columns.

1 INTRODUCTION

A large scale bridge experimental program was conducted in 2007-2010 by the National Research Institute for Earth Science and Disaster Prevention (NIED), Japan (Nakashima et al. 2008). In the program, shake table experiments were conducted for two typical reinforced concrete columns which failed during the 1995 Kobe, Japan earthquake (C1-1 and C1-2 experiments), a typical reinforced concrete column designed in accordance with the 2002 Japan design code (JRA 2002) (C1-5 experiment) and a new generation column using polypropylene fiber reinforced cement composites for enhancing the damage control and ductility (C1-6 experiment). The experiments were conducted using the E-Defense shake table where the table is 20 m by 15 m and has a payload of 1200 tf (12 MN). The maximum stroke of the table is 1 m and 0.5 m in the lateral and vertical directions, respectively. It was designed so that the ground motions during the 1995 Kobe earthquake can be generated.

C1-5 experiment was conducted using the E-Defense shake table with a ground motion 80% of the original intensity of the near-field ground motion recorded at the JR Takatori station during the 1995 Kobe earthquake. This is referred herein as the E-Takatori ground motion. The column performed satisfactorily under this ground motion. However, when the excitations were repeated under much stronger intensity and longer duration near-field ground motion, the column suffered extensive damage with blocks of crushed core concrete spilling out like explosion from the steel cage (Kawashima et al. 2010). Such failure was never seen in past quasi-static cyclic or hybrid loading experiments. Therefore, it is expected to develop columns which contribute to construct damage free bridges using materials that mitigate such damage under severe seismic loading.

Prior to the C1-6 experiment, a series of cyclic loading experiments were conducted on 1.68 m high, 0.4 m by 0.4 m square cantilever regular high strength concrete column and a column each using steel fiber reinforced concrete and polypropylene fiber reinforced cement composite at the plastic hinge region and the footing for deciding the material of C1-6 column (Kawashima et al. 2011). The polypropylene fiber reinforced cement composite column had superior performance in mitigating cover and core concrete damage, longitudinal bar buckling and deformation of tie bars at the plastic hinge region resulting from the crack control capability of polypropylene fiber reinforced cement composite. As a result, C1-6 column was built using polypropylene fiber reinforced cement composite at the plastic hinge region and a part of the footing.

High performance fiber reinforced cement composites (HPFRCC) are materials that exhibit multiple fine cracks upon loading in tension which leads to improvement in toughness, fatigue resistance and deformation capacity (Matsumoto & Mihashi 2002). Engineered cementitious composite (ECC) is an HPRCC that has tensile strain capacity of about 0.03 to 0.05 resulting from the formation of closely spaced micro cracks due to the bridging action of fibers (Li & Leung, 1992). It has low elastic stiffness compared to concrete, and larger strain at peak compressive strength, due to the absence of course aggregates (Li et al. 1995). Polypropylene fiber reinforced cement composite, referred herein as PFRC, belongs to the class of ECC.

Previous investigations have shown the positive effects of using HPFRCC for structural members subjected to seismic loads. Kosa et al. (2007) examined the use of this material with polyvynil alcohol (PVA) fibers for the seismic strengthening of scaled bridge piers similar to concrete jacketing. They found that a pier using PVA-HPFRCC on the cover concrete can provide confinement effect as much as the pier whose entire cross section was constructed of this material. Furthermore, the deformation capacity and the energy absorption capacity were also significantly improved compared with a pier constructed of ordinary concrete.

Saiidi et al. (2009) investigated the effect of incorporating ECC with polyvynil alcohol (PVA) fibers and shape-memory alloys (SMA) on model columns subjected to cyclic loading. Use of PVA-ECC substantially reduced damage in the plastic hinge. Furthermore, the combination of PVA-ECC and SMA led to larger drift capacity compared to the conventional steel reinforced concrete column.

This study aims to investigate the effectiveness of PFRC for enhancing the damage control and ductility capacity of a full-size bridge column subjected to a strong near-field ground motion using the E-Defense shake table. This column is called herein as C1-6 column. The information obtained from the shake table experiments can provide reliable data for verification of structure performance and can provide an insight on the response of such structures subjected to real earthquake conditions.

2 E-DEFENSE SHAKE-TABLE EXCITATIONS

2.1 *Column configuration and properties*

C1-6 column is a 7.5 m tall, 1.8 m by 1.8 m square, cantilever column shown in Figure 1. It was designed based on the 2002 Japan design code assuming moderate soil condition under the Type II design ground motion (near-field ground motion). PFRC was used at a part of the footing with a depth of 0.60 m below the column base and a depth of 2.7 m above the column base to minimize the cost. The 2.7 m depth of PFRC is three times the code specified plastic hinge length of one-half the column width (0.90 m). This height was set to avoid failure at the PFRC-concrete interface. The 0.60 m depth of PFRC at the footing was provided to minimize damage. Regular concrete with design compressive strength of 30 MPa was used in the other parts of the column. The actual 28-day cylinder compressive strength of concrete was 41 MPa.

The design compressive strength of PFRC was 40 MPa. PFRC was made by combining cement mortar, fine aggregates with maximum grain size of 0.30 mm, water and 3% volume of polypropylene fibers. Monofilament polypropylene fibers with diameter of 42.6 μm, length of 12 mm, tensile strength of 482 MPa, Young's modulus of 5 GPa and density of 0.91 kg/m^3 were used (Hirata et al. 2009). Superplasticizers were added to improve the workability of the mix. The actual 28-day cylinder compressive strength of PFRC was 36 MPa with a strain at peak of 0.47%.

Eighty-35 mm diameter deformed longitudinal bars were provided in two layers. The corresponding reinforcement ratio ρ_l was 2.47%. The nominal yield strength of longitudinal bars was 345 MPa (SD345) and the actual yield strength was 386 MPa at 0.2% strain. Deformed 22 mm diameter ties with 135 degree bent hooks lap-spliced with 40 times the bar diameter were provided. The outer ties were spaced at 150 mm and the inner ties were spaced at 300 mm throughout the column height. Cross-ties with 180 degree hooks at 150 mm spacing were provided as shown in Figure 1 to increase confinement of the square ties. Volumetric tie reinforcement ratio ρ_s within a height of 2.7 m from the column base was 1.72%. The nominal yield strength of ties was 345 MPa (SD345) and the actual yield strength was 396 MPa at 0.2% strain. Concrete cover of 150 mm was provided.

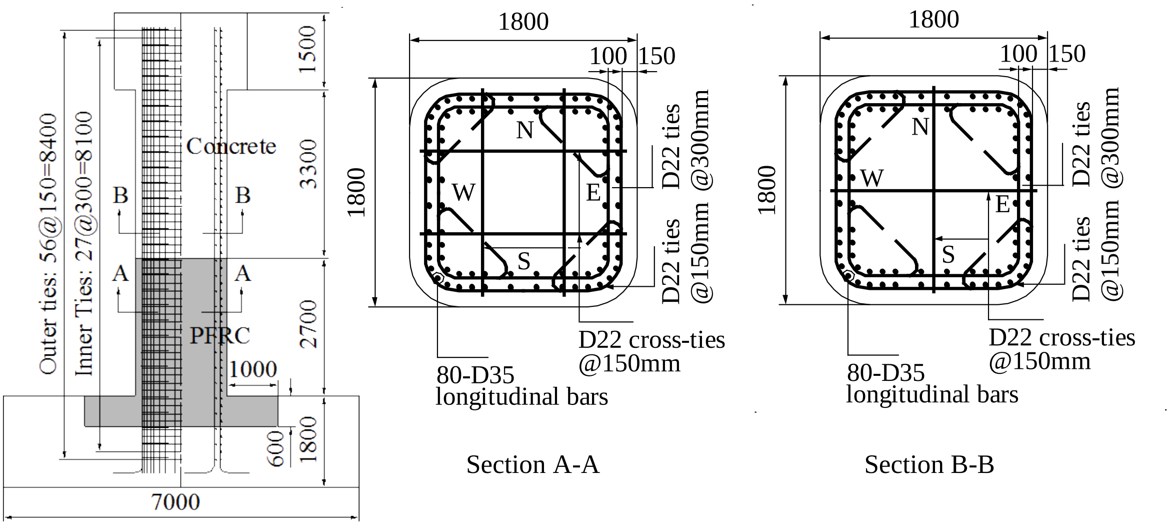

Figure 1. C1-6 column configuration and dimensions (mm)

2.2 *Experiment set-up and shake-table excitations*

Photo 1 shows the experiment set-up using the E-Defense shake table. Four mass blocks were set on the column through two simply supported decks. Note that the decks were not designed to idealize the stiffness and strength of real decks. Each deck was supported by the column on one side and by the steel end support on the other side. Tributary mass to the column by two decks including four weights was 307 tf (3011 kN) and 215 tf (2109 kN) in the longitudinal and transverse directions, respectively. The column was excited using the E-Takatori ground motion with the EW, NS and UD components, shown in Figure 2, applied in the longitudinal, transverse and vertical directions of the column, respectively. This ground motion is referred herein as the 100% E-Takatori ground motion.

Photo 1. Experiment set-up using E-Defense shake table

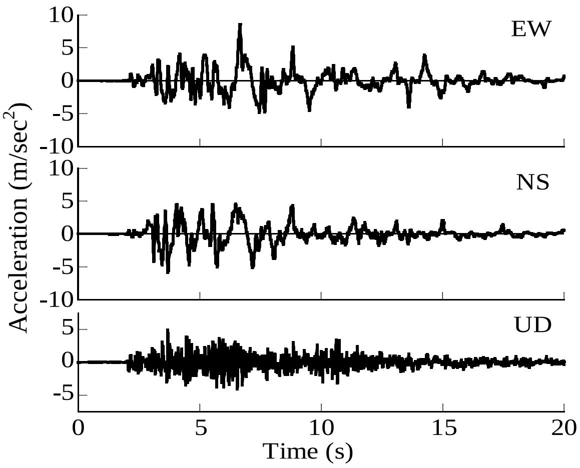

Figure 2. E-Takatori ground motion

Shake table excitations were conducted six times. Excitations were repeated to clarify column performance when subjected to much stronger and longer duration near-field ground motion. The column was excited twice with 100% E-Takatori ground motion (1-100%(1) and 1-100%(2) excitations). After the mass in the longitudinal direction was increased by 21% from 307 tf (3011 kN) to 372 tf (3649 kN), excitations were conducted with 100% E-Takatori ground motion once (2-100% excitation) and 125% E-Takatori ground motion three times (2-125%(1), 2-125%(2) and 2-125%(3) excitations).

3 EFFECT OF POLYPROPYLENE FIBER REINFORCED CEMENT COMPOSITE ON COLUMN SEISMIC PERFORMANCE

3.1 *Progress of failure*

Photos 2 to 4 show the damage progress within 1.2 m from the column base at the SW and NE corner during 1-100%(1), 2-100% and 2-125%(3) excitations at the instance of peak response displacement where the SW corner was subjected to compression while the NE corner was subjected to tension. As shown in Photo 2, during 1-100%(1) excitation, only micro cracks were observed around the column. During 1-100%(2) excitation, very thin flexural cracks as wide as 0.1 - 0.2 mm occurred within 1.6 m from the base all around the column.

During 2-100% excitation, with the mass increased by 21%, damage progressed as shown in Photo 3. Flexural cracks propagated and a crack 0.6 m from the column base at the NE corner opened about 8 mm at the peak response displacement. After the excitation, the maximum residual crack at the above location was 1 - 2 mm wide. Although only flexural cracks occurred all around the column with the cover concrete remaining as a whole shell due to the bridging action of fibers, vertical hairline cracks started to occur at the NE and SW corners within 0.6 m from the column base due to the large strut action of cover concrete shell resulting from the footing reaction when the column was laterally displaced.

During 2-125%(1) excitation, in which the seismic excitation intensity was increased by 25%, at the peak response displacement, the crack 0.6 m from the base opened to 14 mm at the NE corner which was subjected to tension while a vertical crack opened to 9 mm at the opposite SW corner subjected to compression. As the loading progressed, at the SW corner subjected to tension, a crack 1.2 m from the base opened to 9 mm and vertical cracks started to widen at the opposite NE corner.

Succeeding excitations resulted to further propagation of flexural cracks within 2 m from the base around the column and the widening of the vertical crack at the SW corner. As shown in Photo 4, the damage progressed during 2-125%(3) excitation wherein at the peak response displacement, the crack 0.6 m from the base at the NE corner opened to 20 mm and the vertical crack at the SW corner opened to 15 mm. Note that at the NW corner, cover concrete spalled within 200 mm from the column base when it was subjected to compression while flexural cracks opened to 13 mm at the opposite SE corner subjected to tension. After the excitation, the cracks which opened to over 10 mm during the excitation almost closed with widths of only 5 - 8 mm in flexural cracks and 7 - 12 mm in vertical cracks. Moreover, majority of other small cracks closed to hairline cracks after the excitations due to the fiber bridging action of fibers. Cover concrete spalling was much restricted and there were no exposed longitudinal bars and ties in C1-6 column after 2-125%(3) excitation.

(a) SW corner (b) NE corner

Photo 2. Column damage during 1-100%(1) excitation

(a) SW corner (b) NE corner

Photo 3. Column damage during 2-100% excitation

(a) SW corner (b) NE corner

Photo 4. Column damage during 2-125%(3) excitation

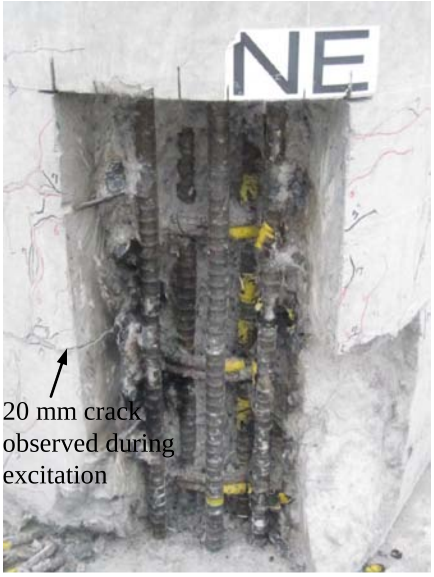

(a) Opened section at NE corner

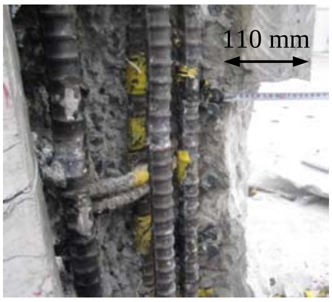

(b) Longitudinal bar buckling

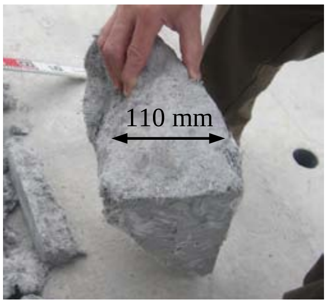

(c) PFRC cover concrete block

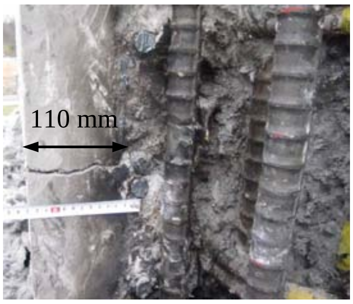

(d) Crack on PFRC cover concrete

Photo 5 Damage of PFRC cover concrete and buckling of longitudinal bars at the NE corner after 2-125%(3) excitation

To investigate how the damage progressed in the core and in the longitudinal bars at the NE corner after 2-125%(3) excitation, the column was opened at the area shown in Photo 5. Note that removal of cover concrete in the fiber mixed concrete was very difficult because of its solid nature compared to that of regular reinforced concrete.

In Photo 5, only the outer and inner longitudinal bars and inner ties can be seen because outer ties and a part of the PFRC cover concrete were removed. Maximum lateral offset among three outer longitudinal bars from their original vertical axis was 8 mm. On the other hand, the inner longitudinal bars did not buckle because they were constrained by the undamaged concrete between the outer and inner longitudinal bars. At the SW corner which was subjected to the largest compression during the peak response displacement, the maximum lateral offset of the outer longitudinal bars due to local buckling was 5 mm which was much less than the buckling of bars at the NE corner. In general, local bar buckling was limited.

At the location where crack opening of 20 mm was observed, it was found that the crack occurred only in the PFRC cover concrete with a depth of 110 mm and did not propagate into the core concrete. Also shown is the block of cover concrete that was removed at the bottom right portion where the presence of fibers held the cover concrete together preventing the disintegration of cover concrete. Hence, it is worthy to note that even after six times of excitation, the damage sustained by C1-6 column was much less than the damage of regular reinforced concrete columns.

3.2 *Response acceleration and displacement*

The principal response angle θ_P is defined to identify the principal response direction when the maximum column response displacement occurs. It is given by

$$\theta_P = \tan^{-1}\left(\frac{u_{TR}}{u_{LG}}\right) \tag{1}$$

where u_{LG} and u_{TR} are the response displacements in the longitudinal and transverse directions, respectively.

Figure 3 shows the acceleration and displacement at the top of column in the principal response direction and Table 1 summarizes the peak acceleration, displacement, residual displacement and moment at each excitation. The principal response angle θ_P varied from 194 to 205 degrees during the six excitations which was almost at the NE-SW direction. The measured peak response acceleration during the series of excitations varied from 13-20 m/s^2.

Due to the high acceleration pulse in the input ground motion, the column experienced high amplitude displacement during each excitation. The peak response displacement was equal to 0.078 m (1% drift) during 1-100%(1) excitation and increased to 0.45 m (6% drift) during 2-125%(3) excitation. As the excitation progressed with increasing intensity of ground motion, the response displacements increased due to column stiffness deterioration resulting from the damage. The residual displacement was only -0.004 m (0.05% drift) after 2-100% excitation, increased to -0.037 m (0.49% drift) after 2-125%(2) excitation then decreased to -0.013 m (0.13% drift) after the last excitation. Since the allowable residual drift for a cantilever column based on the 2002 JRA code is 1%, the residual drift of the column was still smaller than the allowable limit. It is important to note that residual displacement not only increases but also decreases during seismic excitations because it is more affected by the ratio of post elastic stiffness to elastic stiffness as well as the instantaneous structure period (MacRae & Kawashima 1997).

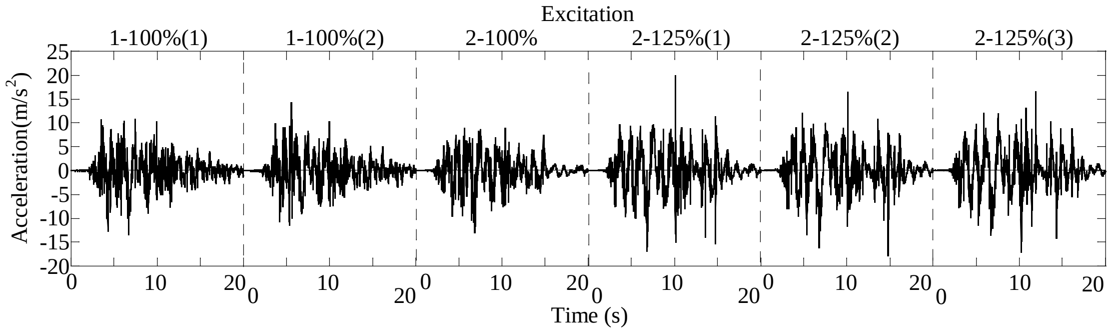

(a) Response acceleration

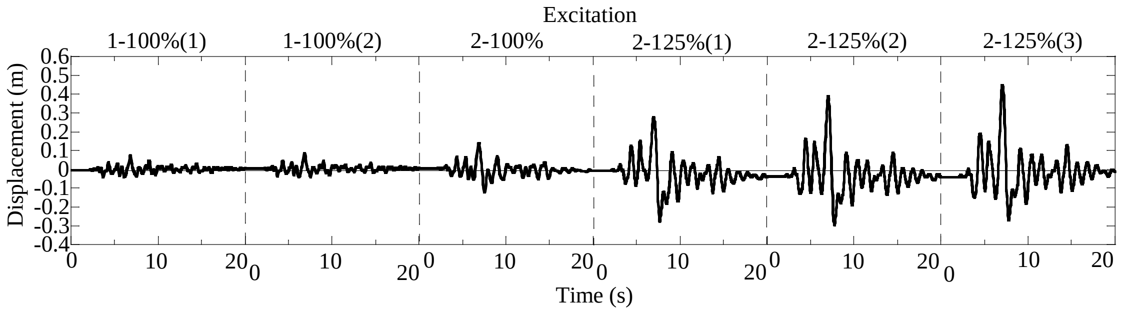

(b) Response displacement

Figure 3. Column response acceleration and displacement in the principal direction

Table 1. Column response in the principal direction

Excitation	θ_P (Degrees)	$\ddot{u}_P$ (m/s^2)	u_P (m)	u_P Drift (%)	Residual displacement (m)	M_P (MNm)
1-100%(1)	201.9	-13.4	0.078	1.0	0.005	20.5
1-100%(2)	193.5	14.2	0.089	1.2	0.007	21.8
2-100%	196.0	-13.0	0.144	1.9	-0.004	24.0
2-125%(1)	201.1	19.9	0.280	3.7	-0.035	24.3
2-125%(2)	204.8	-17.9	0.392	5.2	-0.037	25.3
2-125%(3)	204.6	-17.1	0.450	6.0	-0.013	24.9

3.3 *Moment and ductility capacity*

The bending moment at the column base was evaluated as

$$M_k = M_{Bk} + M_{Ck} \tag{2}$$

where M_{Bk} and M_{Ck} represent the moment based on measured load cell forces and based on pier and column mass accelerations, respectively, and are given by

$$M_{Bk} = \sum_{i=1}^{N} \{F_{Lki} h_{Li} - V_{Li}(x_{ki} + u_k)\} \tag{3}$$

$$M_{Ck} = \int_0^{h_B} m_C \ddot{u}_{Ck} dz + \int_{h_B}^{h} m_B \ddot{u}_{Bk} dz \tag{4}$$

where F_{Lki} is the inertia force measured by the i-th load cell in the k direction ($k =$ LG and TR corresponding to the longitudinal and transverse directions, respectively); V_{Li} is the vertical force measured by the i-th load cell in the k direction; h_{Li} is the height from the base to the i-th load cell; x_{ki} is the load cell coordinate in the k direction from the column center; u_k is the response displacement at top of column in the k direction; N is the load cell number ($N = 32$); z is the coordinate of the column from the base upward; m_C and m_B are the mass per unit length of the column and pier cap, respectively; $\ddot{u}_{Ck}$ is the column acceleration response; $\ddot{u}_{Bk}$ is the pier cap acceleration response; h_B is the height from base to the bottom of the pier cap and h is the height from base to the top of pier cap.

Figure 4 shows the hysteresis of moment at the base vs. displacement at the top of the column in the principal response direction. The hysteresis during the entire six times of excitation is stable with sufficient energy dissipation. As summarized in Table 1, the peak moment gradually increased as the excitation progressed. A maximum capacity of 25.3 MNm at 5.2% drift was developed during 2-125%(2) excitation. During this excitation, flexural cracks further propagated all around the column and the vertical cracks at the SW corner widened as described in 3.1. During the subsequent 2-125%(3) excitation, the peak drift increased to 6% while the peak moment slightly deteriorated by 2%. It should be noted that even during the 2-125%(3) excitation, the moment vs. lateral displacement hysteresis was still very stable.

3.4 *Strains of longitudinal and tie bars*

Figure 5 shows strains of longitudinal and tie bars of C1-6 column at the plastic hinge zone (300-400 mm from the base) at the SW corner where the most extensive damage occurred. Only strains during 1-100%(1), 2-100%, 2-125%(1) and 2-125%(3) excitations are shown due to space limitation. Because longitudinal bars were set in two layers, strains of both the outer and inner longitudinal bars and tie bars are shown here. Noting that the yield strain of both longitudinal and tie bars was nearly 2,000 μ, the longitudinal bars started to yield in tension during 1-100%(1) while tie bars started to yield in tension during 2-125%(1) excitation. The outer and inner longitudinal bars and tie bars exhibited similar response however the amplitude of strains were generally larger in the outer longitudinal and tie bars than the respective inner longitudinal and tie bars.The difference of strain amplitude between outer and inner tie bars is particularly large during and after 2-125%(1) excitation resulting from local buckling of longitudinal bars, which will be described later.

An interesting point in Figure 5 is that the compression strains of the outer and inner longitudinal bars were nearly the same with tension strains during the early excitations. For example, the compression strain of the outer longitudinal bar was 1,800 μ while the tension strain was 1,400 μ during 1-100%(1) excitation. This obviously resulted from the low elastic modulus of PFRC. Resulting from further softening and failure of core concrete, the compression strains of the outer and inner longitudinal bars progressed during 2-125%(1) excitation. Thus, compression strain of the outer longitudinal bar reached 19,000 μ while tension strain reached 18,000 μ during 2-125%(1) excitation. The large compression strain must have caused the outer longitudinal bar to buckle. Note however that in spite of the bar buckling as described in 3.1, spalling of cover concrete did not occur indicating that the presence of fibers made the cover concrete remain as a whole shell.

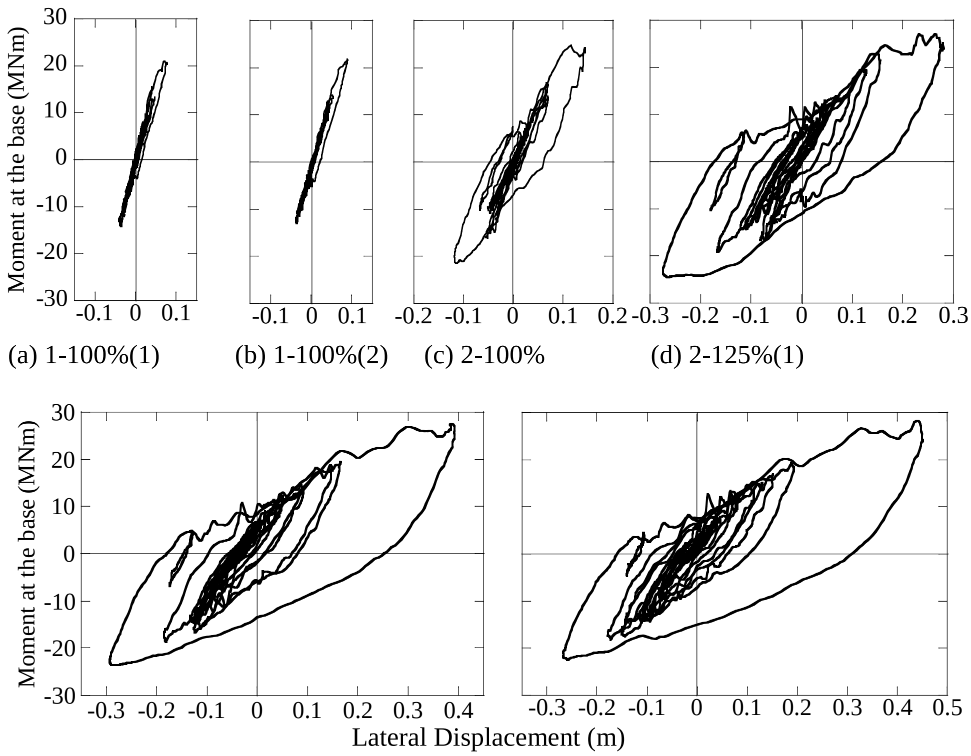

(a) 1-100%(1) (b) 1-100%(2) (c) 2-100% (d) 2-125%(1)

(e) 2-125%(2) (f) 2-125%(3)

Figure 4. Hysteresis of moment at the base vs. displacement at the top of column in the principal direction

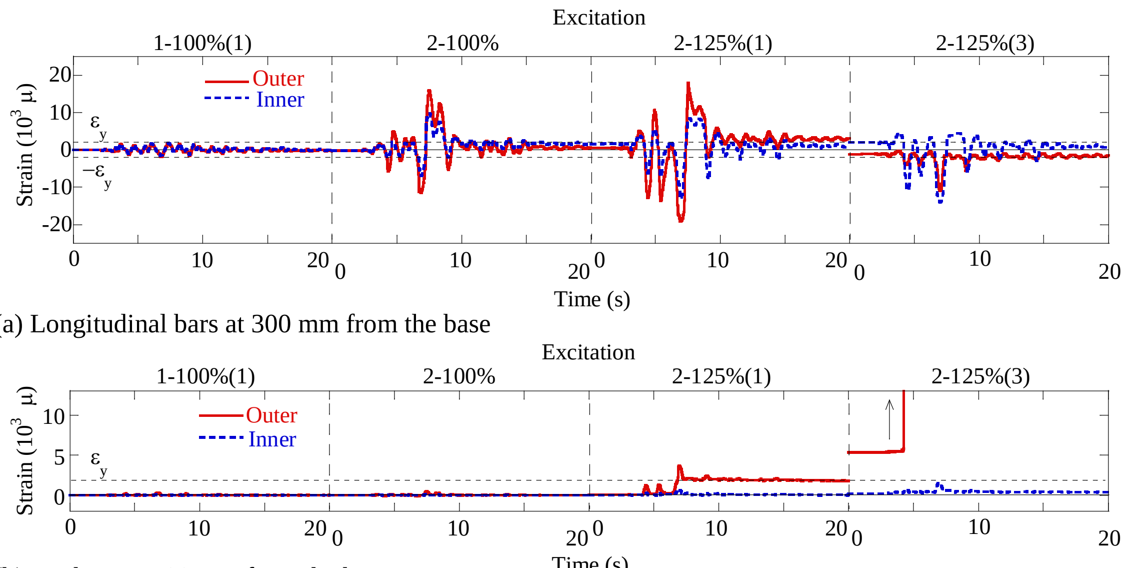

(a) Longitudinal bars at 300 mm from the base

(b) Tie bars at 400 mm from the base

Figure 5. Strains of longitudinal bars and tie bars at the SW corner during 1-100%(1), 2-100%, 2-125%(1) and 2-125%(3) excitations

On the other hand, the tie bar was still elastic during 1-100%(1) until 2-100% excitations. At the instance when compression strain of the outer longitudinal bar sharply increased during 2-125%(1) excitation, the outer tie strain started to increase to 3,700 μ, indicating that the tie resisted the longitudinal bar buckling. Compression strain of the inner longitudinal bar also sharply increased at the same time, however, the inner tie strain did not increase indicating that the inner longitudinal bar did not buckle. This was because confinement for bar buckling was larger at the inner longitudinal bar than the outer longitudinal bar due to the resistance of core concrete between outer and inner ties which was still intact as shown in Photo 5.

Figure 6 further shows the interaction of a longitudinal bar with a tie bar for outer and inner bars. The tie strains during 2-125%(3) excitation were larger than 5,000 μ and only reliable data are shown here. A sharp increase of the outer tie strain resulting from restraining local buckling of the outer longitudinal bar under high compression strain is clearly seen during and after 2-125%(1) excitation while the inner tie strain remained below 2,000 μ because inner longitudinal bars did not yet buckle.

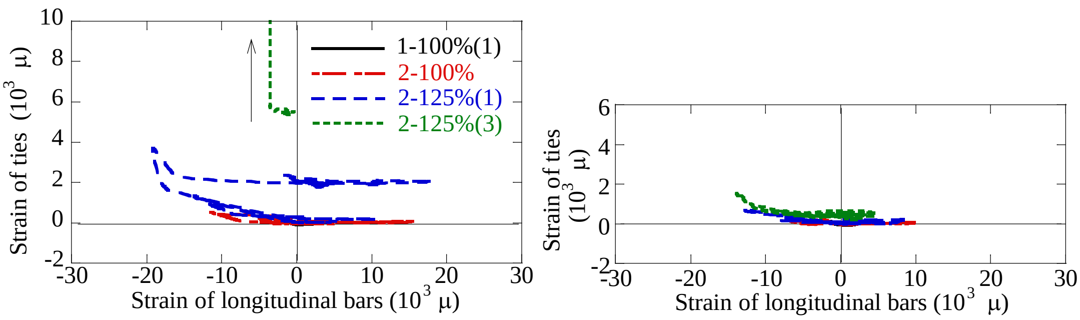

(a) Outer bars (b) Inner bars

Figure 6 Strain of a tie at 400 mm from the base vs. strain of a longitudinal bar at 300 mm from the base at the SW corner of C1-6 column

4 CONCLUSIONS

A series of shake table experiments of a full-size bridge column using polypropylene fiber reinforced cement composites (PFRC) at the potential plastic hinge and part of the footing, referred herein as C1-6 column, were conducted. Based on the results presented, the following conclusions were deduced:

1. PFRC did not have the brittle compression failure of regular reinforced concrete under repeated large inelastic deformation due to the bridging mechanism of fibers. This prevented the brittle crushing of cover and core concrete.
2. As a consequence of a), the use of PFRC reduced buckling of longitudinal bars and deformation of tie bars thus mitigating the damage of C1-6 column even after six times of strong excitations.
3. As a result of the damage mitigation properties of PFRC, the column had a stable flexural capacity and enhanced ductility reaching until 6% drift.

REFERENCES

Japan Road Association 2002. *Specifications for Highway Bridges*. Maruzen: Tokyo.

Hirata, T., Kawanishi, T., Okano, M. & Watanabe, S. 2009. Study on material properties and structural performance of high-performance cement composites using polypropylene fiber. *Proc. Japan Concrete Institute* 31(1): 295-300.

Kawashima, K., Sasaki, T., Ukon, H., Kajiwara, K., Unjoh, S., Sakai, J., Kosa, K., Takahashi, Y., Yabe, M. & Matsuzaki, H. 2010. Evaluation of seismic performance of a circular reinforced concrete bridge column designed in accordance with the current design code based on e-defense excitation. *Journal of Japan Society of Civil Engineers* 65(2): 324-343.

Kawashima, K., Zafra, R., Sasaki, T., Kajiwara, K. & Nakayama, M. 2011. Effect of polypropylene fiber reinforced cement composite and steel fiber reinforced concrete for enhancing the seismic performance of bridge columns. *Journal of Earthquake Engineering* (accepted for publication).

Kosa, K., Wakita, K., Goda, H. & Ogawa, A. 2007. Seismic strengthening of piers with partial use of high ductility cement. In C. U. Grosse (ed.), *Advances in construction materials*: 269-277. Springer: Berlin Heidelberg.

Li, V. & Leung, C. 1992. Steady-state and multiple cracking of short random fiber composites. *Journal of Engineering Mechanics*, *ASCE* 118(11): 2246-2264.

Li, V., Mishra, D. & Wu, H. 1995. Matrix design for pseudo-strain-hardening fibre reinforced cementitious composites. *Materials and Structures* 28: 586-595.

MacRae, G. & Kawashima, K. 1997. Post-earthquake residual displacements of bilinear oscillators. *Earthquake Engineering and Structural Dynamics* 26: 701-716.

Matsumoto, T. & Mihashi, H. 2002. JCI-DFRCC summary report on dfrcc terminologies and application concepts *JCI International Workshop on Ductile Fiber Reinforced Cementitious Composites – Application and Evaluation*. Takayama: Japan.

Nakashima, M., Kawashima, K., Ukon, H. & Kajiwara, K. 2008. Shake table experimental project on the seismic performance of bridges using E-Defense. *14th World Conference on Earthquake Engineering*. Paper S17-02-010 (CD-ROM). Beijing: China.

Saiidi, M., O'Brien, M. & Sadrossadat-Zadeh, M. 2009. Cyclic response of concrete bridge columns using superelastic nitinol and bendable concrete. *ACI Structural Journal* 106(1): 69-77.

The European research project SYNER-G: Systemic seismic vulnerability and risk analysis for buildings, lifeline networks and infrastructures safety gain

K. Pitilakis
Coordinator of SYNER-G project,
Department of Civil Engineering, Aristotle University of Thessaloniki, Greece

ABSTRACT:

SYNER-G (2009-2011) is a European Collaborative Research Project focusing on the systemic seismic vulnerability and risk analysis of buildings, lifelines and infrastructures. It is integrated across different disciplines with an internationally recognized partnership from Europe, USA and Japan. The 14 participants in the consortium represent a variety of organizations, from universities and academic institutions to research foundations and SMEs. The objectives and the deliverables are focused to the needs of the administration and local authorities, which are responsible for the management of seismic risk, as well as the needs of the construction and insurance industry.

SYNER-G proposes to develop an integrated general methodology and a comprehensive simulation framework for the vulnerability assessment and the evaluation of the physical and socio-economic impact and losses of an earthquake, allowing also for consideration of multiple interdependent systems within the infrastructure. The end result will be implemented into an open, modular and expandable software package for effective seismic risk management.

Webpage: http://www.syner-g.eu

1 MOTIVATION

- Past and ongoing research on the vulnerability assessment and seismic risk analysis of assets and urban systems is focused on individual elements exposed at risk.
- Systemic vulnerability and the associated increased impact and losses have not been considered so far in a rigorous and unified way for all kind of systems.
- There is an urgent need to develop fragility functions for all elements at risk in the European context respecting the European distinctive features.
- The physical and socio-economic vulnerability and losses of independent elements at risk is far from being studied in a homogeneous and coherent way.
- There is a need in Europe to develop a unified tool to evaluate seismic vulnerability and losses considering both physical and socio-economic aspects.

SYNER-G is proposing to tackle these needs in order to improve the European know-how and to propose a unified methodology for the vulnerability assessment and loss estimate at system level.

2 MAIN OBJECTIVES

- Encompass all past and ongoing knowledge and know-how on this topic.

Past and ongoing research on the vulnerability assessment and seismic risk analysis of assets and urban systems (buildings, building aggregates, lifeline networks and infrastructures), at international, European and national level are focused on the vulnerability assessment of individual elements exposed at risk. The systemic approach considering intra and inter dependencies is necessary as it is well known that their effect on the actual losses is very important. Moreover the uncertainties associated with the proposed empirical, semi empirical and analytical vulnerability and loss estimate models are very important and further research is needed to improve them.

Expected results: Review of current state of the art, understanding of systemic vulnerability and risk and development of a general methodology including the inter and intra dependencies.

- Select the most advanced fragility functions and methods to assess the physical and societal-economic vulnerability of all assets.

There is an urgent need to develop appropriate fragility functions for all elements at risk in the European context respecting the European distinctive features of the elements at risk and the European seismotectonic characteristics.

Expected results: Appropriate fragility curves/functions are proposed for each element at risk (buildings, building aggregates, utility and transportation components and critical facilities) according to the typological features of European construction and practice.

- Propose the most appropriate means of selecting seismic scenarios at system level.

The seismic risk analysis of spatially distributed systems requires efficient intensity measures and simulation methods of ground motion fields including secondary effects (liquefaction displacements, landslides, etc).

Expected results: Development of an enhanced seismic hazard model adequate for spatially distributed systems to be implemented in SYNER-G methodology and tools.

- Develop a unified methodology to assess vulnerability at a system level

The basis and principles of a unified methodology, as well as appropriate tools, for systemic vulnerability assessment accounting for all components (structural and non-structural) exposed to seismic hazard, considering interdependencies within a system unit and between different systems as a whole at city and regional scale.

Expected results: A general methodology will be proposed, to evaluate and quantify vulnerability and losses considering systemic interdependencies, which will be further specified for each particular network.

- Develop methodology and tools to assess the socio economic vulnerability and losses.

Transfer the interdependencies and consequences of losses in physical systems (buildings, utility and transportation network components, critical facilities) to their direct and indirect consequences on society and economy as measurable indicators and values of socio-economic losses upon which policy and decision-making can take place.

Expected results: Methodology and tools to assess the socio-economic impacts due to seismic damages that influence preparedness and response activities in the context of short-term emergency relief and recovery (emergency shelter, health care facilities, transportation infrastructure, utility systems). Appropriate methodologies including indicator based systems for integrating socio-economic impacts with fragility functions and performance models.

- Build an appropriate open-source software and tool to deal with systemic vulnerability.

A new generation of tools is needed to allow owners, practicing engineers and researchers the means to carry out realistic risk assessment and to provide the ability to leverage investment in new methodologies and software infrastructure while enabling customization to local conditions.

Expected results: An appropriate open source and unrestricted access software tool where the SYNER-G methodology and tools will be implemented.

- Validate the effectiveness of the methodology and the tools to specific and well selected case studies at city and regional scale.

SYNER-G integrated methodology will be validated through the application in appropriately selected and well constrained test sites in city scale (Thessaloniki, Vienna), regional scale (a transportation network in North-Eastern Italy, an electric power transmission network in Central Italy and a gas pipeline network) and in complex systems (the harbor of Thessaloniki and a large hospital facility in Reggio di Calabria, Italy). The efficiency of SYNER-G will be measured largely in these engineering applications which surpass the present state-of-the-art.
Expected results: Verification of the systemic vulnerability assessment approach with applications at the selected case studies. Efficiency evaluation of the SYNER-G methodology and software tools.

- Propose guidelines and dissemination schemes for all products of the project.

SYNER-G will ensure the distribution and exploitation of results at all levels; to the scientific and technical earthquake engineering communities, dissemination and recommendations to policymakers and stakeholders, to the European Construction Industry (ECI) and the European Construction Technology Platform (ECTP), to insurance industry, public buildings administrators, associations and federations of European physical infrastructures and networks, dissemination of results toward the general public.
Expected results: Several technical guidelines will be prepared to use in practice and appropriate dissemination schemes at European and International level will be built for the entire community and administration entities. A dissemination plan for the output from the project, will be developed and implemented

3 PROJECT STRUCTURE

SYNER-G is designed with eight work packages (fig. 1): WP1-Project coordination and management; WP2 - Development of a methodology to evaluate systemic vulnerability; WP3- Fragility functions of elements at risk; WP4 - Socio-economic vulnerability and losses; WP5 - Systemic vulnerability specification; WP6 - Validation studies; WP7 - Build prototype software; WP8 - Guidelines, recommendations and dissemination.

The following test sites and systems are selected for application and to validate the efficiency of the methodology and tools: Thessaloniki in Greece; Vienna in Austria; Messina in Italy (for calibration of census and remote sensing data); a motorway system in North-East Italy (regional scale); an electric power network of regional extension in Central Italy; the gas system of L’Aquila in Italy; the harbor of Thessaloniki and a hospital facility in South Italy (Reggio di Calabria).

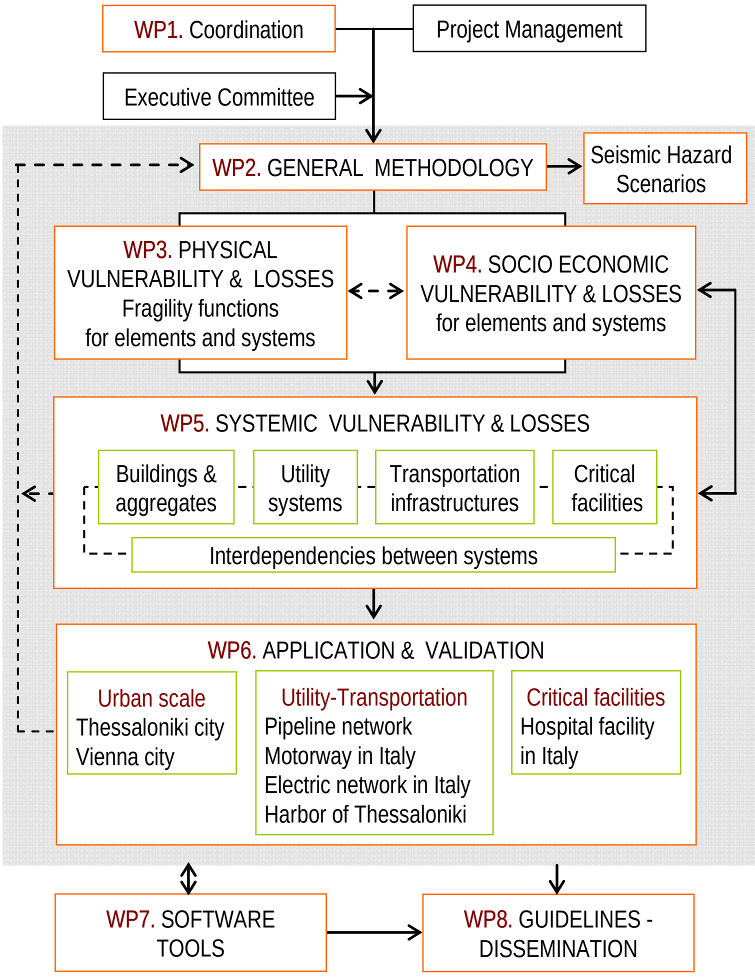

Figure 1. SYNER-G project general workflow.

4 SOCIO-ECONOMIC IMPACT AND WIDER SOCIETAL IMPLICATIONS

The high seismic vulnerability of humans and built environment in Europe and the lack of mitigation programs, together with the overall moderate to high or very high seismicity resulted to significant direct and indirect earthquake losses in the past 30 years with a rapidly growing tendency. The vulnerability assessment methodology proposed by SYNER-G will have considerable impact on the seismic risk assessment and mitigation in Europe. The vulnerability assessment considering system inter and intra dependencies is in general higher than individual vulnerability of the elements within each system or even at a system. This new and advanced approach and products will help to apply the mitigation measures in an optimized way which can make them more effective. The consequences, besides the reduction of loss of life will be considerably reduced economic and social losses. SYNER-G will have impact on the following levels:

- Technology: A unique advanced European approach will be created which is well advanced other approaches available in USA and Japan.
- Society: The protection and safety of the population will be considerably improved.
- Economy: The results will enable to improve European building environment, infrastructures and lifelines, thus avoiding excessive losses from earthquakes to come.
- Standards: A standard modular methodology will be created allowing a European approach to the subject and allowing application all over the continent and enabling the construction industry to improve the built infrastructure.
- ERA: The European Union will be enabled to implement greater economic integration with its neighbors and internationally who are also considerably in need of these new methodologies.

- International Collaboration: The results of the project will make collaboration with Europe more attractive particular from the view of the USA, Japan, China, India and other important countries. Europe will be enabled to take the lead on this subject.
- Technology Transfer: Europe will be seen as enabling the rising problems of mega cities in earthquake prone areas.

In particular the main results of SYNER-G will have the following impact:

- The development of a unified advanced methodology for the systemic vulnerability and loss assessment of buildings, utility and transportation networks and critical facilities due to seismic hazard at a European level, will help policy-setters and decision makers to optimize urban development and infrastructure planning and the efficiency of seismic risk mitigation strategies.
- The development of advanced methods and software for systemic vulnerability and loss assessment of buildings, lifelines and networks related to earthquakes will provide an increased understanding of the combined vulnerability of various societal elements at risk, including the inter-element and intra-system dependencies which generally increase vulnerability and losses. The validation of the tools through appropriate test sites will investigate their applicability and effectiveness in European level.
- The available fragility functions will be reviewed and evaluated in order to propose the most appropriate ones for all elements at risk or improve and in some cases develop new ones. This is a key step for the whole methodology which will include the setting up of adequate advanced fragility expressions considering the specific typological features of European elements and systems.
- The guidelines and recommendations concerning the fragility and loss assessment of individual elements at risk and the systemic vulnerability and losses of the entire networks and of a system of networks will constitute a European reference world-wide. They will provide guidance to stakeholders on where to direct research and development efforts and to allocate resources where uncertainties need to be reduced or where cost-effectiveness can be increased.
- The establishment of links and collaborative research between the engineering community (universities, research institutes and centers, companies) and the insurance industry will lead to significant developments regarding the financial and social losses due to earthquakes, and facilitate direct output to interested stakeholders with an immediate impact for decision makers and policymakers.
- The various dissemination activities and the web portal, together with the guidelines and recommendations will be the instruments to disseminate the latest developments in lifeline risk assessment and management and the proposed approaches and tools. In this way, a valuable toolbox will be provided to the decision-makers to assist the development of mitigation measures, while their implementation in practice will be encouraged, thus again contributing to changing the perception and confidence in risk management.

5 THE SYNER-G CONSORTIUM

Aristotle University of Thessaloniki (coordinator) (Greece), Vienna Consulting Engineers (Austria), Bureau de Recherches Geologiques et Minieres (France), Commission of the EC - Joint Research Centre (Belgium), Norwegian Geotechnical Institute (Norway), University of Pavia (Italy), University of Roma “La Sapienza” (Italy), Middle East Technical University (turkey), Analysis and Monitoring of Environmental Risks, University of Naples Federico II (Italy), Karlsruhe Institute of Technology (Germany), University of Patras (Greece), Willis Group Holdings (UK), Mid-America Earthquake Center, University of Illinois (USA), Research Center for Urban Safety and Security, Kobe University (Japan)

6 REFERENCES

SYNER-G, (2009-2011). Systemic Seismic Vulnerability and Risk Analysis for Buildings, Lifeline Networks and Infrastructures Safety Gain. Research Project, European Commission, 7th Framework Program, Contract Number: 244061.

PERPETUATE Project: the performance-based assessment for the earthquake protection of cultural heritage

S. Lagomarsino, C. Calderini & S. Cattari
Dept. of Civil, Environmental and Architectural Engineering, University of Genoa, Italy

H. Modaressi
Bureau de Recherches Géologiques et Minières, France

K. Pitilakis
University of Thessaloniki, Greece

V. Bosiljkov
University of Ljubljana, Slovenia

D. D'Ayala
University of Bath, UK

D. Benouar
University of Sciences and Technology Houari Boumediene, Algeria

G. Gazetas
Soil Mechanics Laboratory, National Technical University, Athens, Greece

S. Gostic
ZRMK, Ljubliana, Slovenia

R. Ginanni Corradini
Il Cenacolo, Rome, Italy

ABSTRACT: The paper describes the methodology proposed in the PERPETUATE Project (funded by the Seventh Framework Programme – Theme ENV.2009.3.2.1.1). The methodology proposed in PERPETUATE uses a displacement-based approach for the vulnerability evaluation and design of interventions. The use of safety verification in terms of displacement, rather than strength, orients to new strengthening techniques and helps in the comprehension of interaction between structural elements and unmovable artistic assets. The procedure is based on the following fundamental steps: definition of performance limit states, specific for the cultural heritage assets (considering both structural and artistic assets); evaluation of seismic hazard and soil-foundation interactions; construction knowledge (non-destructive testing, material parameters, structural identification); development of structural models for the seismic analysis of masonry structures and artistic assets and design of interventions; application and validation of the methodology to case studies. Two main scales are considered: the seismic risk assessment at territorial scale and at the scale of single historic building or artistic assets. The final aim of the project is to develop European Guidelines for evaluation and mitigation of seismic risk to cultural heritage assets.

1 INTRODUCTION

PERPETUATE (www.perpetuate.eu) is a project funded by the Seventh Framework Programme (Theme ENV.2009.3.2.1.1) developed by a consortium which includes 6 Universities, 2 Public Institutions and 3 SMEs. In particular, 5 European Countries (France, Greece, Italy, Slovenia, United Kingdom) and 1 International Cooperation Partner Country (Algeria) are represented[1]. The project will last from 2010 to 2012.

The driving ideas of the project are:

- adoption of a performance-based approach for the evaluation of seismic safety of cultural assets and the design of strengthening interventions;
- identification of proper safety levels for cultural heritage, considering both conservation and safety issues;
- minimization of strengthening interventions through increasing knowledge and improving modelling tools.

The name of the project derives from the idea that preventive actions must be adopted in order to PERPETUATE the life of monuments in seismic areas, in due time, before an earthquake interrupts their life forever.

The final aim of PERPETUATE is the development of European Guidelines for evaluation and mitigation of seismic risk to cultural heritage assets. In particular, the Italian "Guidelines for the evaluation and mitigation of seismic risk to cultural heritage" [1] will be the framework for the drawing up of this document. Focusing the attention on masonry structures, the project will face the problem for both architectonic assets (historic buildings or parts of them) and artistic assets (frescos, stucco-works, statues, pinnacles,…). Both seismic risk assessment at territorial scale, oriented to plan mitigation policies, and assessment of single cultural heritage assets, oriented to design suitable interventions, will be considered.

PERPETUATE methodology adopts a displacement-based approach. The use of safety verification in terms of displacement, rather than strength, suggests new strengthening strategies and helps in the comprehension of the interaction between structural elements and unmovable artistic assets.

The procedure is based on the following fundamental steps: 1) definition of performance limit states, specific for the cultural heritage assets (both structural and artistic assets are considered); 2) evaluation of seismic hazard and soil-foundation interactions; 3) construction knowledge (non-destructive testing, material parameters, structural identification); 4) development of structural models for the seismic analysis of masonry structures and artistic assets and for the design of interventions; 5) application and validation of the methodology to case studies. Experimental campaigns (in situ and indoor), considering also shaking table tests, will be carried out in order to support the formulation and validate the models.

In the following, the innovative contents concerning each step will be described.

2 PERFORMANCE LIMIT STATES FOR CULTURAL HERITAGE ASSETS

Many national and international technical rules and guidelines for the rehabilitation of existing buildings [2-6] have acknowledged the concepts of performance-based design. This approach allows the seismic design or upgrade of buildings with a realistic risk estimation (safety of life, occupancy, economic loss). Since earthquake is a rare environmental action, it must defined through a probabilistic approach (hazard scenario). Moreover, since it is impossible that ancient masonry constructions withstand without any damage to strong ground motions, the definition of proper performance levels is needed.

In FEMA documents [2], different rehabilitation objectives are identified, with various combinations of structural requirements and seismic action levels, divided into three categories (limited, basic safety, enhanced). In particular, four performance levels (operational performance, immediate occupancy, life safety, collapse prevention) are defined which precise exceedance probability values in 50 years (50%, 20%, 10% and 2% respectively) correspond to.

---

[1] University of Genoa, Italy – Coordinator; ENEA (Italian National Agency for new technologies, energy andsustainable economic development), Italy; Bureau de recherches géologiques et minières (BRGM), France; Aristotle University of Thessaloniki, Greece; National Technical University of Athens, Greece; University of Ljubljana, Slovenia; University of Bath, UK; University of Sciences and Technology Houari Boumediene, Algeria; Building and Civil Engineering Institute (ZRMK), Slovenia; Il Cenacolo S.r.l., Italy; Proind S.r.l, Italy.

In European codes, the concept of performance-based design is also present. In case of new buildings [4], two performance conditions are described: the damage limitation state and the ultimate limit state. These limit states are related to two different hazard levels: those related to an earthquake having probability of exceedance of 50% and 10% in 50 years, respectively. They may be set (using FEMA terminology) among the "limited objectives"; in fact, in the U.S. documents, the "basic safety objective" is reached only if also the collapse in case of the earthquake having probability of exceedance of 2% in 50 years is avoided. In case of existing buildings [5] three performance levels are considered; they are related to damage limitation, significant damage and near collapse conditions, which correspond to probabilities of exceedance of 20%, 10% and 2% in 50 years, respectively.

Even in Italy, the recent seismic decree [6] introduces performance-based design approach. In particular, in case of existing buildings, four performance levels are defined (corresponding to operational performance, damage limitation, life safety and collapse prevention conditions) which probabilities of exceedance are defined with reference to a reference life V_R value. If a reference life V_R of 50 years is considered, the values of 81%, 63%, 10% and 5% are obtained, respectively. In particular the reference life combines concepts associated to both the usable life (that is the time in which the building can be considered safe only assuring structural health monitoring and proper maintenance) and the use (occasional, frequent or frequent with crowding). The concept of reference life has been recently introduced in a new updated version of the Italian Guidelines [1]. The definition of a proper reference life is particularly important in case of cultural heritage assets since it is an efficient tool for timing mitigation strategies and balancing safety and conservation requirements keeping into account the cultural significance of assets

Moreover, with respect to the case of ordinary unreinforced masonry buildings, in case of cultural heritage assets, also the damage induced in artistic assets has to be taken into account by introducing proper performance levels related to(i.e. in case of frescos or decorative elements attached to masonry panels).

Need of preservation of cultural heritage and recent improvements in seismic codes impose to focus the attention on feasible procedures for safety assessment and design of possible interventions. Although the documents afore mentioned point out the need for a quantitative evaluation in case of historic buildings, they do not propose a specific methodology. The Italian Guidelines [1] partially try to overcome this lack; however, they simply outline a conceptual approach to this problem, lacking in the definition of operative models and in the identification of specific limit states for cultural heritage. Thus, the identification and definition of reliable measures of limit state are needed and represent an open issue for cultural heritage assets (e.g. in the case of artistic assets like as frescos, stucco-works, …).

In particular, among the seismic verification procedures proposed in the literature, the use of non linear static procedures, based on the evaluation of pushover curves (that is a force-displacement curve able to describe the overall inelastic response of the structure) is particularly encouraged. Performance levels (or limit states) may be defined on the pushover curve with reference to both structural elements and artistic assets. Once defined the earthquake hazard level, displacement demand may be then evaluated by referring to methods like as the Capacity Spectrum Method (as adopted in [7]), using an acceleration–displacement response spectrum properly reduced. Figure 1 summarizes, even in schematic way, this whole procedure.

In particular, in this context, PERPETUATE aims to define proper limit states for cultural heritage assets and the related reference seismic input, taking into account both human life safety and specific conservation requirements (aesthetics, serviceability, reparability, …). These limit states will be correlated to proper damage measures, specifically defined for the different cultural heritage assets, in order to allow safety verifications. As known, in case of masonry buildings damage measures are usually related to drift limits (shear deformation of masonry panels) or rotation limits (for out-of-plane mechanisms). In particular, at building scale, PERPETUATE intends to define damage measures for both single structural elements (i.e. piers, arches, vaults, domes) and the entire building; in this latter case, particular attention will be posed to the weigth associated to the different failure mechanisms which may occur (i.e. in plane and out-of-plane) and to the number of elements which are involved. Moreover, at artworks scale, the more original contributions are oriented to definition of damage measures for decorative elements and drift limits for frescos or stuccos. The experimental campaigns specifically addressed to this aim will constitute a fundamental support.

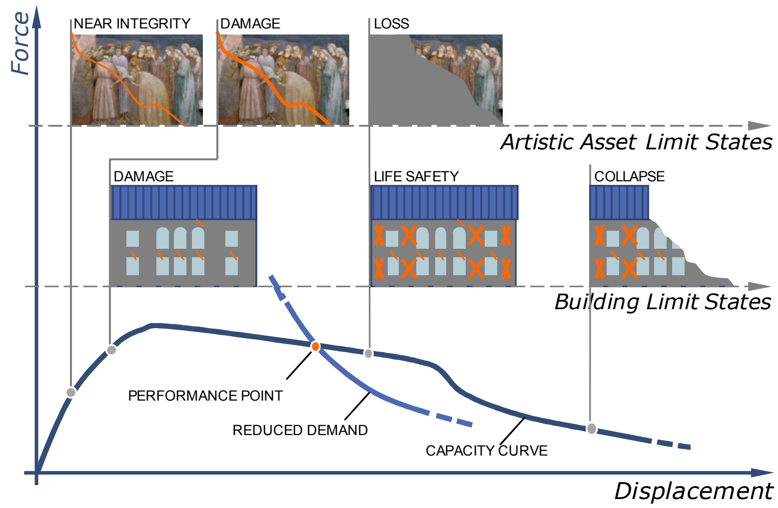

Figure 1: Displacement-based approach and performance levels definition on the pushover curve

3 EVALUATION OF SEISMIC HAZARD AND OF SOIL-FOUNDATION INTERACTION

In order to evaluate the displacement demand through non linear static procedure, the pushover curve needs to be compared with the seismic demand, properly defined. Thus, probabilistic and deterministic methods to assess seismic hazard and ground motion characteristics have to be combined with specific models to account for local soil and site effects including topography, soil non-linearity, basin edge effects and other important parameters regarding "source" and "path" effects. A good knowledge about the complexity of surface geology and the complex nature of earthquake generation process has a crucial effect on the reliability of the hazard maps. In fact, numerous and substantial uncertainties characterise all steps of seismic hazard assessment, independently of the method used.

In this context, PERPETUATE aims to define Demand Spectra for different soil categories and seismic hazard appropriate for masonry historic buildings of various types. Indeed, it is well known that seismic input cannot be defined by a single parameter (e.g. peak ground acceleration, macroseismic intensity); in addition to acceleration-displacement response spectra (ADRS), other intensity measures will be evaluated (Arias intensity, Housner intensity, various duration measures, number of cycles of motion). The seismic input will be defined for longer return periods than those adopted by codes for new buildings because lower annual probabilities of exceedance are desired for cultural heritage assets. This input motion will be generally higher than code-defined input motions.

In particular, a comprehensive set of numerical, analytical and experimental studies to evaluate the role of the foundation compliance and associated soil-foundation interaction (SFI) and soil-foundation-structure interaction (SFSI) effects in the response of massive masonry structures (monuments, building aggregates in historical centres) and their vulnerability assessment will be provided. The aim is to develop an improved foundation model for the vulnerability assessment of classified masonry structures and monuments. The role of the foundation and SFSI effects will be studied both for seismic ground shaking and induced permanent ground deformations.

4 CONSTRUCTION KNOWLEDGE

The knowledge phase of an existing building (or artwork) plays a fundamental role in the assessment of its structural safety. Lacks in knowledge are usually considered as uncertainties affecting the modelling of the structure. Thus, a decreasing degree of knowledge imposes to consider increasing safety factors and, thus, lower conventional resistances. In general, this means that a maximization of the knowledge of the structure (in term of geometry, material properties …) may lead to a minimization of the interventions to guarantee acceptable safety levels. For ordinary buildings, the choice knowledge/interventions is purely economic (ratio between knowledge and intervention costs). For cultural assets, this choice should take into account also conservation requirements, which impose, as far is possible, a minimization of the interventions. For the achievement of all these data, an effective on-site testing campaign by means of application of different test methodologies as a combination of DT (destructive tests), MDT (minor destructive tests) and NDT (non-destructive tests) needs to be performed. From the results of recently carried EU research project ONSITEFORMASONRY [8], where a comprehensive set of Guidelines and Recommendations for the application of different test methodologies in evaluation of the state of the structure and material was made, in PERPETUATE an extension will be made to optimize developed methodologies regarding achieved confidence factor and their cost effectiveness and to propose new methods for structural identification.

5 STRUCTURAL MODELS FOR THE SEISMIC ANALYSIS AND FOR THE DESIGN OF INTERVENTIONS

Starting from a literature review, the more suitable modelling strategies for the cultural heritage assets, both for the analysis of buildings or architectonic elements and for artistic assets, will be identify and classified. The displacement-based approach for the seismic analysis requires the development of nonlinear static procedures (pushover), in order to evaluate the capacity curve and identify the performance point. After a classification of different types of buildings, architectonic elements and artistic assets, reliable innovative mechanical models will be developed, capable to describe the non linear behaviour of the assets under seismic actions, till to their collapse. As known, the idealisation of the structure at the building scale may be performed considering: a) meshing of the material continuum (Finite Element Models); b) subdivision into significant structural elements (Structural Elements Models); c) predefined collapse mechanisms of rigid blocks. In the first two approaches, the pushover curve may be obtained by finite element incremental static analyses, while in the third one, an incremental equilibrium limit analysis (kinematic approach) may be adopted, by considering a set of varied displacement configurations. All these modelling strategies will be considered. Moreover, seismic verification procedures will be established overcoming some of the open issues present in literature related to their application to masonry historical structures (e.g. the evaluation of the sensitivity of the verification procedure in terms of target displacement in presence of flexible floors; the correlation of the displacement capacity of the structure to predefined limit states in the case of FEM models). In case of the analysis of out-of-plane local mechanisms, also the amplification of motion due to their position in the main building will be taken into account.

Operative procedures, practical tips and clarifying examples will be provided. Moreover the Soil Foundation Interaction results and the soil-foundation model will be included in the development of the general structural model.

Non linear models and modelling strategies developed will be used for the evaluation of effectiveness and reliability of the different interventions techniques, both traditional (like as insertion of tie-rods, new buttresses,….) and much more innovative. In particular, the performance-based approach will be adopted in order to assess the effect on the displacement capacity of the structure (performance approach vs. strength approach). It is important to broaden the knowledge on modelling historical structures with new, innovative modelling tools because modern codes are prepared mostly for new structures. In fact, applying the same models and safety factors proposed for new structures to historical structures is usually inappropriate and leads to invasive interventions, in order to assure seismic safety of historical buildings, which are in collision with conservation requirements. Moreover, particular attention will be paid to the modelling of the cultural assets at different scales, in order to evaluate the effect of interventions not only on the structure of the building but also on the unmovable cultural assets present in it.

Finally, in addition to models applicable at scale of the single assets, innovative methodologies for the vulnerability evaluation on a large number of assets (buildings and artworks) will be developed in order to develop mitigation strategies at territorial scale, defining priorities of interventions and providing criteria for the budget optimization. In particular, such methodologies will be based on quick surveys and will be focused on simplified mechanical models or statistical models (derived by damage assessment data, obtained by previous earthquakes).

6 APPLICATION AND VALIDATION OF THE METHODOLOGY TO CASE STUDIES

All results obtained by the previous steps will be collected in order to define an integrate methodology, to be validated and applied to case study areas. An innovative contribution is the procedure for estimation of uncertainties, both aleatory (randomness) and epistemic (due to incomplete, vague or imprecise information). In particular, epistemic uncertainties in the field of earthquake risk assessment require the development of adequate tools, by the use of logic tree approach, in which expert judgement compensates for the incompleteness of existing information. The final result is a range of capacity curves associated with weights, and the choice of the fragility curve for the risk evaluation can be made by using the fuzzy set theory.

The validation and demonstration of the proposed methodology will consider relevant case studies, selected to be representative of two scales of analysis considered (the territorial one and that of the single asset), in particular: the Citadel of Algiers; the historical centre of Rhodes; the Cathedral St. Nicholas in Ljubljana; Santa Maria Paganica church and Ardinghelli palace in the historical centre of L'Aquila (Italy) hit by the earthquake on 6th april 2009; the St. Pardo Cathedral in Larino (Molise Region, Italy). In particular, the Citadel of Algiers and the historical centre of Rhodes (both in the UNESCO list of the World Cultural Heritage) are made up of a complex aggregation of historical buildings, which represent a cultural heritage asset as a whole but also contain a wide number of single important monuments. For this reason, they are both an optimal example for the application of the methodology at the two different scales: a) an overall evaluation inside the historical centre (singling out of the cultural heritage assets at higher risk; proposal of a cost-efficient and reliable mitigation strategy); b) a detailed evaluation of the most significant monuments and artistic assets (proposal of strengthening interventions or of a structural health monitoring protocol).

ACKNOWLEDGMENTS

The research has received funding from the European Community's Seventh Framework Programme (FP7/2007-2013), under grant agreement n° 244229 (www.perpetuate.eu).

REFERENCES

Guidelines for evaluation and mitigation of seismic risk to cultural heritage, Directive of the Prime Minister, 12/10/2007, G.U. n.24 of 29/1/2008, Gangemi Editor, Rome. ISBN 978-88-492-1269-3, 2007.

FEMA 356. *Prestandard and commentary for the seismic rehabilitation of buildings.* ATC: Washington, 2000.

Seismic Rehabilitation of Existing Buildings, ASCE Standard ASCE-SEI 41-06, ISBN-13: 978-0-7844-0884-1, 2007.

Eurocode 8. Design provisions for earthquake resistance of structures. Part 1-1: General rules – Seismic actions and general requirements for structures. ENV 1998-1, CEN: Brussels, 2005.

Eurocode 8. *Design of structures for earthquake resistance. Part 3: Assessment and retrofitting of buildings*. ENV 1998-3, CEN: Brussels, 2005.

Norme Tecniche per le Costruzioni (Italian Technical Code for the design of constructions). D.M. 14/1/2008, Official Bullettin no. 29 of February 4 2008 (In Italian).

ATC-40. *Seismic evaluation and retrofit of concrete buildings*. ATC: Redwood City, 1996.

ONSITEFORMASONRY. On-site investigation techniques for the structural evaluation of historic masonry buildings, EU Project funded by 5 Framework Programme, EVK4-CT-2001- 00060, 2002-2004.

Seismic Vulnerability Assessment and Retrofitting of the Historic Brooklyn Bridge

Yegian, M. K.[1], Arzoumanidis, S. G[2],

[1]Northeastern University, myegian@neu.edu
[2]Parsons Corp., serafim.g.arzoumanidis@parsons.com

ABSTRACT: A comprehensive seismic investigation of the Brooklyn Bridge including its masonry approach spans was completed to assess its potential retrofit needs. The Brooklyn Bridge, built in 1883, has become a world landmark, a U.S. national treasure, and an architectural and engineering marvel. To ensure that the seismic retrofit needs of the bridge were based on a rational framework, avoiding overconservatism that would potentially lead to unnecessary retrofit and impacting negatively on the architecture of the bridge, advanced engineering investigations of the condition of the bridge and its seismic response were made. Specifically, the seismic investigation of the main bridge was performed following two approaches, referred to as the **global** and **local analyses**. In the global analysis, the entire main bridge with its foundation caissons was modeled, and the effects of soil-foundation interaction were incorporated through the use of foundation impedances. In the local analysis, each bridge tower with its caisson and the surrounding soils was investigated with a model using solid finite difference and slip and gap interface elements. The local analyses of the towers were performed to confirm quality of the motions and foundation impedances used in the global analysis, and to ensure that the conclusions regarding the potential need for foundation retrofitting was realistic and essential. The seismic analysis of the masonry approach spans was performed following the response spectrum method including soil-foundation interaction effects. This paper presents details of the seismic vulnerability assessments of the Brooklyn Bridge, and includes a brief summary of the retrofit needs that have been identified.

INTRODUCTION

The Brooklyn Bridge "The Great East River Bridge" (Figure 1) is the oldest of the East River Bridges in New York City.

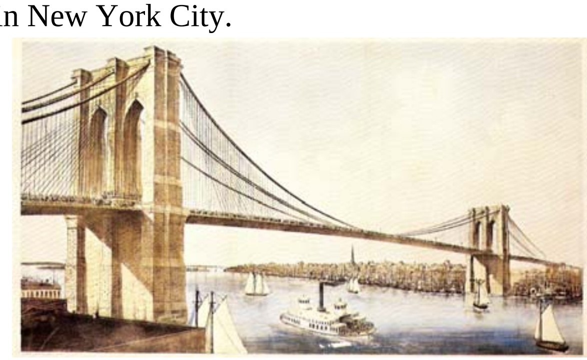

Fig. 1 Color lithograph of the Brooklyn Bridge, (Brooklyn Museum collection)

When completed in 1883, it was the world's first steel suspension bridge and had a center span more than 40% longer than other bridges. The Bridge has become one of most recognizable and nationally celebrated historic landmarks. It is a suspension bridge with diagonal stays radiating from the top of the towers and four stiffening trusses with expansion joints in the middle of the main and side spans. It carries six lanes for H15 vehicles, a pedestrian walkway and a bicycle lane (promenade).

(a)

(b)

Fig. 2 The Brooklyn Bridge, a) the promenade and b) the westbound roadway

The main span is 1595.5 ft. and the two side spans are 930 ft. long each. The cable anchorages, constructed of granite and limestone blocks, are founded on a 4 foot thick timber grillage constructed of 12 inch by 12 inch Southern Pine. The size of the grillage is 119.5 feet by 132 feet. Figure 3 shows elevations of the cable anchorages.

(a)

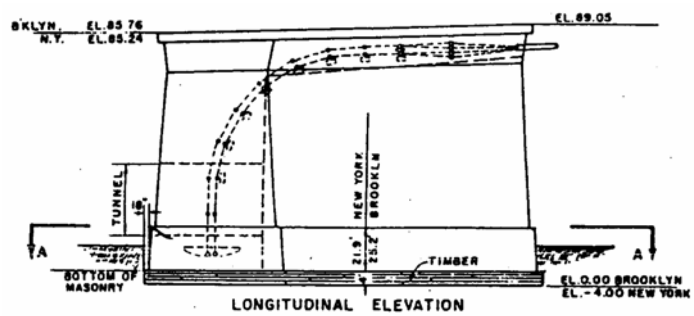

(b)

Fig. 3 a) Manhattan Cable Anchorage, b) elevations of the Manhattan and Brooklyn Cable Anchorages

The two towers of the Bridge are supported on caissons, which include a timber grillage 22 feet thick at the Manhattan Tower caisson, and 15 feet thick at the Brooklyn Tower caisson. Figure 4 shows elevations of the Manhattan and Brooklyn Towers consisting of large size granite blocks on the outside and smaller size stones embedded in concrete inside.

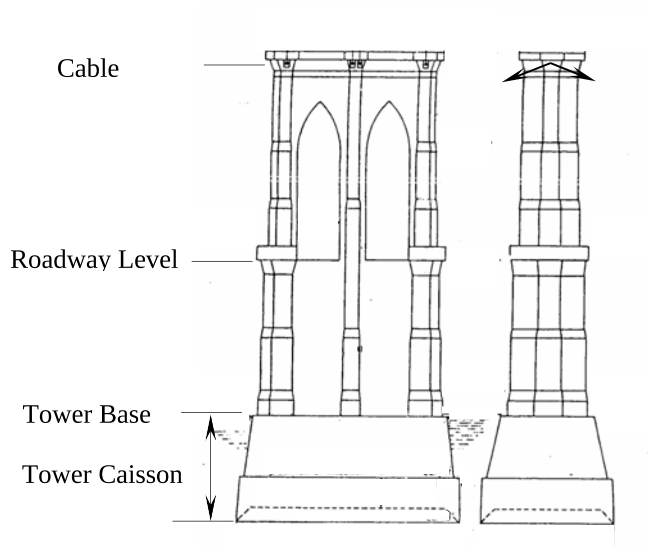

(a)

(b)

Fig. 4 a) elevations of the Manhattan and Brooklyn Towers and their caissons, b) Brooklyn Tower

The Manhattan Tower caisson is entirely in the East River and is founded generally at elevation -78 feet on an approximately 7 foot thick layer of very dense gravel, cobbles, and boulders overlying bedrock. The Brooklyn Tower caisson is on land and there is a bulkhead that laterally holds 40 feet of fill adjacent to the tower foundation. The base of the caisson is at elevation -45 feet, in a sand and gravel layer, overlying a 30 foot thick till layer over bedrock. The bedrock at the tower locations is slightly weathered.

The Manhattan Approach is a continuous arch masonry structure consisting of brick, granite, limestone and infill concrete. The Manhattan Approach arches, Figure 5, are formed from brick barrel vaults supported on transverse bearing walls and longitudinal granite arch facades filled with brick walls. The arches have been grouped into Blocks A to E. The barrel vaults are topped by infill concrete and support six lanes of the approach roadway and a central pedestrian walkway/bikeway. The interior space of the approach is divided into several stories and a basement. The Brooklyn Approach is similar in construction to the Manhattan Approach except for the irregular geometry due to the local streets intersecting in highly skewed angles. The approach consists of three blocks of brick arches with granite masonry facade. All arch blocks in the Manhattan and Brooklyn Approaches are founded on spread footings consisting of rubble or concrete.

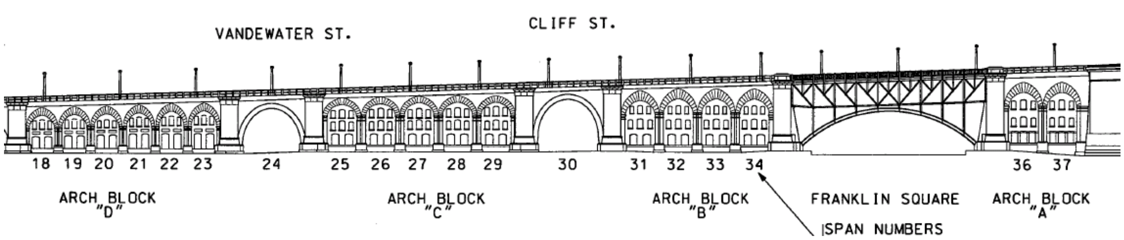

Fig. 5 Arch Blocks A, B, C and D of the Brooklyn Bridge Manhattan Approach

The Brooklyn Bridge is an unusual structure with foundations constructed of massive limestone blocks, unreinforced concrete, and timber grillage. A comprehensive seismic evaluation of the bridge with its masonry approaches and approach ramps was recently completed to assess the potential retrofit needs. Its seismic evaluation warranted the applications of the most advanced and rigorous engineering evaluations to ensure that the assessment of seismic retrofit is made on rational and realistic scenarios, avoiding overconservatism that may lead to unnecessary retrofit and potential negative impact on the architecture of the bridge.

This paper describes two advanced seismic analysis approaches that were utilized to assess the retrofit needs of the *main bridge*. In the first approach, referred to as **global analysis**, the entire main bridge with its foundations was modeled in a single model in ADINA. Rigid elements were used to model the cable anchorages. The soil-caisson interaction was included through the use of foundation impedances. A spine model from beam elements and rigid links was used to represent the tower caissons. Non-linear springs with gap features along with dashpots represented the soil-structure interaction effects. Kinematic motions (motions influenced by the presence of the foundation caissons) were then applied to the foundation springs and dashpots. In the second approach, referred to as **local analysis**, each bridge tower, its caisson, and the surrounding soils were modeled in the computer program FLAC. In the analysis, the tower, caisson, and the soils were modeled using solid elements. The potential slip and gapping along the soil-caisson interfaces were modeled through the use of interface elements. The program uses the finite difference numerical technique to solve the static and dynamic response of the continuum consisting of the bridge tower, its caisson, and the surrounding soils. The purpose for using two soil-foundation-bridge interaction analysis approaches was to confirm the quality of the kinematic motions and foundation impedances, validate the analytical results from both models, and ensure that the final conclusions regarding the potential need for retrofitting, especially the bridge foundations are realistic and essential.

The seismic analysis of the *approach spans* was performed following the response spectrum analysis approach using soil-foundation-structure interaction to account for the effect of the flexibility of the foundations on the seismic response of the unreinforced arched walls.

This paper presents descriptions of the global and local analysis approaches and demonstrates how these two analysis techniques complement each other in the seismic evaluation of the foundations of long span and critical bridges. The paper also summarizes the retrofit needs of the main and approach spans of the Bridge.

SEISMIC VULNERABILITY ASSESSMENTS – MAIN BRIDGE

Soil-Foundation-Bridge Analysis (Global Analysis)

A global analysis of the bridge was performed using the computer program ADINA. The model of the bridge included the super- and sub-structures as well as foundation caisson elements. Figure 6 shows the global model of the bridge. The cable elements of the bridge were modeled with non-linear beam elements and the suspended structure and the towers with linear beam elements. Non-linear springs were included to account for cracking of the towers at specific locations. This cracking was identified using a detailed model from solid elements that was developed in the computer program ABACUS and the material properties of ANACAP-U material model 3 (2003). For the needs of the global analysis, the caissons were modeled in a manner that captured potential gapping and slipping along the caisson-soil interfaces.

The caisson models consisted of three-dimensional elastic beam elements representing the spine of the caissons, rigid links, dashpots and truss elements with elasto-plastic hysteretic material properties and gapping features. In particular, the caisson base, which is a rigid surface 168 feet long by 102 feet wide, was modeled with rigid link elements and twenty-five non-linear truss elements in a configuration that facilitated the incorporation of the soil-caisson interaction at the base and calculation of peak soil stresses. This representation assumed rigid body motion of the base, which followed the deformations of the truss elements. The twenty-five elasto-plastic truss elements were connected at the other end to a rigid boundary surface, which was excited by the ground motions. This model was supplemented by two traction elements, one for each horizontal direction, to simulate the friction behavior between the caisson base and the soil. The horizontal elements were similar to the twenty-five vertical elements except that they represented the behavior of the entire base.

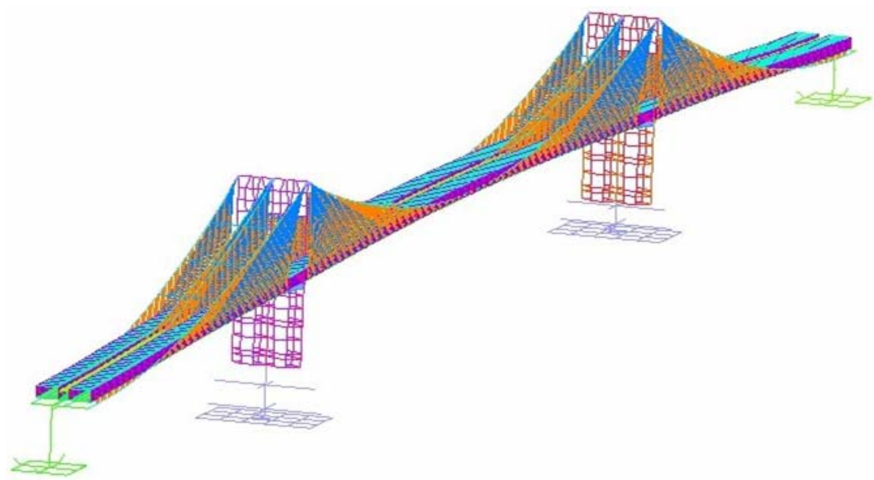

Fig. 6 Global analysis model of the Brooklyn Bridge

The interaction between the caisson walls and surrounding soils was modeled in a similar fashion as the base of the caissons. Following the limits of the soil strata and caisson configuration, the vertical walls were divided into several zones. Outrigger rigid link elements were used from the centerline (spine) of the caissons to the walls and elasto-plastic truss elements with similar properties as those at the caissons' base. Traction elements with elasto-plastic multi-linear material properties were also used at each outrigger to represent friction in the tangential and vertical directions.

The geotechnical input to the global analysis consisted primarily of ground motions and foundation impedances. Extensive field geotechnical and geophysical testing programs were implemented to characterize the site conditions and obtain reliable estimates of the shear and compression wave velocities of the soils, bedrock, foundation timber grillage, and limestone blocks.

Cable Anchorage Motions and Foundation Impedances

In the global model of the Bridge, the soil-foundation effects were incorporated through the use of distributed springs and dashpots. Figure 7 shows typical locations of the springs and dashpots for the Brooklyn Cable Anchorage. Similar springs and dashpots were used for the Manhattan Cable Anchorage.

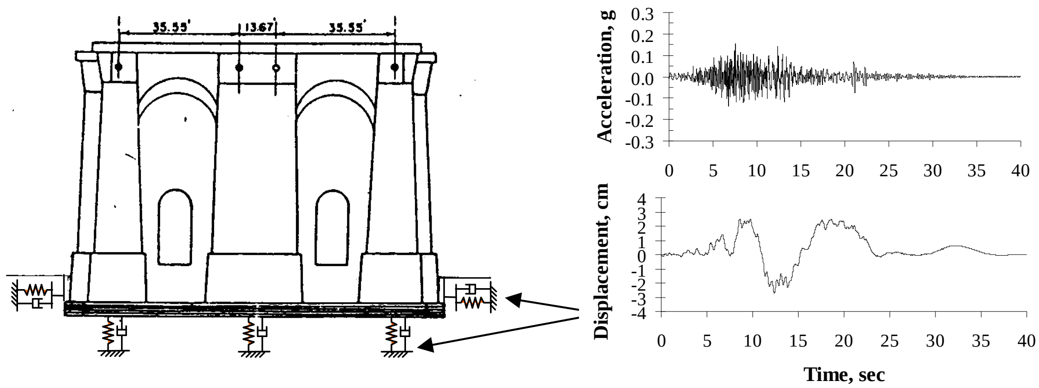

Fig. 7 Transverse elevation of the Brooklyn Cable Anchorage showing the locations of foundation springs and dashpots, and the kinematic displacement record used in the global analysis

Springs and dashpots were placed at nine locations within the base and four locations along the sides of each anchorage. The kinematic motions of the anchorage that needed to be applied at each of the spring and dashpot locations were computed using the computer program SASSI. Figure 8 shows the SASSI model of the Brooklyn Cable Anchorage.

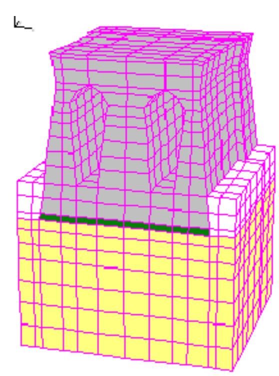

Fig. 8 SASSI model used in the kinematic motion and foundation impedance calculations for the Brooklyn Cable Anchorage

Several rock motion time histories were selected from the set of records that the NYCDOT released in 2004 for analysis of its bridges. The appropriate records were selected and modified to represent the spatial variability of the motions and the rock condition at each of the bridge foundation locations. This paper presents motions corresponding to the 2500-year event.

The kinematic motions (motions ignoring the mass of the anchorage) at the base and along the sides of the cable anchorage were computed using the strain compatible shear moduli obtained from initial applications of one-dimensional site response analyses. To account for the effect of the spatial variability of the motions along the longitudinal axis of the bridge, the global analysis was performed using multi-support excitation, in which displacement time histories were specified at all foundation springs and dashpots, representing the interaction between foundations of the bridge and the soils. These displacement records for the cable anchorage caissons were obtained from the acceleration records calculated from SASSI after making the appropriate baseline corrections. The computed motions along the sides and base of a cable anchorage caisson were almost identical, and hence in the global analysis the base displacement motions were specified at all foundation springs of the two cable anchorages as shown in Figure 7.

While the seismic input motions for the cable anchorages were computed using SASSI, it was of interest to compare these motions with those obtained from a more approximate approach, which is based on one-dimensional wave propagation analysis, SHAKE. Figure 9 shows comparisons of the spectra of the kinematic motions computed for the Brooklyn Cable Anchorage (BCA) in the three-dimensional SASSI analysis with the spectra of the motions computed in the more conventional way of assuming a one–dimensional wave propagation (SHAKE analysis) without considering the presence of the caisson (free-field motion). It is noted that the 37-ft thick stiff soil layer present below the BCA caisson base has a large amplifying effect on the motion in the period range (0.47 seconds) of the stiff cable anchorage.

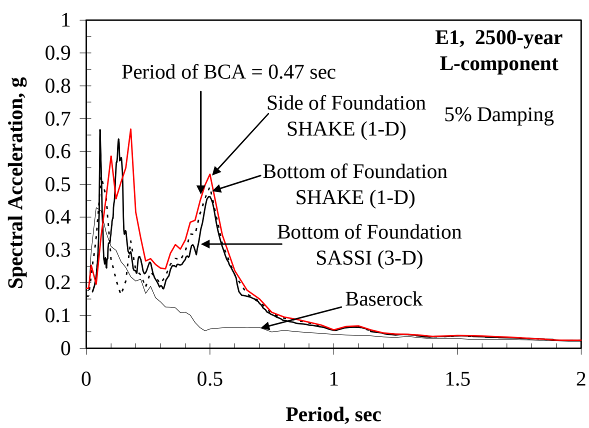

Fig. 9 Comparison of spectra from three-dimensional SASSI analysis with spectra obtained from one-dimensional SHAKE analysis

As shown in Figure 9, the simplified one-dimensional analysis would have overestimated the intensity of the motion in the period range of the cable anchorage (0.47 seconds) by as much as 35%.

The coefficients of the foundation springs and dashpots representing the soil-caisson interaction of the cable anchorages were computed using SASSI. The computed frequency-dependent stiffness coefficients in the longitudinal direction of the bridge for the Manhattan Cable Anchorages are shown in Figure 10.

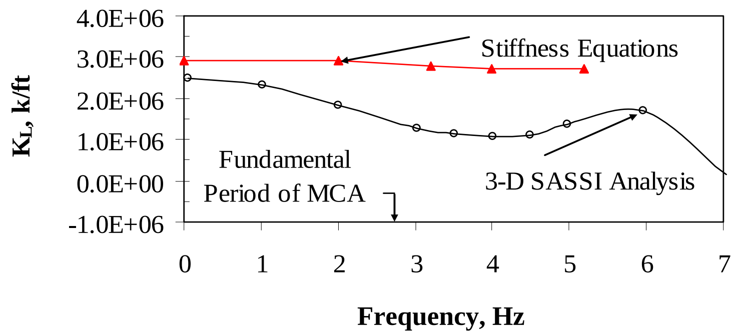

Fig. 10 Stiffness coefficients for the Manhattan Cable Anchorage, MCA, obtained from SASSI, compared with stiffness coefficients obtained from stiffness equations for shallow foundations

Included in Figure 10 are the stiffness coefficients computed based on simple stiffness equations for shallow foundations suggested by Gazetas (1991). Typically, within the frequency range of relevance to the anchorages (greater than 2 Hz), the simple equations overestimate the stiffness coefficients for the two cable anchorages. For example, the stiffness coefficient from the simple equations, for the Manhattan Cable Anchorage with a fundamental period of 0.37 seconds (frequency of 2.7 Hz), is higher than the value computed from SASSI by a factor of 2. Such overestimation of the stiffness would have resulted in the underestimation (by 40%) of the intensity of the motion experienced in the global analysis at the cable anchorage locations.

Through the comparisons made above, it is evident that simplified analysis procedures compared to more rigorous approaches may under- or over-estimate the dynamic responses of a structure depending on the characteristics of the soil and the foundation. Realistic estimates of seismic responses, especially for a critical structure such as the Brooklyn Bridge, warranted the application of advanced analytical procedures.

Tower Motions and Foundation Impedances

In the global analysis of the bridge, the soil-tower caisson interactions were considered through the use of springs and dashpots similar to those described for the cable anchorage. Figure 11 shows a transverse cross section of the Brooklyn Tower foundation depicting the locations of the springs and dashpots that were used in the global analysis model.

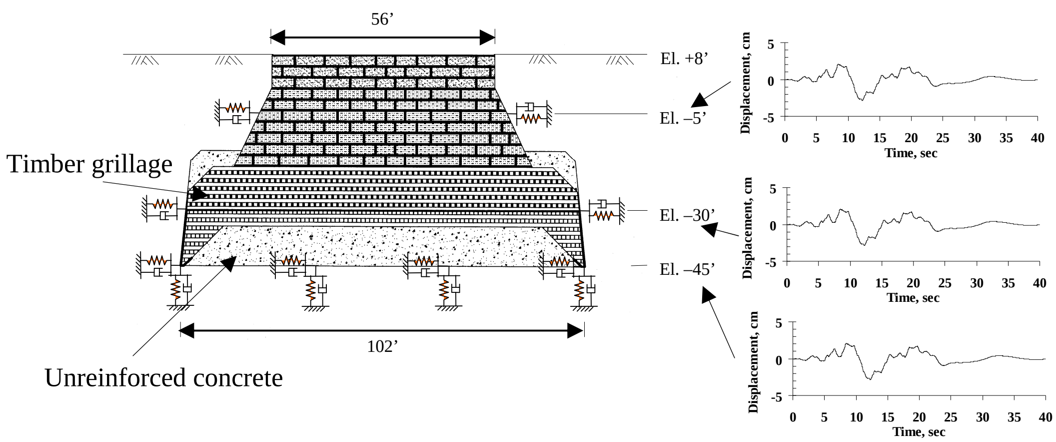

Fig. 11 Transverse elevation of the Brooklyn Tower foundation showing the locations of foundation springs and dashpots, and the kinematic displacement records used in the global analysis

The kinematic motions applied at the locations of the springs were computed using the computer program FLAC. Figure 12 shows the FLAC model of the Brooklyn Tower foundation.

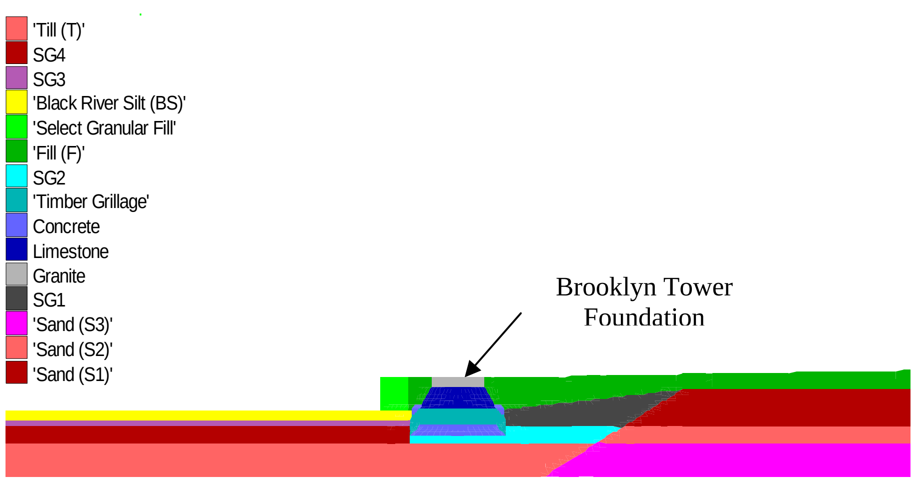

Fig. 12 FLAC model used to compute kinematic motions and impedances for the Brooklyn Tower foundation

In the kinematic motion calculations, the foundation of the tower was given rigid properties and the mass of the structure was excluded. The baserock motion used in FLAC was computed using the rock outcrop motion appropriate for the Brooklyn Tower location and one-dimensional site response analysis. The dynamic soil-caisson interaction analysis performed by FLAC utilized a hysteretic soil model in which at every step of time integration, the soil moduli and damping ratios were adjusted according to appropriate normalized moduli reduction and damping ratio versus shear strain relationships.

As mentioned earlier, the global analysis of the bridge was performed using variable support excitation. In such an analysis, the input motions are specified at each foundation spring and dashpot as displacement time-histories. Typical computed displacement time histories along the base and sides of the Brooklyn Tower caisson were shown in Figure 11. Similar calculations were made for the Manhattan Tower caisson. The acceleration response spectra of the computed motions for the three elevations shown in Figure 11 are compared in Figure 13. It is evident that the Brooklyn Tower caisson, because of its large base and stiff foundation soils, has little tendency to rock, and hence, all the translational motions along the sides of the caissons are very similar to the motion at its base. The computed displacement records were subsequently used as input in the global analysis of the bridge.

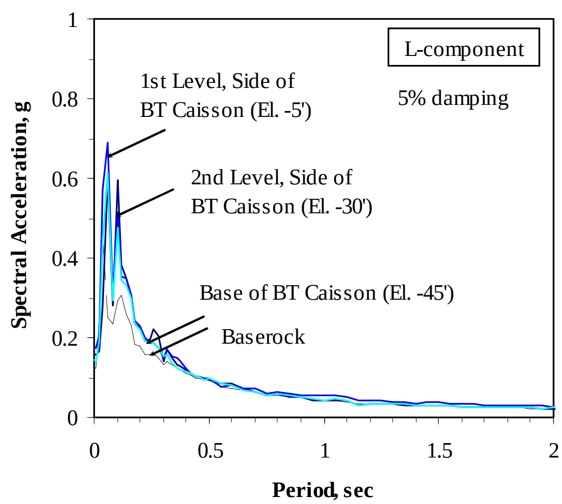

Fig. 13 Comparison of the spectra of the motions computed by FLAC for the sides and base of the Brooklyn Tower caisson

The foundation impedances for the Brooklyn Tower caisson were initially computed, as a function of frequency and estimated loads on the caissons, using FLAC and the hysteretic soil constitutive model. Typical force-displacement and moment-rotation hysteresis loops at two levels along the side and at the base of the caissons were computed by applying sinusoidal forces and moments at the center of gravity of the caissons. The amplitudes of the forces and moments, as well as the frequency of excitation, were varied to capture the effect of soil non-linearity and frequency dependency of the caisson responses.

Figure 14 shows typical results where an estimated seismic force of 88,000 kips was applied with a frequency of 10 Hz. The results show that the primary resistance to lateral inertial forces from the tower and caisson come from the base of the caisson (El. -45').

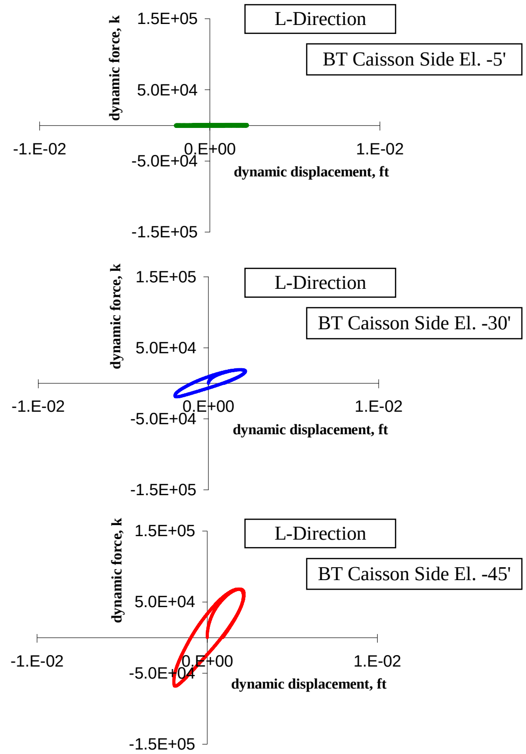

Fig. 14 Brooklyn Tower caisson force-displacement loops along the sides and base of the caisson for an estimated caisson longitudinal inertial force of 88,000 kips

Using such hysteresis loops along the sides and base of the tower caisson, equivalent stiffness and damping coefficients were calculated for the Manhattan and Brooklyn Tower caissons. These coefficients were subsequently distributed to 25 springs along the base of the caisson and 20 springs at each of two elevations along the sides of the caisson. The distribution was made ensuring the cumulative total stiffness and damping of the individual springs along the sides and base of a caisson matched the total stiffness and damping coefficients computed for each tower caissons using FLAC. These foundation impedances were used in a preliminary seismic global analysis of the bridge to estimate the inertial loads on the caissons of the towers, and to make a preliminary assessment of the retrofit need of the tower caissons.

To account for the effect of potential sliding and tilting of the tower caissons on the non-linear soil-caisson response, the FLAC analyses were repeated using models that included the entire tower, and the tower caisson with its surrounding soils. In these models, slip and gap elements were included along the soil-caisson interfaces. The analysis involved first applying gravity to compute the initial stresses within the interface elements. Then, forces and moments were applied on the caissons, one direction at a time (pushover analysis) and the displacements and rotations of the caisson were computed.

Figure 15 shows the entire model of the Brooklyn Tower and its caisson in which slip and gap elements were included.

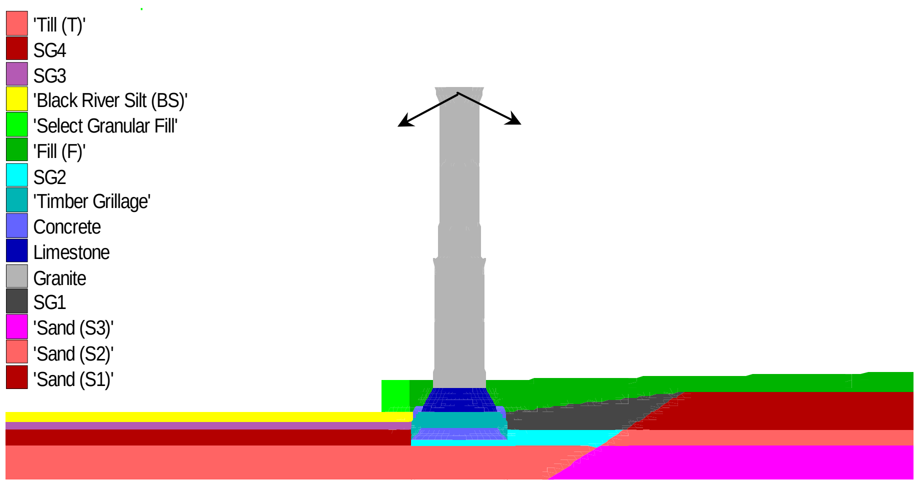

Fig. 15 Longitudinal model of the Brooklyn Tower and its foundation used in FLAC to compute non-linear force-displacement and moment-rotation relationships for the caisson, which included interface elements along its sides and base

Also included in the model, were static and equivalent dynamic cable forces and deck loads on the tower that were computed by the initial global analysis of the bridge. The properties of the interface elements included: the friction angle of the cohesionless soils, the undrained shear strength of the clay, and the normal and shear stiffness of the interface elements, which were based on the shear modulus of the soil and the dimensions of the soil elements adjacent to the interface elements.

The moduli of the timber grillage and the limestone of the tower foundation were measured in the field using the geophysical technique of shear and compression wave tomography. Figure 16 shows the results obtained using two boreholes drilled through the Brooklyn Tower foundation.

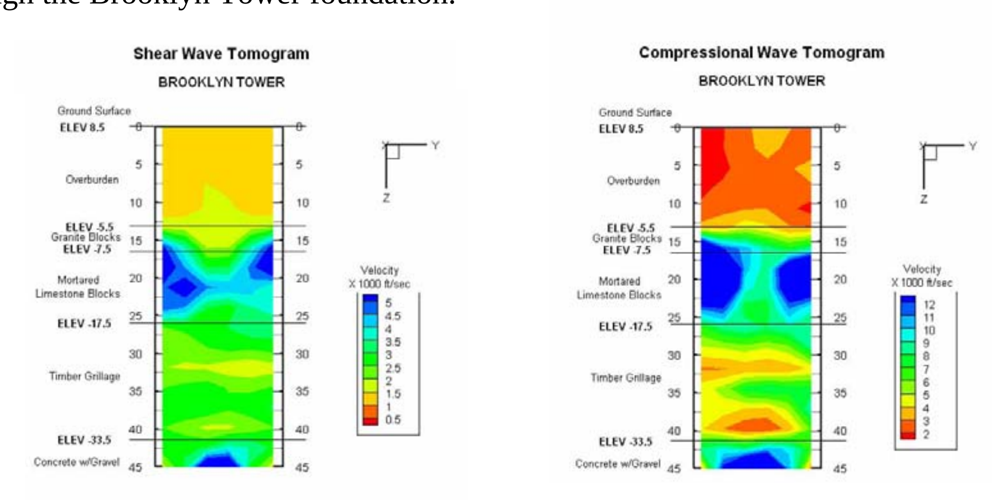

Fig. 16 Shear and compression wave tomography results of the timber grillage, and the limestone and granite blocks of the Brooklyn Tower foundations

On average, the shear and compression wave velocities of the timber grillage were 2700 fps and 5700 fps, respectively. The corresponding values for the limestone and granite blocks were 8700 fps and 13,600 fps, respectively.

Figure 17 shows a typical force-displacement curve obtained for the Brooklyn Tower caisson, in the longitudinal direction. The solid curve represents the total stiffness of the caisson. The dashed curves show the relative contributions from the sides and base of the caisson.

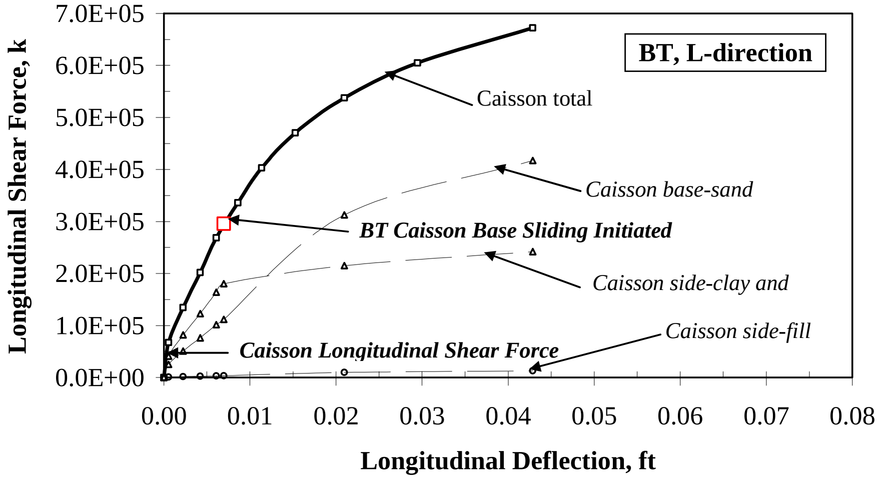

Fig. 17 Non-linear force-displacement relationship in the longitudinal direction for the Brooklyn Tower caisson, computed from the pushover analysis of the caisson, using FLAC with interface elements

A number of observations are made from the results shown in Figure 17. Sliding of the caisson is initiated at a total shear force of about 300,000 kips acting at the center of gravity of the caisson. This is far larger in magnitude than what was computed (33,000 kips) from the initial global analysis using foundation impedances. Hence, sliding of the caisson under the design event is not likely to occur, a conclusion based on the non-linear force-displacement relationships and the results from the global analysis. This conclusion is later confirmed by the results from the local analysis. Also, at small levels of shear force, the total stiffness is linear and the primary resistance to the caisson inertial forces comes from its base, conclusions that are consistent with those arrived at from the frequency dependent impedance analysis of the caisson (Figure 14).

Figure 18 shows the transverse moment versus rotation curve of the Brooklyn Tower caisson. Again, the results show that gapping will be initiated along the base of the caisson only if the transverse moment exceeds 5.5×10^6 kip-feet, which is much greater than what was computed from the initial global analysis (3.5×10^6 kip-feet) using frequency dependent foundation impedances. Hence, the Brooklyn Tower caisson is not expected to separate from its base during the 2500-year event, a conclusion later confirmed using the local analysis of the tower and its foundation.

Similar calculations using the Manhattan Tower caisson led to the same conclusions that the caisson is safe against sliding and separation from its base soil.

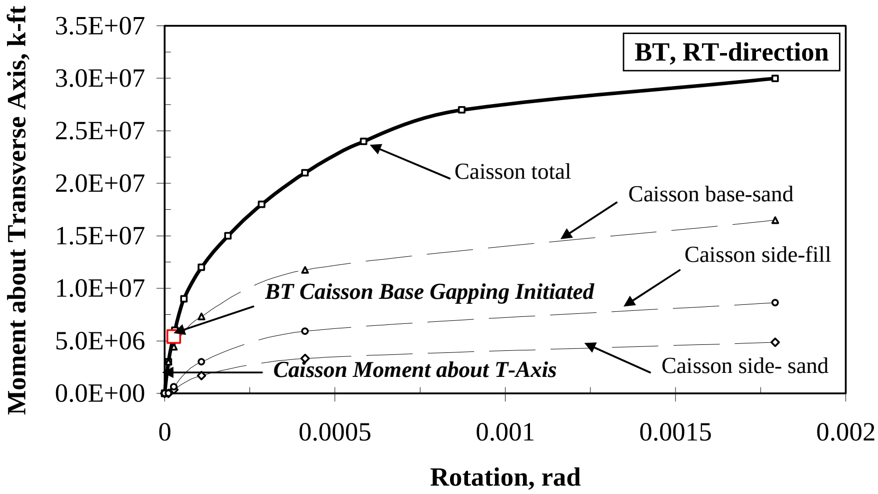

Fig. 18 Non-linear moment-rotation relationship about the transverse axis for the Brooklyn Tower caisson, computed from the pushover analysis of the caisson, using FLAC with interface elements

A total of three translational force-displacement and three moment–rotation curves were generated for each tower caisson using FLAC and interface slip and gap elements. These total stiffness curves were then distributed to the base and side springs and the global analysis was repeated for the final results. In ADINA, these curves were used as initial loading backbone curves for base shear tractional and for normal contact springs. Unloading of tractional springs was considered through the use of full Masing hysteresis, and of normal contact springs through the use of initial tangent stiffness. Later in this paper, selected results from the global analyses will be compared with corresponding results from the local analysis, which is described in the next section.

Soil-Foundation-Tower Analysis (Local Analysis)

The Brooklyn Bridge towers are massive and rigid, while its superstructure is flexible in comparison with the towers. Furthermore, the design rock motions are rich in high frequencies and have little energy in the low frequency range. Therefore, it is quite reasonable to expect that the dynamic inertial loads from the deck and the dynamic component from the cables will make only a small contribution to the seismic response of a tower and its caisson. This expectation was clearly observed in the global analysis of the bridge. Hence, it was of interest to perform a local seismic analysis of each of the two towers with their caissons and surrounding soils using FLAC. Such an analysis avoided the various assumptions made in the calculations of the kinematic motions and foundation impedances and provided added benefits of including initial stresses, more accurate modeling of the soil non-linear behavior, and computing the stress distributions within the caisson as well as along its sides and base.

The Brooklyn Tower caisson model shown in Figure 15 was further used to investigate the vulnerability of the caisson. It also included static and equivalent dynamic cable forces, and hydrostatic effects. For the soils the hysteretic soil model was utilized in which the soil moduli and damping ratios were adjusted at every step of time integration based on parameters that approximated appropriate normalized moduli versus shear strain curves. The soil-caisson-tower model first was subjected to gravitational loads and all the initial total and effective normal stresses were calculated and saved within FLAC. The model was then subjected to the 2,500-year baserock horizontal and vertical motions used earlier in the calculations of the kinematic caisson motions. The time histories of acceleration, displacement, shear stress, and vertical normal stress were computed at various nodes of interest including at the top and bottom of the interface elements. The results were then processed to evaluate the response of the tower and its foundation.

Figures 19a and 19b present summary plots of the accelerations and response spectra at various nodes within the transverse model of the Brooklyn Tower and its foundation, under transverse earthquake excitation. Similar results were obtained from the analysis of the longitudinal model of the tower.

These results show that the baserock motion is amplified as it propagates through the structure.

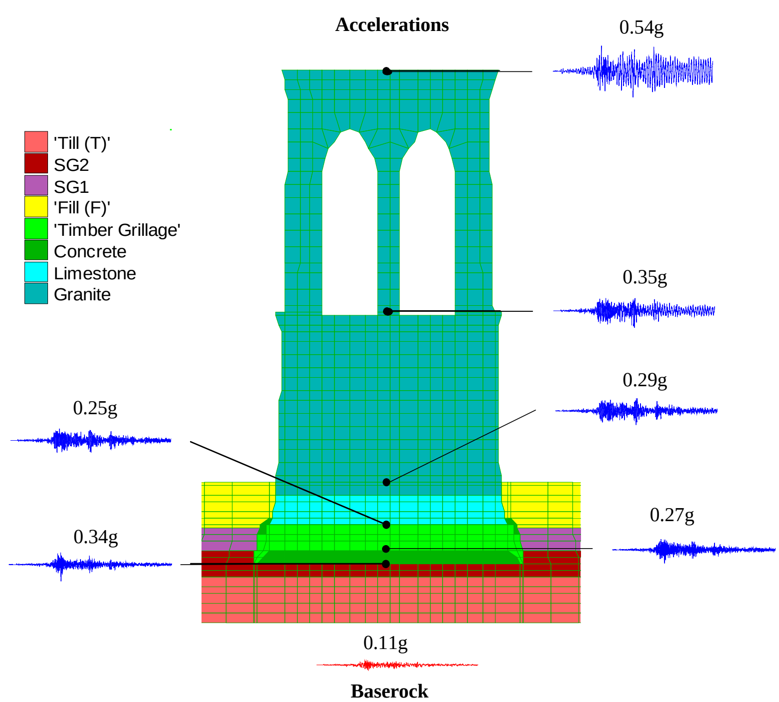

(a)

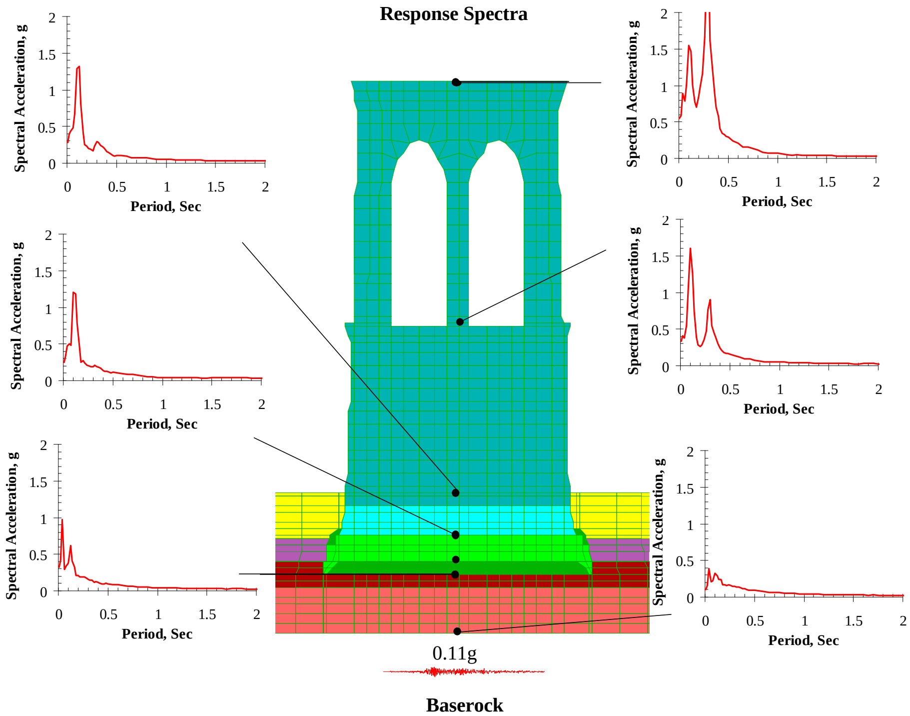

(b)

Fig. 19 Transverse responses of the Brooklyn Tower and its foundation, a) acceleration time histories, b) corresponding response spectra, under the 2,500-year event

Figure 20 shows spectral acceleration ratios from the longitudinal model obtained by dividing the spectra at various elevations within the tower and its caisson with the spectrum at the base of the caisson.

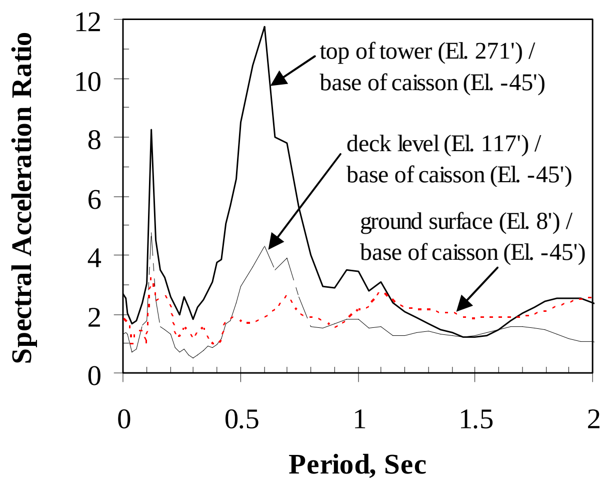

Fig. 20 Ratios of the longitudinal spectral accelerations, relative to the caisson base

Two modal frequencies can be seen clearly to occur at about 0.12 seconds and 0.6 seconds. Simple calculations of the horizontal and rocking periods of the tower and its caisson confirmed that the first period corresponded to the longitudinal period of the tower and the second is most likely associated with the rocking period about the transverse axis of the bridge. These modal periods were also within the period ranges that were observed through ambient vibration measurements of the bridge.

The FLAC analyses of the tower caissons also provided information to assess if the caissons would slide or if gapping between the caisson base and its foundation soils would occur during the 2500-year seismic excitation. Typical results are shown in Figure 21. The figure displays the vertical displacements at the top and bottom of the caisson base interface elements under the combined horizontal (longitudinal) and vertical motions. Even under this most severe condition, when the vertical motion can potentially reduce the base stresses, the vertical displacements at the top and bottom of the interfaces are exactly the same, indicating that there is no gapping (loss of contact) along the base of the caisson.

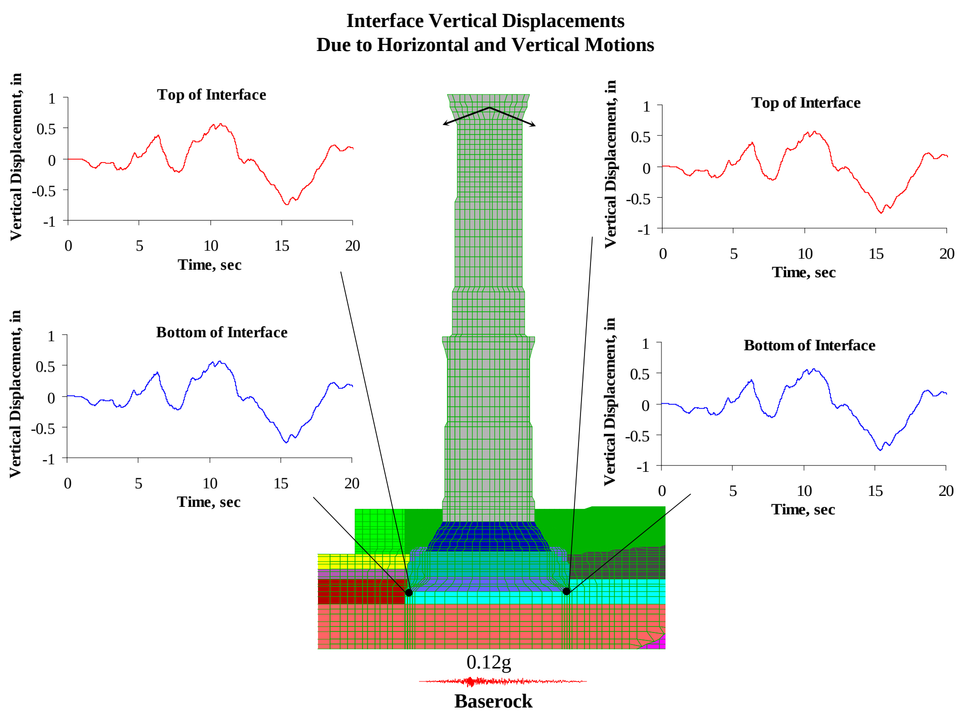

Fig. 21 Comparison of vertical displacements at the top and bottom of the interface elements along the base of the Brooklyn Tower caisson, induced by the combined longitudinal and vertical motions of the 2500-year event

Figure 22 shows a summary of the initial static and dynamic shear stresses along selected cross sections within the Brooklyn Tower and its caisson. The maximum shear stress in the concrete of the caisson is about 45 psi (6.5 ksf) and in the timber grillage is about 50 psi (7.2 ksf). These values are significantly smaller than the shear capacities that were measured in the laboratory for the concrete and timber specimens.

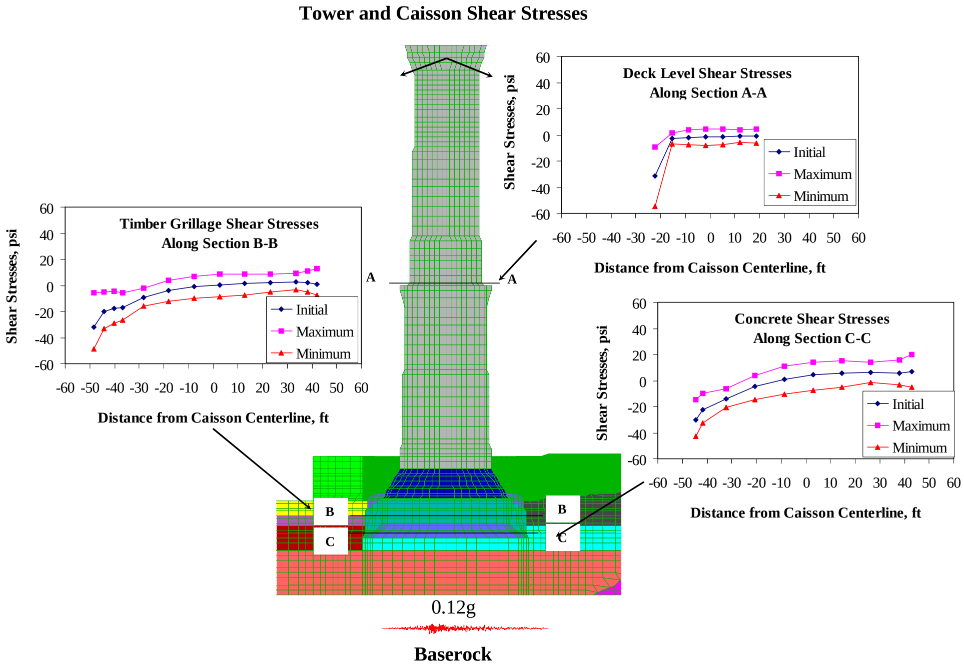

Fig. 22 Longitudinal shear stresses computed using the FLAC model of the Brooklyn Tower and its foundation, under the 2500-year event

The total shear force time history along a cross section through the middle of the caisson (Section B-B) was computed by integrating the shear stress time histories along the cross section. The result is shown in Figure 23. This total shear force time history, obtained from the local analysis, is compared later in this paper with the results from the global analysis.

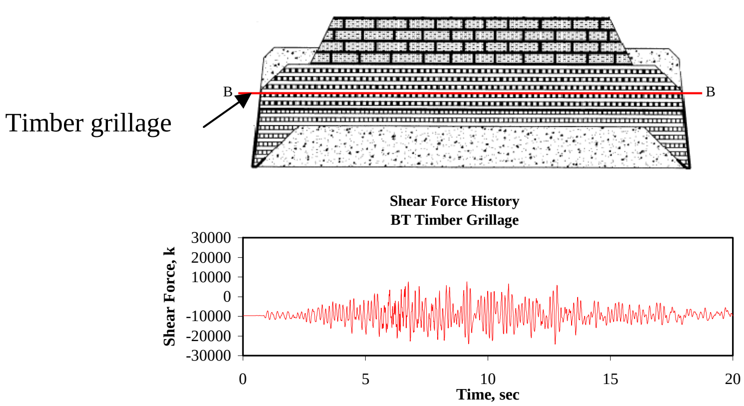

Fig. 23 Total longitudinal shear force history along cross section B-B in the middle of the timber grillage of the Brooklyn Tower caisson

The maximum value of the total shear force within the caisson is about 20,000 kips as shown in Figure 23. Under such a magnitude of shear force, the caisson is not expected to slide or tilt as was demonstrated through the use of the force-displacement and moment-rotation curves described in the previous section of this paper.

Figure 24 shows the shear and effective vertical stresses along the base of the caisson induced by gravity and the combined horizontal and vertical excitations. Under this load combination, the maximum effective normal stress is about 125 psi (18 ksf), and the minimum effective normal stress is about 0 psi.

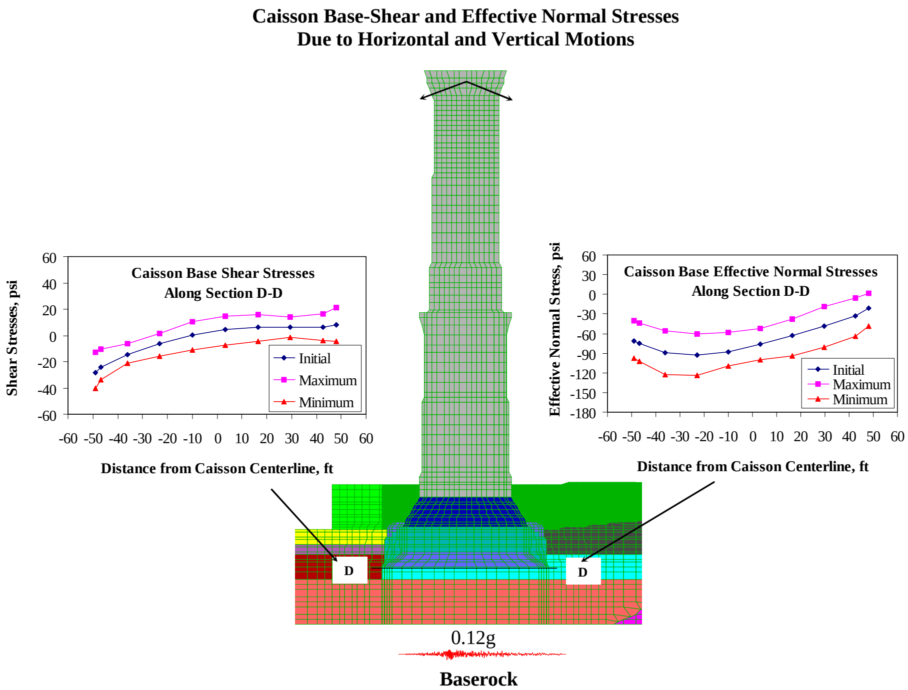

Fig. 24 Brooklyn Tower caisson base shear and effective normal stresses induced by the combined longitudinal and vertical motions of the 2500-year event

Similar investigations of the Brooklyn Tower and its caisson were made considering seismic excitation in the transverse direction. The results were similar to those inferred from the longitudinal analyses.

In summary, seismic longitudinal and vertical analyses of the Brooklyn Tower caisson and the surrounding soils led to the conclusion that the effective normal stresses at the bottom of the caisson are small (18 ksf) relative to the ultimate capacity (>100 ksf). Additionally, the caisson is safe against sliding and will not lose contact with its base soils under the longitudinal and vertical components of the 2500-year earthquake.

Comparisons of Global and Local Analysis Results

As described earlier, the global analysis of the Brooklyn Bridge incorporated the entire bridge including the towers, cables, suspended structure and foundations. Thus, it provided the means to consider the cable effects and the masonry tower potential for cracking. The caissons were modeled using beam elements, which permitted the calculation of stresses at only a few selected locations where the springs were placed.

The local analysis that involved the investigation of the seismic interaction of the bridge tower with its foundation and surrounding soils permitted more accurate considerations of the non-linear soil caisson interaction as well as the direct consideration of the potential slip and gapping around the caissons. The local analysis also provided a more detailed distribution of stresses that included initial effective vertical normal stresses, and the shear stresses within the tower and its foundations.

It is of interest to compare selected results from both the global and local analyses. Figure 25 shows a comparison of the total shear force time history in the longitudinal direction along cross section B-B of the Brooklyn Tower caisson. The results from both analyses are quite comparable both in intensity and general frequency content.

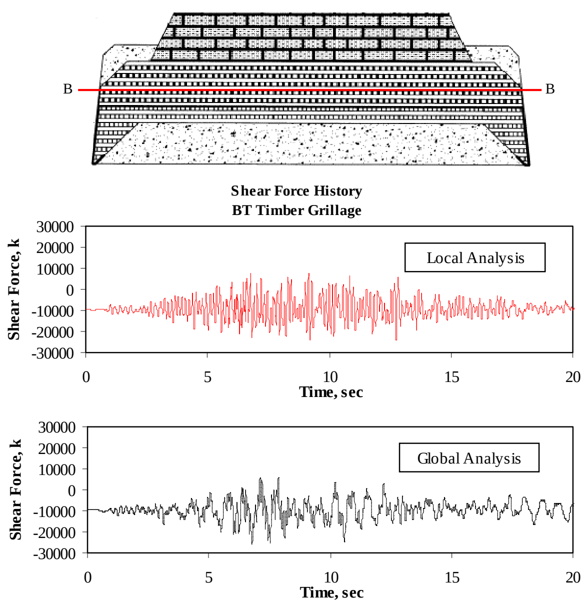

Fig. 25 Comparison of longitudinal total shear force time histories along cross section B-B of the BT caisson, from the local and global analyses

In Figure 26, a comparison is made of the effective vertical normal stress along the base of the Brooklyn Tower caisson obtained from the global and local analyses. Again, the agreement is quite good considering the wide differences in the analysis approaches.

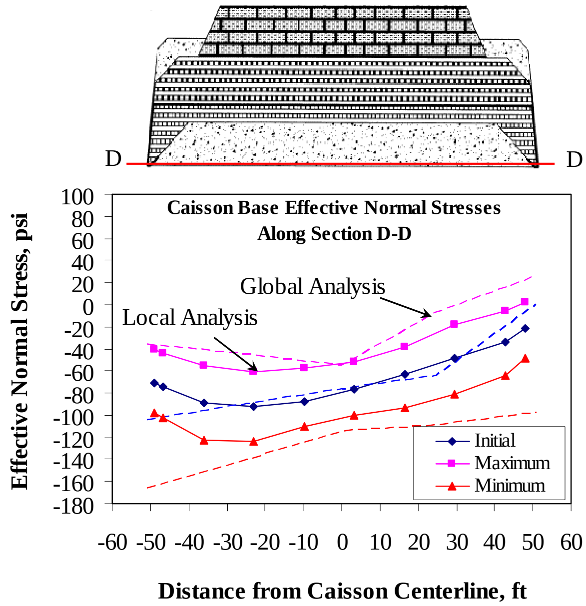

Fig. 26 Comparison of effective vertical normal stresses along the base of the Brooklyn Tower caisson obtained from the local and global analyses.

Finally, in Figure 27 a comparison is made of the drift of the Brooklyn Tower normalized with respect to the displacement at the base of the tower caisson

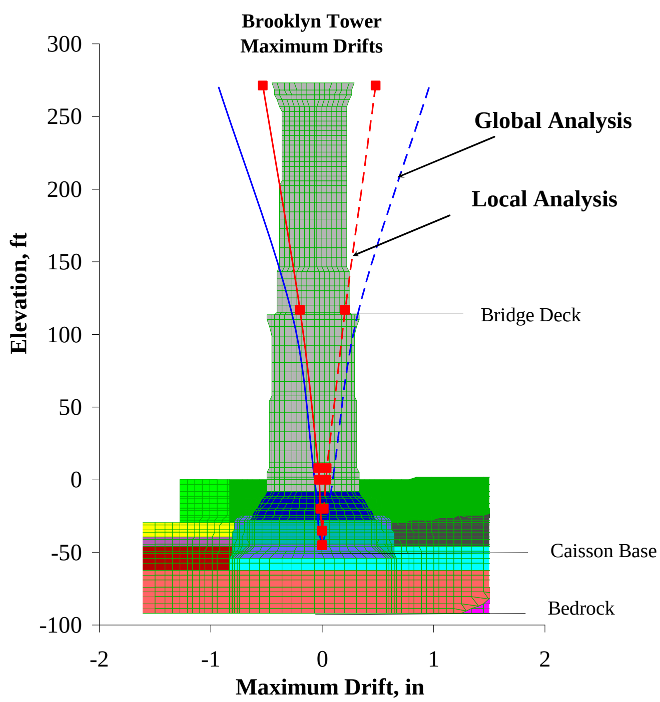

Fig. 27 Comparison of drifts along the Brooklyn Tower caisson and its foundation, normalized with respect to the drift at the base of the caisson, from local and global analyses

It is noted that these drifts are maximum values and do not necessarily occur at the same time. The drift values from the local analyses are comparable with the global analysis results.

Comparisons of the results obtained from the analyses of the Manhattan Tower and its foundation led to the same conclusion, that the local and global analyses yield similar results and the main tower foundations are adequate to safely resist the 2500-year event without experiencing sliding or uplift along its base, nor bearing capacity failure, and hence do not require retrofitting.

To assess the seismic vulnerability of the super-structure of the Brooklyn Bridge, the results from non-linear time-history analysis, using three sets of time histories (transverse, longitudinal, vertical) at each ground nodal point, were used. Such analyses were performed for three different 2,500-year return period earthquakes and one 500-year.

Detailed assessment of all bridge components identified relatively minor vulnerabilities for the stiffening trusses and some undesirable cracking of the masonry towers. The problems are closely related with the particular features of the bridge and are straightforward to visualize. The stiffening truss vulnerabilities are due to the fixed support conditions of the trusses at the ends of the bridge and the absence of a conventional rigid lower lateral system to transfer horizontal seismic loads. The vulnerability of the trusses is being addressed with the addition of a lateral system at the ends of the bridge. The towers will be reinforced with high strength steel bars to be inserted in selected locations.

SEISMIC VULNERABILITY ASSESSMENTS – APPROACH SPANS

All components of the masonry Manhattan and Brooklyn approach spans such as brick walls, barrel vaults, concrete fill, concrete deck and granite facades were modeled in SAP2000 using solid elements, see Figure 28.

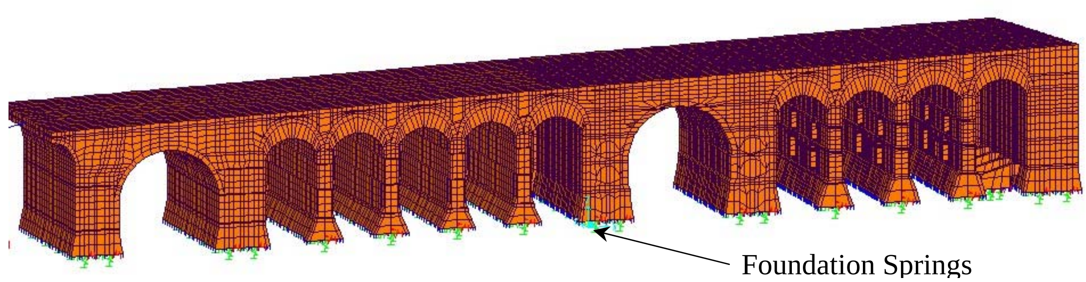

Fig. 28 Model of Manhattan Approach Arch Block C with foundation springs (Infill Walls not included)

Foundation springs representing the soil-structure interaction effects were developed and were introduced at the base of the foundations. Initially, each approach was analyzed assuming the infill walls are a part of the structure. Under the 2,500-year return period earthquake, the developing extensive zones of tensile stresses in the infill walls demonstrated that these walls are highly vulnerable. Therefore, each approach was analyzed further assuming no infill walls, which demonstrated the vulnerabilities of the remaining structural components after failure of the infill walls.

The results of the seismic response analyses led to the conclusion that the critical direction of seismic loading and vibration of the Manhattan Approach is along the longitudinal axis. The structure behaves as a series of portal frames with the transverse walls bending out of their plane (longitudinal direction of structure). The critical zones for each wall are at the top near the arch vaults and the bottom. The unreinforced masonry transverse walls do not have adequate capacities to safely resist the seismic stresses. Similar analysis was performed for the Brooklyn Approach, and the results are similar except for some differences due to the more complex in-plan geometry of the approach.

The selected retrofit for the Manhattan Approach is the replacement of the existing infill walls with reinforced concrete walls having a facade from bricks to maintain the existing aesthetics (reinforcement of the walls was chosen at the Brooklyn Approach). These walls span the arches of the stiff granite facade forming a rigid shear wall at either side of the structure, thus, eliminating the longitudinal vibrations of the structure. A section of the transverse brick wall with the granite facade and the proposed reinforced concrete infill wall are shown in Figure 29.

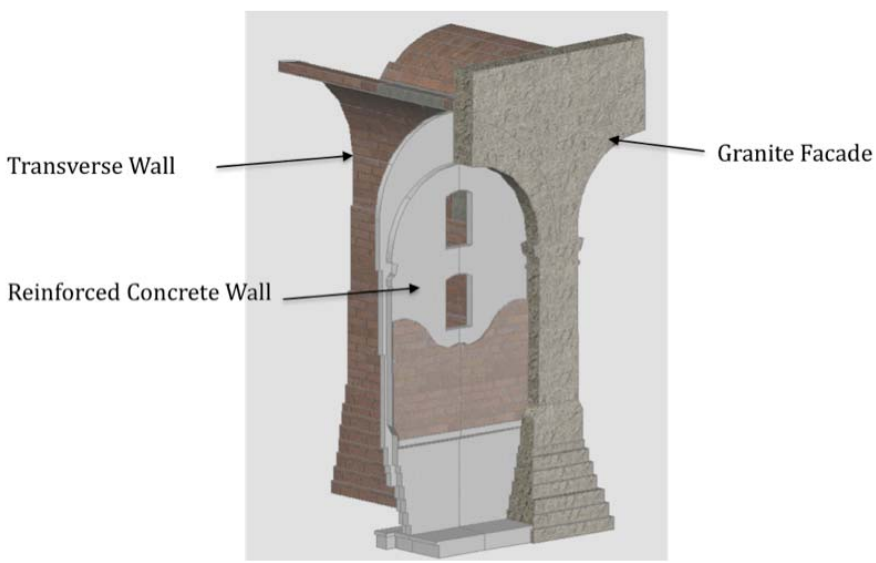

Fig. 29 Section of Transverse Brick Wall with Granite Facade and proposed Reinforced Concrete Infill Wall

The seismic vulnerabilities of the approach footings were also evaluated. Three modes of potential footing failure were investigated as shown in Figure 30, namely, sliding, uplift (initiation of loss of footing-soil contact) and bearing pressure.

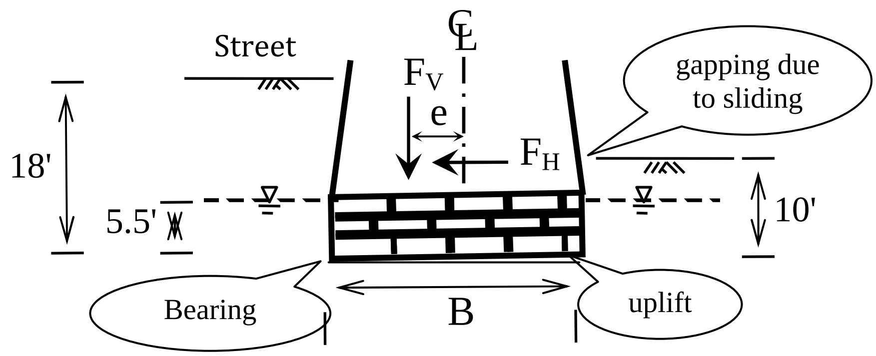

Fig. 30 Modes of potential failure of approach structure footings

In all cases, the sliding mode of failure was not a concern. The calculations showed that the existing footings of the transverse walls may experience forces and moments that may cause uplift at some footing corners, leading to excessive bearing pressures. Uplift develops when the eccentricity, e, of the resultant vertical force exceeds 1/6 of the width of the footing B. It is noted that under seismic excitations, the AASHTO Specifications for Highway Bridges permit potential loss of up to 50% of a footing contact area (e = B/3). This assumes that the shallow footing is a rigid structure and rotates as a solid block. However, the footings of the approach spans consist of rubble or unreinforced concrete and, therefore, they are inadequate for resisting seismic loads causing eccentricities in excess of B/6 (initiation of uplift). Hence, it was recommended that certain footings of the transverse walls to be retrofitted.

Figure 31 shows preliminary concepts of encasing the unreinforced masonry wall foundations. Such a design increases the static and seismic loads on the foundations but widens the footings, thus reducing the bearing pressures on the soils. In Arch Block C (Figure 5), due to poor quality soils and evidence of foundation soils erosion caused by flow of ground water, the retrofit concept that is being explored utilizes piles, specifically pin piles due to limited head room at the basement of the block.

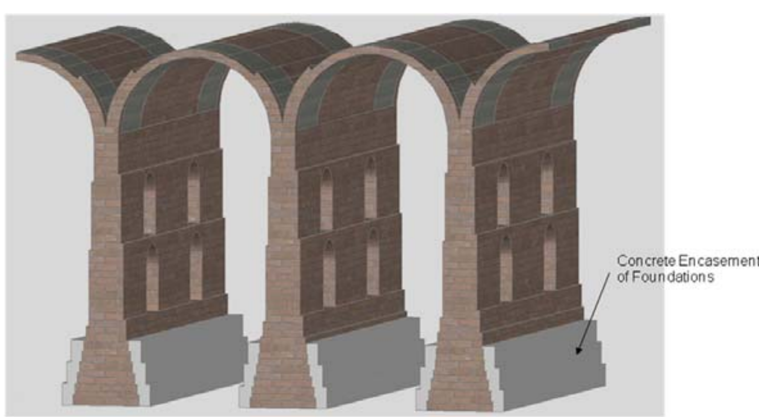

Fig. 31 Retrofit concept for the transverse wall foundations

CONCLUSIONS

Seismic investigation of the historic Brooklyn Bridge was performed to assess its potential need for retrofitting. The bridge serves a critical transportation need in New York City, and very importantly is a national landmark and a world recognized architectural and engineering achievement. The seismic assessment of the bridge was completed using the most advanced engineering investigations to ensure that the evaluation of retrofit needs were based on a rational framework and avoided "pitfalls" (as described by Peck, 1977) of overconservatism, including implementation of unnecessary retrofit schemes which may negatively impact the architecture of the bridge.

Two approaches were followed to determine the soil-foundation-bridge interaction, namely, **global** and **local analyses**. In the global analysis model, the soil-foundation interaction was introduced through the use of non-linear hysteretic springs with gapping features and dashpots. In the local analysis, each of the towers with their foundation caissons and the surrounding soils were investigated. The local analysis models included hysteretic soil behavior as well as interface slip and gap elements. Comparisons of various results obtained from the global and local analyses showed satisfactory agreement and led to the same conclusion, that the foundations of the Brooklyn Bridge under the 2500-year design event do not require retrofitting.

Based on extensive seismic evaluations of the Brooklyn Bridge, using global and local analytical approaches, the following observations and conclusions are drawn.

1. The Brooklyn Bridge is a long span bridge with massive cable anchorages and towers. The superstructure contributes very little to the tower dynamic responses. The global analysis has shown that, for the level of seismic loads in the New York City metropolitan area, very little cracking of the masonry towers is anticipated. Thus, the local analysis of the towers with their foundation caissons yielded dynamic responses of the towers and the caissons very similar to those obtained following the current state of practice of seismic analysis for critical bridges (global analysis).

2. The agreement in the results between the global and local analyses is a confirmation of the quality of the kinematic motions and the foundation impedances used in the global analysis of the bridge as well as a confirmation of the validity of the caisson modeling approach in the global analysis.

3. Quality kinematic motions and foundation impedances were computed following advanced soil-structure interaction analysis procedures. Such procedures, considered the three-dimensional kinematic effect of the foundations on the ground motions, and the non-linear force-displacement and moment-rotation stiffness relationships that included the effect of potential slip and gapping along the sides and bases of the caissons of the towers. These non-linear stiffness curves were obtained by performing pushover

analyses of the foundation caissons. If ground motions and foundation impedances were computed using more simplified analytical procedures, the caisson and tower responses computed by the global analysis would not have been in agreement with those obtained from the local analysis.

4. The local analysis provided the advantage of considering the effect of the initial static tower and soil stresses, accounting for the non-linear soil response directly in the computations, modeling more accurately the potential sliding and gapping of the tower caissons, and computing caisson static plus dynamic internal and external stresses as well as the stresses in the tower structure.

5. In suspension bridges, seismic response of bridge towers with large foundation caissons can be reliably evaluated following a local analysis in which the bridge support components with the soil continuum are considered together in a single model.

6. The Main Span of the Brooklyn Bridge will require little structural retrofitting. The foundations are adequate to safely carry the seismic loads from a 2500-year event.

7. The approach spans of the Brooklyn Bridge, especially on the Manhattan side, will require retrofitting. The transverse unreinforced masonry walls and their foundations will require retrofitting.

REFERENCES

ACS SASSI-C, "An Advanced Computational Software for Dynamic Soil-Structure Interaction Analysis on PCs," GP Technologies Inc. 6 South Main St., Pittsford, New York, (2004).

ADINA Software Program, ADINA R&D, Inc. Watertown, MA 02172, USA.

SAP2000 Software Program, CSI, 1995 University Avenue, Suite 540, Berkeley, CA 94704 USA.

FLAC 5.0 (2005), "Fast Lagrangian Analysis of Continua," ITASCA Consulting Group, Inc., 111 Third Avenue South, Minneapolis, Minnesota.

Dunham, R.S. and Rashid, Y.R., (2003), "ANACAP Material Modeling of Reinforced Concrete," Anatech Corp.

Gazetas, G., (1991). "Foundation Vibrations." Foundation Engineering Handbook, Van Nostrand Reinhold.

New York City Department of Transportation, Ground Motion Time Histories, 2004.

Peck, R. (1977), "Pitfalls of Overconservatism in Geotechnical Engineering," ASCE Civil Engineering Magazine.

PROSHAKE, (1998), "Ground Response Analysis Program," EduPro Civil Systems, Inc. Redmond, Washington, Version 1.0.

Steinman Report (1945), "Brooklyn Bridge Technical Survey Final Report," Department of Public Works, City of New York.

ACKNOWLEDGMENTS

The support and contributions of the following personnel from the New York City Department of Transportation are acknowledged: Henry Perahia, Deputy Commissioner; Jay Patel, Deputy Chief Engineer; Hasan Ahmed, Director East River Bridges; Walter Kulczycki, Project Manager East River Bridges; and Jagtar Khinda, Seismic Projects Engineer. Also acknowledged are the contributions of Thomas Thomann of URS Corp. to the geotechnical field and laboratory investigations, Paul Fisk of NDT Corp. to the geophysical field investigations, and Bryan Strohman, a former Civil Engineering graduate student at Northeastern University.

Testing a cross vault and a two storey masonry building on the shaking table: Preliminary experimental results

E.Vintzileou
Faculty of Civil Engineering, National Technical University of Athens, Greece

ABSTRACT: The project NIKER, funded by the European Union, deals with structural interventions to cultural heritage. Within the project, tests of subassemblies and models of entire buildings on the shaking table are carried out. Selected results from testing a cross vault connected with vertical piers are presented. Comparison of the behaviour of the strengthened specimen with that of the model tested as built is provided. Adding (wooden) struts and (steel) ties to the arches, as well as vertical prestressing to the piers, made the subassembly resist three times higher acceleration than the as built specimen. Results from testing the as-built model of a two storey rubble stone masonry buildings are also presented. Shaking of the building to acceleration approximately equal to 0,25g resulted to shear cracks in piers, as well as to separation of walls due to out of plane bending.

1 INTRODUCTION

Cultural heritage buildings in Europe and elsewhere have some typical characteristics that make them vulnerable to seismic actions, namely: (a) Poor construction type of masonry. Two or three leaf masonry, very common in cultural heritage buildings, is vulnerable especially in out-of-plane actions, (b) Poor diaphragm action of (timber) floors and roof: Vertical elements are not deformed in a uniform way, whereas due to deficient "box action" large deformations are applied to the building. Masonry, a brittle material, failing under limited deformations is, therefore, liable to damages, (c) Deficient connection among perpendicular walls, leading to behaviour similar to that described under (b), (d) Relatively small values of compressive stresses on vertical elements, due to the fact that almost 90% of the total vertical load the building transfers to the foundation is due to its self weight. Thus, both the in-plane shear capacity and the out-of-plane bending capacity of bearing elements are limited, (e) In case of a system of curved horizontal members, such as vaults, cupolas and arches, the vertical elements are subjected to horizontal thrust, which imposes out-of-plane deformations and bending moments to the vertical elements.

Thus, a systemic approach is needed, for an adequate scheme of interventions to be planned with the purpose to reduce the vulnerability of historic structures, without altering, however, their original bearing system. Within the framework of the project NIKER (www.niker.eu), such systemic intervention techniques are investigated experimentally and analytically. Part of the experimental work is being carried out at the Laboratory of Earthquake Engineering, NTUA. This experimental campaign comprises tests on two subassemblies, as well as on two models of entire buildings. In this paper, the experimental programme is described, whereas preliminary test results are presented and commented upon.

2 THE SPECIMENS

2.1 *Subassemblies*

Two subassemblies are tested at NTUA, namely, a cross vault supported by two masonry piers (Figure 1) and a system of one T-shaped wall and a rectangular wall connected by means of a timber floor (Figure 2). Both subassemblies are first tested as built, until (repairable) damages occur. Subsequently, they are repaired and strengthened and retested until severe damages occur.

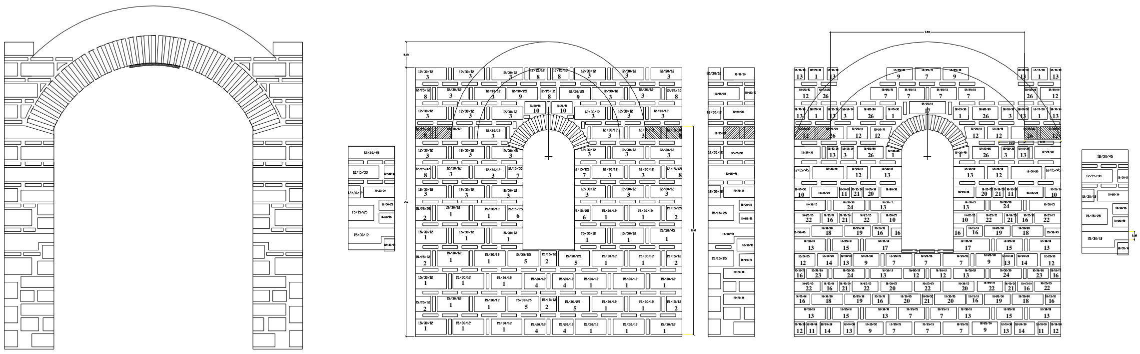

Figure 1. The geometry of the first subassembly (cross vault and piers).

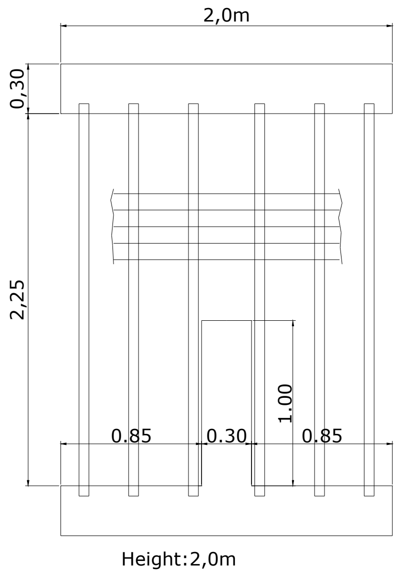

Figure 2. The geometry of the second subassembly (T-shaped and rectangular walls)

In both subassemblies, the vertical elements are made of three-leaf stone masonry. In the first subassembly, the arches and the vault are constructed using solid bricks. A lime-pozzolan mortar is used for the construction of both subassemblies.

2.2 *Models of entire buildings*

Figure 3 shows the two models (scale 1:2) of two storey stone masonry buildings. Both models are made of three-leaf stone masonry. They are provided with timber floors (bearing timber beams covered with a pavement of timber planks). The two models are identical in geometry. However, the second model is provided with horizontal timber ties at various levels, to check the efficiency of this traditional and widely applied construction system (in Greece and in most earthquake prone areas, such as the entire Eastern Mediterranean, Latin America, Afghanistan, Iran, etc.).

Figure 3 The two models of entire two storey buildings. The construction type of masonry, the positioning of timber beams and timber pavement are shown.

3 TESTING PROGRAM

Up to now, tests on the cross vault are completed, whereas the model building without timber ties was tested as built and its repair/strengthening is under way. Thus, this presentation is limited to the experimental results available to date.

3.1 *Tests on the cross vault*

The subassembly with the cross vault was tested as built within a previous research project, funded by the Ministry of Culture and Tourism, for the needs of restoration of the Katholikon (main church) of Dafni Monastery. The subassembly was subjected to the Irpinia (Italy) 1980 earthquake (E-W and N-S directions). Subsequently, it was strengthened through grouting of the piers, whereas steel ties were placed at the base of the two arches. The subassembly was retested, along its weak direction (out of the plane of the piers). Within the present research project, the subassembly was strengthened as follows: (a) All cracks in the piers were grouted, using a hydraulic lime based grout, developed and characterized within the project NIKER, (b) the arches and the vault were repaired and their cracks were grouted using the same grout as for the piers. Furthermore, timber struts and steel ties were provided at the base of the two arches (Figure 4), (c) In order to enhance the out-of-plane bearing capacity of the piers, vertical prestressing was applied to the piers through CFPR strips, using a system developed by SIKA (Figure 5).

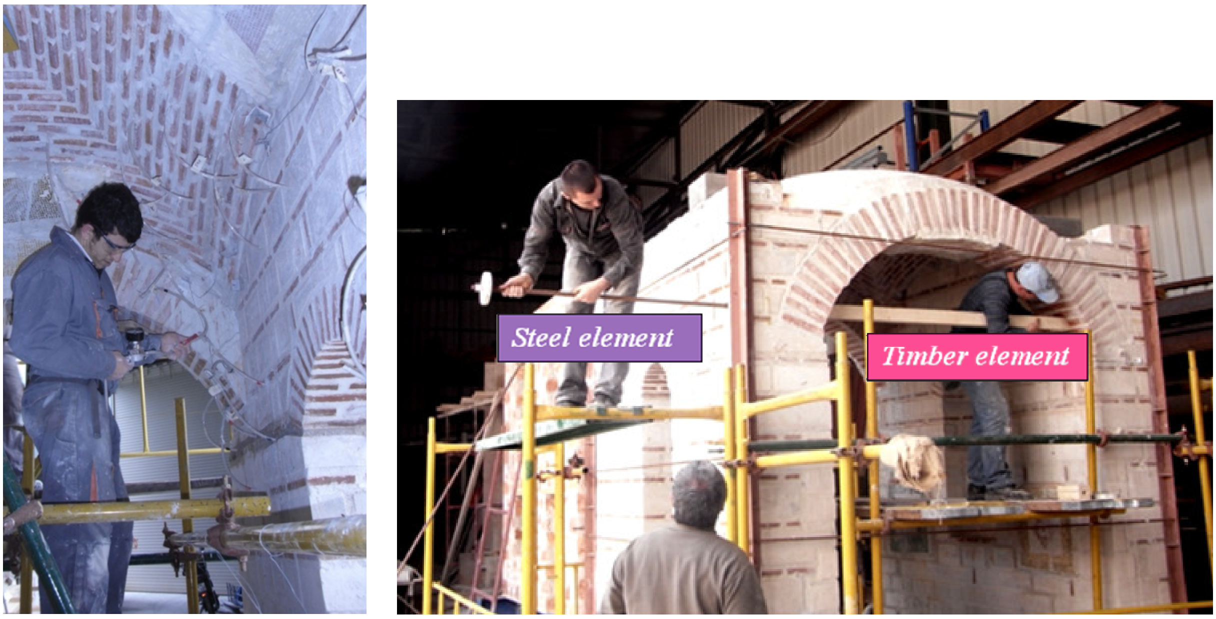

Figure 4 Grouting of cracks; positioning of timber struts and steel ties

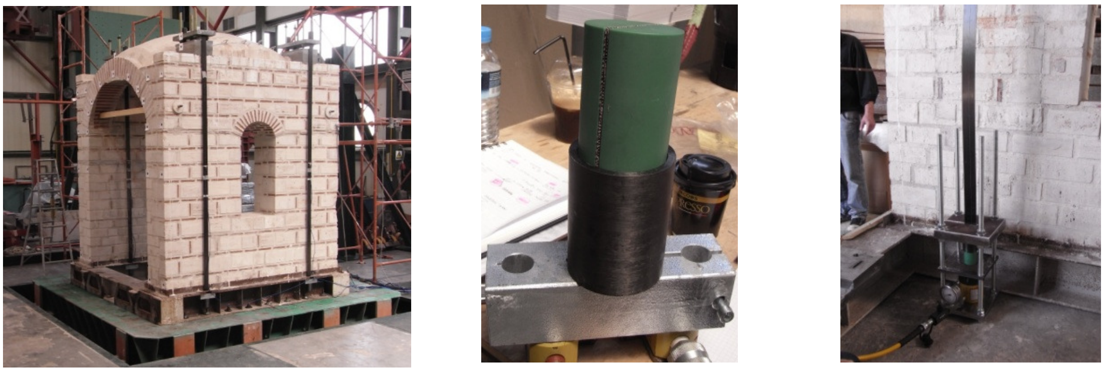

Figure 5 The subassembly on the shaking table, after strengthening; the anchorage system of the CFRP strips

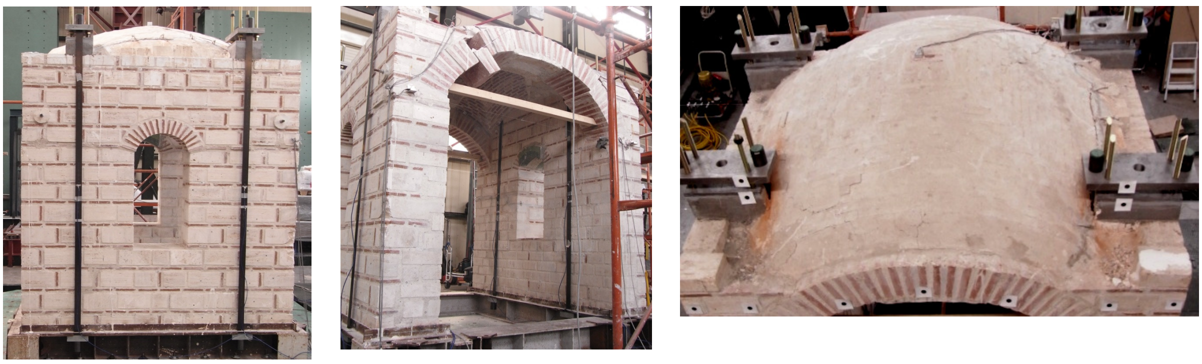

Figure 6 Typical damages of the subassembly

The subassembly was subjected to a series of accelerograms, with stepwise increasing maximum acceleration. Comparing the results of testing the subassembly in its original state with the results obtained from testing the strengthened subassembly, the following observations are made: (a) The damages observed in both cases are similar. They imply horizontal cracks in the piers (due to out-of-plane bending), damage of the arches and cracks in the vault (parallel to the piers). The damage pattern of the bearing elements is shown in Figure 6, (b) the damages of similar morphology and degree occurred at different imposed seismic actions. Actually, the as built subassembly sustained a motion equal to 150% the Irpinia earthquake, whereas the strengthened subassembly sustained a motion as high as 450% the Irpinia earthquake, (c) Significant increase of the damping was observed (1-2% for the as-built and 3-4% for the strengthened subassembly), finally, (d) the strengthened subassembly was able to sustain significantly larger deformations than the as-built (40,5mm compared to 11,4mm at the top of a pier).

Although the evaluation of the experimental results is still underway and their analytical verification is not yet completed, one may observe that the strategy of interventions was correct, as it led to significant improvement of the seismic resistance of the subassembly, without altering the bearing system (as proven by the pathological image after strengthening, which coincides with that of the as-built case) and without application of devastating intervention techniques.

3.2 *Testing of the model without timber ties*

For similitude purposes, additional masses were placed on both floors of the building. Additional masses at the top of the model are shown in Figure 7. The model was subjected to a series of tests with gradually increasing acceleration. In this case the Kalamata (Greece, 1986) earthquake was imposed (along the two main directions of the model). The test was completed when significant (but repairable) damages were observed, at acceleration almost equal to 90% the Kalamata earthquake maximum acceleration (~0,25g).

Figure 7 View of the interior of the ground floor and view of the model on the shaking table

The damages observed on the model are typical for this type of structures. Actually, as shown in Figure 8, shear cracks appeared in piers, lintels and in the corners of openings, whereas almost vertical cracks were observed close to the corners of the building. Those cracks are due to the out-of-plane bending of the walls. As shown in Figure 9, the cracks separating perpendicular walls were initiated at the top of the building and they propagated towards its base.

Furthermore, at several locations, separation of the two leaves of masonry occurred, as shown in Figure 9b. This separation (that reached at some locations-at the top of the model-the value of 10mm) is due to the out-of-lane bending of vertical elements and proves the vulnerability of this type of masonry.

After completion of the test, the model was removed from the shaking table. It is under repair and strengthening. Actually, all cracks were grouted, whereas homogenization of the three-leaf stone masonry through grouting is completed. For this purpose, the same hydraulic lime based grout used for the repair of the cross vault was used. The application of this technique aims at improving the mechanical properties of masonry, as well as at reducing the vulnerability of three-leaf masonry especially to out-of-plane actions. The interventions to this model comprise also the enhancement of the diaphragm action of the two floors. It should be noted that, within the same project NIKER, at the University of Padova (Italy), an experimental campaign is in progress aiming at investigating various techniques for the enhancement of the diaphragm action of floors. On the basis of the experimental results obtained at the University of Padova, one technique will be selected and applied to the model building before its retesting on the shaking table.

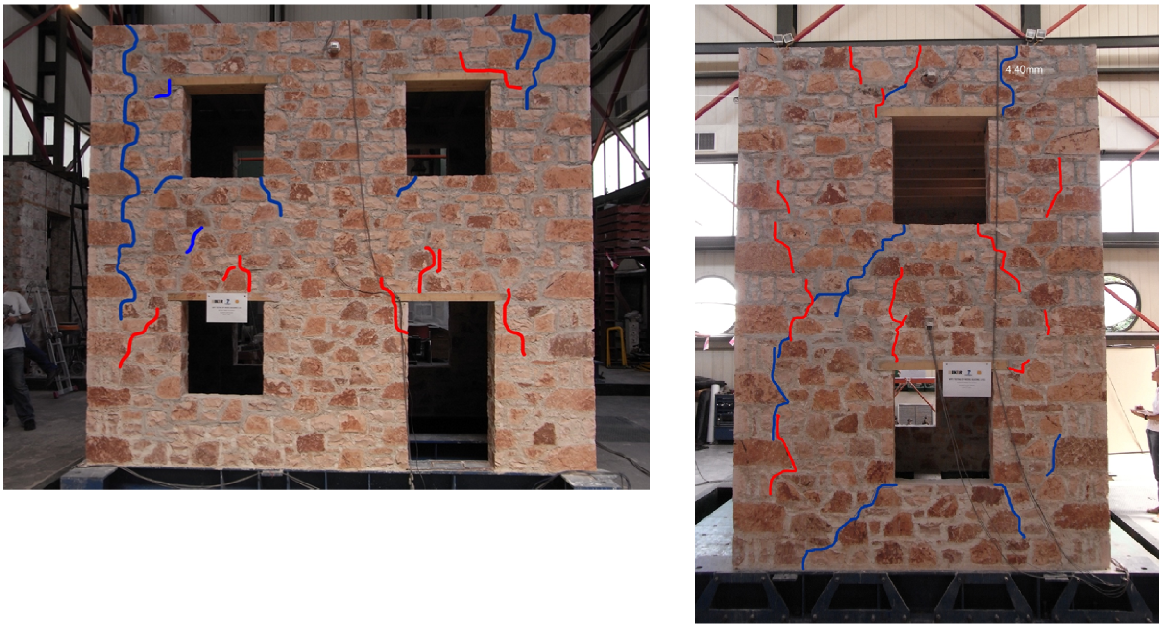

Figure 8 North and east view of the model. Red colour indicates cracks occurred at acceleration=0,16g; blew colour shows cracks opened at acceleration=0,24g.

a b

Figure 9 (a) View of vertical cracks separating perpendicular walls, (b) cracks within the thickness of masonry

4 ACKNOWLEDGEMENTS

The system of vertical prestressing was offered and applied by SIKA.

Submitted Papers

Damage Analysis of Utatsu Bridge Affected by Tsunami due to Great East Japan Earthquake

K. Kosa
Kyushu Institute of Technology, Kitakyushu, Japan

L. Fu
Research School of Kyushu Institute of Technology, Kitakyushu, Japan

H. Shimizu
Nippon Engineering Consultants Co. Ltd., Fukuoka, Japan

T. Sasaki
Nippon Engineering Consultants Co. Ltd., Sendai, Japan

ABSTRACT: Utatsu Bridge, a prestressed concrete bridge, suffered enormous damage from the destructive tsunami wave triggered by Great East Japan Earthquake, on March 11th, 2011. Based on the field survey the damage condition and the possible mechanisms of Utatsu Bridge have been summarized by authors. It has been found that the superstructures of Span 3 to Span 10 suffered serious dislocations while all piers did not flow out. Superstructure damage was able to be judged by the comparison of wave acting force and resistance. On the other hand, pier's no displacement was able to be judged by comparing the moment of wave action and resistance.

1 INTRODUCTION

The 2011 Tohoku Earthquake, known as the Great East Earthquake as well, occurred at 2:46 p.m (JST) on March 11th with a magnitude 9.0. It was one of the most powerful earthquakes to have hit Japan. Besides that, the earthquake caused an extremely destructive tsunami wave which induced an extensive loss in Tohoku region. Many bridges in Tohoku region have suffered tremendous damage by tsunami. The authors have conducted a reconnaissance visit to the coast of Tohoku region to observe the damage condition of a number of bridges.

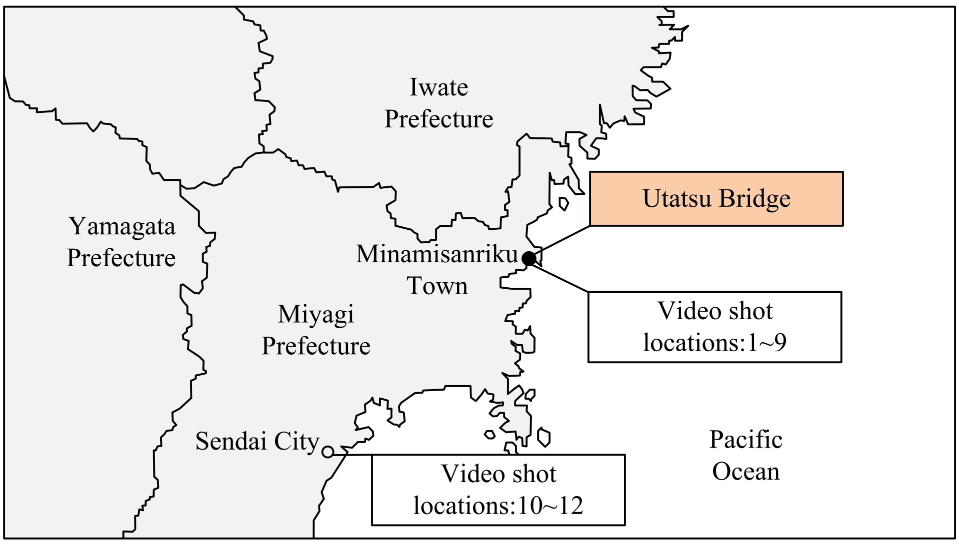

Figure 1. Location of Utatsu Bridge

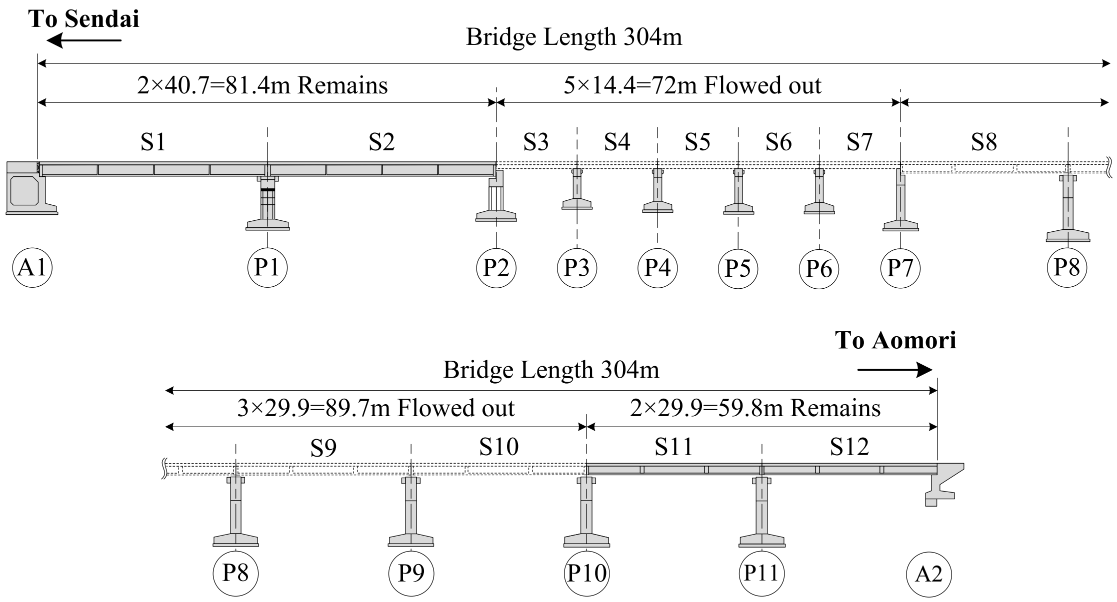

Figure 2. Bridge side view (after damaged, view from seaside)

The Utatsu Bridge, located in MInamisanriku Town and the coast of Irimae Bay, is a 304m long, 8.3m wide, 12 spans, prestressed concrete bridge which consisted of 3 types of superstructures and the location of it is shown in Figure 1. Based on the detailed field survey it was observed that for the damage of superstructures the central 8 spans (S3~S10) have been washed away by tsunami.

The detailed damage performance of Utatsu Bridge is presented in the following chapter and this paper also provides a method about how to obtain the wave flow velocity and wave height at the location of Utatsu Bridge. Besides that, comparisons of wave acting effect and bridge resistance have been conducted to check the outflow of superstructures and to approach the damage condition of piers.

2 DAMAGE SITUATION

2.1 *Introduction of bridge structure*

The Utatsu Bridge, located at Minamisanriku Town over Irimae Bay, is composed of 3 types of superstructures varying in length from 14.4m to 40.7m, as shown in Figure 2. For simplicity, the authors assigned numbers for the superstructures and piers from Sendai side to Aomori side. The 12 superstructures were numbered from S1 to S12 while the 11 piers were numbered from P1 to P11.

2.2 *Outflow Condition of Superstructures*

Based on the detailed survey, superstructures S3~S10 moved off their supports under the wave-induced lateral load while the superstructures of S1, S2, S11 and S12 did not flow out. The displacements of S3~S10 have been illustrated in Figure 3. The directions of displacements are transverse to the bridge axis. The characteristic of outflow condition is that the central spans such S5~S7 and S8 experienced long displacements (28m and 41m). On the contrary, the side spans such as S1, S2, S11 and S12 did not flow out.

It was also observed that S3~S4 and S5~S7 flowed out with no separation respectively. Due to a great wave-induced uplift force, S8~S10 were inverted when they moved off.

However, contrary to the damage of superstructures, during the tsunami attack, all piers of Utatsu Bridge withstand the wave action and did not collapse. The main damage of the piers is

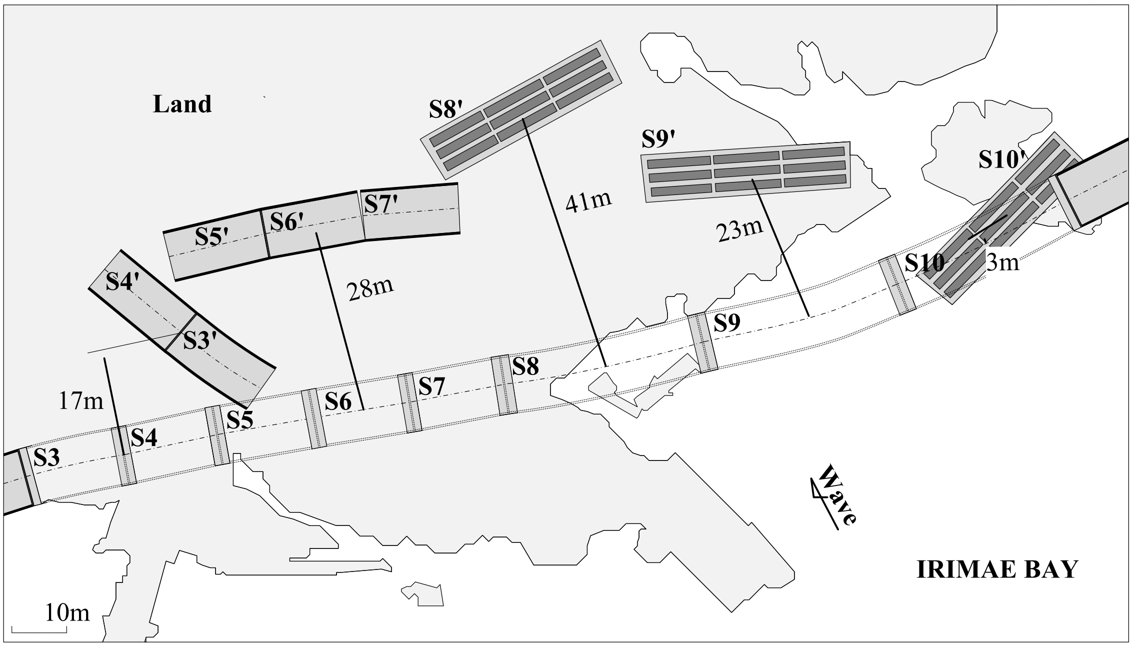

Figure 3. Outflow condition of Utatsu Bridge

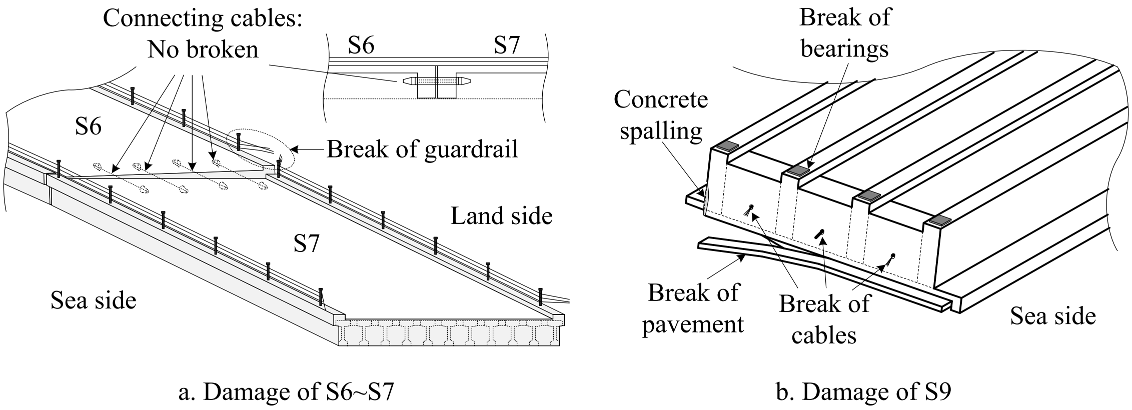

Figure 4. Typical damage of superstructures

that the concrete surfaces of beams dropped due to a collision with girders and most of bridge collapse preventions were crushed or flowed out.

2.3 *Detailed damage of superstructures*

The damage of S3~S7 is one of the typical ones, which flowed out connecting with each other, and the damage of S6~S7 was selected as an example to state in the following content. Under the wave action, S6 and S7 experienced a displacement of 28m together thus it is proper to regard them as a whole. When the bridge was retrofitted, 2 cables, which were used to prevent the relative movement in axis direction of superstructures, were installed between S6 and S7. The details of the cables are plotted in Figure 4-a. These cables played an important role to keep S6 and S7 flowing out together. Besides that, the damage of guardrails between S6 and S7was observed as well.

S9 is one of the inverted superstructures, the damage of which is shown in Figure 4-b. S9 experienced a displacement of 23m and was inverted by the wave-induced uplift. At the end surface of S8 side, different from the damage of S6 and S7, all of the cables which connected S8 and S9 were broken by the force between superstructures and the fracture traces could be

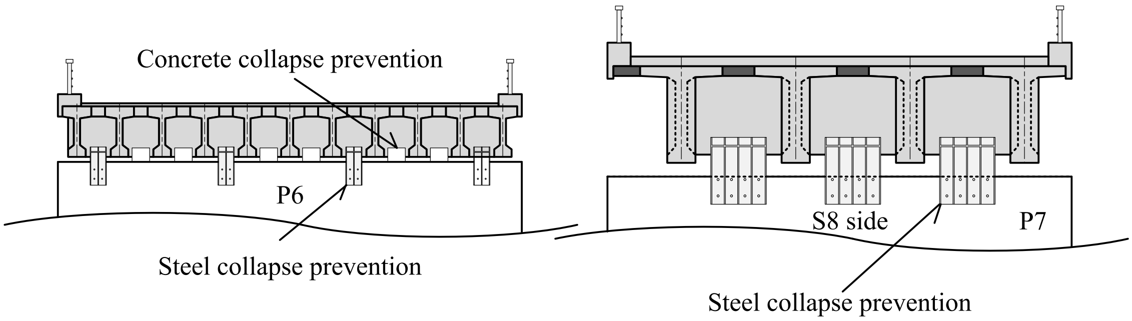

a. Superstructure collapse preventions on P6 b. Superstructure collapse preventions on P7

Figure 5. Details of collapse preventions on P6 and P7

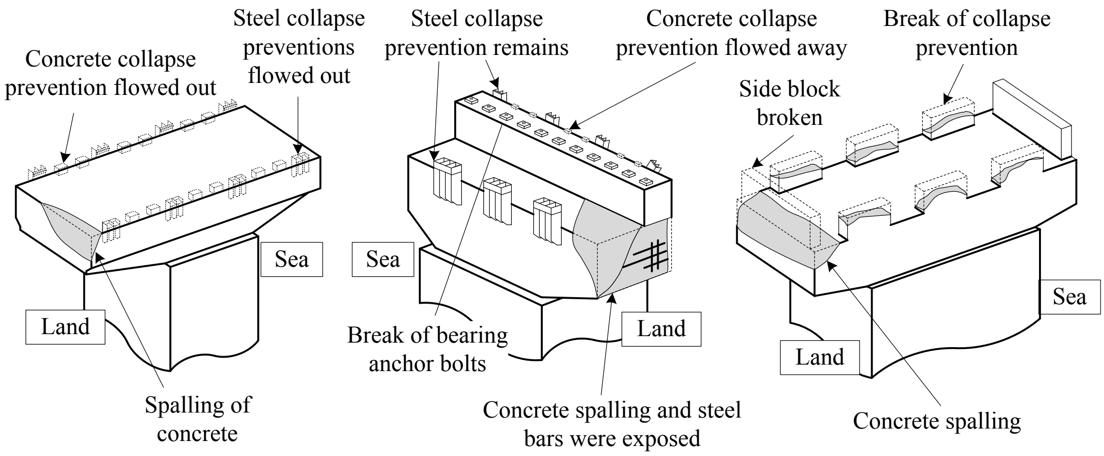

a. Damage of P6 b. Damage of P7 c. Damage of P8

Figure 6. Detailed damage to P6~P8

found. Moreover, at the supporting area of girders, the remains of bearing plates were noted. In light of this, it is obvious that during the tsunami attack the bearings fractured. Besides that, at the connection of the 2 decks, the debris of pavement connection was observed.

2.4 *Detailed damage of piers*

It was found that the 11 piers supported 3 types of superstructures. In this section, 3 piers were selected basing on their different supporting superstructures. P6 and P8 respectively supported one type of superstructures and in contrast, P7 supported 2 types of superstructures, illustrated in Figure 2. Therefore P6~P8 were selected to analyze. For P6 and P7, except for the concrete collapse preventions, they also had been installed steel preventions the installing details of which are shown in Figure 5. Different from P6 and P7, only concrete collapse preventions were set up at the top of P8. These collapse preventions not only limit the superstructure's movement along the axis direction but also the transverse direction of bridge.

The detailed damage of P6 is shown in Figure 6-a. When S6 and S7 were separated from P6, they imposed a horizontal collision on the concrete collapse preventions. Therefore, on the supporting plate of P6, 12 concrete collapse preventions were crushed. And for the same reason, the 8 steel collapse preventions, anchored on the sides of the beam, flowed out as well. Apart from the damage to the collapse preventions, the concrete surface of the beam which was located at the land side was also crushed.

Figure 6-b illustrates the detailed damage of P7 which supported 2 types of superstructures: S7 and S8. At S7 side, the installing details of superstructure collapse preventions were same as P6. Although the 6 concrete collapse preventions were crushed, the 4 steel ones were left. However, due to the girder-induced impact, the steel ones tilted. At S8 side, different from P6, only 3 larger steel collapse preventions were anchored and they did not flow out. The damage condition of steel collapse preventions demonstrates that when the superstructures, located on P7, displaced they were elevated by a wave-induced uplift. Because of this, the superstructures flowed from the top of the steel collapse preventions and did not impose a sufficient impact to make them separate from supports. Besides that, at the land side, the concrete surface of the beam was crushed and some steel bars could be observed.

The damage of P8 is plotted in Figure 6-c. On the top of beam, 6 concrete collapse preventions and 2 side concrete blocks had been set up. For the same force situation as the preventions of P6, the 6 concrete collapse preventions and one side block, which was at the land side, were crushed. Besides that, it was found that while the side block flowed out, a damage of the concrete surface, which under the side block, occurred.

3 DETERMINATION OF WAVE VELOCITY AND HEIGHT

3.1 *Determination of wave velocity*

In order to evaluate the wave action on bridge, it is necessary to obtain the wave flow velocity and height at Utatsu Bridge. Due to the lack of the wave velocity and height, a measurement was conducted by authors. 12 videos which recorded the tsunami attack in Minamisanriku Town and Sendai City were collected and based on these video records, the shot locations of which are shown in Figure 1, a measurement of wave velocity and height was conducted.

For instance, in a video the authors were able to search for 2 distinguished place points where a piece of floating debris passed through. By using Google Earth's distance measurer and the timer in the video, it is possible to obtain the distance and the time span for the floating debris flowed from one place point to the other. At last the kinematics Equation 1 was applied to calculate the velocity of the floating debris which is assumed to be the wave flow velocity.

$$v = S / t \qquad (1)$$

Where, v is wave flow velocity (m/s); S is the distance between 2 place points (m); t is the time span for the debris flowing from one point to the other (s).

In this paper, the velocity calculation of location 5, which is about 7.5km south west from Utatsu Bridge, is shown as an example. As shown in Figure 7-a, the flow of the floating debris was recorded. The distance from point 1 to point 2, which the debris passed through, was measured as 63m. When the debris passed point 1, the timing was starting and while it passed point 2 the timing was over. Based on the video's timekeeper, t=10s was obtained, as shown in

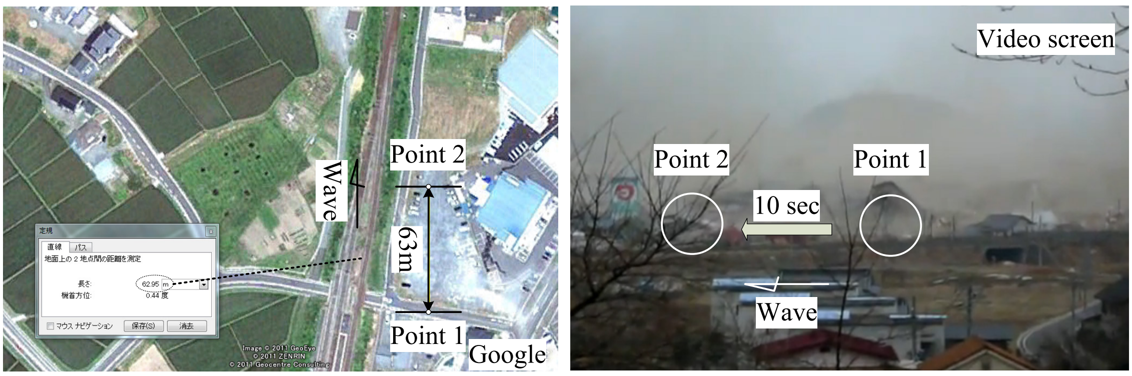

a. Distance between 2 points

b. Time span for the debris flowed from point 1 to point 2

Figure 7. Measurement of distance and time span for the debris flowed between 2 points

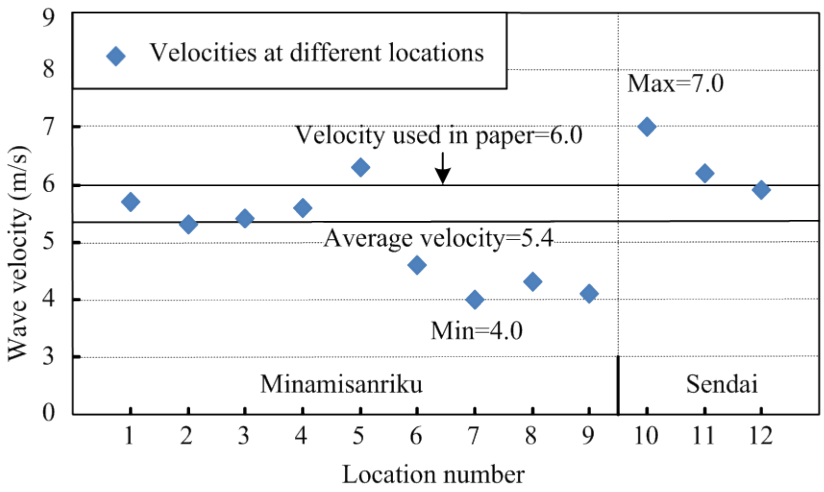

Figure 8. Computing result of wave velocity

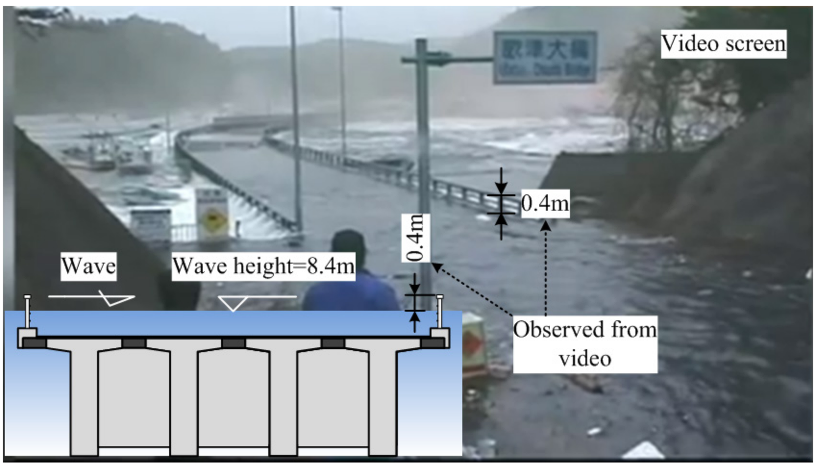

Figure 9. Calculation of wave height at S12

Figure 7-b. In the end, by using the Equation 1, the wave velocity at location 1 was calculated as 6.3m/s. By the same method, 12 groups of velocity data are available, illustrated in Figure 8.

Owing to the lack of the video data at the Utatsu Bridge, the authors assumed the wave velocity at Utatsu Bridge by using the 12 groups of data in other places. From Figure 8, it is observed that the maximum, average, and minimum velocities are respectively 7.0m/s, 5.4 m/s, and 4.0m/s. Combining the huge losses of the Utatsu Bridge, it is proper to assume the velocity at Utatsu Bridge as 6.0m/s, which is slightly larger than the average velocity.

3.2 *Determination of wave height*

The wave height was able to be determined as well by using video records. An evaluating example at S12 of the Utatsu Bridge was stated. Depending on the video record, the height from the wave top surface to the top of guardrail was able to be roughly determined as 0.4 m, refer to Figure 9.

After h was obtained, combining the detailed dimensions of the bridge and the sea level before wave coming, it is available to determine the wave height as 8.4m. Utilizing the same method, the wave heights of all spans could be roughly determined.

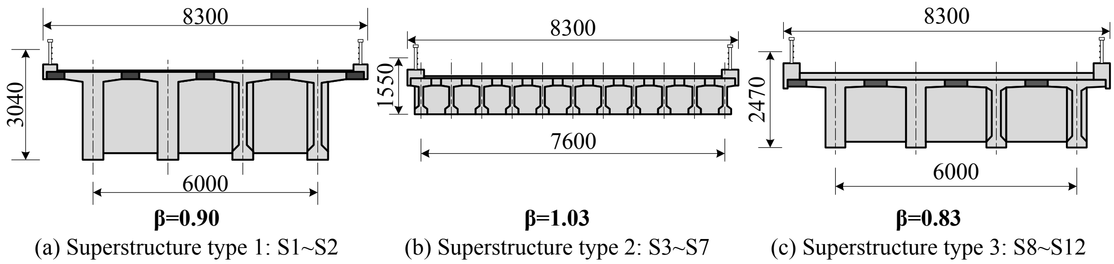

Figure 10. β values of 3 types of superstructures

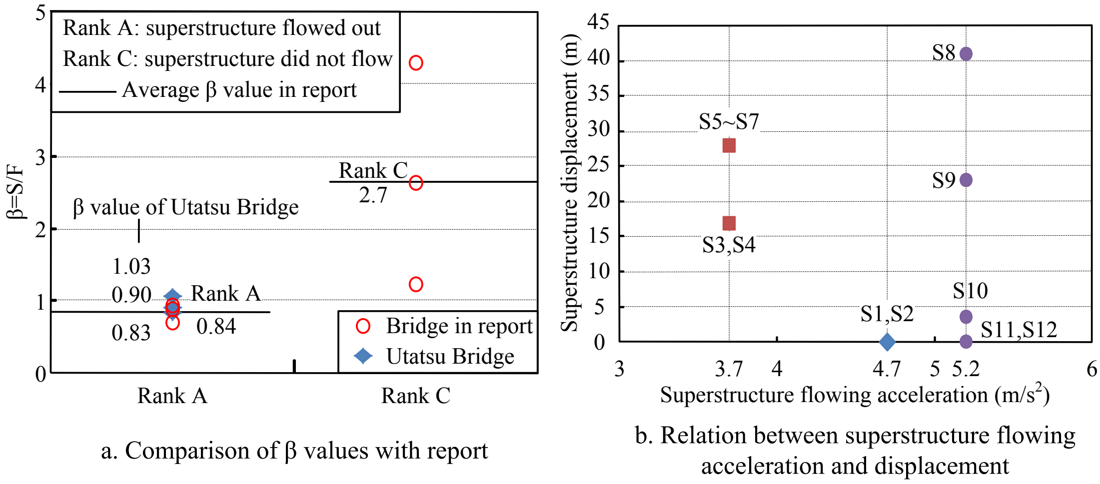

Figure 11. β result and α-L relationship

4 OUTFLOW JUDGMENT OF SUPERSTRUCTURE

4.1 *Outflow judgment by the comparison of wave acting force and frictional resistance*

In this chapter, the simple judging equations were applied to evaluate the outflow of superstructures. In order to judge the outflow of superstructures, the concept of ratio β between superstructure resistance and wave acting force was utilized (Kosa et al. 2010). The wave acting force could be calculated by Equation 2, in which the wave flow velocity had been verified as 6.0m/s, as mentioned in Chapter 3, and the resistant coefficient C_d was determined according to the Japanese specification (Japan Road Association, 2002). The superstructure resistance against wave force could be calculated by the product of the frictional coefficient and the superstructure weight, according to Equation 3.The frictional coefficient was assumed as 0.6, depending on the experimental result of the research (Shoji et al. 2009). Because when the wave was about to affect on the superstructures, no wave buoyancy acted on the bottoms of superstructures, the buoyancy was not considered in Equation 3.

After wave acting force and superstructure resistance were calculated, the Equation 4 was applied to compute the ratio between superstructure resistance and wave acting force for the sake of the outflow judgment of the superstructures. A large β value indicates a relative large resistance and the superstructure might not move off its support.

$$F = \frac{1}{2} \cdot \rho_w C_d v^2 A \tag{2}$$

$$S = \mu W \tag{3}$$

$$\beta = \frac{S}{F} \tag{4}$$

Where, F is wave acting force (kN); β is sea water density (1.03g/cm^3); Cd is resistant coefficient; v is wave velocity (m/s); A is side area of projection of superstructure (m^2); S is superstructure resistance (kN); μ is frictional coefficient (0.6); W is weight of superstructure (kN).

3 different β values have been calculated, because the Utatsu Bridge consists of 3 types of superstructures, illustrated in Figure 10. Based on the survey report (The Earthquake Engineering Committee, JSCE, 2011) the average β value of the bridges, located at the Tohoku area, which suffered serious dislocations, is 0.84. The β values of the Utatsu Bridge are 1.03, 0.90 and 0.83, which are close to 0.84. Therefore, it is sufficient for the wave acting force to make S3~S10 move off, as shown in Figure 11-a.

4.2 *Outflow judgment by the comparison of wave acting force and frictional resistance*

A further study was conducted to care that, at different acceleration cases, when superstructures were flowing out, the corresponding damage degrees of superstructures. Taking buoyancy effect into account, the authors have tried to find out the relation between superstructure accelerations and displacements. Equation 6 is derived from Equation 5 and at the right side of the Equation 5, the first item is wave acting force and the second item is superstructure resistance. Superstructure flowing accelerations could be calculated from Equation 6. Equation 7 expresses that the displacements of the superstructures are decided by their accelerations and the time spans they moved.

$$m\alpha = \frac{1}{2}\rho_w C_d v^2 A - \mu(mg - \rho_w gV) \tag{5}$$

$$\alpha = [\frac{1}{2}\rho_w C_d v^2 A - \mu(mg - \rho_w gV)]/m \tag{6}$$

$$L = \frac{1}{2}\alpha t^2 \tag{7}$$

Where, α is superstructure flowing acceleration induced by horizontal wave effect (m/s^2); m is the quality of superstructure (kg); g is gravity acceleration (m/s^2); V is the volume of superstructure (m^3); L is the displacement of superstructure (m).

The calculating result is plotted in Figure 11-b. It is found that the superstructures S1, S2, S11and S12 did not experience movements although their calculating accelerations are larger than S3~S7 and the possible reason is that for these spans, some huge obstacles in front of superstructures reduced the wave velocity which caused a decrease of acting force. By ignoring the superstructures which did not displace, it is found that the displacements of superstructures which had a same acceleration are different. For example, S8 moved 41m while S10 moved 3m although they had the same acceleration. The possible reason was put forward. Based on Figure 2, it is obvious that from the middle span to side spans the displacements reduce gradually from 41m to 0m, which expresses the wave force kept the same trend. Therefore, the acceleration of S8 should have been larger than S10 which resulted in their distinguished displacements.

5 JUDGMENT OF PIER DAMAGE

All of the piers of Utatsu Bridge did not collapse under the effect of tsunami. During the Great Eastern Japan Earthquake, it was a common phenomenon that bridge piers collapsed at the bottom of pier columns, so in this chapter, a comparison of acting moment and resistant moment at the bottom of the piers was presented to jutisfy the damage condition of piers. Considering that the wave effect on the middle span of the bridge was strongest, P8 is shown as an example.

In order to calculate the acting moment at the bottom (section A) of column, all of the external forces on P8 were found. As being illustrated in Figure 12-a, the external forces affected on Pier 8 have been divided into 2 types. The first type (F1) is wave-induced acting force, which affected on the side area of pier, and is able to be determined by Equation 8 (Japan Road Association, 2002). Before retrofit, the wave pressure area of P8 is 1.8m × 7.1m.

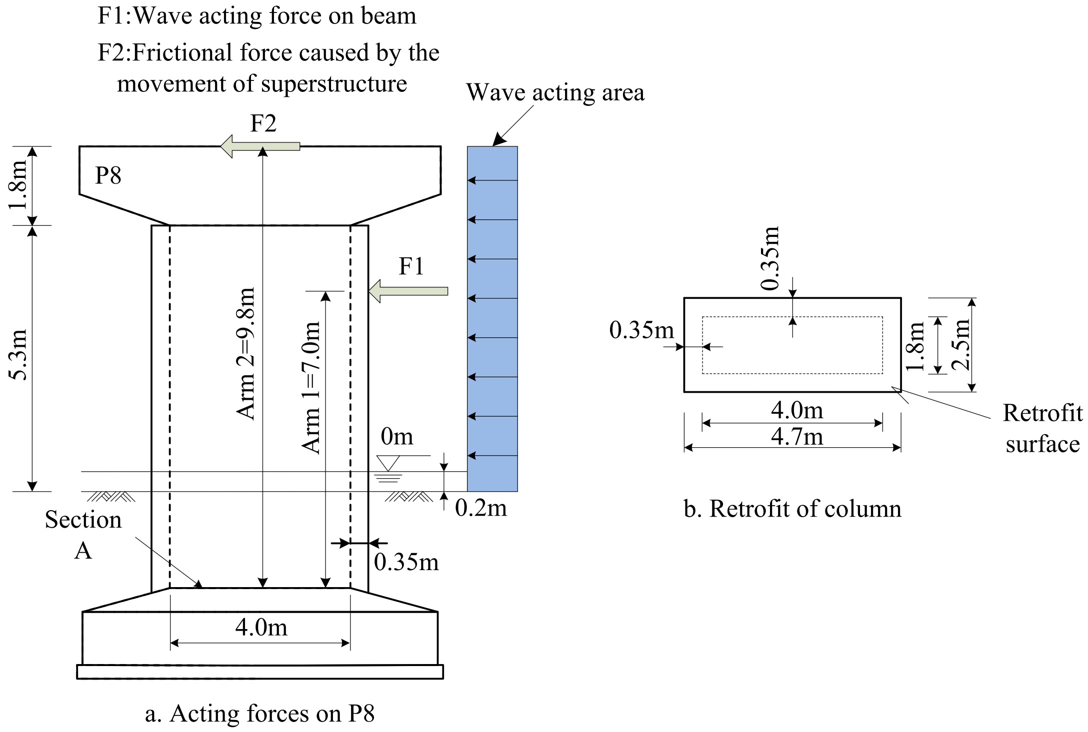

Figure 12. Calculation of acting moment at the base of column

Table 1. Calculation of acting moment

Acting force number	Acting force (kN)	Moment arm (m)	Acting moment (kN·m)
F1	322.6 (448.6)	7.0	2258 (3140)
F2	2040	9.8	19992
Total			22250 (23132)

*The data in () are after retrofit

$$P = K \cdot v^2 \cdot A \tag{8}$$

Where, P is wave acting force (kN); K is the coefficient determined by the shape of pier (assumed as 0.7 according to Japanese specification (Japan Road Association, 2002); v is wave flow velocity (6.0m/s); A is wave pressure area on piers (m^2).

The second type of acting force is the frictional force imposed by the movement of the superstructure upon P8. This type was determined by using the Equation 3 in Chapter 2. After these 2 external forces determined, the moment arms of them were searched according to Japanese specification (Japan Road Association, 2002). In the end, both 2 acting moments caused by F1 and F2 could be determined and the result is shown in Table 1. The total acting moment on section A was calculated as 22250 kN·m. The column of P8 has been retrofitted with the reinforcement concrete surface, as shown in Figure 12-b, so the wave pressure area became 2.5m×7.1m. And by the same method, the total acting moment was calculated as 23132 kN·m.

Aiming at checking the P8's strength at an extreme adverse situation, the authors assume the superstructure collapse preventions hold sufficient resistance to prevent the flow of superstructures on P8. In this case, F2 would become the wave acting force on the superstructures on P8. By the same method above, the total acting moment was calculated as 29208 kN·m (before retrofit) and 30090 kN·m (after retrofit), as shown in Figure 13.

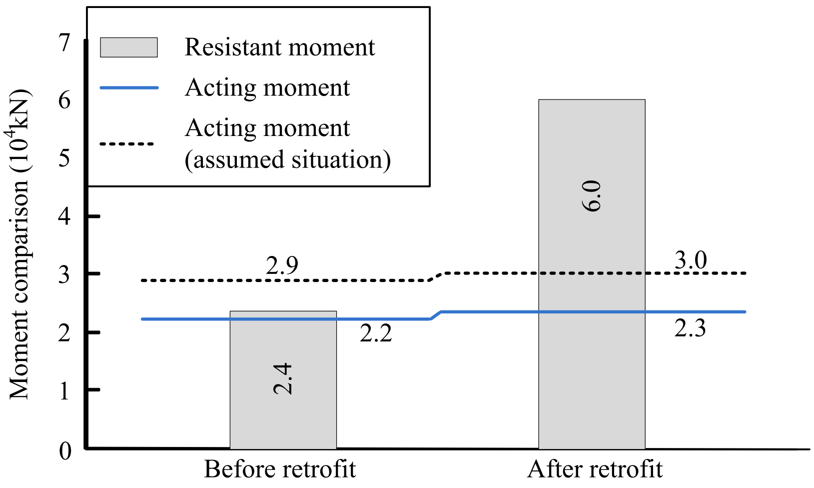

Figure 13. Comparison of acting moment and resistant moment

Based on the dimensions of section A (before retrofit), 4.0m (width) ×1.8m (height), and the reinforcement at section A: SD295D13ctc150, assumed based on the similar piers, the resistant moment has been obtained as 24000 kN·m. Nevertheless, if take the retrofit of the reinforcement concrete surface into account, the resistant moment becomes 60000 kN·m, refer to Figure 13. Obviously, the resistant moment after retrofit is sufficient to prevent P8 collapsing even for the extreme situation assumed. By the same method, the damage condition of all piers could be evaluated. Then after retrofit, all piers kept enough strength to resist collapse.

6 CONCLUCUSIONS

From the field survey and the comparison between the wave acting force and the resistance, the conclusions have been stated below:

(1) Based on the field survey, for the damage of superstructures, S3~S10 experienced serious dislocations. For the damage of piers, all piers did not collapse and the main damage is that their superstructure collapse preventions flowed out.

(2) The values of ratio β between superstructure resistance and wave acting force respectively are 0.90, 1.03 and 0.83. Comparing with the average β value (0.84) of the bridges, located at the Tohoku region, which suffered serious dislocations, the β values of the Utatsu Bridge are close to Rank A. So it is easy for S3~S10 to flow out under the wave force in horizontal direction.

(3) By the comparison of the wave acting moment and the resistant moment, after retrofit, at the bottom (section A) of P8, as an example, it was summarized that the resistant moment is 2.0 times stronger than the acting moment of the extreme situation assumed, so P8 did not collapse. By the same method, it can be verified that all piers kept sufficient strength to prevent collapse.

7 REFERENCES

Kosa, K., Nii, S., Shoji, G., Miyahara, K. 2010: Analysis of Damaged Bridge by Tsunami due to Sumatra Earthquake, *Journal of Structural Engineering*, Vol.55A: 456-460

Japan Road Association. 2002. *Specifications for Highway Bridges Part I Common*. Tokyo

Shoji, G., Moriyama, T., Fujima, K., Shigihara, Yo., Kasahara, K. 2009: Experimental Study Associated with A Breaking Tsunami Wave Load Acting onto A Single Span Bridge Deck, *Journal of Structural Engineering*, Vol.55A: 460-470

The Earthquake Engineering Committee, Journal of Structural Engineering. 2011: The Urgent Damage Survey Report of Great Eastern Japan Earthquake, Chapter 9: 90-91

Japan Road Association. 2002. *Specifications for Highway Bridges Part I Common*. Tokyo

Seismic Response Analysis Using Energy Transmitting Boundary in the Time Domain

Naohiro Nakamura
R&D Institute, Takenaka Corporation, Chiba, Japan

ABSTRACT: The energy-transmitting boundary, using in the models of the finite element method (FEM), is a quite efficient technique for the earthquake response analysis of buildings considering soil-structure interaction. However, it is applicable only in the frequency domain. The author has proposed methods for transforming frequency dependent impedance into the time domain. In this paper, an earthquake response analysis method for a soil-structure interaction system, using the energy-transmitting boundary in the time domain, was proposed. First, the transform of the transmitting boundary matrices to the time domain using the proposed transform method was studied. Then, time history earthquake response analyses using the boundary were performed. Through these studies, the validity and efficiency of the proposed methods were confirmed.

1 INTRODUCTION

It is important to consider the effects of soil-structure interaction to accurately estimate the behavior and the damage of buildings during large earthquakes. In the FEM analyses, wave boundary models are necessary at the side or bottom of the soil model to express a semi-infinite extent of the soil. In this paper, the side boundary is studied, since it is more important generally. As side boundary models, the viscous boundary (Lysmer et al. 1969), and the non-reflecting boundary (e.g. Smith 1973, Kunar et al. 1980) are well known to be applicable to analyses in the time domain.

In the viscous boundary (hereafter referred to as VB), a viscous damper is installed between the ends of the inner field model and a 1-dimensional model indicating the infinite far field (hereafter referred to as the free field model). It is well known that a wave motion propagated at right angles to the boundary is completely absorbed, but the wave motion in an oblique direction is not absorbed completely. Therefore, the region of the inner field model must be expanded to improve the analysis accuracy. The non-reflective boundary is applied to the analyses in the time domain as a method of eliminating the reflected wave. However, this method is rarely used due to many problems in actually applying it to the analyses.

As mentioned above, currently the cyclic and viscous boundaries are generally used as side boundary models. However, since the accuracy of these models is not particularly high, the boundary cannot be placed in the vicinity of the structure that is the main subject of analysis. Therefore, the modeling region for the inner field is enlarged, and the computational burden for the analyses is increased.

On the other hand, the energy-transmitting boundary (hereafter referred to as TB) is generally known as a highly accurate wave boundary (Lysmer et al. 1972, Waas 1972, Lysmer et al. 1975a, Kausel 1974, Lysmer et al. 1975b). The use of TB can sharply reduce the modeling region. TB is composed of an impedance matrix with strong frequency dependency and an additional force vector. It has been difficult, so far, to transform the former to the time domain. Therefore, the application of TB is limited to an equivalent linear analysis in the frequency domain.

The author has been carrying out investigations related to the transform of the frequency dependent dynamic stiffness to the time domain (Nakamura 2006a, 2006b, 2008). Furthermore, using the transform methods, a practical causal hysteretic damping model, in which the damping ratio is nearly independent of the frequency, was proposed (Nakamura 2007). In this paper, application of TB to the 2-D in-plane problem is described as the first stage of development. Then, an earthquake response analysis method, using this TB in the time domain, is proposed. This proposed method corresponds to the time history analysis version of the FLUSH program (Lysmer et al. 1975a).

First, outline of TB is introduced and the summary of the proposed transform methods is shown. Next, the validity of the transform of the TB impedance matrix to the time domain is investigated. Then, a time history response analysis method using TB is proposed. By conducting time history response analyses for a soil structure interaction model, the validity of the proposed method is demonstrated. The analysis results are compared with the results using TB in the frequency domains and the results using VB.

2 OUTLINE OF TRANSMITTING BOUNDARY

TB, which is called "the energy transmitting boundary" or "the consistent transmitting boundary," is applied at the ends of the inner field model. The main assumption of TB is that the free field consists of horizontally layered soil on rigid bedrock. TB is a highly accurate boundary, rigorous in a horizontal direction, and obeys the displacement interpolation function of elements in a vertical direction. (In the case of first-order linear elements, the displacement varies linearly.) As a result, this boundary can almost completely absorb wave motions propagating from any direction.

Lysmer & Waas (1972) proposed TB first for the 2-D anti-plane problem. Waas (1972) expanded TB to the in-plane problem. Based on these studies, Lysmer et al. developed the soil-structure interaction system analysis program, FLUSH (Lysmer et al. 1975a). In this program, pseudo-3D analyses can be carried out using the anti-plane VB. Kausel (1974) expanded this program for 3-D problems using a cylindrical coordinate system, and Lysmer et al. developed an axi-symmetric analysis program, ALUSH (Lysmer et al. 1975b).

As mentioned above, it is well known that TB is accurate, but can be analyzed only in the frequency domain. Therefore, it has been thought that TB cannot easily be applied in the time domain while maintaining its accuracy. In this study, investigations on the 2-D in-plane (Rayleigh wave) problem, corresponding to the FLUSH, are carried out. The outline of the TB used in this problem is introduced below.

As shown in Figures 1 and 3, half-scale models, each with TB only on its right side (a skew-symmetric condition at the central axis) are considered in this study. To the left of the TB is the inner field, and to its right is the free field. The wave equation of the free field in the 2-D in-plane problem is shown by Eq.(1).

$$([A]k^2 + i[B]k + [G] - \omega^2[M])\{u^*(\omega)\} = \{0\} \tag{1}$$

Here k: wave number, $\{u^*(\omega)\}$: displacement vector of the free field, and $[A]$,$[B]$,$[G]$,$[M]$: matrices of $2n \times 2n$ (n: node number), which can be given as the superposition of the submatrices $[A]_j$,$[B]_j$,$[G]_j$,$[M]_j$ for each of the following elements.

$$[A]_j = \frac{h_j}{6}\begin{bmatrix} 2(2G_j+\lambda_j) & 0 & (2G_j+\lambda_j) & 0 \\ 0 & 2G_j & 0 & G_j \\ (2G_j+\lambda_j) & 0 & 2(2G_j+\lambda_j) & 0 \\ 0 & G_j & 0 & 2G_j \end{bmatrix}, \quad [B]_j = \frac{1}{2}\begin{bmatrix} 0 & (G_j-\lambda_j) & 0 & (G_j+\lambda_j) \\ -(G_j-\lambda_j) & 0 & (G_j+\lambda_j) & 0 \\ 0 & -(G_j+\lambda_j) & 0 & -(G_j-\lambda_j) \\ -(G_j+\lambda_j) & 0 & (G_j-\lambda_j) & 0 \end{bmatrix}$$

$$[G]_j = \frac{1}{h_j}\begin{bmatrix} G_j & 0 & -G_j & 0 \\ 0 & (2G_j+\lambda_j) & 0 & -(2G_j+\lambda_j) \\ -G_j & 0 & G_j & 0 \\ 0 & -(2G_j+\lambda_j) & 0 & (2G_j+\lambda_j) \end{bmatrix}, \quad [M]_j = \frac{\rho_j h_j}{6}\begin{bmatrix} 2 & 0 & 1 & 0 \\ 0 & 2 & 0 & 1 \\ 1 & 0 & 2 & 0 \\ 0 & 1 & 0 & 2 \end{bmatrix} \tag{2}$$

Where, under the condition of Eq. (3), the eigenvalue problem related to the wave number in Eq. (4) is solved.

$$[C] = [G] - \omega^2[M] \tag{3}$$

$$\left| [A]k^2 + i[B]k + [C] \right| = \{0\} \tag{4}$$

From the obtained 4n eigenmodes, 2n modes corresponding to the waves propagating toward the right are extracted, and the mode matrix [V] is set using these modes. [K] is the diagonal matrix consisting of the eigenvalues. With this, the TB matrix on the right side of the model can be indicated with [R] in Eq. (5). [D] is set with the superposition of the sub-matrix $[D]_j$. Although [R] is not symmetric originally, in the following discussion, the matrix is made symmetric by averaging terms at symmetric positions.

$$[R] = i \cdot [A][V][K][V]^{-1} + [D] \quad , \quad [D]_j = \frac{1}{2}\begin{bmatrix} 0 & \lambda_j & 0 & -\lambda_j \\ G_j & 0 & -G_j & 0 \\ 0 & \lambda_j & 0 & -\lambda_j \\ G_j & 0 & -G_j & 0 \end{bmatrix} \tag{5}$$

Accordingly, the equation of motion for the entire model is given by Eq. (6), where [M_I]: mass matrix of the inner field, [K_I]: stiffness matrix of the inner field, and {$u(\omega)$}: displacement vector of the inner field
{$F(\omega)$} of Eq. (7) indicates the boundary force vector and −[D] {$u^*(\omega)$} shows the additional force vector, in the case of seismic motion being input from a vertical lower direction. [R], {$u^*(\omega)$}, and {$F(\omega)$} are defined with 2n degrees of freedom in the boundary part up to Eq. (5). However, hereafter they are extended to the number of degrees of freedom of the inner field to superimpose them on the values of the inner field.

$$(-\omega^2[M_I] + [K_I] + [R])\{u(\omega)\} = -\ddot{y}(\omega)[M_I]\{1\} + \{F(\omega)\} \tag{6}$$

$$\{F(\omega)\} = ([R] - [D])\{u^*(\omega)\} \tag{7}$$

3 TRANSFORM TB MATRIX TO TIME DOMAIN

Next, the transform of Eq. (6) to the time domain is considered. The vectors $F(\omega)$, $u(\omega)$, and $\dot{u}(\omega)$ can be transformed to the time domain using the usual inverse Fourier transform. Since the mass $[M]$ and stiffness matrices $[K]$ are not frequency dependent, there is no problem in the transform to the time domain. On the other hand, it is not easy to transform the frequency dependent TB matrix $[R]$ to the time domain. Therefore, the problem in the transforming Eq.(6) to the time domain reduces to transforming $[R]$ to the time domain. This chapter investigates this problem. First, the proposed transform methods are explained; then, the equation of motion in the time domain is described.

Although many methods to transform frequency dependent complex stiffness to the time domain have been proposed, most of them employed either the past displacement or the past velocity in the formulation of the impulse response. The author [9] proposed some transform methods using both the past displacement and velocity.

In this paper, following Method B' and Method C were used for the transform. The complex stiffness and the reaction of method B' are expressed as shown in Eqs. (8) and (9) respectively.

$$S'_B(\omega) = -\omega^2 \cdot m_0 + i\omega \cdot c_0 + k_0 + \left\{ i\omega \cdot \sum_{j=1}^{n'} c_j \cdot e^{-i\omega t_j} + \sum_{j=1}^{n'} k_j \cdot e^{-i\omega t_j} \right\} \tag{8}$$

$$F'_B(t) = m_0 \cdot \ddot{u}(t) + c_0 \cdot \dot{u}(t) + k_0 \cdot u(t) + \left\{ \sum_{j=1}^{n'} c_j \cdot \dot{u}(t - t_j) + \sum_{j=1}^{n'} k_j \cdot u(t - t_j) \right\} \tag{9}$$

Where $u(t)$ is the displacement. $t_j = j\Delta t$ where Δt is discrete time interval for the transform. It should be noted that Δt is usually different from ΔT (the time interval of the time history response analysis) as shown in Nakamura (2006a). c_j (= $c(t_j)$) and k_j (= $k(t_j)$) are the damping term and the stiffness term of the obtained impulse response function at t_j respectively. c_0 and k_0 are those of simultaneous components and $c_1 \sim c_{n'}$ and $k_1 \sim k_{n'}$ are those of the time-delay components. m_0 is the simultaneous component of mass term. All the unknown impulse response components are solved by simultaneous equations with given complex stiffness data $D(\omega_i)$ (i=0,1,2…N).

In the case of the hysteretic damping being large, the accuracy of the recovered value of the complex stiffness tends to deteriorate. In order to improve this problem, the simultaneous components (m_0, c_0, k_0) are corrected. This method is called method C'. The simultaneous components for the modified impulse response are set to be $m'_0=m_0+\Delta m$, $c'_0=c_0+\Delta c$ and $k'_0=k_0+\Delta k$. Where, Δm, Δc and Δk indicate the modification terms determined by the least square method (Nakamura 2008). The recovered value of the complex stiffness can be expressed using Eq. (10).

$$S'_C(\omega) = S'_B(\omega) - \omega^2 \cdot \Delta m + i\omega \cdot \Delta c + \Delta k \tag{10}$$

Using Eq.(10), the equation of motion in the frequency domain shown in Eq. (6) can be indicated in the time domain by Eq. (11), where $\{u(t)\}$ and $\{F(t)\}$ are values obtained by inverse Fourier transform, corresponding to $\{u(\omega)\}$ and $\{F(\omega)\}$, respectively. The force $[R]\{u(\omega)\}$ in the frequency domain is separated into the simultaneous component $\{R_0(t)\}$ and the time delay component $\{R_1(t)\}$ in the time domain, as shown in Eqs.(11) and (12).

$$[M_I]\{\ddot{u}(t)\} + [K_I]\{u(t)\} + \{R_0(t)\} = -\ddot{y}(t)[M_I]\{1\} + \{F(t)\} + \{R_f(t)\} \tag{11}$$

Where

$$\{R_0(t)\} = [m_0]\{\ddot{u}(t)\} + [c_0]\{\dot{u}(t)\} + [k_0]\{u(t)\} \quad , \{R_f(t)\} = -\sum_{j=1}^{n'}[c_j]\{\dot{u}(t-t_j)\} - \sum_{j=1}^{n'}[k_j]\{u(t-t_j)\} \tag{12}$$

4 CAUSAL HYSTERETIC DAMPING MODEL

In this study, a causal hysteretic damping model [12] is used for the inner field, to express the frequency independent material damping in the time history response analysis. This model is used for the quad element indicating the soil and for the shear spring element indicating the building. A summary of the model is shown below (details in Nakamura 2007). Eq. (13) shows the element displacement–element force relation in the frequency domain including hysteretic damping. This was obtained using the causal unit imaginary function $Z'(\omega)$ in place of the function $\mathrm{sgn}(\omega)\, i$ of the complex damping model $[K_e](1+2h\,\mathrm{sgn}(\omega)\, i)$.

$$\{F_e(\omega)\} = [K_e](1 + 2h \cdot Z'(\omega)) \cdot \{u_e(\omega)\} \tag{13}$$

Where $[K_e]$: element stiffness matrix, h: damping factor, $\{F_e\}$: element force vector, and $\{u_e\}$: element displacement vector. The imaginary part of $Z'(\omega)$ is set as a function, which has an almost constant value (=1) in a certain frequency range. The real part is set as a causal function, calculated using Hilbert transform of the imaginary part. $Z'(\omega)$ is transformed into the impulse response in the time domain. The obtained impulse response consists of both the damping term simultaneous component (c_0) and the stiffness term time delay components ($k_1, k_2, \ldots, k_n$, where $k_j = k(\Delta t \cdot j)$, Δt is the time step). From this, Eq. (13) can be expressed as Eq.(14) in the time domain.

$$\{F_e(t)\} = [K_e]\left[\{u_e(t)\} + 2h\left(c_0\{\dot{u}_e(t)\} + \sum_{j=1}^{n} k_j\{u_e(t - t_j)\}\right)\right] \tag{14}$$

This study focused on the frequency range of 0 to20Hz and Δt= 0.05 s for this damping model. Nine data points were used for the transform (2, 4, 6, … 18Hz). This model is equivalent to “the 8 term model” in Nakamura (2007).

5 EXAMPLE ANALYSES

The validity of the transform of TB to the time domain and the efficiency of the proposed time history response analysis method are investigated through example analyses. First, after making a TB matrix in the frequency domain for the soil model, the behavior of the transform in the time domain is investigated. Furthermore, considering a building embedded in this soil, time history seismic responses to the soil–structure interaction system are analyzed.

5.1 *Transform of the TB Matrix to the Time Domain*

The soil model used for the investigation is shown in Figure 1. Table 1 lists the properties of the soil. The model has a unit thickness in the anti-plane direction. The anti-plane VB is not taken into consideration in this study.

First, the TB matrix $[R]$ in Eq. (5) and the boundary force vector $\{F(\omega)\}$ in Eq. (7) are calculated in the frequency domain. The 6 × 6 TB matrix composed of horizontal and vertical degrees of freedom. The frequency range under consideration is 0–20 Hz for both $[R]$ and $\{F(\omega)\}$. Next, the transform of TB matrix to the time domain is carried out using method C. Table 2 shows the conditions for the transform.

Figure 2 compares the matrices recovered from the obtained impulse response and the original data points. For recovery from the impulse response, the simultaneous components k_0, c_0, and m_0 and the time delay components k_1–k_{10}, and c_1–c_{10} are used. The recovered values correspond quite well with almost all the data points. Therefore, the results of the transform of the TB matrix by method C are valid.

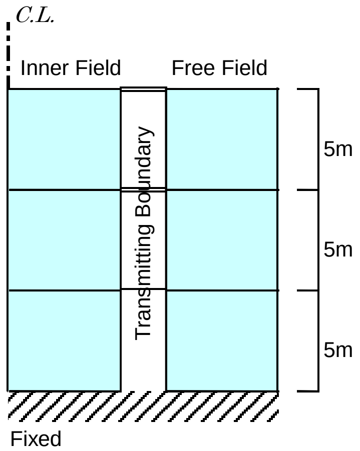

Figure 1. Soil model (skew-symmetric model)

Table 2. Conditions for Transform into the Time Domain

Impedance	
No. of data	Frequencies of data (Hz)
21	0.1, 1.0, 2.0, 3.0, … 19.0, 20.0

Impulse response		
Δt (s)	Simultaneous components	Time delay components
0.05	k_0, c_0, m_0	$k_1 \sim k_{20}$, $c_1 \sim c_{19}$

Table 1. Properties of Soil

Shear Velocity Vs (m/s)	400
Poisson's Ratio ν	0.4
Density ρ (t/m^3)	2.0
Damping ratio h	0.02

Table 3. Data for the building model

No.	Mass (t)	Rotational inertia (tm^2)	Shear stiffness ($\times 10^6$ kN/m)	Damping ratio h
1	480	-	1.755	0.03
2	480	-	2.924	
3	480	-	3.509	
4	480	-	∞	
5	720	88000	-	-

Table 4. Comparison of maximum response horizontal acceleration (Gal) (Inner field problem)

Node No.	Results of frequency response	Results of time history response					
		Stiffness proportional damping model		Strain energy proportional damping model		Causal hysteretic damping model	
1	2837	2762	0.97	2772	0.98	2908	1.03
2	2099	2015	0.96	2031	0.97	2101	1.00
3	1270	1253	0.99	1243	0.98	1273	1.00
4	749	700	0.93	736	0.98	720	0.96
5	723	667	0.92	703	0.97	694	0.96
6	515	477	0.93	516	1.00	510	0.99
7	321	323	1.01	323	1.01	323	1.01
34	811	755	0.93	805	0.99	780	0.96
35	722	667	0.92	702	0.97	693	0.96
36	518	494	0.95	521	1.01	506	0.98
37	321	323	1.01	323	1.01	323	1.01

Note: Gray parts show the ratio to the results of frequency response

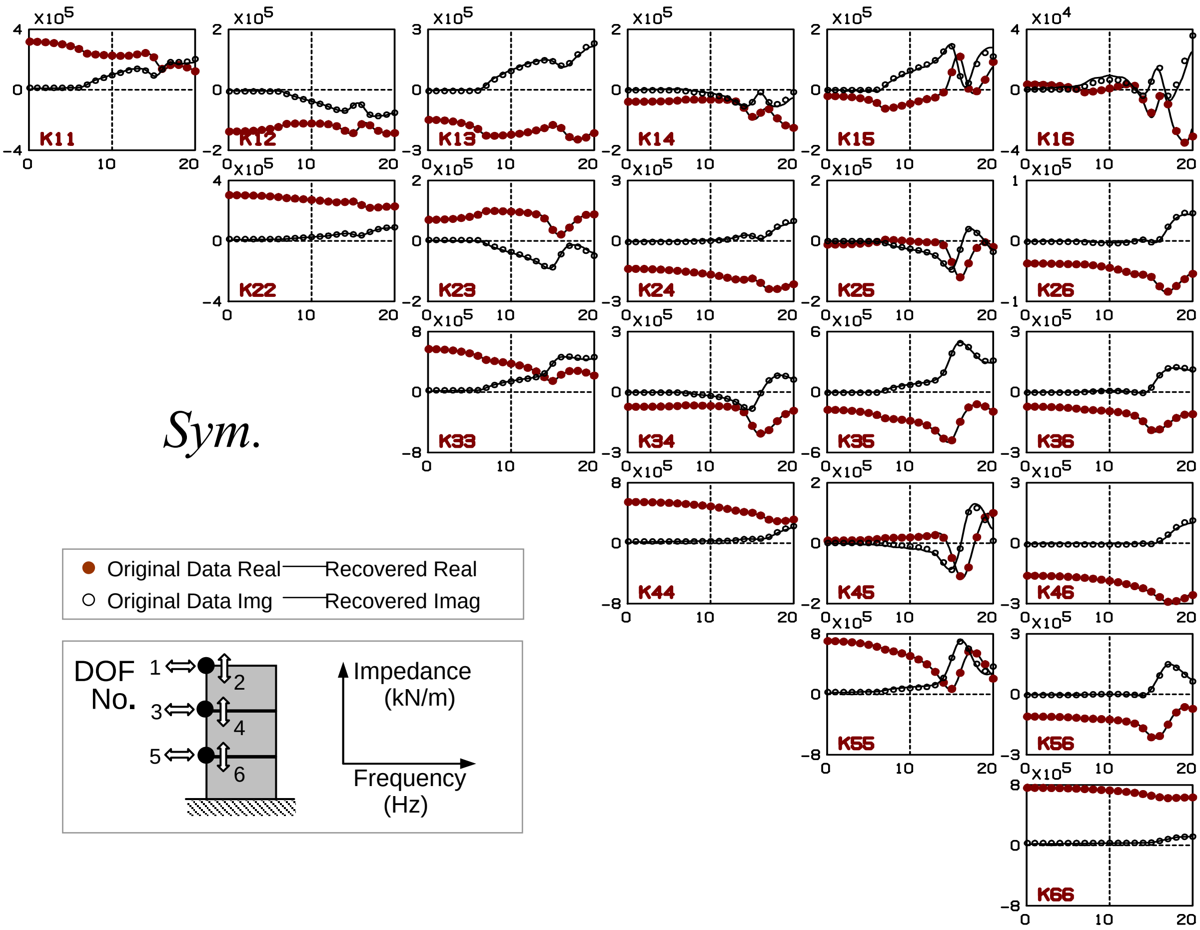

Figure 2. Accuracy of transform (Method C') of TB matrix to the time domain
(Comparison between values recovered from obtained impulse response and original data point)

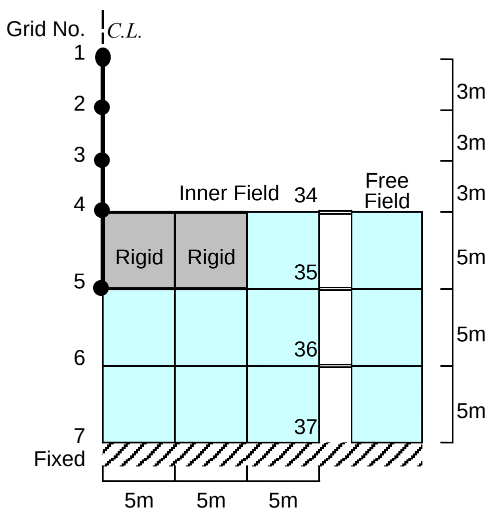

Figure 3. Soil-structure interaction analysis model

5.2 *Linear Seismic Response Analysis*

Next, to carry out response analyses, seismic ground motions were input into the soil–structure interaction system. The analysis model is shown in Figure 3, and the physical properties of the model are shown in Table 1. The building is a reinforced concrete structure. It has three stories above ground and a rigid basement. The plan of the building is 20m×20m. Table 3 shows the data of the building model. The TB matrix is the same as that in Figure 2, however, the thickness in the anti-plane direction of Figure 3 is 20 m, while that in Figure 1 is 1 m. El Centro 1940 NS wave (Δt = 0.005 s, continuous time = 10s, maximum acceleration =323.4 Gal) was used for the input ground motion.

5.3 *Investigations of the Material Damping Model*

Damping models were investigated using the inner field model with a free boundary, as shown in Figure 3. The stiffness proportional damping model, the strain energy proportional damping model, and the causal hysteretic damping model are studied.

The results of the time history response analyses using these damping models are compared to those of the frequency response analysis using the complex damping. With the stiffness proportional model, the damping ratios for the soil (2%) and the building (3%) are set at the primary eigenfrequency of the total model (4.92 Hz).

Table 4 indicates the maximum horizontal acceleration of the soil and building nodes. Using each damping model, the time history response analyses were carried out. The numbers 1–7 show the nodes on the central axis, and the numbers 34–37 show the nodes on the outer ends. The numbers in the colored parts in each column show the ratio of the time history response analysis results to the results of the frequency response analysis, which is considered the accurate value in this study.

For the stiffness proportional model, the maximum differences are about 8% at the nodes on both the central axis and at the outer ends. Thus, the accuracy of this model is not high. The strain energy proportional model and the causal hysteretic damping model showed a maximum difference of 3% and 4% at the nodes, on both the central axis and the outer ends, respectively. Both values are fairly favorable. Thus, the causal hysteretic damping model, for which the quad elements are used, has relatively good accuracy — almost the same degree as the strain energy proportional model.

Table 5. Comparison of maximum response horizontal acceleration (Gal)

Node No.	Results using TB (Freq. domain)	Results using TB (Time domain)			
		Strain energy proportional damping model		Causal hysteretic damping model	
1	4092	3836	0.94	4152	1.01
2	2692	2551	0.95	2736	1.02
3	1380	1318	0.96	1365	0.99
4	669	608	0.91	703	1.05
5	674	588	0.87	682	1.01
6	519	483	0.93	514	0.99
7	321	323	1.01	323	1.01
34	744	639	0.86	758	1.02
35	684	604	0.88	700	1.02
36	515	497	0.97	556	1.08
37	321	323	1.01	323	1.01

Note: Gray parts show the ratio to the results of frequency response

Table 6. Comparison of maximum response horizontal acceleration (Gal)

Node No.	Results using TB			Results using VB					
	Freq. Domain	Time Domain (Proposed)		(a) Base width × 1.5		(b) Base width × 5		(c) Base width × 10	
1	4092	4152	1.01	4756	1.16	4013	0.98	3962	0.97
2	2692	2736	1.02	2940	1.09	2677	0.99	2668	0.99
3	1380	1365	0.99	1305	0.95	1378	1.00	1379	1.00
4	669	703	1.05	978	1.46	803	1.20	771	1.15
5	674	682	1.01	976	1.45	831	1.23	791	1.17
6	519	514	0.99	648	1.25	645	1.24	591	1.14
7	321	323	1.01	323	1.01	323	1.01	323	1.01

Note: Gray parts show the ratio to the results using TB

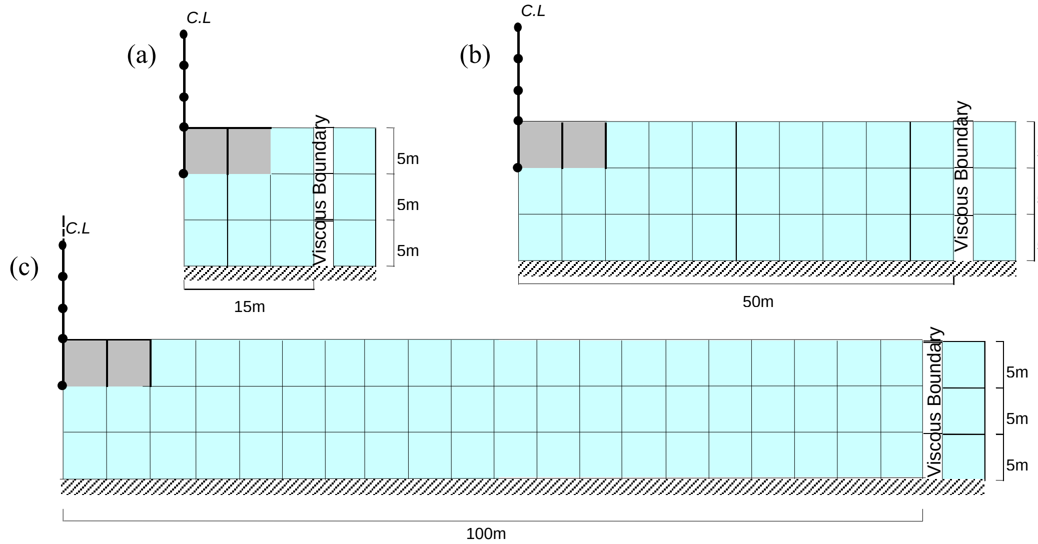

Figure 4. Model used for response analysis using VB Foundation breadth
(a) Base width × 1.5, (b) Base width × 5, (c) Base width × 10

5.4 *Response Analyses using the TB Matrix Transformed to Time Domain*

The results of the proposed time history response analyses, carried out using the TB matrix transformed to the time domain, are compared with the response analysis results in the frequency domain (Super FLUSH/2D by Kozo Keikaku Engineering (1999) is used here to investigate the validity of the proposed method.

For a damping model, both the strain energy proportional model and the causal hysteretic damping model were used, because of their high accuracy.

The simultaneous components (k_0, c_0, and m_0) and the time delay components (k_1–k_{10} and c_1–c_{10}) were used for the TB matrix from among the impulse response components obtained from the transform to the time domain. These are identical to the components used for the recovery calculation in Figure 2.

Table 5 compares the maximum response horizontal acceleration from the proposed method with that obtained from frequency analysis. The nodes subjected to comparison were positioned on the central axis and the outer ends. These are the same nodes shown in the previous section. The outer edge was set as TB in this section, whereas it was a free boundary in the previous section.

As shown in Table 5, in comparing the time history response results using the causal hysteretic damping model with the frequency analysis results, the difference is ≤ 2% at almost all nodes, except for a node on the outer edge where the difference is 8%. This comparison indicates that, on the whole, the results obtained from both analyses correspond well, and confirms the validity of the proposed method.

On the other hand, when the results from the strain energy proportional model, which was nearly equivalent in accuracy to the causal hysteretic damping model in the previous section, are compared with the frequency analysis results. The difference is ≥ 5% at half of the nodes, and the maximum difference is 14% at the node on the outer edge. This is a decrease in accuracy from the previous section. The reason for this decrease is thought to be as follows.

In this study, the damping matrix was computed using all eigenmodes, by carrying out eigenvalue analyses of the inner field with the outer edge considered as the free boundary (the same conditions as in the previous section). It is thought that the connection of the TB matrix to the inner field causes a variation in the eigenvalue of the model, and this variation causes the decrease in accuracy. If this is true, the obtained damping matrix might be modified based on component mode synthesis methods (e.g. Craig et al. 1968).

However, the efficiency of the strain energy proportional damping model appears low. This is because the model uses full matrix damping and requires eigenvalue analyses to obtain the total eigenmodes. Therefore, the computational burden of using the model is heavy for large-scale problems.

It is necessary to memorize the past displacement and velocity when using the causal hysteretic damping model, however, eigenvalue analyses and full matrix damping are not necessary. This lightens the computational burden is to a high degree. Thus, the causal hysteretic damping model can be effective as the damping model in this proposed method.

5.5 *Comparison with Response Analysis using VB*

The validity of the proposed method was investigated by comparison with the viscous boundary (VB), which is a representative boundary model in the time domain. Figure 4 shows the analysis models used in this investigation. The causal hysteretic damping model served as the inner damping model.

The width of the inner field of the analysis model was varied to (a) 1.5 times, (b) 5 times and (c) 10 times the base width (20m). Since a 1/2 scale skew-symmetric model is used, the width of the inner field in the figure is set to 1/2 of the width mentioned. Model (a) has the same shape as the analysis model used for TB, as shown in Figure 3.

Table 6 compares the maximum horizontal acceleration at the central axis position of each model with the results of frequency response analysis using TB. Model (a), showed a difference of 16% at the building's top (node # 1) and ≥45% at the foundation (nodes # 4 and 5) — its accuracy is low. For models (b) and (c), however, which had a wider inner field, the difference is improved. Compared with these results, the accuracy of the model using TB in the time domain (proposed model) is higher than model (c).

5.6 *Nonlinear Seismic Response Analysis*

To confirm the efficiency of the proposed method, nonlinear response analyses were carried out. The skeleton curves for the nonlinear relationships between the shear force and the shear strain for each story of the building are shown in Fig. 5. The normal tri-linear model is used for the hysteresis curve. The other analysis conditions are the same as those in the previous section, but the initial damping of the building is set to zero.

Table 7 compares the maximum horizontal acceleration of models using VB and TB. All the results in this table were obtained from the time history response analysis. Similar to Table 6, an increase in the inner field width of VB models caused the results to approach those of TB model. However, this approach seems to be more gradual than that of the linear problem.

The maximum shear forces and strains for each story are also plotted in Fig. 5. In particular, in the plots of 1F, a certain difference is seen between the result with TB and that with VB (base width 1.5). In general, the differences decrease gradually with an increase in the inner field

width as before, whereas in the plots of 2F and 3F, the results with VB do not closely approach those with TB.
Therefore, the results with TB are thought to be valid; thus, the proposed method is efficient and practical for nonlinear problems.

Table 7. Comparison of maximum response horizontal acceleration (Gal)

Node No.	Results using TB in Time domain (Proposed)	Results using VB							
		Base width × 1.5		Base width × 5		Base width × 10		Base width × 15	
1	681	719	1.06	643	0.94	633	0.93	635	0.93
2	976	989	1.01	913	0.94	923	0.95	932	0.95
3	1046	1104	1.06	1106	1.06	1079	1.03	1039	0.99
4	738	1061	1.44	1019	1.38	949	1.29	853	1.16
5	722	1003	1.39	986	1.37	925	1.28	833	1.15
6	545	664	1.22	691	1.27	647	1.19	601	1.10
7	323	323	1.00	323	1.00	323	1.00	323	1.00

Note: Gray parts show the ratio to the results using TB

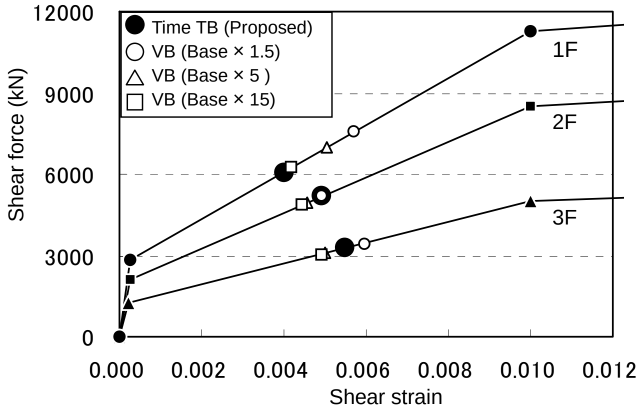

Figure 5. Skeleton curves for each story

6 CONCLUSIONS

In this study, the transmitting boundary for the 2-D in-plane problem (corresponding to the boundary in the FLUSH program) was transformed to the time domain, and a method for carrying out time history seismic response analyses for a soil–structure interaction system using this boundary was proposed.
It was confirmed that the frequency dependent impedance matrix of the transmitting boundary can be transformed to the time domain with excellent accuracy. Then, through earthquake response analyses, the validity of the proposed method was confirmed. Furthermore, by comparison with the viscous boundary, which is a representative boundary model in the time domain, the efficiency of the proposed method was shown.

ACKNOWLEDGEMENT

This work was supported by the Grand-in-Aid for Scientific Research C (No. 20560543) from Japan Society for the Promotion of Science.

REFERENCES

Lysmer, J. Kuhlelameyer, R.L. 1969. Finite Dynamic Model for Infinite Area, *J. Eng. Mech. Div*., ASCE, 95(EM3):859-877.

Smith, W. 1973. A Non-reflecting Plane Boundary for Wave Propagation Problems, *Journal of Computational Physics.*15:492-503.

Kunar, R.R. Rodriguez-Ovejero, L. 1980. A Model with Non-reflecting Boundaries for Use in Explicit Soil-Structure Interaction Analysis, *Earthquake Engineering and Structural Dynamics* 8:361-374.

Lysmer, J. Waas, G. 1972. Shear Wave in Plane Infinite Structures. *J. Eng. Mech. Div*., ASCE; 98(EM1):85-105.

Waas, G. 1972. Earth Vibration Effects and Abatement for Military Facilities Analysis Method for Footing Vibrations Through Layered Media, *Technical Report S-71-14, U.S. Army Engineer Waterways Experiment Station*.

Lysmer, J. Udaka, T. Seed, H.B. Hwang, R.N. 1975a. FLUSH, a Computer Program for Approximate 3-D Analysis of Soil-structure Interaction Problems, *Report No.EERC75-30, University of California, Berkeley*.

Kausel, E. 1974. Forced Vibration of Circular Foundations on Layered Media, *Research Report R74-11 Soils Publication No. 336, Dept. of Civil Eng., M.I.T.*

Lysmer, J. Udaka, T. Tsai C.F. Seed, H.B. 1975b. ALUSH a Computer Program for Seismic Response Analysis of Axisymmetric Soil-structure Systems, *Report No. EERC75-31, University of California, Berkeley*.

Nakamura, N. 2006a. A Practical Method to Transform Frequency Dependent Impedance to Time Domain, *Earthquake Engineering and Structural Dynamics*, 35:217-234.

Nakamura, N. 2006b. Improved Methods to Transform Frequency Dependent Complex Stiffness to Time Domain, *Earthquake Engineering and Structural Dynamics*, 35:1037-1050.

Nakamura, N. 2008. Transform Methods for Frequency Dependent Complex Stiffness to Time Domain Using Real or Imaginary Data Only, *Earthquake Engineering and Structural Dynamics*, 38:495-516.

Nakamura, N. 2007. Practical Causal Hysteretic Damping, *Earthquake Engineering and Structural Dynamics*, 36:597-617.

Kozo Keikaku Engineering Inc. Jishin kougaku kenkyusho Inc, 1999. *Super FLUSH/2D Theoretical Manual*

Craig, R.R. Bampton, M.C.C. 1968. Coupling of Substructures for Dynamic Analysis, *AAIA Journal*, 6(7):1313-1319.

Nakamura, N. 2009. Nonlinear Response Analysis of Soil-Structure Interaction System Using Transformed Energy Transmitting Boundary in the Time Domain, *Soil Dynamics and Earthquake Engineering* 29:799-808.

Influence of the Embedded Length of Friction Pile on Seismic Isolation Effect of Elevated Railway Bridge Rigid Frame

H. Kimata
P. Rungbanaphan
Civil Engineering Division, Shimizu Corporation, Japan

K. Fukutake
J. Jang
Institute of Technology, Shimizu Corporation, Japan

Y. Murono
A. Toyooka
T. Nishimura
Structures Technology Division, Railway Technical Research Institute, Japan

ABSTRACT: A non-linier dynamic analysis of elevated railway bridge rigid frame using the true dimension has been carried out. By variation of the length of piles, the influence of embedded length of friction pile on the seismic isolation effect of the structure have been studied and compared with the case of using bearing pile. It is found that using friction pile with relatively short embedded length significantly gives lower ductility ratio in the structure members under large scale seismic motion, comparing to using longer embedded or bearing pile.

1 INTRODUCTION

In previous paper, the seismic isolation effect of the friction piles and bearing piles for the elevated railway bridge rigid frame have been compared and investigated. For the current paper, by performing the similar analysis with different lengths of the friction piles, the effect of embedded length of pile on the seismic isolation effect for the same rigid frame structure is studied and the results are summarized in this paper.

2 ANALYSIS MODEL AND PARAMETER

Figure 1 shows a standard 3-span elevated railway bridge rigid frame with true dimension. By assuming plain strain condition in transverse direction, a non-linear dynamic analysis using 2-D FEM has been performed.

The analysis model is shown in Figure 2. In the previous study, dynamic analysis for shallowly embedded friction piles with pile tips down to the soft soil layer, AC2, (Case 1) has been performed. In the current study, additional analysis of deeply embedded friction piles with pile tips down to the intermediately supporting layer, DS1, (Case 2) is presented. By means of the analysis, the effect of changes of embedded lengths of friction piles on the seismic isolation effect for the elevated bridge rigid frame, comparing to those of bearing piles, can be investigated.

According to the Design Standards for Railway Structures and Commentary, non-linear behavior of each structure member is considered by (1) assuming the relationship between bending moment

(M) and curvature (φ) for the upper girders and piles; (2) assuming plastic hinges and bending moment (M)-rotation angle (θ) relationship for the columns and the ground girders (refer to Figure 3. Changes of axial force have been considered. The relationship for the case of zero-axial force is also presented). To cope with the non-linear behavior of soil, extension of the Ramberg-Osgood model in 2-dimensional problem has been used. The soil parameters used in the analysis is summarized in Table 1.

Table1 Input soil parameter

Soil layer	Soil Type	Level GL(m)	γ (kN/m^3)	N Value	Vs (m/s)	$\gamma_{0.5i}$	h_{max}
Ac1	Clay	-3.301	12	0	70	1.4×10^{-4}	0.23
Ac2	Clay	-13.301	17	10	130	1.4×10^{-4}	0.23
Dc1	Clay	-20.001	16	15	220	1.4×10^{-4}	0.23
Ds1	Sand	-23.701	19	50	300	3.5×10^{-5}	0.27
Ds2	Sand	-24.501	19	30	300	3.5×10^{-5}	0.27
Dc2	Clay	-27.801	16	15	220	1.4×10^{-4}	0.23
Ds3	Sand	-32.181	20	75	400	—	—

Remarks: 1) Ground water level of GL±0.0 is assumed.

2) $\gamma_{0.5}$ refers to confining pressure dependency of soil. $\gamma_{0.5i}$ refers to $\gamma_{0.5}$ at unit effective confining pressure σ_m' = 1kN/m^2.

3) Soil classification：G4 type soil（natural period, T=0.55s）

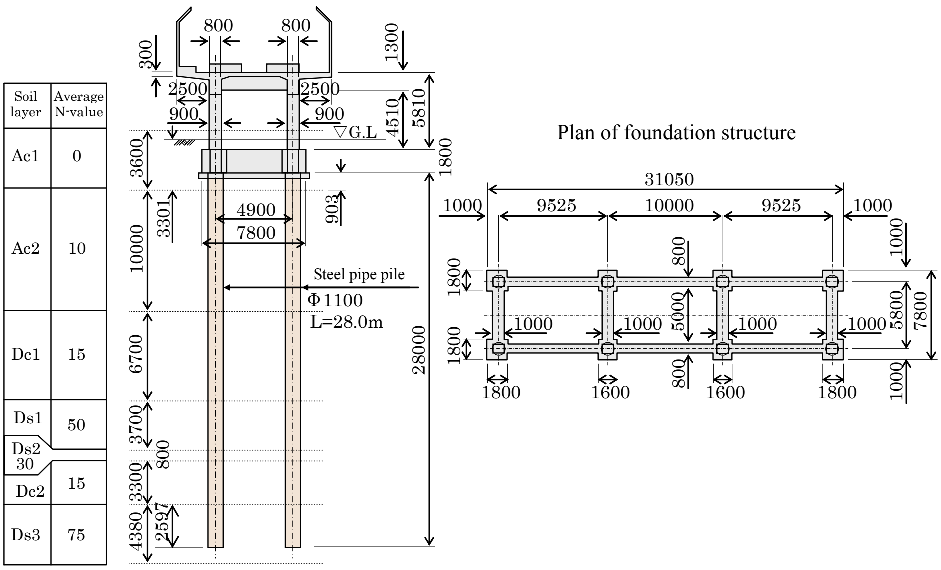

Figure1 3-span elevated railway bridge frame model with true scale

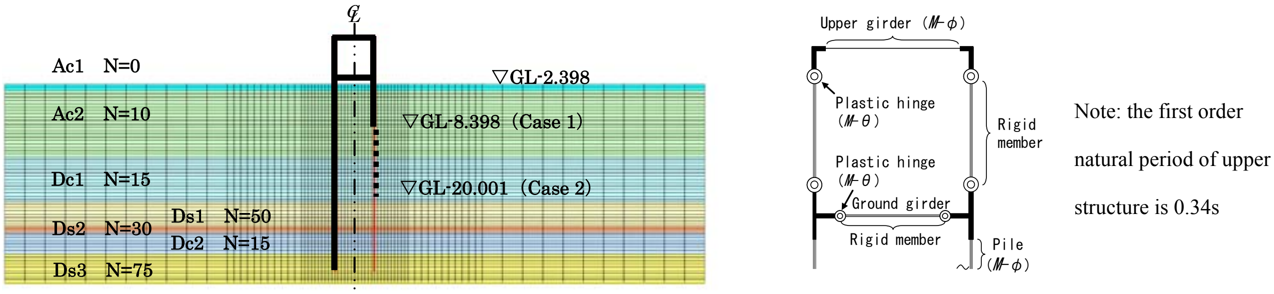

(a) bearing pile model (b) friction pile model (c) Detail model of upper structure

Figure 2 2-D FEM model for non-linear dynamic analysis（bottom surface condition: permeable boundary, side surface condition: periodic boundary）

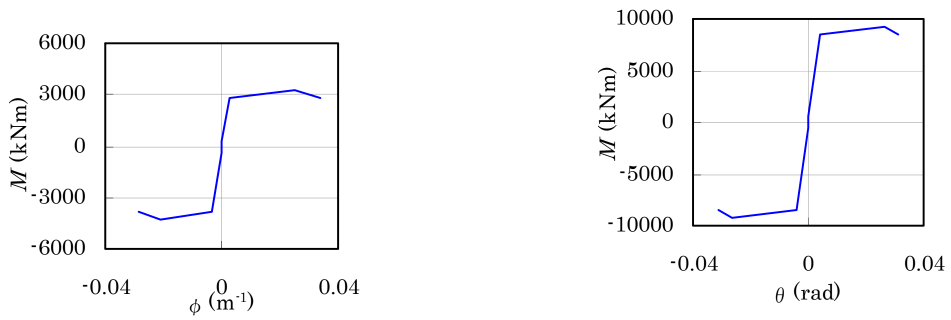

(a) *M*-φ relationship of the upper girder (b) *M*-θ relationship of the ground girder

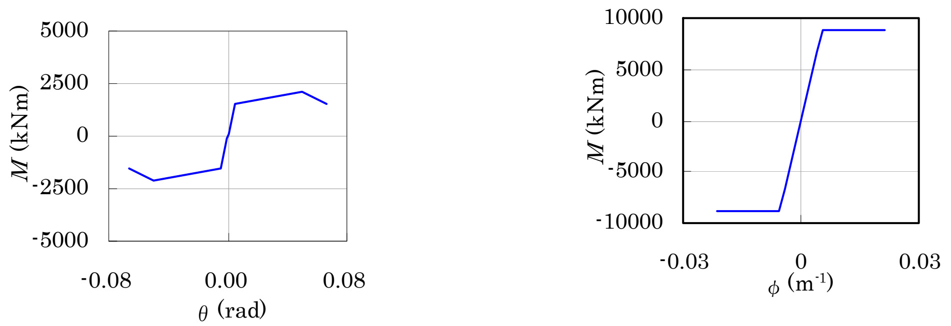

(c) *M*-θ relationship of the column (d) *M*-φ relationship of the upper part of pile

Figure 3 non-linear behavior of structural members

3 INPUT SEISMIC MOTION

Based on the Design Standards for Railway Structures and Commentary, L1 seismic motion and L2 seismic motion (Spectrum I, II compatible wave) are chosen to be used as an input seismic motion. Acceleration time history and acceleration response spectrum of the input seismic motion is shown in Figure 4.

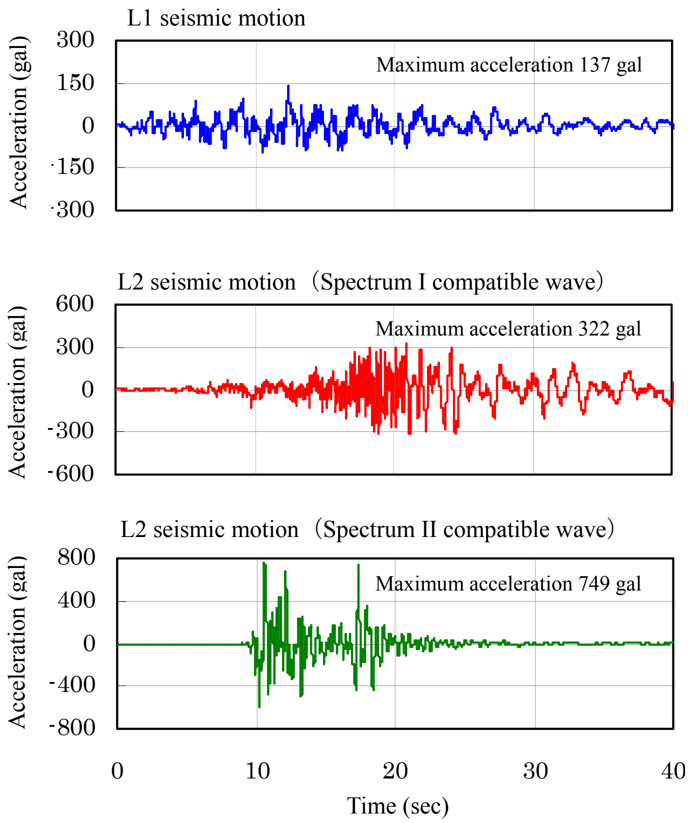

(a) Acceleration time history

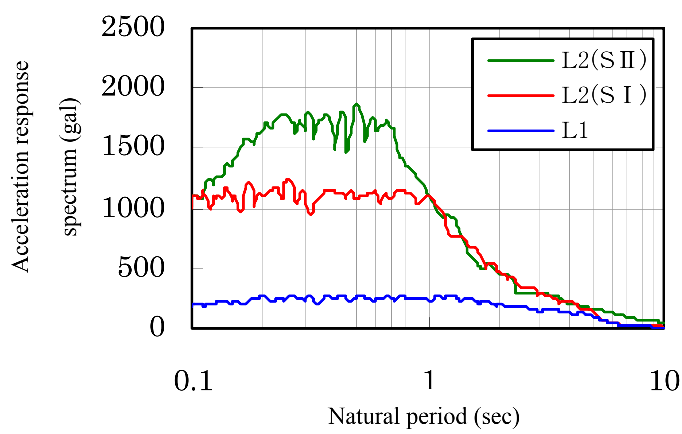

(b) Acceleration response spectrum

Figure 4 Input seismic motion

4 RESULTS OF NON-LINIER DYNAMIC ANALYSIS USING 2-D FEM

The distribution of maximum shear strain and displacement and for the Case of L2 seismic motion (Spectrum II) is illustrated in Figure 5, while the maximum ductility ratio of the column and the ground girder is presented in Figure 6, as the examples for the analysis results.

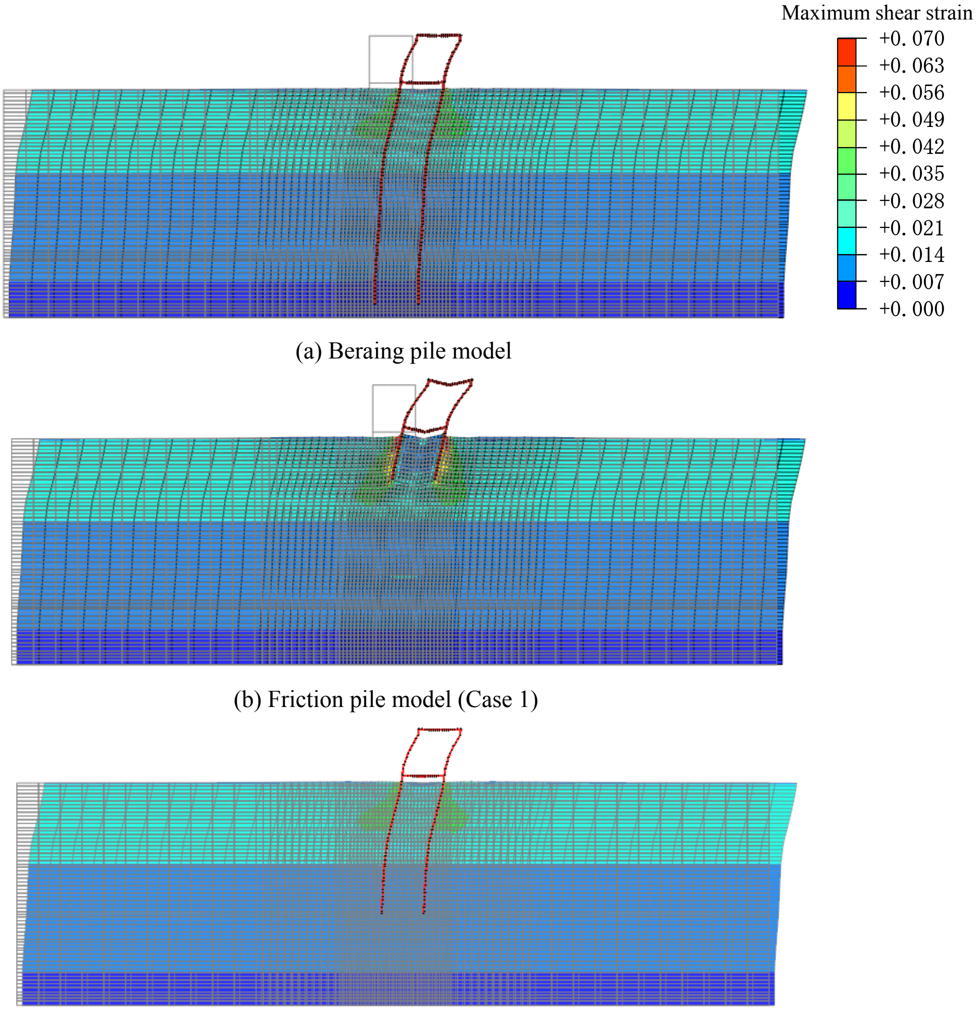

(a) Beraing pile model

(b) Friction pile model (Case 1)

(c) Friction pile model (Case 2)

Figure 5 Distribution of maximum shear strain and displacement (L2 seismic motion: Spectrum II compatible wave)

Considering maximum ductility ratio in the columns and ground girders, even though the significant difference between the bearing pile and the friction pile for the case of L1 seismic motion is not appeared, ductility ratio is found to be reduced in friction pile comparing to bearing pile for the case of L2 seismic motion. The reduction is especially obvious for Spectrum II compatible wave. The reduction of ductility ratio under L2 seismic motion is corresponding to the fact that the maximum shear strain around the friction piles in Ac2 layer is greater than those around the bearing piles (Figure 5). In other words, using friction pile can reduce the seismic isolation effect and locking effect of the structure member through the non-linier behavior of soil.

As for effect of the embedded length, change of the length from Case 1 to Case 2 does not give any significant difference in the maximum ductility ratio of the column. However, for the ground girder, the piles with shallower embedded length of Case 1 obviously shows the larger reduction of ductility ratio, comparing to the piles with deeper embedded length of Case 2.

Concerning the acceleration response of the upper structure, it is found that using friction pile can reduce the acceleration response at the ground girder for about 15～40% under L2 seismic motion.

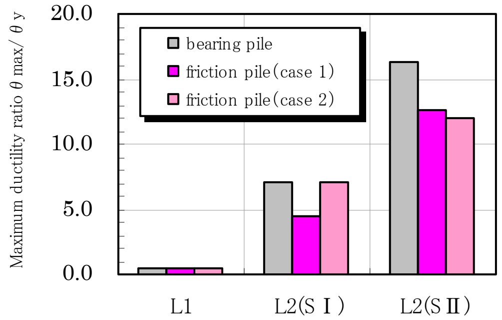

(a) Column（Left side・upper hinge）

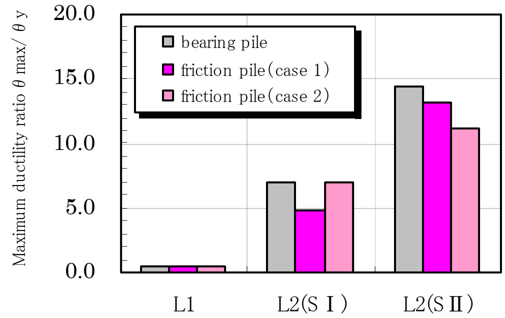

(b) Column（Right side・upper hinge）

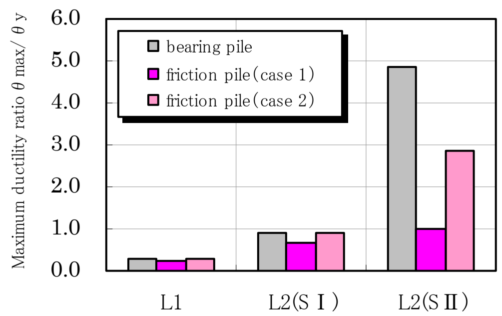

(c) Ground girder（left side hinge）

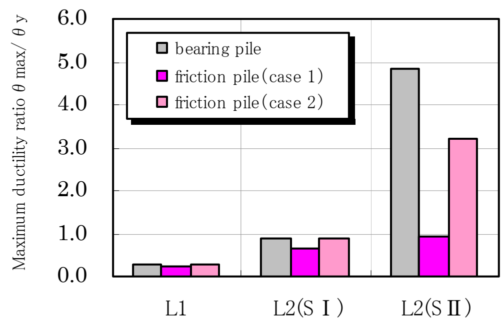

(d) Ground girder（Right side hinge）

Figure 6 Maximum ductility ratio (L2 seismic motion : Spectrum II compatible wave）

5 CONCLUSION

The non-linier dynamic analysis of elevated railway bridge rigid frame using the true dimension has been preformed and the comparison of the seismic isolation effect between the cases of using bearing piles and friction piles with different embedded lengths has been carried out. The analysis result shows that using the friction pile can largely reduce ductility ratio in both column and ground girder under large scale seismic motion. Moreover, it is found that the friction pile with shorter embedded length gives more reduction than the longer one.

REFERENCES

Kimata, H. et al. 2010. Study on Seismic Isolation Effect of Elevated Railway Bridge Rigid Frame supported by friction piles. *65th Annual Conference of JSCE* (in Japanese).

Kimata, H. et al. 2010. Influence of the upper layer soil condition on Seismic Isolation Effect of Elevated Railway Bridge Rigid Frame supported by friction piles. *65th Annual Conference of JSCE* (in Japanese).

Railway Technical Research Institute: Design Standards for Railway Structures and Commentary. 1999.10. Seismic Design (in Japanese).

Soil-water Coupling Analysis of Real-scale Field Test on Group-Pile Foundation Subjected to Cyclic Horizontal Loading

Y. Jin
Korea Institute of Construction Technology (KICT), Seoul, Korea

X. Bao
Postgraduate School of Nagoya Institute Technology, Nagoya, Japan

F. Zhang
Nagoya Institute of Technology, Nagoya, Japan (E-mail: cho.ho@nitech.ac.jp)

ABSTRACT: Group-pile foundations are used extensively for supporting buildings, bridges, and other structures to transfer structural loads safely to the ground and to avoid excess settlement or lateral movement. Therefore, it is necessary to understand the behaviors of the group-pile foundations and superstructures during a major earthquake. In this paper, numerical simulation of real-scale group-pile foundation subjected to horizontal cyclic loading is conducted using a program named as DBLEAVES. In the analysis, nonlinear behaviors of ground and piles are described by subloading tij model (Nakai and Hinokio, 2004) and axial force dependent model (AFD model, Zhang and Kimura, 2002) which considered the axial-force dependency in the nonlinear moment-curvature relations. The purpose of this paper is to verify the applicability of the proposed numerical method by comparing the numerical results with the test results.

1 INTRODUCTION

Horizontal forces may form a major part of the loading system for structures supported on pile groups and may often be repetitive or cyclic in nature, and include forces due to earthquake shocks. It is known that during a strong earthquake, the dynamic behavior of a group-pile foundation is related not only to the inertial force coming from the superstructures but also to the deformation of the surrounding ground. Therefore, it is necessary to understand the behaviors of the group-pile foundations and superstructures during a major earthquake.

Numerous tests either in model scale or in real-scale on group-pile foundation subjected to lateral loading can be found in literatures in order to elucidate the ultimate state of the foundations during strong earthquakes, e.g., Tokimatsu et al. (2007) conducted shaking table test using E-defense to estimate the effects of dynamic soil-pile-structure interaction on pile. Needless to say, a full-scale loading test is the most accurate way to determine the mechanical behaviors of deep foundations though it might be extremely expensive and time consuming. On the other hand, numerical simulation also plays a very important role in determining the behaviors and a large number of numerical studies have been done in this field. Kimura and Zhang (1999) developed a three-dimensional static and dynamic finite element analysis code (DGPILE-3D) in order to investigate the static and dynamic interaction between soil and pile foundation.

The purpose of this paper is to provide an applicable numerical way of evaluating the mechanical behavior of a pile foundation subjected to cyclic lateral loading up to an ultimate state. Three-dimensional (3D) finite element analyses of a real-scale group-pile foundation (Kosa et al. 1998) subjected to horizontal cyclic loading is conducted using a program named as 「DBLEAVES」 (Ye, 2007). In this research, nonlinear behaviors of ground and piles are described by *subloading* t_{ij}

model proposed by Nakai and Hinokio (2004) and AFD model proposed by Zhang et al. (2002), respectively. The numerical analyses are conducted by the total stress and effective stress methods. By comparing the numerical results with the test results, the applicability of the proposed numerical method is verified.

2 RESULTS AND DISCUSSION

2.1 *Brief description of real-scale test for 9-pile foundation subjected to horizontal cyclic loading*

The static horizontal cyclic loading test of 9-pile foundation in real-scale was conducted in Kishiwada, Osaka Prefecture. An elevated highway bridge is supported by a group-pile foundation made of cast-in-place reinforced concrete piles. The plan view of the test site is presented in FIG. 1. The test piles with 1.2m in diameter and 30.4m in length are installed in a 3×3 pattern with a 3m pile spacing center to center. Reaction piles have pairs of group piles 3×2 and 3×3. The surface layer of the ground at the test site is a very young reclaimed layer with a thickness of 13m, constructed only three years before the loading test. The cyclic horizontal loading up to a maximum value of 20.5MN was applied with oil jacks installed between the test pile-group and the reaction pile-groups as shown in Figure1.

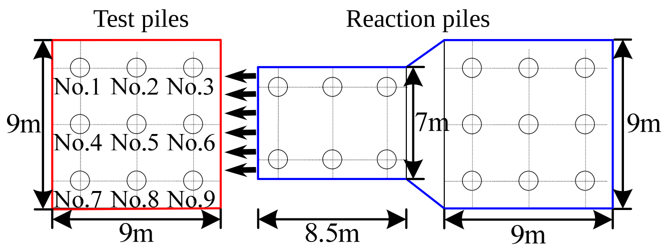

Figure 1. Schematic layout of real scale group-pile in plan view

2.2 *Determination of the material parameters*

Theoretical simulations of drained triaxial compression test were conducted to determine the material parameters of the reclaimed layer. The particle size of the test specimens was adjusted by the removal of coarse grain with diameter greater larger than 50mm. This remold specimens were collected from 11~12m below the ground. Figure 2 shows the comparison of experimental and theoretical results of triaxial compression test under different four confining stresses. The test results at low confining stress, as shown in Figure 2(a) and (b), are reproduced considerably well in stress-strain relations while in the volumetric strain, a small discrepancy between the test and the theory results exists. The results at high confining stress, as shown in Figure 2(c) and (d), are reproduced quite well quantitatively in both results. On the whole, the constitutive model is extremely precise in describing the behaviors of the soil. The material parameters of the ground are listed in Table 1. Only the bottom layer of the ground was supposed to an elastic material in the numerical analysis.

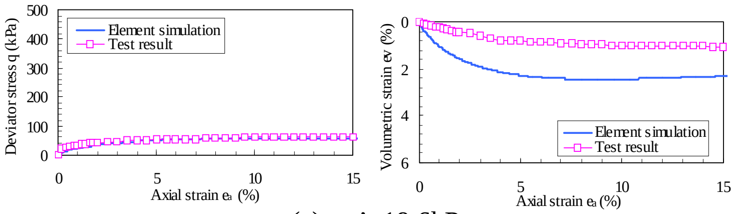

(a) σ $_3$'=19.6kPa

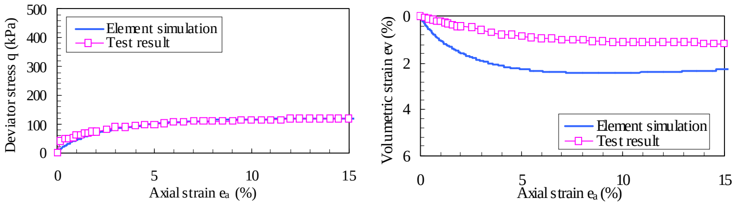

(b) σ $_3$'=39.2kPa

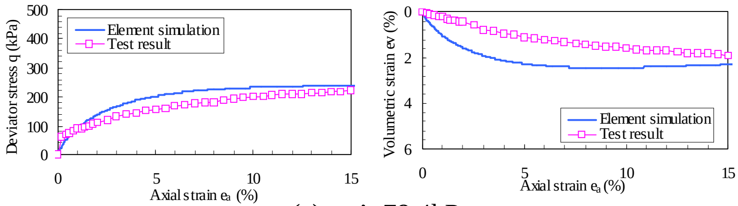

(c) σ $_3$'=78.4kPa

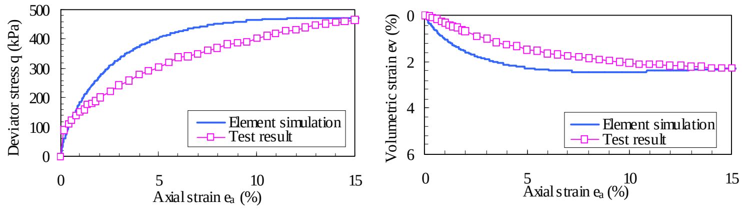

(d) σ $_3$'=156.8kPa

Figure 2. Theoretical simulation and test results

Table1. Parameters of ground

Soil	E (kPa)	ν	λ	κ	N	R_f	a	β	OCR	ρ (tf/m^3)	*k (cm/s)*
B1	-	0.3	0.089	0.002	0.9	3.9	500	1.5	3	1.97	6.56E-01
B2	-	0.3	0.089	0.002	0.9	3.9	500	1.5	3	1.97	3.61E-02
B3	-	0.3	0.089	0.002	0.9	3.9	500	1.5	3	1.97	1.09E-01
As1	-	0.3	0.23	0.046	0.8	3.69	500	1.5	10	1.80	1.00E-02
Ac1	-	0.38	0.23	0.046	0.7	4	500	1.5	2	1.70	1.00E-06
Dc	1.00E+05	0.3	-	-	-	-	-	-	-	1.80	1.00E-07

The pile is modeled by hybrid element proposed by Zhang et al. (2000), composed of beam element and solid element, to take into consideration the volume of pile. The beam element bears most of the loading acting on the pile, while the neighboring solid elements bear less loading but occupy the volume of the pile. The sharing ratio of bending stiffness between the beam element and the solid elements is 9 to 1. In order to consider the influence of axial force on bending stiffness of pile, AFD model is employed in the analysis. The material parameters of the pile are listed in Table 2. The concrete footing above pile heads is modeled with elastic elements.

Table2. Parameters of piles

1. Physical properties of RC
Compressive strength of concrete : σ_C=3.8×10^4kPa
Young`s modulus of concrete : E_C=2.5×10^7kPa
Young`s modulus of steel : E_S=2.1×10^8kPa
Yield stress of steel :σ_y=3.8×10^5kPa
2. Arrangement of the reinforcement :
D29-24 (upper part : 14.5m from the surface of the ground)
D22-12 (lower part:15.9m)
Overburden of the reinforcement : 15cm

2.3 *FEM mesh and boundary conditions*

Figure 3 shows the geologic profile of ground and FEM mesh. The ground is composed of 6 layers based on the soil property chart. The water table is located 1m below the ground surface. The initial stress of the ground is regarded as stratification bedding without considering the effect of pile installation.

Because of the symmetric condition of the geometry and the load, only half of the domain is taken under consideration. The boundary conditions of the ground are fixed at the bottom, sliding at the two sides whose normal direction is parallel to y-axis and x-axis. The boundary condition of the pile in the calculation is that the head of the pile is rotation fixed with the footing and the tip of the pile is free.

2.4 *Numerical results*

The cyclic horizontal load with a maximum value of 20.5MN adopted in the numerical analysis is the same as the test load shown in Figure 4. In the simulation of one-side cyclic lateral loading test, a concentrate lateral load is applied at the center of the side surface same as the field test, where all the nodes on the side surface placed 0.9m from the ground surface are kept to be equal to each other in the x, y, z directions as a rigid, as shown in Figure 5.

Figure 6 shows the lateral load and displacement relations at node No.1 shown in Figure 5. The result of total stress analysis underestimates the test result at the maximum and residual displacements while the result of effective stress analysis coincides well with the test result until sixth cycle and the maximum and residual displacements are close to the test results. In the field test, many cracks occurred on the ground surface around sixth loading cycle. In calculation, however, it is impossible to describe the cracks, which might be the reason why a discrepancy between the test and the calculated results occurred after sixth cycle in effective analysis, as shown in Figure 6.

Figure 7(a) shows the position of the piles in the pile group, among which No.4 pile located in front row is discussed in detail. It is known from Figure 7(b) and (c) that test and calculated results agree well with each other and that the effective stress analysis performs better than total stress analysis when the maximum value and its occurring depth are concerned. Figure 8 shows comparisons of test and calculated results of sectional forces at the loading of 8MN. The maximum bending moment are in the order of front pile, middle pile and rear pile. It is seen from the figure that the front pile bears larger bending moment than the rear pile because of the difference of axial forces, that is, compressive axial force in the front pile and tensile axial force in rear pile. It is seen that both the calculated and test results clearly reflect the phenomenon and agree well with each other, showing that the mechanical behavior of pile group can be described properly by using the axial force dependent (AFD) model in the numerical simulations.

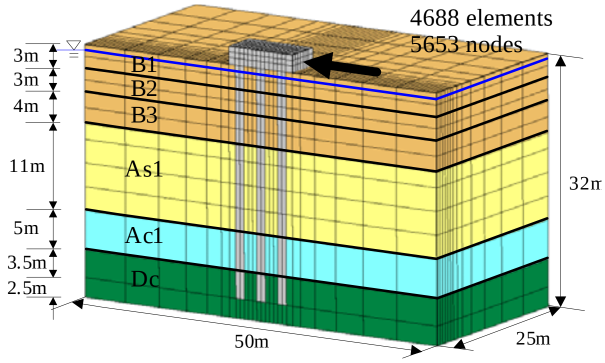

Figure 3. Time history of lateral load in field test

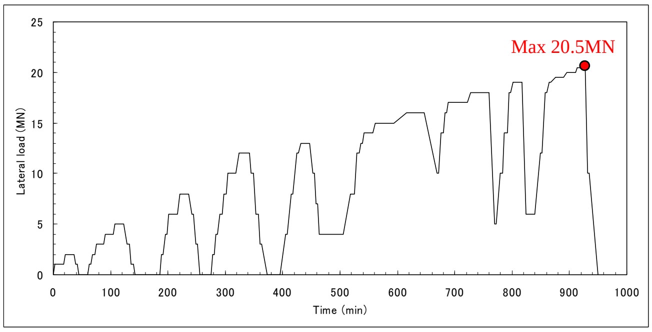

Figure 4. Time history of lateral load in field test

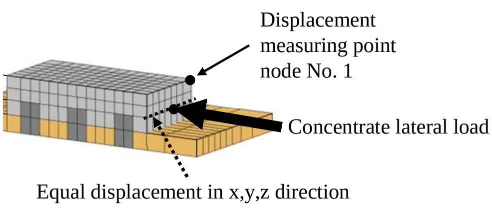

Figure 5. Loading method

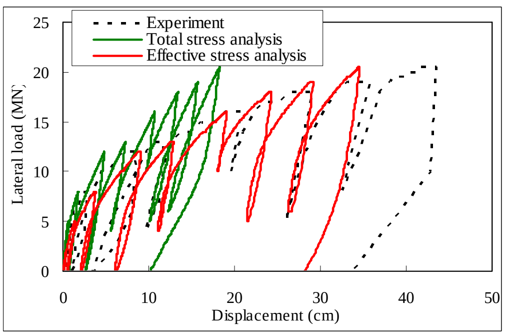

Figure 6. Lateral load-displacement relations

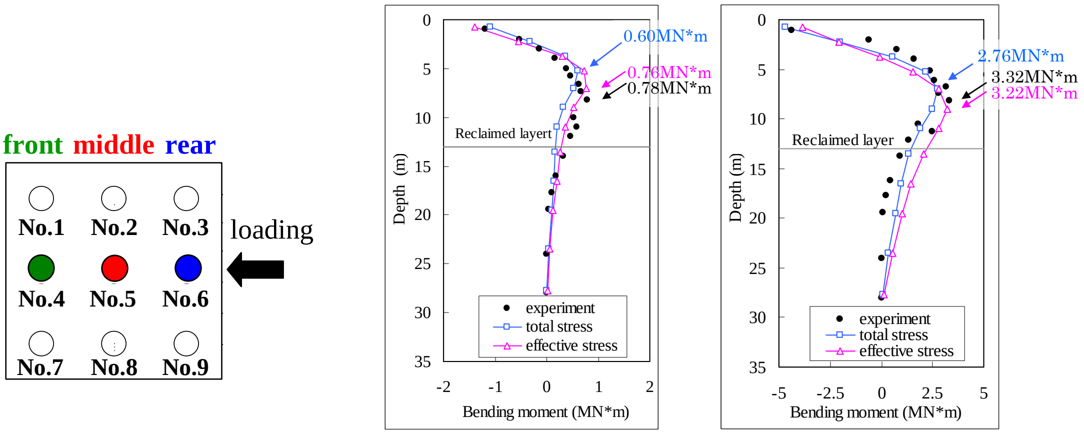

(a) Arrangement of test piles (b) Load=8MN (c) Load=20.5MN

Figure 7. Comparisons of test and calculated results of bending moment in pile No.4

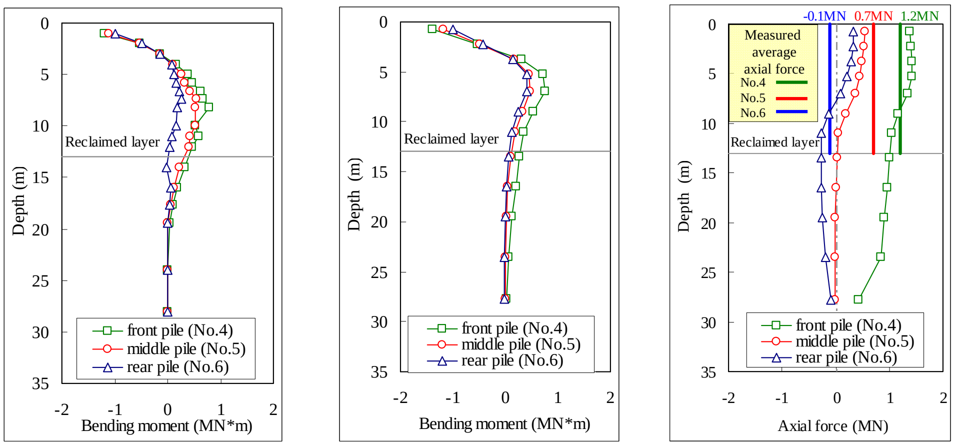

(a) Bending moment (Test) (b) Bending moment (Calculation) (c) Axial force

Figure 8. Comparisons of test and calculated results of sectional forces at the loading of 8MN

Residual lateral displacements at the measuring points, obtained from field measurement and numerical analyses, are listed in Table 3. The calculated lateral displacements at the ground surface show reasonably good agreement with the field measurements.

Figure 10 denotes the distributions of volumetric strain ε_v at the maximum loading of 20.5MN. In both analyses, the ground in the area near the front of the footing is compressive in a wide area; while the ground in the area behind the footing is expanded in a narrow area. In the field test, many cracks were observed in the ground near the footing, while in the calculation, large volumetric strain happened at the same place where cracks occurred in the field test.

Figure 11 shows stress paths of ground at different positions during cyclic loading in which J_2 is the second invariant of the deviatoric stress tensor. The stress path of the element 1 located in front of the footing increases and decreases repeatedly with a relatively large stress range during the cyclic loading. The degree of change in the stress, however, is different in which, effective stress analysis gives a much larger change in the stress path, showing that dilatancy affects directly the stresses due to the consideration of soil-water coupling effect. As to the behaviors of elements 2 & 3, effective analysis gives a quite different description, compared to the total stress analysis, about the stress paths in the way that after the stress decreased to some extent, it will turn to increase again due to the dilatant behavior of sand after undergone some shear strain. In the total stress analysis, however, it is impossible to describe this behavior because dilatancy dose not affect the stress directly.

Table 3. Residual lateral displacement at the measuring points

Measuring point	Test resuslt (m)	Total stress result (m)	Effective stress result (m)
K-1	0.13	0.12	0.15
K-2	0.07	0.03	0.05
P-1	0.11	0.12	0.15
P-2	0.07	0.07	0.11
P-3	0.12	0.10	0.10
P-4	0.08	0.05	0.09

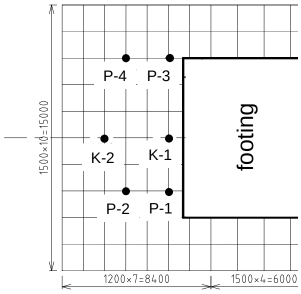

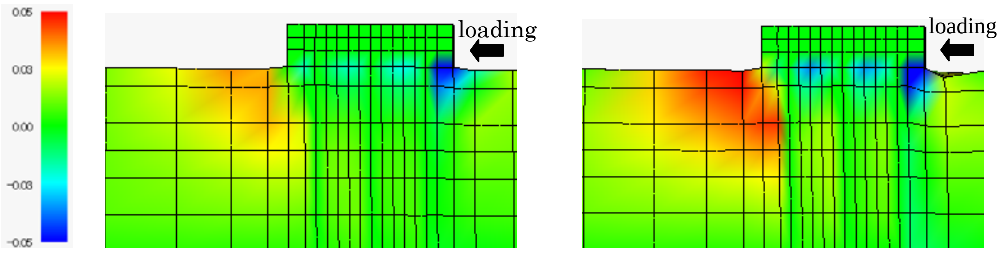

(a) Total stress (b) Effective stress

Figure 10. Distributions of volumetric strain at the loading of 20.5MN

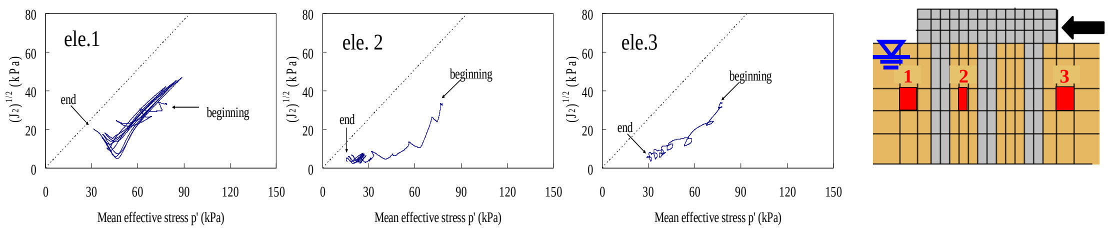

(a) Total stress analysis

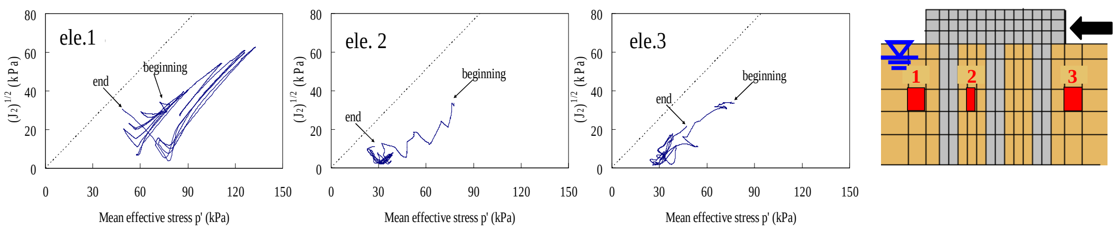

(b) Effective stress analysis

Figure 11. Stress paths of the surrounding ground during cyclic loading

3 CONCLUSIONS

In this study, 3D finite element-finite difference soil-water coupling analyses on a real-scale group-pile foundation subjected to horizontal cyclic loading are conducted to investigate the mechanical behaviors of group-pile foundation. By comparing the test and the numerical results, the applicability of the proposed numerical method is verified and the following conclusions can be given.

⑴ Simulations of drained triaxial compression test are conducted to determine the material parameters of the reclaimed layer. The element simulation is extremely precise in describing the behaviors of the soil.

⑵ In the lateral load and displacement relations, the total stress analysis underestimates the test result, while the effective stress analysis considering soil-water coupling well predicts the test result at the maximum and residual displacements.

⑶ The calculated results of bending moment and axial force also agree well with the field observation. The difference of the bending moment due to axial force can be properly simulated by the calculation based on AFD model. Although the shapes of the distributions of the bending moment and the axial force are similar to the test results in both analyses, the results of the effective stress are much closer to the test results.

⑷ The lateral displacement of the ground surface at the end of the test shows reasonably good agreement with the field measurements.

From the results mentioned above, the applicability of the proposed numerical method is encouraging and therefore it is quite confident to say that the method can be used to predict the mechanical behaviors of group-pile foundation to a satisfactory accuracy, particularly with the effective stress analysis.

4 REFERENCES

Kimura, M. and Zhang, F. (1999). "Seismic evaluation of pile foundation by static and dynamic 3-D finite element analyses" *Proc. of the 11th Asian Regional Conf. of Int. Society for Soil Mechanics and Geothch. Engrg*., Vol. 1, 507-510.

Kosa, K. Suzuki, N., Kimura, R., Kimura, Y. and Morita, Y. (1998). "Lateral loading test of full-scaled pile foundation focused on ultimate behavior", *JSCE*, No.596/III-43, pp. 249-260, 1998. (in Japanese).

Nakai, T. and Hinokio, M. (2004). "A simple elastoplastic model for normally and over consolidated soils with unified material parameters", *Soils and Foundations*, Vol.44, No.2, 53-70.

Tokimatsu, K., Suzuki, H., Tabata, K. and Sato, M. (2007). "Three dimensional shaking table tests on soil-pile-structure models using E-defense facility", *4th International Conference on Earthquake Engineering*, June 25-28, Thissaloniki, Greece.

Ye, B. (2007). "Experiment and Numerical Simulation of Repeated Liquefaction -Consolidation of Sand", *Doctoral Dissertation, Gifu University.*

Zhang, F., Kimura, M., Nakai, T. and Hoshikawa., T. (2000). "Mechanical behavior of pile foundations subjected to cyclic lateral loading up to the ultimate state", *Soils and Foundations*, Vol.40, No.5, 1-17.

Zhang, F. and Kimura, M. (2002). "Numerical prediction of the dynamic behaviors of an RC group-pile foundation", *Soils and Foundations*, Vol.42, No.3, 77-92.

Dynamic centrifuge tests to study the transient bending moments in piles during liquefaction

S. Bhattacharya, S.R.Dash, D.Lombardi, N.A.Alexander
University of Bristol (U.K)

T. Tazoh & J.Jang
Institute of Technology, Shimizu Corporation, Japan

M. Sato
National Research Institute for Earth Science & Disaster Prevention, Japan

ABSTRACT: Failures or collapse of structures (building or bridges) supported on small diameter slender piles are still observed in the recent earthquakes. The collapse of these structures often occur with crack formation or plastic hinging of the pile suggesting that the bending moment generated in the pile during the earthquake exceeded the plastic moment capacity. It has been observed (though in a limited number of cases as excavations of piles are not an easy task) that the hinge or cracks forms at random locations (near the pile head, middle of the pile) along the length of the pile. Theories based on bending mechanism (lateral loads due to inertia and/or lateral spreading), buckling instability (pile becomes lateral unsupported similar to a slender column in the liquefiable zone) or settlement of the pile due to loss of shaft resistance have been proposed. However, all these theories fail to explain the reasons behind the location of the hinge formation. This paper presents results from a series of centrifuge study to study the behaviour of pile in the transient phase during liquefaction.

1 STATE-OF-THE ART UNDERSTANDING OF PILE FAILURE IN LIQUEFIABLE SOILS

1.1 *Codes of practice on pile design in liquefiable soils*

Following 1995 Kobe earthquake, lateral spreading of the ground (downward slope movement) has been reported to be the main source of distress in piles which led the Japanese Code of Practice (JRA 1996 or 2002) to advise engineers to design piles against bending failure assuming that a non-liquefied crust exerts passive pressure and the liquefied soil applies a lateral pressure of 30% of the total overburden pressure to the pile. Eurocode 8 (1998) advises designers to design piles against bending due to inertia and kinematic forces arising from the deformation of the surrounding soil recommending that piles should be designed to remain elastic, but that the sections at the pile cap and at the interfaces between layers of soil with markedly different properties should have the capacity to form plastic hinges. Other codes, such as NEHRP code and Indian Code [IS 1893, 2002] also focus on bending strength of the pile. Therefore major codes of practice in pile design in liquefiable soils, such as EC8, JRA, NEHRP and IS 1893 advises engineers to treat piles as laterally loaded beams i.e. essentially resisting bending failure. This can be also be substantiated by the fact that most of the piles reported in the literature are small diameter piles.

1.2 *Theory of pile failure based on buckling instability*

Bhattacharya (2003), Bhattacharya et al (2004, 2009) argues that piles become laterally unsupported in the liquefiable zone during strong shaking which may led to buckling type instability failure mechanism under the action of axial load acting on the pile at all times. Essentially, the soil around the pile liquefies and loses much of its stiffness and strength, so the piles now act as unsupported long slender columns, and simply buckles under the action of the vertical superstructure (building) loads. The stress in the pile section will initially be within the elastic range, and the buckling length will be the entire length in the liquefied soil. Lateral loading, due to slope movement, inertia or out-of-line straightness, will increase lateral deflections, which in turn can cause plastic hinge to form, reducing the buckling load, and promoting more rapid collapse. This theory has later been verified by other researchers; see for example Lin et al (2005), Kimura and Tokimatsu (2007), Shanker et al (2007), Knappett and Madabhushi (2005). Figure 1 shows the various loading regimes that affect the pile stresses and further details can be found in Adhikari and Bhattacharya (2008).

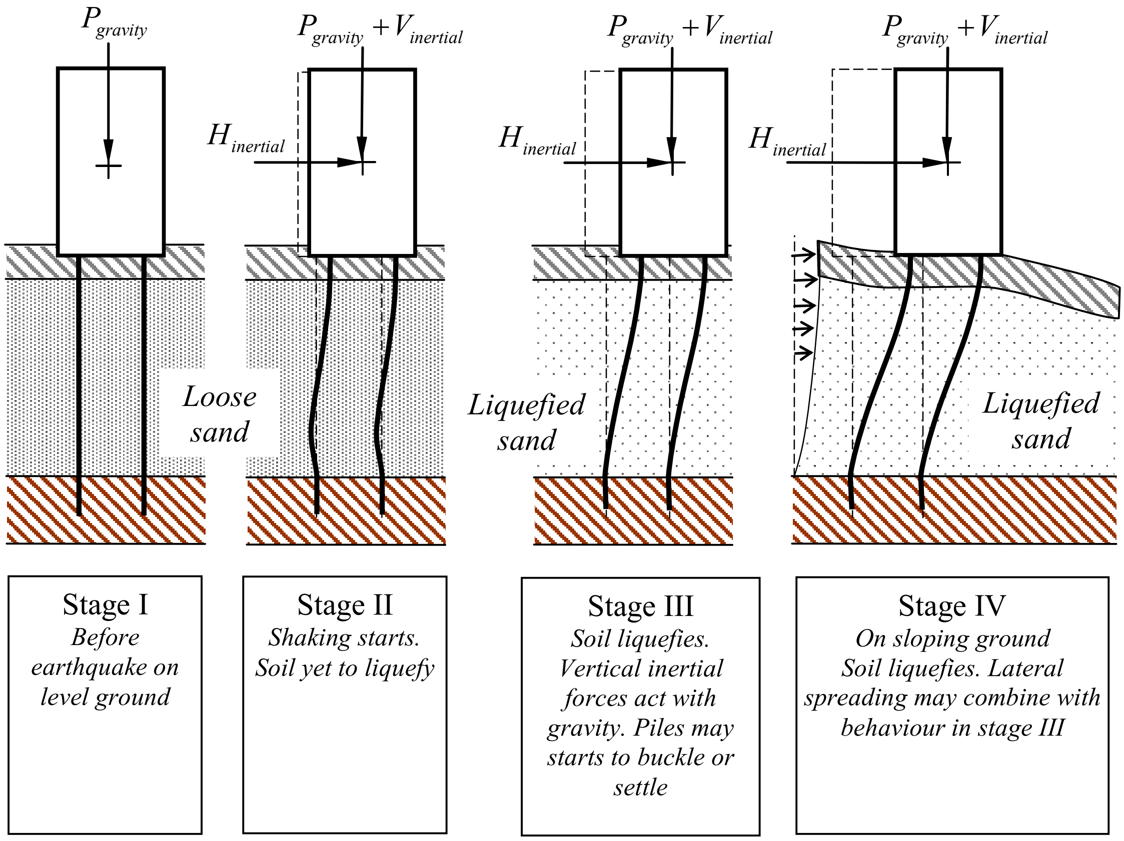

Figure 1: Various stages of loading, Bhattacharya et al (2009)

Analysis of 14 case histories of pile foundation performance (from various historic earthquakes) was carried out assuming that a pile is unsupported slender column in the liquefiable zone, see Bhattacharya et al (2004). In the study the r_{min} (minimum radius of gyration of the pile i.e. where I is the second moment of area and A is the area) and the L_{eff} (effective buckling length of the pile in the liquefiable zone i.e. Euler's equivalent pin-ended strut) of the piles, see Figure 2. Obviously, L_{eff} (not the length of pile in liquefiable soils) is based on the boundary condition of the pile below and above the liquefiable zone and is necessary to normalise the pile length. Six of the piled foundations were found to survive while the others suffered severe damage. Details can be found in Bhattacharya et al (2005).

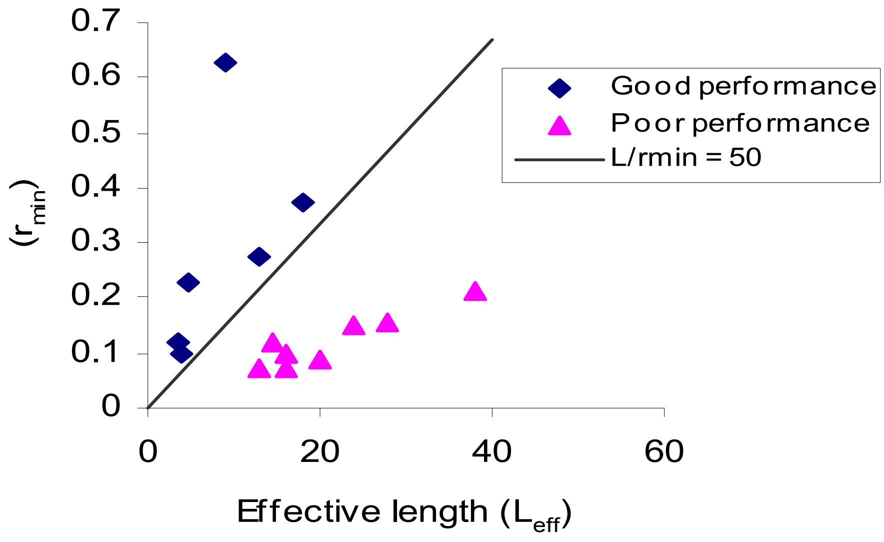

Figure 2: Plot of L_{eff} and r_{min} of 14 pile foundation performance in liquefiable soils

The study of case histories showed a line representing a slenderness ratio of 50 can distinguish between unacceptable and acceptable pile performance. This line is of some significance in structural engineering, as it is often used to distinguish between "long" and "short" columns. Columns having slenderness ratios below 50 are expected to fail by plastic squashing whereas those above 50 are expected to fail by buckling, both modes being modified by induced bending moments. This slenderness ratio of 50 signifies length to diameter of about 12 for RCC columns. This suggests that piles in liquefiable soil should be designed as axially loaded columns carrying lateral loads i.e. stiffness design.

1.3 *Limitations of the theories and the need for further research*

While buckling mechanism can classify pile failures, the location of hinge formation/ cracks in the piles (cracks or hinges forms at various depths along the length of the pile) cannot be explained by buckling instability theory or bending theory. This led to the search of any other mechanisms of failure. A good review on the types and form of failure can be found in Bhattacharya and Madabhushi (2008). A method to study the combination of bending and buckling mechanism can be found in Dash et al (2010).

Bhattacharya et al (2008) argued that the dynamics of the pile-supported system is linked with static instability phenomenon. It can be argued that buckling of slender columns can be viewed as a complete loss of lateral stiffness to resist deformation. During liquefaction, if a pile buckles - it can be concluded that the lateral stiffness of the pile is lost. From a dynamics point of view as the applied axial load approaches the buckling load it can also be observed that the fundamental natural frequency of the system drops to zero, Thompson and Hunt (1984). Essentially, at the point where the natural frequency drops to zero, the inertial actions on the system no longer contribute. Thus, the system's dynamical equations of motion degenerate into a statics stability problem.

In pile context, during seismic liquefaction, the axial load on the pile in the liquefied zone increases due to the loss of shaft resistance. Due to this extra axial load, the stiffness of the pile-soil system reduces and so does the vibration frequencies. At the point of instability the fundamental vibration mode and buckling mode shapes are identical. Thus, as the soil transforms from solid to a fluid-like material i.e. from partial-liquefaction stage to full-liquefaction stage, the modal frequencies and shapes of the pile change. Considering the first natural frequency of the pile-soil-superstructure system, it can be argued that another mechanism may probably be the two effects arising from the removal of the lateral support the soil offers to the pile while in liquefied state which are:

(a) increase in axial load in the pile in the potentially unsupported zone due to loss of shaft resistance;

(b) dynamics of pile-supported structure due to frequency dependent force arising from the shaking of the bedrock and the surrounding soil than can cause dynamic amplification of pile head displacements leading to resonance type failure.

1.4 *Aims and scope of the paper*

In practice, there are many methods to analyse pile-soil interaction. One of the widely used models is BNWF (Beam on Non-linear Winkler Foundation) model (Figure 3). BNWF model is extensively used in practice due to its simplicity, mathematical convenience and ability to incorporate nonlinearity. In a BNWF model (as in Figure 3), the lateral soil-pile interaction (LPSI) is normally modeled as a lumped soil spring with nonlinear backbone curve. These nonlinear backbone curves are normally called p-y curves, where ‘p’ refers to the lateral soil pressure per unit length of pile and the ‘y’ refers to the relative pile-soil displacement. The paper aims at the following:
(1) Present the results of a series of centrifuge tests to study the shape and magnitude of p-y curve during seismic liquefaction.
(2) Compare the back-calculated p-y curve of liquefied soil from the centrifuge test data with the available API type p-y curve.
(3) Develop an understanding on the transient bending moment on the piles

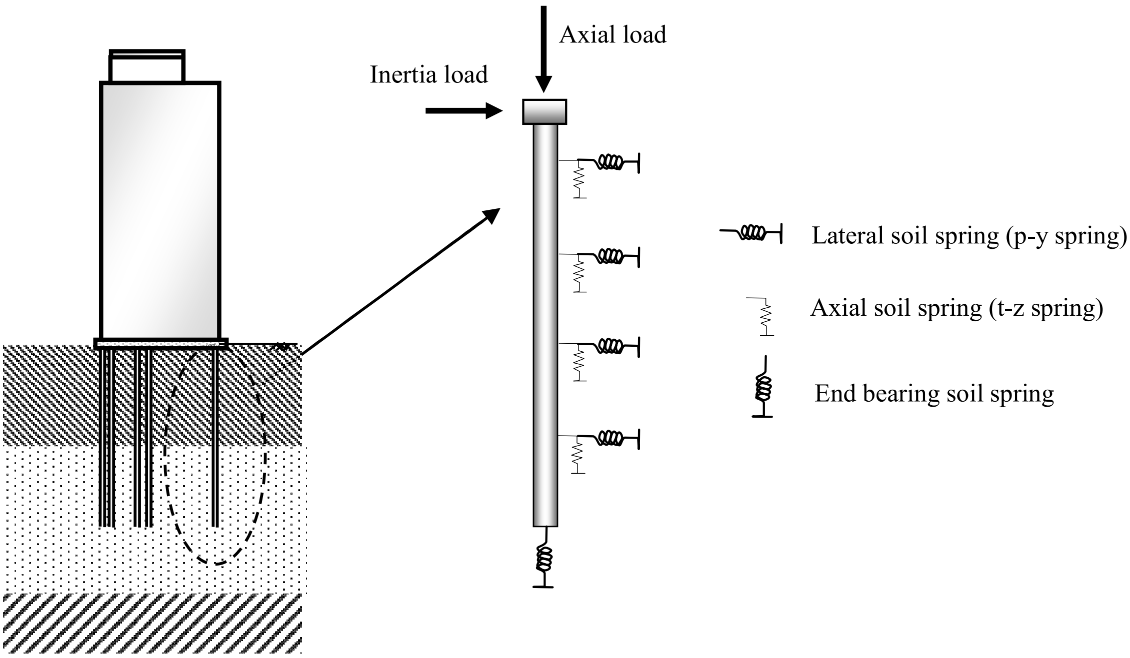

Figure 3: Definition of Winkler Model for piles

2 DYNAMIC CENTRIFUGE TESTS

Centrifuge modeling is regarded as a powerful technique to study small scale model behaviour under prototype stress condition. In geotechnical earthquake engineering, model tests with 1:N linear scale under 1-g conditions cannot always reproduce the prototype behaviour because the stress level due to self-weight is much lower than that in prototype scale. The centrifuge test runs at N-g centrifuge acceleration, hence, is particularly useful in a 1:N scale model to ensure the soil stress in the model is same as that in the prototype by increasing the self-weight due to gravity. The centrifuge tests presented in this study were conducted in the centrifuge facility of Shimizu Corporation, Japan. Figures 4(a) and 4(b) provides the details of the centrifuge. The next section describes the various aspects of the testing.

Figure 4(a): Centrifuge at Shimizu Corporation

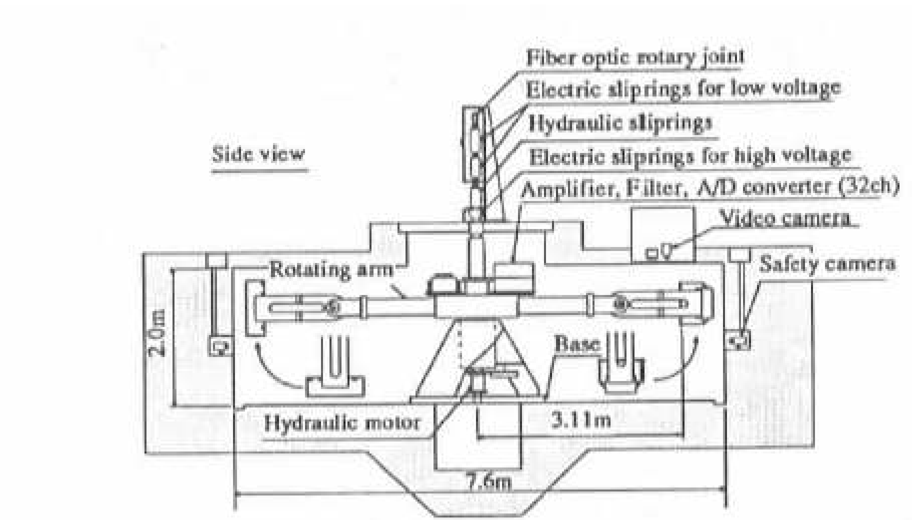

Figure 4(b): Centrifuge

2.1 *Set-up used for the tests*

The test facility used in the present study (pile-soil interaction model) includes a centrifuge, a shaking table, a laminar box (805mm long, 475mm wide, 324 mm high) and data acquisition setup. The tests were carried out at a centrifugal acceleration of 30-*g*. The stress and strain parameters were modelled by a factor of unity and the linear dimensions by the scale factor of 1: 30 (model: prototype). See Figure 5 for the test setup and Figure 6 for the instrumentation layout of a typical test. Details of the soil used can be found in Table 1. Figure 7 on the other hand shows the photograph of the pile which was also strain gauged. The pile used is made of steel having an outside diameter of 10mm, wall thickness of 0.2mm.

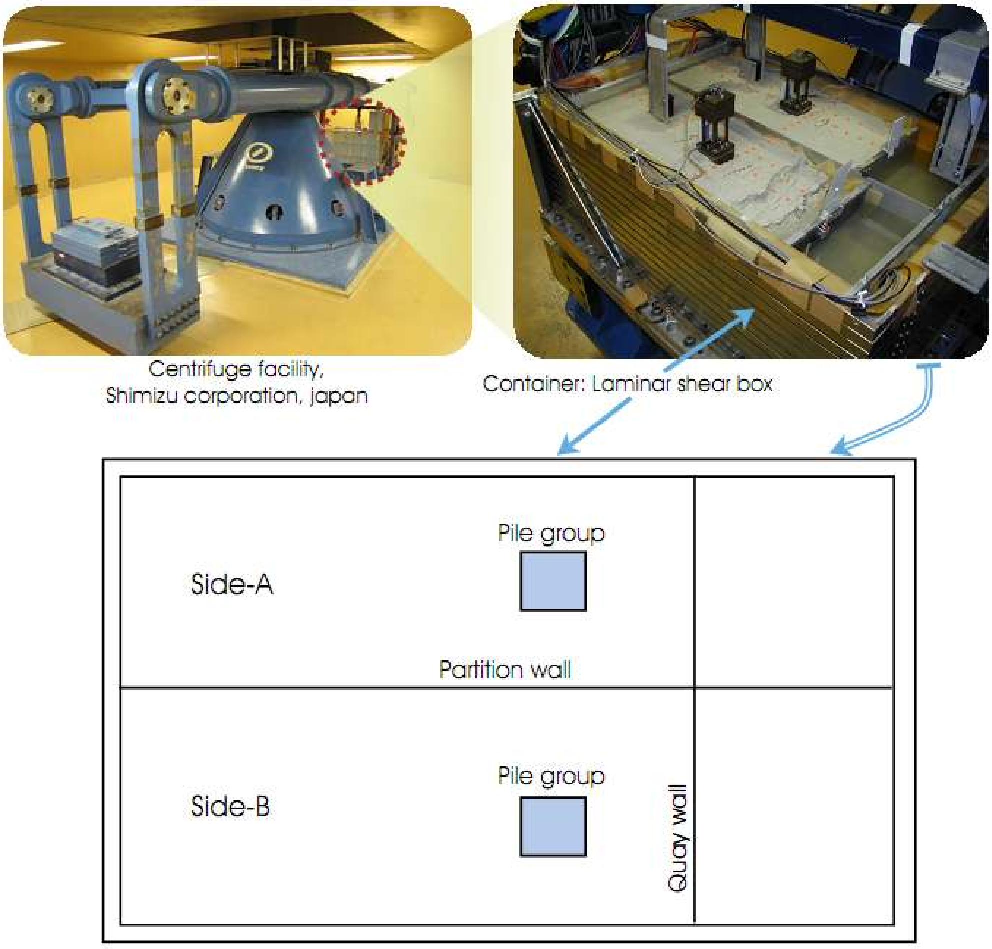

Figure 5: Test set-up

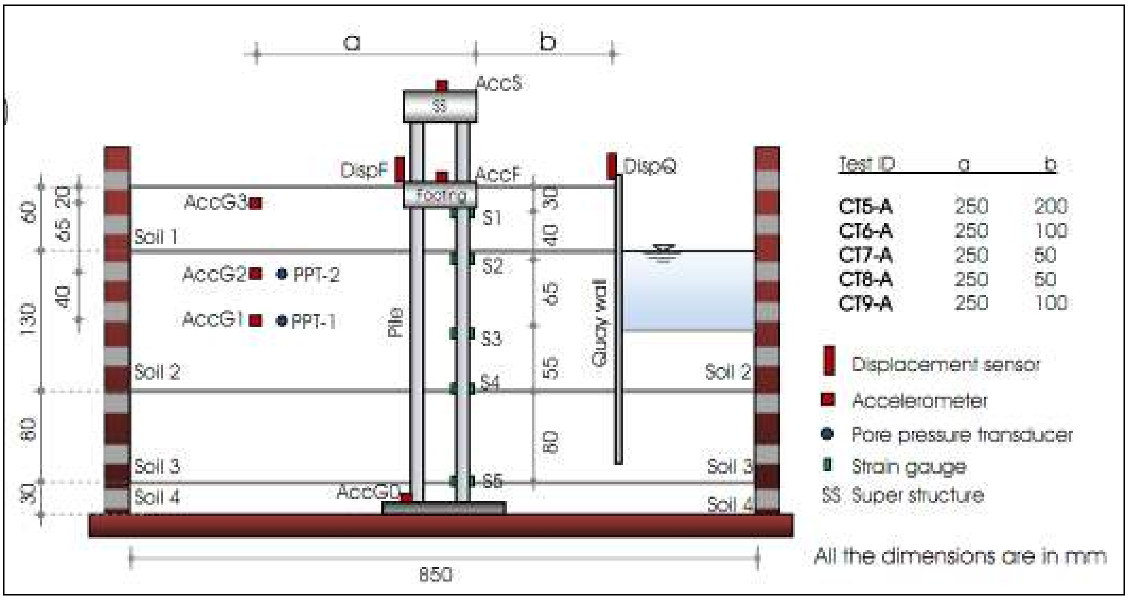

Figure 6: Instrumentation layout of the test

Table 1: Geotechnical properties of the sand used in the test

Symbol	*Unit*	*Soil 1*	*Soil 2*	*Soil 3*	*Soil 4*
		Unsaturated Silica sand No. 8	Saturated Silica sand No. 8	Saturated Toyoura sand	Saturated Silica sand No. 3
G_s	kg/m^3	2631	2631	2645	2632
e_{max}	--	1.385	1.385	0.951	0.974
e_{min}	--	0.797	0.797	0.593	0.654
D_r	%	50	50	90	90
γ'_t (sat.)	kN/m^3	7652	7652	9908	9496
γ_t (unsat)	kN/m^3	12851	17462	19718	19306
S_r	%	10	100	100	100

2.2 *Measurements carried out in the tests*

Strain measurements were taken at both sides of the pile at the extreme fibre on the locations as shown in Figure 6. From the total strain measurements, the axial strain and the bending strain components were separated as given in the equations in Figure 8. The next section of the paper analyses the bending moment

Figure 7: Photograph of the pile

$$\text{Axial strain} = \varepsilon_a = \frac{\varepsilon_{1p} + \varepsilon_{2p}}{2}$$

$$\text{Bending Strain} = \varepsilon_b = \frac{\varepsilon_{1p} - \varepsilon_{2p}}{2}$$

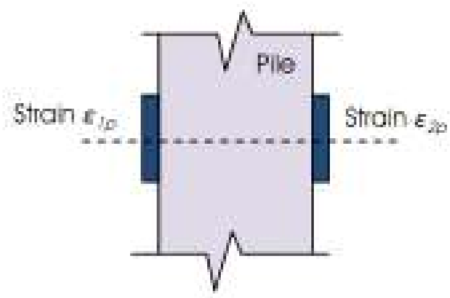

Figure 8: Axial and bending strain estimation from measured strain data.

Table 2: Details of the centrifuge test

SERIES -1 having three tests CT1, CT2 and CT3. In each test, two structures were tested (A and B). All the piled foundations had a superstructure. The distance between the quay wall and the piled foundations were varied in three cases. The quay wall is fixed at the base in Side A (no lateral spreading) and free at base in Side B (lateral spreading).	CT1A and CT1B	Two vertical pile groups near a quay wall were tested. In Side-B the quay wall collapsed and in Side-A the wall did not collapse. The pile group was placed 200mm from quay wall.
	CT2A and CT2B	Same condition like Case 11, except the pile group was placed 100mm from quay wall.
	CT3A and CT3B	Same condition like Case 11, except the pile group was placed 50mm from quay wall.
SERIES-2 having two centrifuge tests (CT-4 and CT-5) The effect of inertia of the superstructure and distance from quay wall were investigated. The quay wall was free at base.	CT4A and CT4B	Two vertical pile groups were tested, one with superstructure and one without superstructure. The foundation was 100mm from quay wall.
	CT5A and CT5B	Two vertical pile groups having superstructure were tested. In one case, the foundation was 50mm from the quay wall and in the other the foundation was 100mm from quay wall.
SERIES-3 having 4 tests (CT6, CT7, CT8 and CT9). Two pile groups were tested; Side-A: vertical pile and Side-B: raked pile. Only vertical pile case is considered in this study. The quay wall was free at base.	CT6A and CT6B	The distance of pile group from the quay wall is 200mm.
	CT7A and CT-7B	The distance of pile group from the quay wall is 100mm.
	CT8A and CT8B	The distance of pile group from the quay wall is 50mm.
	CT9A and CT9B	Repetition of tests CT8

3 ANALYSIS OF RECORDED DATA

Figure 9 shows a typical free field pore pressure response along with the input acceleration. The results indicate that the soil remained liquefied between 6 and 10 seconds.

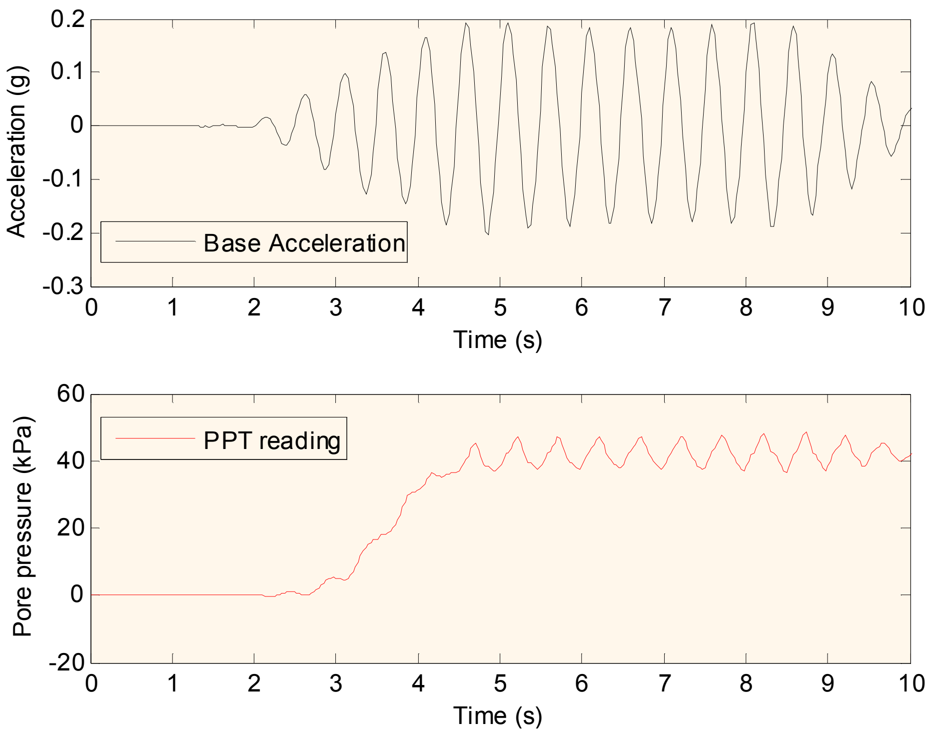

Figure 9: Pore pressure response and the input acceleration

3.1 *General theory of obtaining p-y curves from strain gauge data*

The p-y curve for the lateral pile-soil interaction can be back-calculated from the recorded bending strain (ε_b) on the pile using the beam theory equations. A quick review of beam theory is presented in this section. The recorded bending strain can be used to compute bending moment directly by using the following equation:

$$Moment(M) = EI\frac{1}{R} = 2EI\frac{\varepsilon_b}{D} \tag{1}$$

where
D is the diameter of pile and
EI is the bending stiffness of pile.

The y_p (pile deflection) is computed by integrating the bending moment of the pile twice with respect to the location of strain measurement (x) and divide that by *EI* of the pile. In the other hand, the loading on pile (w) is obtained by double differentiating the bending moment with respect to x.

$$\textit{Pile deflection} = y_p = \frac{1}{E_p I_p}\iint M dx \tag{2}$$

$$\textit{Lateral resistance} = w = \frac{d}{dx}\left(\frac{d}{dx}M\right) \tag{3}$$

The 'y' of p-y curve is then estimated using the equation below, where the soil displacement (y_s) is estimated separately.

$$y = y_p - y_s \tag{4}$$

The 'p' of p-y curve is same as the calculated value of 'w' with a unit of (force/length).

3.2 *Algorithm to back-calculate p-y curves*

The analysis procedure for back-calculating p-y curve is described in detail in the main report. The major steps involved in the analysis include:

- Import the data sets of interest for the analysis
- Filter the data to remove high and low frequency noise from it.
- From the total strain measurements in pile, estimate the bending strain component.
- Estimate the bending moment in pile from bending strain.
- Fit an appropriate curve to the bending moment profile along pile depth at each time step.
- Integrate the bending moment profile twice with respect to depth and divide it by EI of pile to obtain pile deflection (y_p) at each time step.
- Differentiate the bending moment profile twice with respect to depth to obtain lateral loading on pile at each time step, which is same as the soil resistance (p).
- Estimate the free field soil displacement from the measured acceleration time history.
- Assume the soil deflection near to quay wall with a parabolic profile. The maximum soil deflection at top is considered as the recorded deflection of quay wall.

- Estimate the soil deflection profile along depth near to pile by linear interpolation between the free field soil deflection profile and the soil deflection profile near quay wall.
- The other relative pile-soil deflection (y) is then estimated by deducting soil displacement from pile displacement for each time step.
- The results of soil resistance 'p' (from step g) and relative soil-pile deflection 'y' is presented as the p-y curve.

3.3 *p-y curves for no lateral spreading cases (level ground condition)*

Tests CT1-A, CT2-A and CT3-A had a non failing quay wall with no large lateral soil flow. Hence, these cases were considered as liquefiable soil without lateral spreading. Figure 10 shows the p-y curves estimated for these three cases at full liquefaction (6-10 sec) at two depths (top and bottom of the liquefied soil layer). The resistance is normalized by the effective overburden pressure. They were also compared with 10% monotonic API p-y curves for non-liquefiable soils, marked in red lines in the figure. The difference between the magnitudes of the p-y curves in three cases are mostly due to the distance of the pile group from the quay wall, where CT1-A was 200mm, CT2-A was 100mm and CT3-A was 50mm (in model scale) away from the quay wall. The nearer the quay wall, the higher was the resistance due to the stiff boundary, which is seen as a higher magnitude p-y curves in CT3-A as compared to other two p-y curve. Although, the magnitudes differ for the three cases, it varies in the range of 2 to 5% of the API p-y curve for non-liquefied soil.

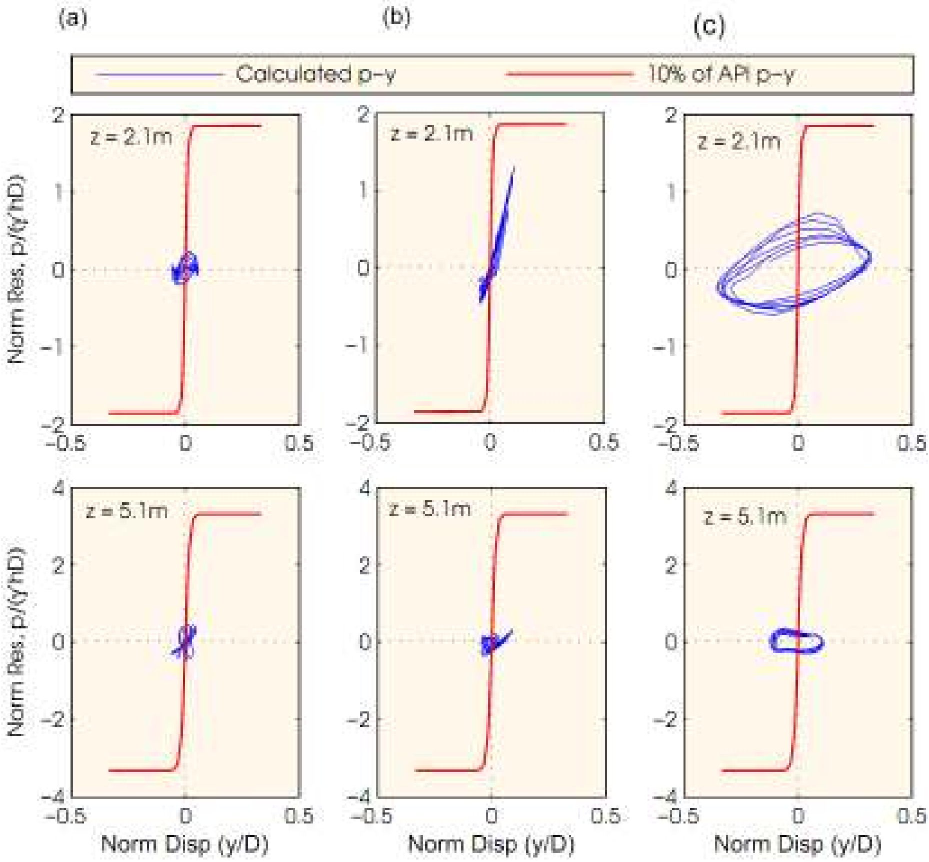

Figure 10: *p-y* curves for cases (a) CT1-A (pile group 200mm away from quay wall), (b) CT2-A (pile group 100mm away from quay wall) and (c) CT3-A (pile group 50mm away from quay wall), where there was no lateral spreading of the soil.

3.4 *Transient bending moment in the pile*

From figure 6 it may be observed that strains were recorded in 5 locations along the length of the pile [S1, S2, S3, S4 and S5]. For plotting purposes, the locations are converted into depths in prototype dimensions and the locations are 0.9m (S1), 2.1m (S2), 4.05m (S3), 5.7m (S4) and 8.1m (S5). Figure 11 plots the recorded bending moments during the entire period of strong motion i.e. from the onset of liquefaction (at about 2.5sec in the time series) to the end of shaking i.e. during the entire phase of liquefaction. The plot shows that the location of maximum bending moment shifts from the top i.e. at 0.9m to the bottom i.e. 8.1m.

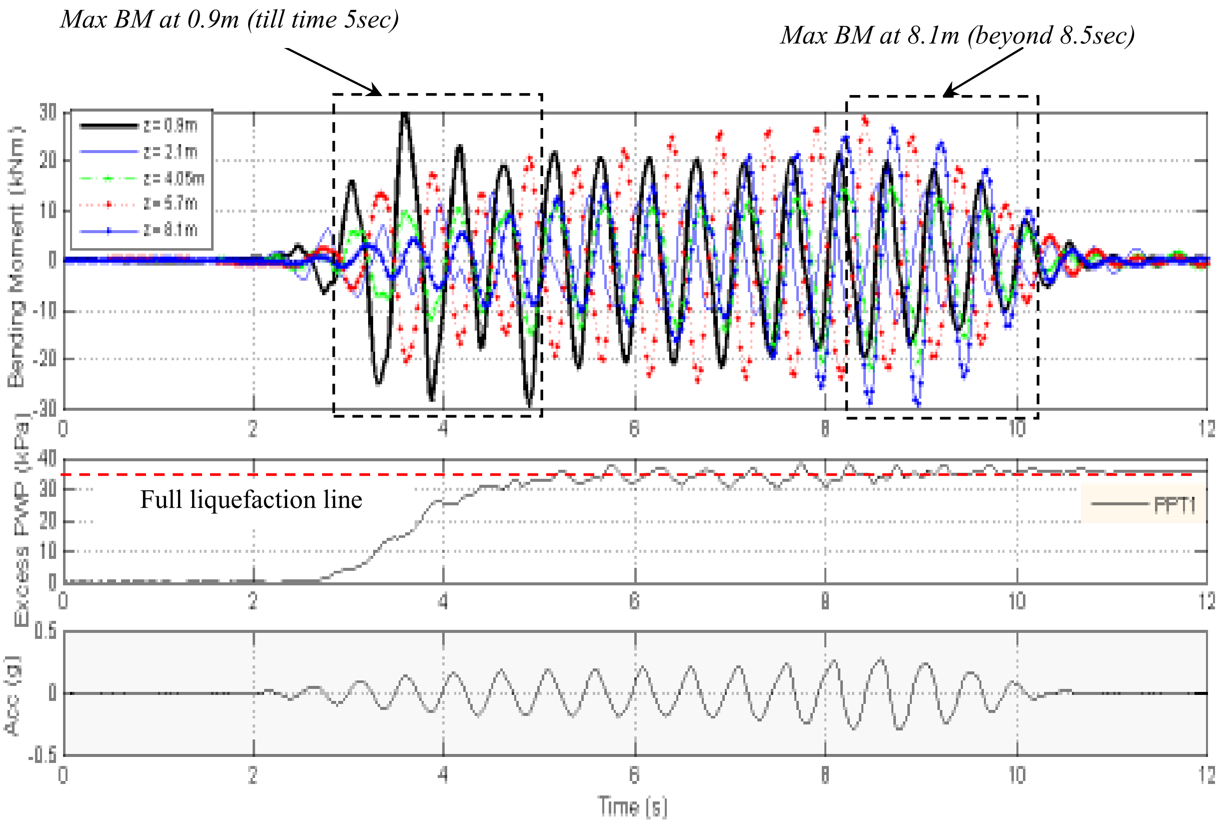

Figure 11: Transient bending moment in the pile, see Figure 6 for instrumentation layout

3.5 *Bending moment amplification in the pile during the transient phase*

Most codes of practice prescribe methods to predict the bending moment in the pile due to inertia. In such methods, the location of maximum bending moment is within the top few diameter of the pile (typically 3 to 5 diameters). This location depends on the relative pile-soil stiffness. In this section of the paper, the Moment Amplification Factor (MAF) for each location of the pile is computed by normalizing the recorded transient bending maximum by the maximum bending moment before 3.5s. This 3.5 second is chosen arbitrarily as this corresponds to inertia moment before full liquefaction. The amplification factor is plotted for all 5 depths for the full liquefaction. The study shows that the inertia bending moment can be amplified by up to 4 times. This amplification, for the case studied, is highest at a depth of about 7 times the diameter of the pile.

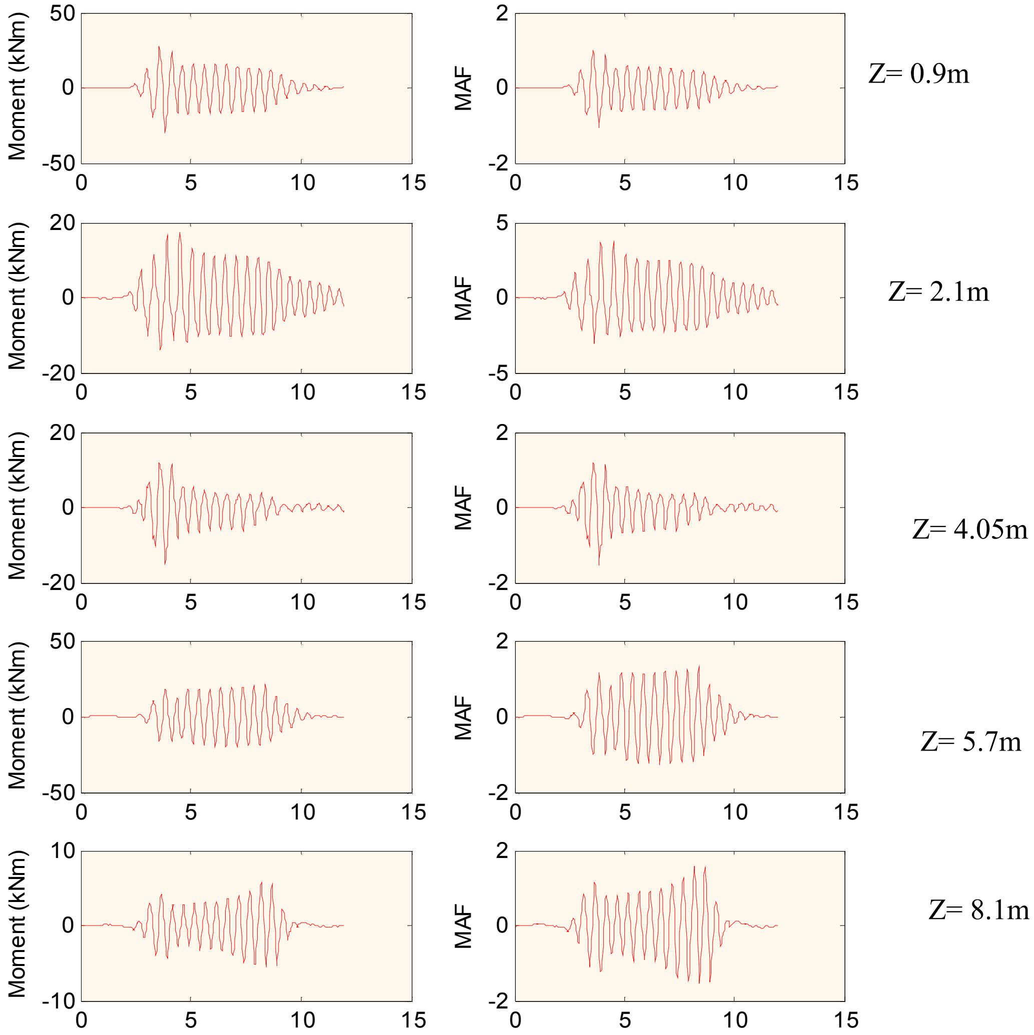

Figure 12: Moment Amplification Factor (MAF) during the full stage of liquefaction

4 DISCUSSIONS AND CONCLUSIONS

The technique of constructing a *p-y* curve is based on the assumption that the *load-deformation* pattern of pile is similar to the *stress-strain* behaviour of the interacting soil. In current practice, the stress-strain curve of the soil is obtained from element testing (e.g., a triaxial test) and the *p-y* curve is then calculated by a set of semi-empirical procedures through non-linear scaling. In other words, the stress in the soil is converted into the pressure on unit length of the pile and the strain on the soil is converted into corresponding pile deflection. These semi-empirical *p-y* curves for non-liquefied soil reflect most of the soil's fundamental stress-strain behaviour. The use of similar kind of formulation in liquefied soil however with only a reduction factor does not provide enough correspondence to the actual stress-strain behaviour. Figure 13 shows some candidate p-y curves taken from the literature. For further details see Dash et al (2009). The *p-y* curve models for non-liquefied soil are well established and have been used in practice for the past few decades. It is therefore evident that considerable inconsistencies however remain in the assumption that the *p-y* curve is similar for liquefied soil. The *p-y* curve's shape, pattern and magnitude needs better quantification when dealing with liquefied soil.

The centrifuge test results indicated that the resistance is minimal at very small strain. The conjectured shape of the p-y curve is shown in Figure 14. Figure 15 shows the expected different of behaviour depending on the shape of the p-y curve.

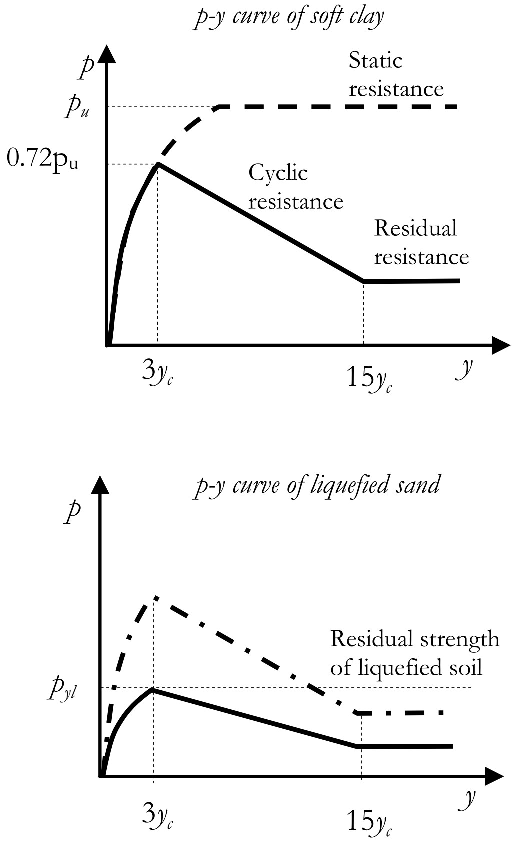

Figure 13: *p-y* curve of liquefied soil modeled as soft clay *p-y* curve, see Dash et al (2009) for further details

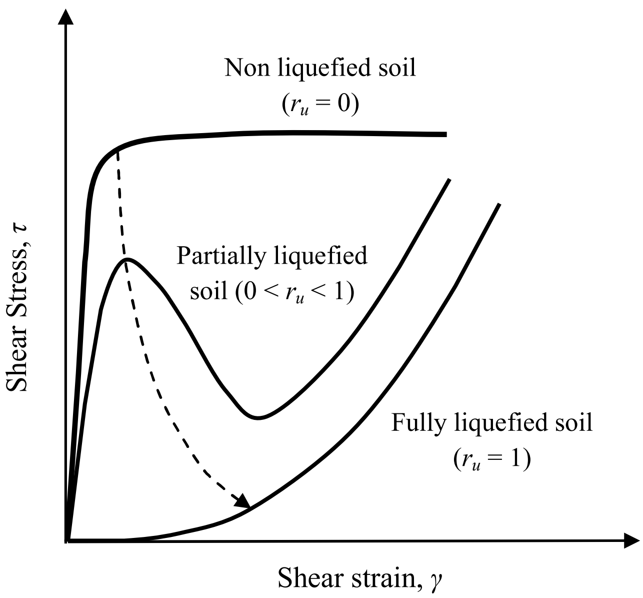

Figure 14: Schematic of the stress-strain behaviour of undrained saturated sandy soil at different stages of liquefaction.

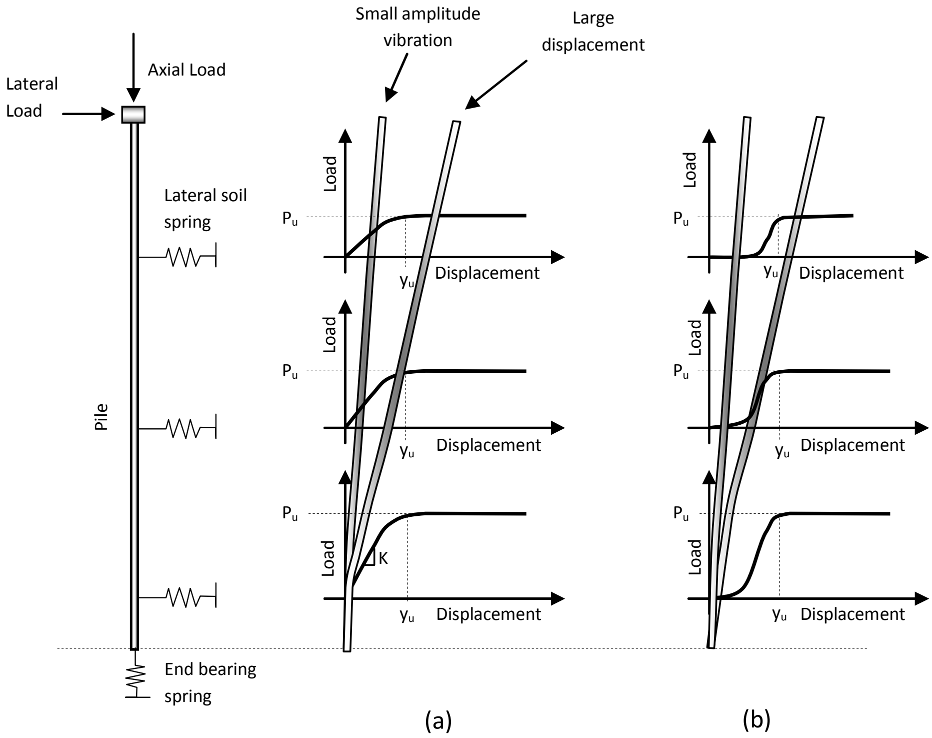

Figure 15: Difference in behaviour for two types of p-y curves

Transient bending moments in piles were studied through centrifuge testing. It has been observed that the location of maximum bending moment changes with time. As soil liquefies, the location of bending goes to deeper depths. The inertial bending moment may get amplified up to 4 times. Further study is necessary to understand these effects.

5 REFERENCE

Adhikari, S. and Bhattacharya, S (2008): "Dynamic Instability of pile-supported structures in Liquefiable soils during earthquakes", Shock and Vibration 2008; 15(6): pp 665-685

Bhattacharya, S., Tazoh, T., Jang. J, and Sato, M. (2009): A study on the behavior of raked piles in seismically liquefiable soils, Proceedings of the 3rd Japan-Greece Workshop on Foundations, Satorini, Greece, 22nd-23rd September 2009.

Bhattacharya, S., Adhikari, S. and Alexander, N.A. (2009): "A simplified method for unified buckling and free vibration analysis of pile-supported structures in seismically liquefiable soils", Soil Dynamics and Earthquake Engineering, 29 (2009), pp 1220-1235.

Bhattacharya, S., Dash, S.R. and Adhikari, S. (2008): "On the mechanics of failure of pile-supported structures in liquefiable deposits during earthquakes", Current Science, Vol 94, No 5 (10th March issue), pp 605-611.

Bhattacharya, S., Bolton, M.D. and Madabhushi, S.P.G. (2005): "A reconsideration of the safety of the piled bridge foundations in liquefiable soils", Soils and Foundations, Volume 45, August 2005 issue, No 4, pp 13-26.

Bhattacharya, S., Madabhushi, S.P.G., and Bolton, M.D. (2004): "An alternative mechanism of pile failure in liquefiable deposits during earthquakes", Geotechnique 54, April issue, No.3, pp 203-213.

Bhattacharya, S (2003): Pile Instability during earthquake liquefaction, PhD thesis, University of Cambridge (U.K).

Dash S.R, Bhattacharya, S. and Blakeborough, A (2009): "A study of *p-y* Curves for Liquefiable soils", Proceedings of the International Conference on Performance -Based Design in Earthquake Geotechnical Engineering" (IS- Tokyo 2009), 15th to 18th June 2009, CRC Press (Balkema) Taylor & Francis Group Book and CD-ROM ISBN 978-0-415-55614-9.

Dash, S.R., Bhattacharya, S., Blakeborough, A. and Hyodo, M (2008): "P-Y curve to model lateral response of pile foundations in liquefied soils", Paper number 04-01-0089, Proceedings of the 14th World Conference on Earthquake Engineering, Oct 12-17, 2008, Beijing.

Eurocode 8 (1998): "Design provisions for earthquake resistance of structures-foundations, retaining structures and geotechnical aspects", European Committee for Standardization, Brussels.

JRA (2002, 1996): Japanese Road Association, Specification for Highway Bridges, Part V, Seismic Design.

Thomson, J.M.T and Hunt, G.W (1984): "Elastic Instability phenomenon", Wiley, Chichester

Kimura, Y. and Tokimatsu, K. (2007): "Buckling stress of slender pile with lateral displacement at the pile head in liquefied soils", Journal of Structural and Construction Engineering, AIJ (Architectural Institute of Japan) No 617, pp 169-175, July 2007.

Knappett, J.A and Madabhushi, S.P.G (2005): "Modelling of Liquefaction-induced Instability in pile groups" ASCE Geotechnical Special Publication No 145 on Seismic Performance and Simulation of Pile Foundations in Liquefied and Laterally Spreading Ground, (Boulanger and Tokimatsu eds), pp 255-267.

Lin S-S, Tseng, Y.J., Chiang, C.C and Hung, C.L (2005): "Damage of piles caused by lateral spreading – Back study of three cases", ASCE Geotechnical Special Publication No 145 on Seismic Performance and Simulation of Pile Foundations in Liquefied and Laterally Spreading Ground, (Boulanger and Tokimatsu eds), pp 121-133

Parametric Study on Pile-Soil Interaction Analyses by Overlaying Mesh Method

A.Ohta
Doctoral Course Student, the graduate school of science and engineering, Yamaguchi University, Ube, Yamaguchi, Japan

F. Miura
Professor, the graduate school of science and engineering, Yamaguchi University, Ube, Yamaguchi, Japan

ABSTRACT: The overlaying mesh method (OMM) is an analytical approach that overlaps two or more independent different-mesh models in the finite element analysis. In the OMM, detailed mesh model is used in the target area under consideration, with coarse mesh model else where, in order to optimize calculation effort. In this study, we performed parametric study to investigate the accuracy of the analysis results by changing the mesh sizes, ground properties and pile characteristics.

1 INTRODUCTION

The Overlaying mesh method (OMM) is an analytical approach that overlaps two or more independent different-size-mesh models. In the OMM, detailed mesh model is used in elected area under consideration, with coarser mesh model else where, in order to optimize calculation effort. In the previous study, different-size-models are used to express a complex area with different material constants, but same type elements, such as plane strain two dimensional elements are used. In this research, we propose a new application method of the overlaying mesh method using different elements such as beam elements and solid elements. We analyzed two types of pile foundation models using OMM, and proved that the proposed method is valid.

2 THEORY OF THE PROPOSED METHOD

2.1 *Derivation of the fundamental equations for the OMM*

In the OMM, two or more different-sized-mesh models are used, one is for modeling the wide area, which we call Global area, the other/others is/are used to model detailed area(s), which we call Local area, where we want to know the detailed behavior. In the soil-structure interaction problem, for example, the former is used to model the ground

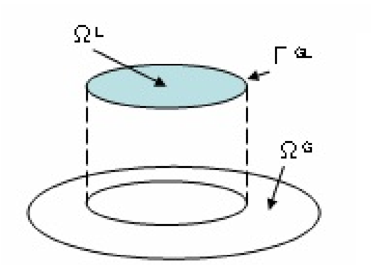

Figure 1. Superimposition of global and local areas

which widely extends, and the latter is used to model the structure of which shape is complex.

Let designate the Global area as Ω^G, the Local area as Ω^L and the boundary between these areas as Γ^{GL}. The image of the relationship of them is illustrated in Figure1.

Displacement fields are independently defined in each Ω^G and Ω^L, i.e., u_i^G and u_i^L, respectively. The actual displacement u_i in Ω^L is defined as the sum of u_i^G and u_i^L, while u_i is equal to u_i^G outside the Ω^L. Namely, the displacement u_i is defined as the following equations.

$$u_i = u_i^G + u_i^L \qquad \text{in} \quad \Omega^L \tag{1}$$

$$u_i = u_i^G \qquad \text{in} \quad \Omega^G - \Omega^L \tag{2}$$

To satisfy the continuity of the displacement at the boundary Γ^{GL}, the following condition is needed.

$$u_i^L = 0 \qquad \text{on} \quad \Gamma^{GL} \tag{3}$$

Displacements u_i^G and u_i^L in Ω^G and Ω^L are expressed by using shape function matrices N^G and N^L and nodal displacement vectors u_i^G and u_i^L as follows.

$$u_i^G = N_{ij}^G \bar{u}_j^G \tag{4}$$

$$u_i^L = N_{ij}^L \bar{u}_j^L \tag{5}$$

By partially differentiating Eq.(1) and using above equations, we obtain strain ε_{ij} as,

$$\varepsilon_{ij} = \varepsilon_{ij}^G + \varepsilon_{ij}^L \tag{6}$$

In which

$$\varepsilon_{ij}^G = B_{ijk}^G \bar{u}_k^G \tag{7}$$

$$\varepsilon_{ij}^L = B_{ijk}^L \bar{u}_k^L \tag{8}$$

By using the principle of virtual work, we can obtain the next equation.

$$\int_\Omega \delta\varepsilon_{ij} D_{ijkl} \varepsilon_{kl} d\Omega = \int_\Omega \delta u_i b_i d\Omega + \int_\Gamma \delta u_i t_i d\Gamma \tag{9}$$

Where, $\delta\varepsilon_{ij}$, ε_{ij}, δu_i, b_i, t_i, D_{ijkl} are virtual strain, strain, virtual displacement, body force, surface traction and constitutive tensor, respectively. The left side of the equation stands for the virtual work due to the internal strains and the right side represents the virtual work done by the external forces. By substituting Eq.s (1), (6), (7) and (8) into Eq. (9), we can obtain the following equations.

$$\begin{aligned} &\int_\Omega \delta(\varepsilon_{ij}^G + \varepsilon_{ij}^L) D_{ijkl} (\varepsilon_{ij}^G + \varepsilon_{ij}^L) d\Omega \\ &= \int_\Omega \delta(u_i^G + u_i^L) b_i d\Omega + \int_\Gamma \delta(u_i^G + u_i^L) t_i d\Gamma \end{aligned} \tag{10}$$

$$\begin{aligned} &\int_\Omega (B_{ijm}^G \delta\bar{u}_m^G + B_{ijm}^L \delta\bar{u}_m^L) D_{ijkl} (B_{ijm}^G \bar{u}_m^G + B_{ijm}^L \bar{u}_m^L) d\Omega \\ &= \int_\Omega (N_{ij}^G \delta u_i^G + N_{ij}^L \delta u_i^L) b_i d\Omega + \int_\Gamma (N_{ij}^G \delta u_i^G + N_{ij}^L \delta u_i^L) t_i d\Gamma \end{aligned} \tag{11}$$

By rewriting the above equations in the matrix form, we obtain the following equation.

$$\begin{bmatrix} K^G & K^{GL} \\ K^{LG} & K^L \end{bmatrix} \begin{Bmatrix} \overline{u}^G \\ \overline{u}^L \end{Bmatrix} = \begin{Bmatrix} \overline{f}^G \\ \overline{f}^L \end{Bmatrix} \tag{12}$$

Where,

$$\begin{aligned}
K^G &= \int_{\Omega^G} B_{ij}^G D_{ijkl} B_{kl}^G d\Omega^G \\
K^{GL} &= \int_{\Omega^L} B_{ij}^G D_{ijkl} B_{kl}^L d\Omega^L \\
K^{LG} &= \int_{\Omega^L} B_{ij}^L D_{ijkl} B_{kl}^G d\Omega^L \\
K^L &= \int_{\Omega^L} B_{ij}^L D_{ijkl} B_{kl}^L d\Omega^L \\
\overline{f}^G &= \int_{\Omega} N_i^G b_i d\Omega + \int_{\Gamma} N_i^G t_i d\Gamma \\
\overline{f}^L &= \int_{\Omega} N_i^L b_i d\Omega + \int_{\Gamma} N_i^L t_i d\Gamma
\end{aligned} \tag{13}$$

In which K^G and f^G are stiffness matrix and external force vector for the global area Ω^G, and K^L and f^L are stiffness matrix and external force vector for the local area Ω^L, respectively.

2.2 *Linking the beam element and the plane strain solid element*

According to the previous work[1)], linkage matrices between global and local plane strain elements, K^{GL} and K^{LG}, are obtained from Eq.(13). Linkage matrices between plane strain elements and beam elements, however, cannot be obtained in the same manner, because the strains are different between the beam element and the solid element. It is, therefore, necessary to develop a new method to link them.

The global nodal displacement at the same position as that of the local node, u'^G can be obtained by using the global shape function N^G and global nodal displacements $\overline{u}_k^G$ as Eq. (14).

$$u_l'^G = N_{kl}^G \overline{u}_k^G \tag{14}$$

Global strain at arbitrary point, ε^G, can be obtained from Eq.(7), and also obtained using other element if the point is included inside the element and the coordinate of the nodal points of the element. Therefore, global strain can be obtained by using u'^G and local shape function B^L.

$$\begin{aligned}
\varepsilon_{ij}^G &= B_{ijk}^G \overline{u}_k^G \\
&= B_{ijl}^L u_l'^G
\end{aligned} \tag{15}$$

Using Eq. (14), we can obtain the following relationships.

$$B_{ijl}^{L} N_{kl}^{G} \overline{u}_{k}^{G} = B_{ijl}^{L} u_{l}'^{G}$$
$$= B_{ijk}^{G} \overline{u}_{k}^{G}$$
$$B_{ijk}^{G} = B_{ijl}^{L} N_{kl}^{G} \tag{16}$$

Therefore, K^{LG} can be obtained as follows.

$$\begin{aligned}\left[K^{LG}\right] &= \int_{\Omega^L} B_{ij}^{L} D_{ijkl} B_{kl}^{G} d\Omega^{L} \\ &= \int_{\Omega^L} B_{ij}^{L} D_{ijkl} B_{klm}^{L} N_{mn}^{G} d\Omega^{L} \\ &= \int_{\Omega^L} B_{ij}^{L} D_{ijkl} B_{klm}^{L} d\Omega^{L} \cdot N_{mn}^{G} \\ &= \left[K^{L}\right]\left[N^{G}\right]\end{aligned} \tag{17}$$

In the same manner, K^{GL} is expressed in the following way.

$$\left[K^{LG}\right] = \left[N^{G}\right]^{T}\left[K^{L}\right] \tag{18}$$

2.3 *Constitution of the local mesh*

Figure 2 shows the total system which includes global model and local model. The local model contains beam elements of which area is designated by Ω^C. The local area modeled by solid elements is expressed by Ω^B and the global area by Ω^A. It is assumed that the areas Ω^A and Ω^C are not in contact. The constants of elasticity in the areas Ω^A and Ω^B are the same and expressed as D^1_{ijkl} and in the area Ω^C, D^1_{ijkl} in the global model and D^L_{ijkl} in the local model.

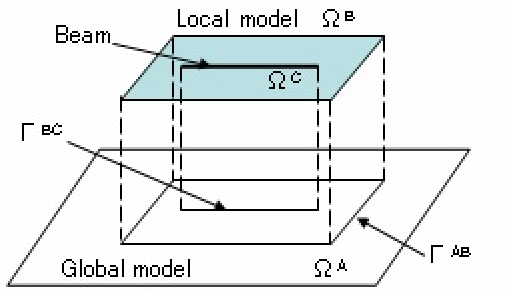

Figure 2. Superimposition of solid and beam elements

As for the boundaries, the boundary between Ω^A and Ω^B is designated by Γ^{AB}, in the same manner, the boundary between Ω^B and Ω^C is designated by Γ^{BC}. The boundary is divided into Γ^A, Γ^B and Γ^C according to the division of the areas Ω^A, Ω^B and Ω^C, respectively.

With the definitions above, K^G, K^L and K^{GL} are obtained as follows.

$$\left[K^{G}\right] = \int_{\Omega^A+\Omega^B+\Omega^C} \left[B_{ij}^{G}\right]^{T}\left[D_{ijkl}^{1}\right]\left[B_{kl}^{G}\right] d\Omega \tag{19}$$

$$\left[K^{L}\right] = \int_{\Omega^B} \left[B_{ij}^{L}\right]^{T}\left[D_{ijkl}^{1}\right]\left[B_{kl}^{L}\right] d\Omega + \int_{\Omega^C} \left[B_{ij}^{L}\right]^{T}\left[D_{ijkl}^{L}\right]\left[B_{kl}^{L}\right] d\Omega \tag{20}$$

$$\left[K^{GL}\right] = \int_{\Omega^B} \left[B_{ij}^{G}\right]^{T}\left[D_{ijkl}^{1}\right]\left[B_{kl}^{L}\right] d\Omega + \int_{\Omega^C} \left[B_{ij}^{G}\right]^{T}\left[D_{ijkl}^{L}\right]\left[B_{kl}^{L}\right] d\Omega \tag{21}$$

Eq. (11) can be written in the tensor form as;

$$
\begin{aligned}
&\int_{\Omega} \delta\varepsilon_{ij}^{G} D_{ijkl}\, \varepsilon_{kl}^{G} d\Omega + \int_{\Omega^L} \delta\varepsilon_{ij}^{G} D_{ijkl}\, \varepsilon_{kl}^{L} d\Omega^L \\
&+ \int_{\Omega^L} \delta\varepsilon_{ij}^{L} D_{ijkl}\, \varepsilon_{kl}^{G} d\Omega^L + \int_{\Omega^L} \delta\varepsilon_{ij}^{L} D_{ijkl}\, \varepsilon_{kl}^{L} d\Omega^L \\
&= \int_{\Omega} \delta u_i^{G} b_i d\Omega + \int_{\Omega^L} \delta u_i^{L} b_i d\Omega + \int_{\Gamma} \delta u_i^{G} t_i d\Gamma + \int_{\Gamma} \delta u_i^{L} t_i d\Gamma
\end{aligned} \tag{22}
$$

The displacements can be written in the following equation, in which symbols G, L, A, B and C stand for Global, Local and areas A, B and C.

$$
u_i = \begin{cases} u_i^G = u_i^{GA} & \text{in} \quad \Omega^A \\ u_i^G + u_i^L = u_i^{GB} + u_i^{LB} & \text{in} \quad \Omega^B \\ u_i^G + u_i^L = u_i^{GC} + u_i^{LC} & \text{in} \quad \Omega^C \end{cases} \tag{23}
$$

As for the global displacement concerning the virtual displacement δu_i^G, and strain $\delta\varepsilon_{ij}^G$, we can obtain the following equation.

$$
\begin{aligned}
&\int_{\Omega^A} \delta\varepsilon_{ij}^{GA} D^1_{ijkl}\, \varepsilon_{kl}^{GA} d\Omega + \int_{\Omega^B} \delta\varepsilon_{ij}^{GB} D^1_{ijkl}\, \varepsilon_{kl}^{GB} d\Omega + \int_{\Omega^A} \delta\varepsilon_{ij}^{GC} D^1_{ijkl}\, \varepsilon_{kl}^{GC} d\Omega \\
&\qquad + \int_{\Omega^B} \delta\varepsilon_{ij}^{GB} D^1_{ijkl}\, \varepsilon_{kl}^{LB} d\Omega + \int_{\Omega^C} \delta\varepsilon_{ij}^{GC} D^L_{ijkl}\, \varepsilon_{kl}^{LC} d\Omega \\
&\qquad = \int_{\Omega^A} \delta u_i^{GA} b_i d\Omega + \int_{\Omega^B} \delta u_i^{GB} b_i d\Omega + \int_{\Omega^C} \delta u_i^{GC} b_i d\Omega \\
&\qquad\quad + \int_{\Gamma} \delta u_i^{GA} t_i d\Gamma + \int_{\Gamma} \delta u_i^{GB} t_i d\Gamma + \int_{\Gamma} \delta u_i^{GC} t_i d\Gamma
\end{aligned} \tag{24}
$$

By partially integrating the left part of Eq.(24) using the Green's formula, the following equation is obtained.

$$
\begin{aligned}
&-\int_{\Omega^A} \left\{ D^1_{ijkl}\varepsilon^{GA}_{kl,l} + b_i \right\} \delta u_i^{GA} d\Omega - \int_{\Omega^B} \left\{ D^1_{ijkl}(\varepsilon^{GB}_{kl,l} + \varepsilon^{LB}_{kl,l}) + b_i \right\} \delta u_i^{GB} d\Omega \\
&-\int_{\Omega^C} \left\{ D^1_{ijkl}\varepsilon^{GC}_{kl,l} + D^L_{ijkl}\varepsilon^{LC}_{kl,l} + b_i \right\} \delta u_i^{GC} d\Omega + \int_{\Gamma^A} (D^1_{ijkl}\varepsilon^{GA}_{kl} n_j^A - t_i) \delta u_i^{GA} d\Gamma \\
&+\int_{\Gamma^B} \left\{ D^1_{ijkl}(\varepsilon^{GB}_{kl} + \varepsilon^{LB}_{kl}) n_j^B - t_i \right\} \delta u_i^{GB} d\Gamma + \int_{\Gamma^C} \left\{ (D^1_{ijkl}\varepsilon^{GC}_{kl} + D^L_{ijkl}\varepsilon^{LC}_{kl}) n_j^C - t_i \right\} \delta u_i^{GC} d\Gamma \\
&+\int_{\Gamma^{AB}} \left\{ D^1_{ijkl}\varepsilon^{GA}_{kl} - D^1_{ijkl}(\varepsilon^{GB}_{kl} + \varepsilon^{LB}_{kl}) \right\} n_j^B \delta u_i^{GAB} d\Gamma \\
&+\int_{\Gamma^{BC}} \left\{ D^1_{ijkl}(\varepsilon^{GB}_{kl} + \varepsilon^{LB}_{kl}) - (D^1_{ijkl}\varepsilon^{GC}_{kl} + D^L_{ijkl}\varepsilon^{LC}_{kl}) \right\} n_j^C \delta u_i^{GBC} d\Gamma = 0
\end{aligned} \tag{25}
$$

As the global displacements u_i^G is continuous in area Ω, the following relations can exist.

$$
\delta u_i^{GA} = \delta u_i^{GB} = \delta u_i^{GAB} \quad \text{on} \quad \Gamma^{AB} \tag{26}
$$

$$
\delta u_i^{GB} = \delta u_i^{GC} = \delta u_i^{GBC} \quad \text{on} \quad \Gamma^{BC} \tag{27}
$$

On the other hand, as for the local displacement concerning the virtual displacement δu_i^L, and strain $\delta\varepsilon_{ij}^L$, we can obtain the following equation.

$$
\begin{aligned}
&\int_{\Omega^B} \delta\varepsilon_{ij}^{LB} D_{ijkl}^{1} \varepsilon_{kl}^{GB} d\Omega + \int_{\Omega^C} \delta\varepsilon_{ij}^{LC} D_{ijkl}^{L} \varepsilon_{kl}^{GC} d\Omega \\
&+ \int_{\Omega^B} \delta\varepsilon_{ij}^{LB} D_{ijkl}^{1} \varepsilon_{kl}^{LB} d\Omega + \int_{\Omega^C} \delta\varepsilon_{ij}^{LC} D_{ijkl}^{L} \varepsilon_{kl}^{LC} d\Omega \\
&= \int_{\Omega^B} \delta u_i^{LB} b_i d\Omega + \int_{\Omega^C} \delta u_i^{LC} b_i d\Omega + \int_{\Gamma^B} \delta u_i^{LB} t_i d\Gamma + \int_{\Gamma^C} \delta u_i^{LC} t_i d\Gamma
\end{aligned}
\tag{28}
$$

In the same manner as in the global area, Eq. (28) can be written as,

$$
\begin{aligned}
&- \int_{\Omega^B} \left\{ D_{ijkl}^{1} (\varepsilon_{kl,l}^{GB} + \varepsilon_{kl,l}^{LB}) + b_i \right\} \delta u_i^{GB} d\Omega \\
&- \int_{\Omega^C} \left\{ D_{ijkl}^{1} \varepsilon_{kl,l}^{GC} + D_{ijkl}^{L} \varepsilon_{kl,l}^{LC} + b_i \right\} \delta u_i^{GC} d\Omega \\
&+ \int_{\Gamma^B} \left\{ D_{ijkl}^{1} (\varepsilon_{kl}^{GB} + \varepsilon_{kl}^{LB}) n_j^B - t_i \right\} \delta u_i^{GB} d\Gamma + \int_{\Gamma^C} \left\{ (D_{ijkl}^{1} \varepsilon_{kl}^{GC} + D_{ijkl}^{L} \varepsilon_{kl}^{LC}) n_j^C - t_i \right\} \delta u_i^{GC} d\Gamma \\
&+ \int_{\Gamma^{AB}} \left\{ D_{ijkl}^{1} \varepsilon_{kl}^{GA} - D_{ijkl}^{1} (\varepsilon_{kl}^{GB} + \varepsilon_{kl}^{LB}) \right\} n_j^B \delta u_i^{GAB} d\Gamma \\
&+ \int_{\Gamma^{BC}} \left\{ D_{ijkl}^{1} (\varepsilon_{kl}^{GB} + \varepsilon_{kl}^{LB}) - (D_{ijkl}^{1} \varepsilon_{kl}^{GC} + D_{ijkl}^{L} \varepsilon_{kl}^{LC}) \right\} n_j^C \delta u_i^{GBC} d\Gamma = 0
\end{aligned}
\tag{29}
$$

And,

$$
\delta u_i^{LB} = 0 \quad \text{on} \quad \Gamma^{\mathrm{AB}} \tag{30}
$$

In the Eq.s (25) and (29), as the virtual displacements are arbitrary, we obtain the following equations.

$$
D_{ijkl}^{1} \varepsilon_{kl,l}^{GA} + b_i = 0 \qquad \text{in} \quad \Omega^A \tag{31}
$$

$$
D_{ijkl}^{1} (\varepsilon_{kl,l}^{GB} + \varepsilon_{kl,l}^{LB}) + b_i = 0 \qquad \text{in} \quad \Omega^B \tag{32}
$$

$$
D_{ijkl}^{1} \varepsilon_{kl,l}^{GC} + D_{ijkl}^{L} \varepsilon_{kl,l}^{LC} + b_i = 0 \qquad \text{in} \quad \Omega^C \tag{33}
$$

$$
D_{ijkl}^{L} \varepsilon_{kl,l}^{GC} + D_{ijkl}^{L} \varepsilon_{kl,l}^{LC} + b_i = 0 \qquad \text{in} \quad \Omega^C \tag{34}
$$

$$
D_{ijkl}^{1} \varepsilon_{kl}^{GA} n_j^A - t_i = 0 \qquad \text{on} \quad \Gamma^A \tag{35}
$$

$$
D_{ijkl}^{1} (\varepsilon_{kl}^{GB} + \varepsilon_{kl}^{LB}) n_j^B - t_i = 0 \qquad \text{on} \quad \Gamma^B \tag{36}
$$

$$
(D_{ijkl}^{1} \varepsilon_{kl}^{GC} + D_{ijkl}^{L} \varepsilon_{kl}^{LC}) n_j^C - t_i = 0 \qquad \text{on} \quad \Gamma^C \tag{37}
$$

$$
(D_{ijkl}^{L} \varepsilon_{kl}^{GC} + D_{ijkl}^{L} \varepsilon_{kl}^{LC}) n_j^C - t_i = 0 \qquad \text{on} \quad \Gamma^C \tag{38}
$$

$$
\left\{ D_{ijkl}^{1} \varepsilon_{kl}^{GA} - D_{ijkl}^{1} (\varepsilon_{kl}^{GB} + \varepsilon_{kl}^{LB}) \right\} n_j^B = 0 \qquad \text{on} \quad \Gamma^{AB} \tag{39}
$$

$$
\left\{ D_{ijkl}^{1} (\varepsilon_{kl}^{GB} + \varepsilon_{kl}^{LB}) - (D_{ijkl}^{1} \varepsilon_{kl}^{GC} + D_{ijkl}^{L} \varepsilon_{kl}^{LC}) \right\} n_j^C = 0 \qquad \text{on} \quad \Gamma^{BC} \tag{40}
$$

$$
\left\{ D_{ijkl}^{1} (\varepsilon_{kl}^{GB} + \varepsilon_{kl}^{LB}) - (D_{ijkl}^{L} \varepsilon_{kl}^{GC} + D_{ijkl}^{L} \varepsilon_{kl}^{LC}) \right\} n_j^C = 0 \qquad \text{on} \quad \Gamma^{BC} \tag{41}
$$

By subtracting Eq. (34) from Eq. (33), Eq. (38) from Eq. (37), Eq. (41) from Eq. (40), we obtain Eq.s (42), (43), (44), respectively.

$$(D^{1}_{ijkl} - D^{L}_{ijkl})\varepsilon^{GC}_{kl,l} = 0 \quad \text{in} \quad \Omega^{C} \tag{42}$$

$$(D^{1}_{ijkl} - D^{L}_{ijkl})\varepsilon^{GC}_{kl} n^{C}_{j} = 0 \quad \text{on} \quad \Gamma^{C} \tag{43}$$

$$(D^{1}_{ijkl} - D^{L}_{ijkl})\varepsilon^{GC}_{kl} n^{C}_{j} = 0 \quad \text{on} \quad \Gamma^{BC} \tag{44}$$

From Eq.s (43) and (44), equilibrium of stress is independently satisfied within the global model on the boundaries Γ^{BC} and Γ^{C}, and normal stress outward direction is 0. From Eq.s (42), (43), (44) we can get the next relationship.

$$(D^{1}_{ijkl} - D^{L}_{ijkl})\varepsilon^{GC}_{kl} = 0 \quad \text{in} \quad \Omega^{C} \tag{45}$$

This means that the stress of beam elements due to global model is 0 on the boundary of area Ω^{C}. And from Eq. (45)

$$\varepsilon^{GC}_{kl} = 0 \quad \text{in} \quad \Omega^{C} \tag{46}$$

Eq.s (33) and (34) become

$$D^{L}_{ijkl}\varepsilon^{LC}_{kl,l} + b_{i} = 0 \quad \text{in} \quad \Omega^{C} \tag{47}$$

In the same way, Eq. (40) and (41) become

$$\left\{D^{1}_{ijkl}(\varepsilon^{GB}_{kl} + \varepsilon^{LB}_{kl}) - D^{L}_{ijkl}\varepsilon^{LC}_{kl}\right\} n^{B}_{j} = 0 \quad \text{on} \quad \Gamma^{BC} \tag{48}$$

This means that the stresses due to displacements in local model within area Ω^{C} on the boundary Γ^{BC}, equilibrium to those within area Ω^{B}. Stresses in the beam elements, therefore, can be expressed only by the local model and obtained only by the stiffness of the beam elements.

3 ANALITICAL EXAMPLES

3.1 *Vertical pile model*

The vertical pile-footing-ground model used in this analysis is illustrated in Figure 3. Ground, piles and footing are assumed to be linear elastic materials. Young's modulus, sectional area, and moment inertia of the section of the pile are 200GPa, $0.2366\text{x}10^{-5}\text{m}^{2}$, and $0.3940\text{x}10^{-5}\text{m}^{4}$, respectively. Each parameter of the plane element is listed in Table1.

Finite element models of the model are shown in Figures 4 and 5. Figure 4 is the ordinal finite element model and Figure 5 is overlaying mesh model.

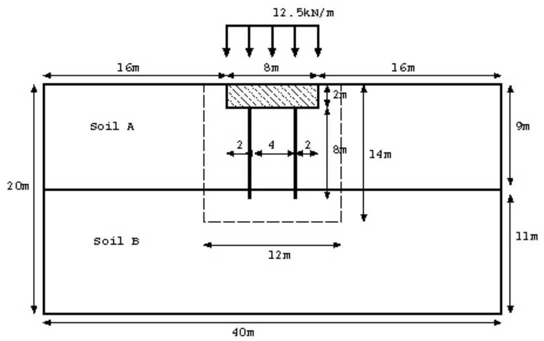

Figure3.Vertical pile model

Table1. Parameter of the plane element

	Shear wave velocity(m/s)	Unit weight(kN/m^{3})	Poisson's ratio
Soil A	150	17	0.3
Soil B	450	17	0.3
Footing	1500	17	0.3

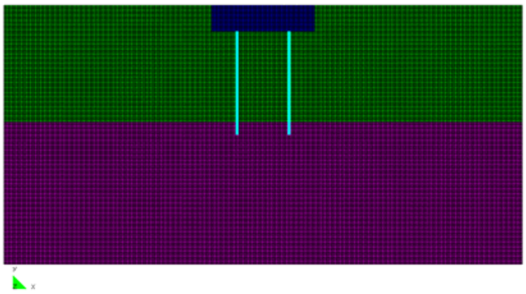

Figure 4. Normal finite element mesh of vertical piles

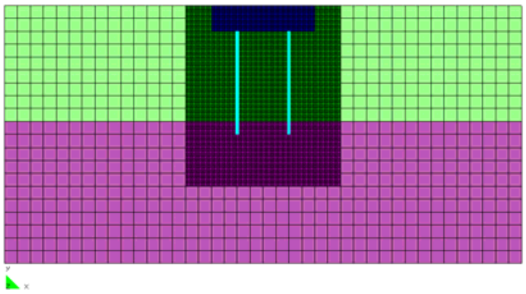

Figure 5. Finite element mesh of vertical piles with OMM

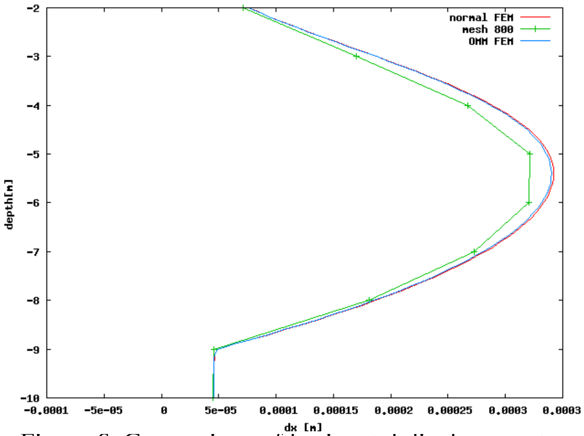

Figure 6. Comparison of horizontal displacements

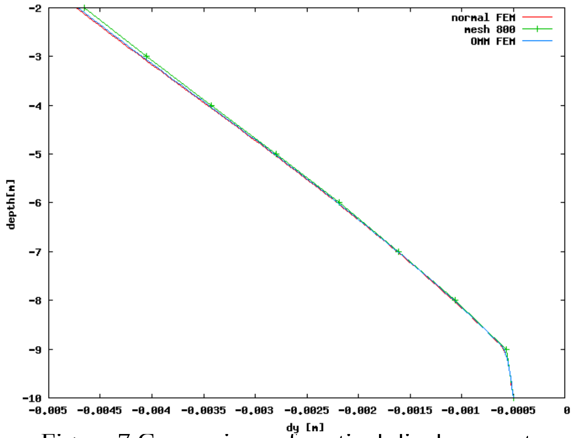

Figure 7.Comparison of vertical displacements

Numerical analysis results are compared in Figures 6, 7 and 8. Horizontal displacements of the beam elements are illustrated in Figure 6, vertical displacements in Figure 7 and rotational angles in Figure 8. In these figures, "normal FEM" means the results from the ordinal element model, "OMM FEM" from the overlaying mesh model, and "mesh 800" from coarser mesh of the same size as Global mesh model.

The difference of the horizontal response displacements is about 0.1mm, and this is very small compared with the maximum response of the system of 2.9mm, in the vertical direction, the difference is about 0.03mm, while the maximum response is about 13.5mm. The distributions of the response displacements in the total system are shown in Figures 9, 10, 11 and 12. From these figures the results are almost same in the two models. This means the validity of the proposed method.

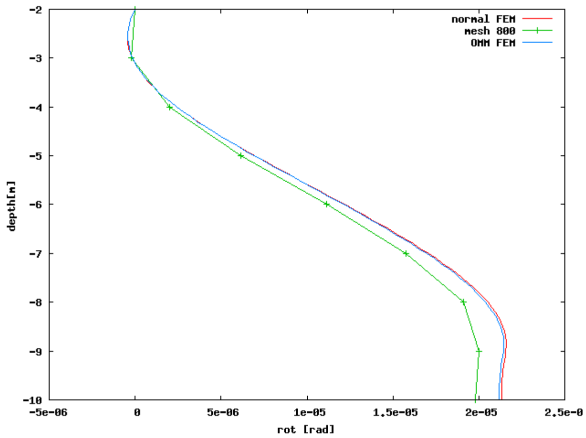

Figure 8. Comparison of rotational angle of pile

3.2 *Battered pile model*

Figure 13 shows the battered pile-ground-footing model. The material constants are the same as those of the vertical pile models. Figures 14 and 15 are ordinal mesh model and OMM, respectively. The mesh of the former model is very complicated to express the battered piles, on the

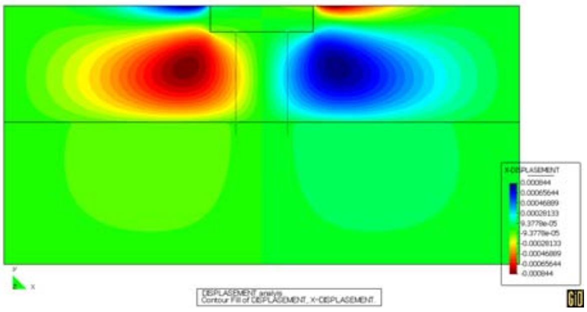

Figure 9. Distribution of horizontal displacement from normal finite element mesh

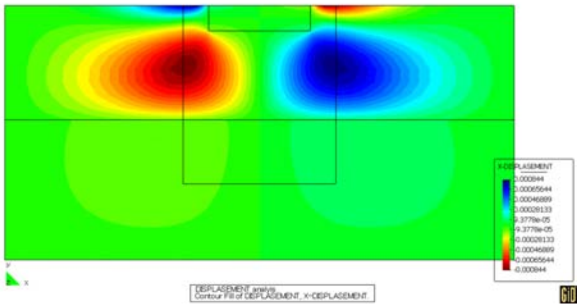

Figure 10. Distribution of horizontal displacement from finite element mesh with OMM

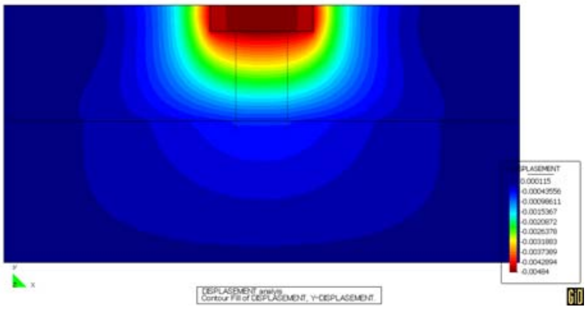

Figure 11. Distribution of vertical displacement from normal finite element mesh

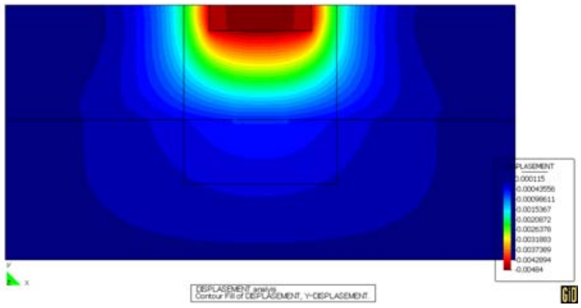

Figure 12. Distribution of vertical displacement from finite element mesh with OMM

other hand, the mesh is very simple for the latter model as shown in Figure 15. Same global mesh as in the vertical pile is used for the OMM.

The comparisons of horizontal and vertical displacements and rotational angle are made in Figures 16, 17 and 18. "normal FEM" means the results from the ordinal element model , "OMM case1", "OMM case2" and "OMM case3" are from the overlaying mesh. The result of Figure 14 and Figure 15 are from "normal FEM" and "OMM case1" respectively. The size of global mesh of "OMM case2" and "OMM case3" is equal to the global mesh of "OMM case1" i.e., 1m. But the local mesh of "OMM case2" is 0.25m and coarser than that of "OMM case1"(0.1m), and the local mesh area of "OMM case3"(mesh size is 0.1m same as "OMM case1") is 6m and narrower than that of "OMM case1"(8m). The differences between these two models are little larger than those from the vertical pile models, especially for the rotational angle.

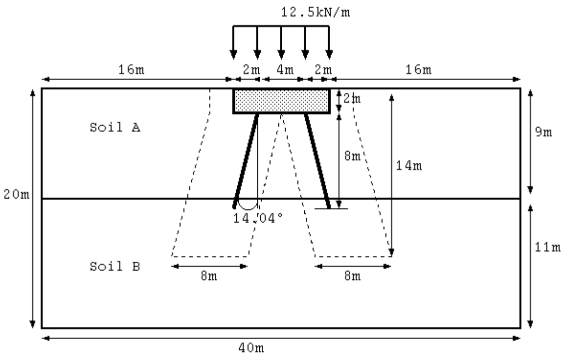

Figure 13. Battered pile model

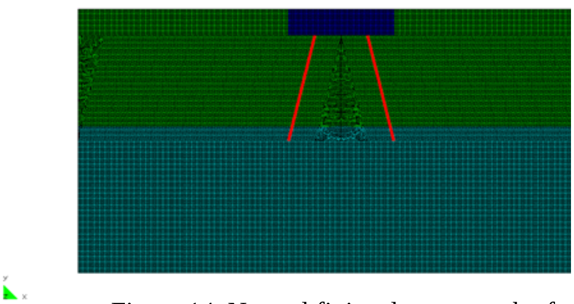

Figure 14. Normal finite element mesh of battered piles

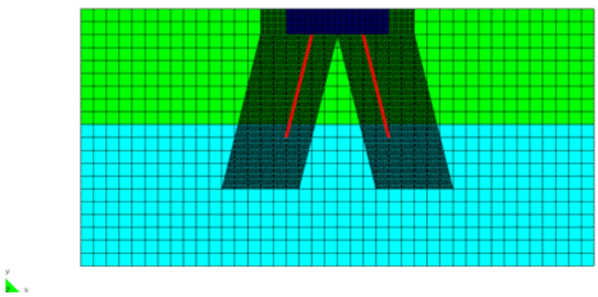

Figure 15. Finite element mesh of battered piles with OMM

The comparisons of the distributions of horizontal and vertical displacements in the global system are shown in Figures 19, 20, 21 and 22. As can be seen in Figures 16 and 17, the difference of the responses can be observed at the middle and the top of the piles, respectively.

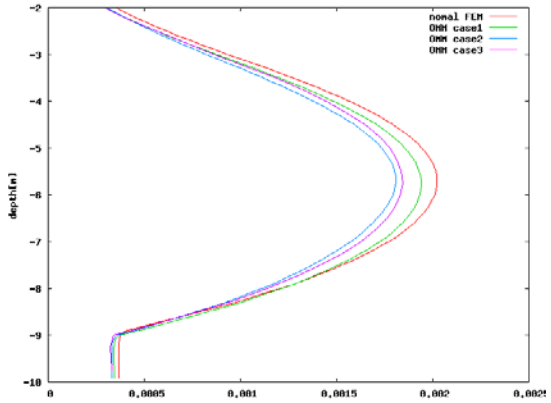

Figure 16. Comparison of horizontal displacements

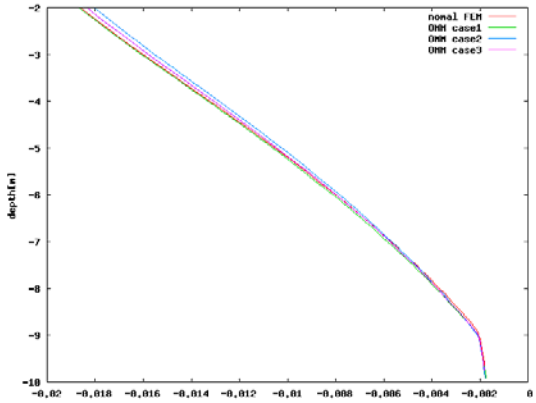

Figure 17. Comparison of vertical displacements

The CPU time to analyze models shown in Figures 12 and 13 are almost same in both cases. To generate the OMM is very easy, because we just put the battered piles models on the global model (ground model). This is a typical advantage of using OMM.

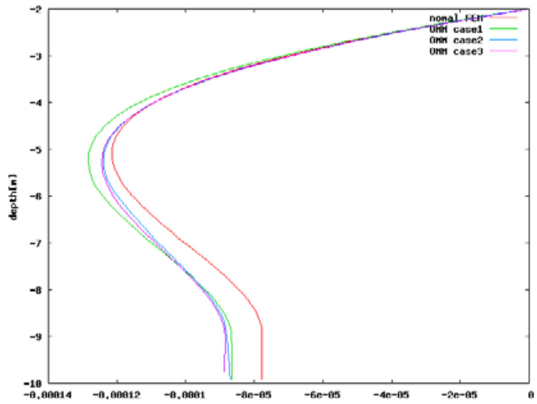

Figure 18. Comparison of rotational angle of pile

4 CONCLISIONS

We derived the basic equations of OMM in application of the soil-structure interaction system. Then we examine the validity of the method. For vertical pile model, we could get good agreement between the ordinal model and the OMM model, but in the analysis of battered pile model, the difference is little larger than those for vertical pile models. We need to examine the reason and establish the analysis method for the soil-structure interaction problem, and more we need to extend the method to three dimensional problem in which the advantage of the method will be remarkable.

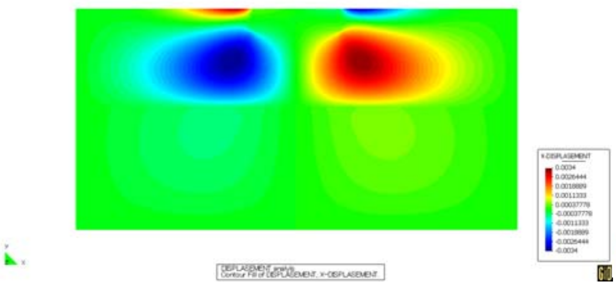

Figure 19. Distribution of horizontal displacement from ordinal finite element mesh

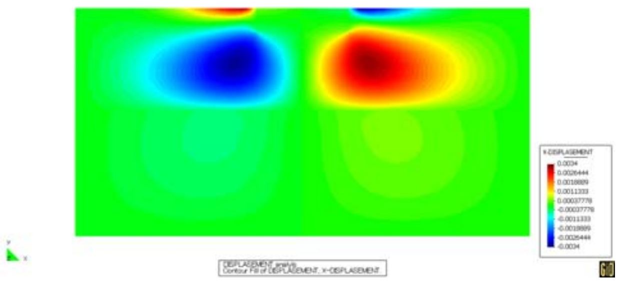

Figure 20. Distribution of horizontal displacement from finite element mesh with OMM

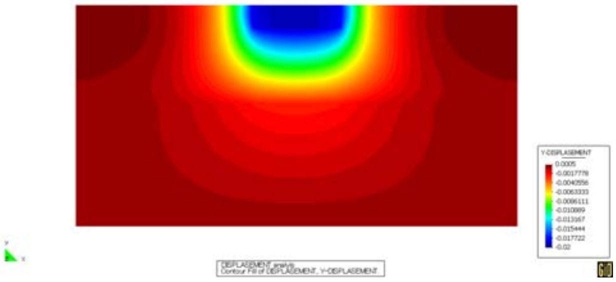

Figure 21. Distribution of vertical displacement from normal finite element mesh

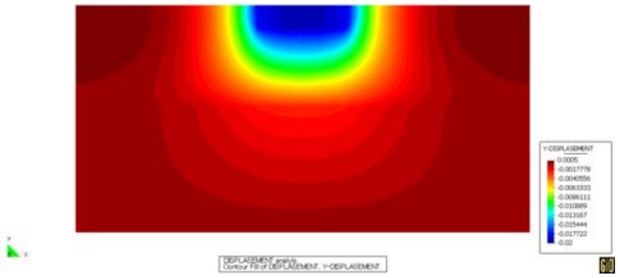

Figure 22. Distribution of vertical displacement from finite element mesh with OMM

REFERENCES

Belytchko, T., Fish, J. and Bayliss, A.: The spectral overlay on finite elements for problems with high gradients, *Computer methods in applied mechanics and engineering* :Vol.81, 71-89.

Ohta, A., Ono, Y., Kiyono, J. and Miura, F.: 2009 Finite element analysis of pile-soil interaction system by overlaying mesh method, Proc. *3rd Greece-Japan Workshop*, Santrini, Greece.

On the Performance of a Mechanical System Emulating Dynamic Stiffness of Soil-Foundation Systems

M. Saitoh[1], T. Saito[1], T. Hikima[1], M. Ozawa[2], K. Imanishi[2],
1 Graduate School of Science and Engineering, Saitama University, Japan
2 Nowest Technology, Japan

ABSTRACT: This paper presents the performance of a so-called “soil-foundation emulator”, which was introduced in the previous Greece-Japan Workshop, Greece. This emulator is constructed based on a newly proposed model that can simulate frequency-dependent oscillations in impedance functions of soil-foundation systems by using a so called “gyro mass”. A gyromass is an element defined as a unit system that generates a reaction force due to the relative acceleration of the nodes between which the gyromass is placed. This emulator is created as a real mechanical system with springs, dampers, and mechanical gyro mass elements based on the proposed model. The impedance characteristics of the emulator show good agreement with those of a target impedance function.

1 INTRODUCTION

In general, soil-foundation systems show various frequency-dependent impedance characteristics, such as rapid oscillations or cut-off frequencies, depending on the types of foundations, soil profiles, and the direction of excitations, etc. In contrast, many recent studies of structural dynamics have focused on the inelastic behavior of structural systems because the methodology of performance-based seismic design, which has been applied to seismic codes and guidelines in many countries, allows modeling of the inelastic behavior of structural systems. The frequency dependency of soil-foundation impedance characteristics is usually considered in a numerical method performed in the frequency domain, whereas the nonlinearity of superstructures is in the time domain because the inelastic behavior of materials and structural members strongly depends on the stress path being integrated stepwise. The effect of the frequency dependency of the impedance functions (IFs) upon the nonlinear responses of superstructures has not yet been investigated, even qualitatively, because numerical techniques considering both frequency dependency and nonlinearity are generally complicated and still immature. The most powerful and acceptable tool in practice is a mechanical representation approximating the IFs by frequency-independent spring, dashpot, and mass elements [e.g., Meek & Veletsos (1974), Wolf & Somaini (1986), Nogami & Konagai (1986, 1988), Wolf (1994), Wolf & Song (2002)]. The reason for this is that the frequency-independent mechanical elements can be applied directly to conventional structural analysis. This mechanically represented system is generally called a “Lumped Parameter Model (LPM)”. In recent years, various types of lumped parameter models have been proposed for soil reaction, shallow foundations, embedded foundations, etc. Although increasing the number of elements and degrees of freedom results in more accurate fitting to the ideal IFs, in practical applications, simple models having a small number of elements and degrees of freedom are used. In general, however, such simple models show a moderate variation with frequency, and thus do not express the frequency-dependent IFs with sufficient accuracy.

Saitoh (2007) proposed a model by which various types of frequency-dependent IFs can be simulated using a mechanical element called a "gyro mass". The gyro mass is frequency-independent and is defined as a unit system that generates a reaction force due to the relative acceleration of the nodes between which the gyromass is placed. The advantage of the use of this element is that a rapid change in the IFs with frequency can easily be expressed by the element.

In the 2009 Greece-Japan Workshop, I introduced a so called “soil-foundation emulator (SFE)” as an innovative research project supported by the Ministry of Education, Culture, Sports, Science and Technology, Japan (Figure 1). SFE is a mechanical system realistically constructed using mechanical elements based on the gyro mass LPM (GLPM). The purpose of this construction is that the soil-foundation emulator can represent a soil-foundation system on a shaking table in experimental researches. In general, a structural system is constructed on a shaking table for investigating its dynamic behavior when subjected to earthquake waves. However, only a superstructure is usually constructed because the soil-foundation system is difficult to create due to the restriction of the space. It is known that the lack of a soil-foundation system may change the natural periods and damping of the systems. In this paper, the performance of a SFE constructed targeting the IF of a 3×5 pile group embedded in a layered soil medium is presented.

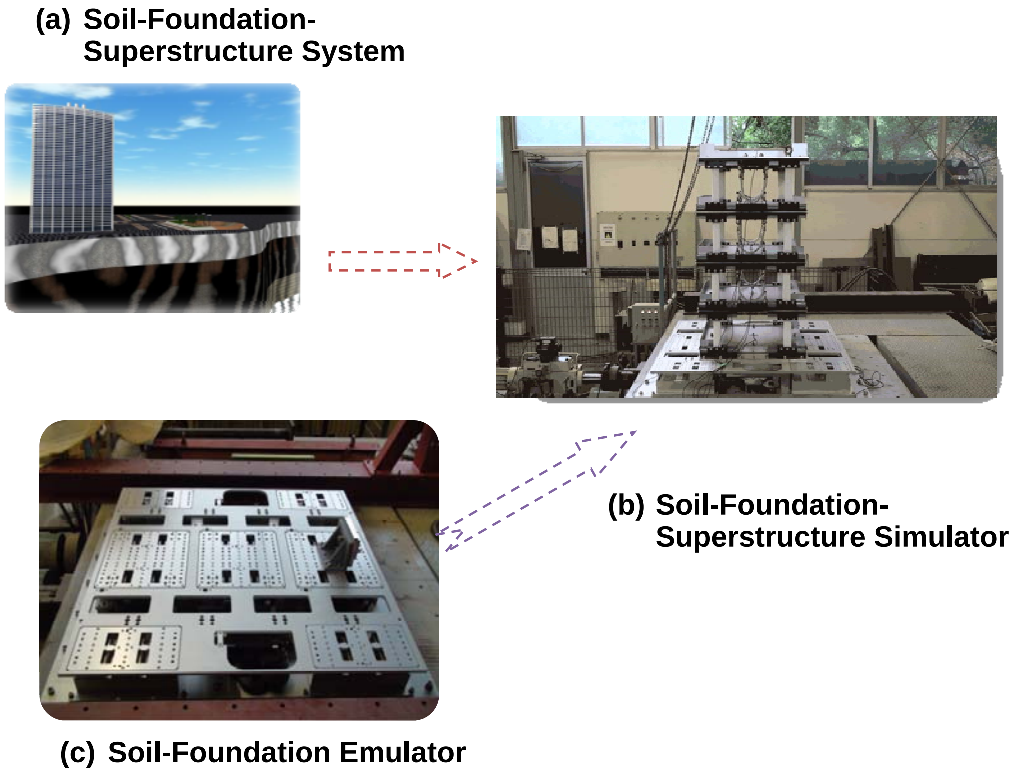

Figure 1. Overview of Soil-Foundation Emulator Project

2 TARGET IMPEDANCE FUNCTION AND GYRO-LUMPED PARAMETER MODEL

One of the most impressive examples is the application to IFs of pile groups. The reason for this is that impedance functions of pile groups in general show complicated oscillations with frequency. These oscillations usually occur due to "in-phase" and "out-of-phase" pile-to-pile interactions, as explained in Dobry and Gazetas (1988). It is known that simulating impedance functions of pile groups by using spring-dashpot-mass models is quite difficult since some of these parameters often take negative values, which is considered to be unrealistic, and in general, unstable in numerical calculations. Here, the impedance function in the horizontal direction (Figure 1) of a 3×5 pile group embedded in a layered soil medium is taken as a target IF. The typical oscillations with frequency can be found in the IF.

In the following simulation, one of the proposed models, called the "Type II Model", is used. Details of this model are described in Saitoh (2007); therefore, an explanation of the fundamentals of this model is omitted here. Figure 1 shows that the Type II model consists of two types of unit systems: one is the base system, and the other is the core system composed of a spring k and a unit having a gyro-mass $\overline{m}$ and a dashpot c arranged in parallel. The base system and the core system are arranged in parallel. As described in Saitoh (2007), an additional core system having different coefficients can be arranged in parallel with the Type II model in order to enhance the precision of the simulation, if needed. The impedance functions of the Type II model having multiple core systems shown in Figure 1 can be expressed by the following formula:

$$F(a_0) = K\left\{1 + \sum_{i=1}^{N} \frac{\beta_i\left[\mu_i a_0^2\left(\mu_i a_0^2 - 1\right) + \gamma_i^2 a_0^2\right]}{\left(1-\mu_i a_0^2\right)^2 + \gamma_i^2 a_0^2} - \mu_0 a_0^2 + i\, a_0\left[\sum_{i=1}^{N} \frac{\beta_i \gamma_i}{\left(1-\mu_i a_0^2\right)^2 + \gamma_i^2 a_0^2} + \gamma_0\right]\right\} u(a_0), \tag{1}$$

where the coefficient K is equivalent to the static stiffness ($a_0 = 0$); γ_i, μ_i, and β_i are, respectively, the dimensionless coefficients of the damper and the gyro-mass, and the stiffness ratio of the i-th core system shown in Figure 2; and N is the total number of core systems.

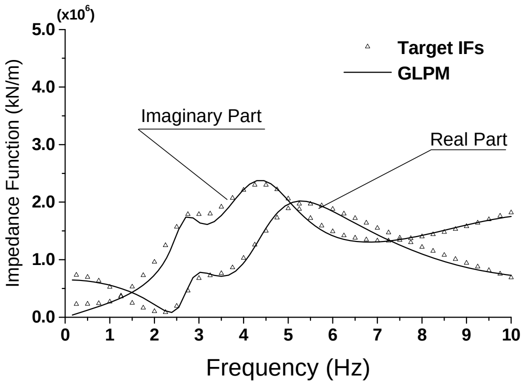

Figure 1. Target IFs and GLPM (Type II Model).

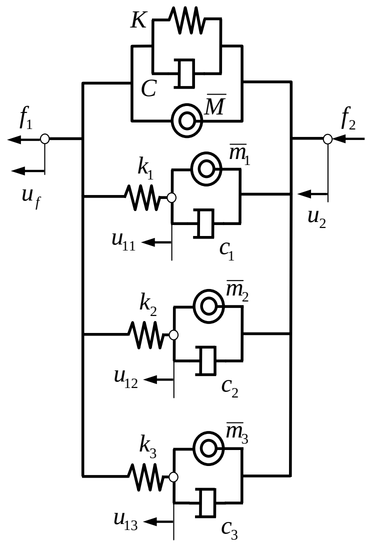

Figure 2. Type II Model.

In this study, three core systems are used to simulate the target IF. The properties of the GLPM are determined by manual fitting. The resultant IF is also shown in Figure 1. It is found that the IF shows good agreement with the target IF.

3 SOIL-FOUNDATION EMULATOR

The role of this emulator in earthquake engineering is to enhance the accuracy of the prediction of damage to structures subjected to earthquake waves in experimental researches where shaking tables are used. In general, only a superstructure is constructed on a shaking table: the soil-foundation system that supports the superstructure is difficult to construct due to the restriction of the space on the table. This soil-foundation emulator can represent the soil-foundation system in a small space. The emulator is constructed based on the lumped parameter model explained above. Therefore, this emulator is a passive-controlled soil-foundation system. The merit of this passive-controlled system is that the system maintains the constant status of a target impedance function while the superstructure shows strong nonlinearity in its structural members. In general, active-controlled systems show signal-delay and convergence problems when the nonlinearity occurs in the superstructure. This emulator consists of springs, dampers, and “gyromass” elements. It is noted that an extremely large mass is necessary for expressing the oscillation in impedance functions in general so that lamped parameter models using general mass (not gyromass) are very difficult to be constructed as a real mechanical system on a shaking table due to a limited space. In contrast, the model proposed in this study consists of no general mass at all; only gyromass elements are used. As described below, a mechanically-created gyromass element in the present study is a markedly compact system owing to a specific mechanical technique.

3.1 *Mechanical System of gyromass elements*

The mechanical analogy of the gyromass element is shown in Figure 3 (a). The analogy consists of a rotational disk and a rod attached to the disk with strong friction, gears for instance. It is assumed that the mass of the rod is negligible. The disk rotates with rotational acceleration $\ddot{\theta}$ as an external force F is given to the rod. The relative acceleration of the rod $\ddot{u}$ with respect to the fixed node at the right hand side is geometrically related to the rotational acceleration $\ddot{\theta}$. Consequently, the following relation between the external force F and the relative acceleration $\ddot{u}$ can be obtained:

$$F = \overline{m}\ddot{u} \tag{2}$$

where

$$\overline{m} \propto \frac{J}{r^2}. \tag{3}$$

Here, r is the distance from the center of the disk to the point where the rod is attached; J is the mass moment of inertia of the disk; and $\overline{m}$ is the equivalent mass generated by the rotation of the disk. Thus, the reaction force at the left hand side of the rod is identical to the product of the equivalent mass $\overline{m}$ and the relative acceleration $\ddot{u}$. Accordingly, the equivalent mass $\overline{m}$ is termed “gyro-mass” in order to be distinguished from ordinary mass. In order to increase the gyromass much larger value than the mass of the disk itself, the following conventional techniques can be used in mechanical engineering: (1) increasing the radius of gyration of the disk by concentrating the mass at the edge of the disk; and (2) increasing the rotational acceleration of the disk by combinations of disk gears. These techniques make the ordinary mass of the disk negligible when compared with the gyromass in the system. Figure 3 (b) shows the real mechanical system of the gyromass element, where the second technique is used in the system.

3.2 *Impedance characteristics of emulator*

Figure 4 shows the SFE constructed in this project. The similitude applied to the SFE is that the geometric scaling and the mass scaling are 3 and 2500, respectively. Figure 5 shows the IF of the SFE. The IF was obtained from the time-history displacement response and the harmonic force applied at the center of the top plate of the SFE. Figure 5 indicates that, on the whole, the SFE shows fairly good agreement with the frequency dependent characteristics in the target IF. In details, the real part of the SFE tends to be smaller than that of the target one above 9Hz. In addition, the imaginary part, which is associated with damping of the system, tends to be smaller than that of the target IF. This decrease in the imaginary part may occur due to the fact that realizing the perfect fixity condition at the ends of the mechanical dampers in the high frequency region is difficult owing to a large force accompanied by increases in the excitation frequency so that damping effects does not appropriately appear.

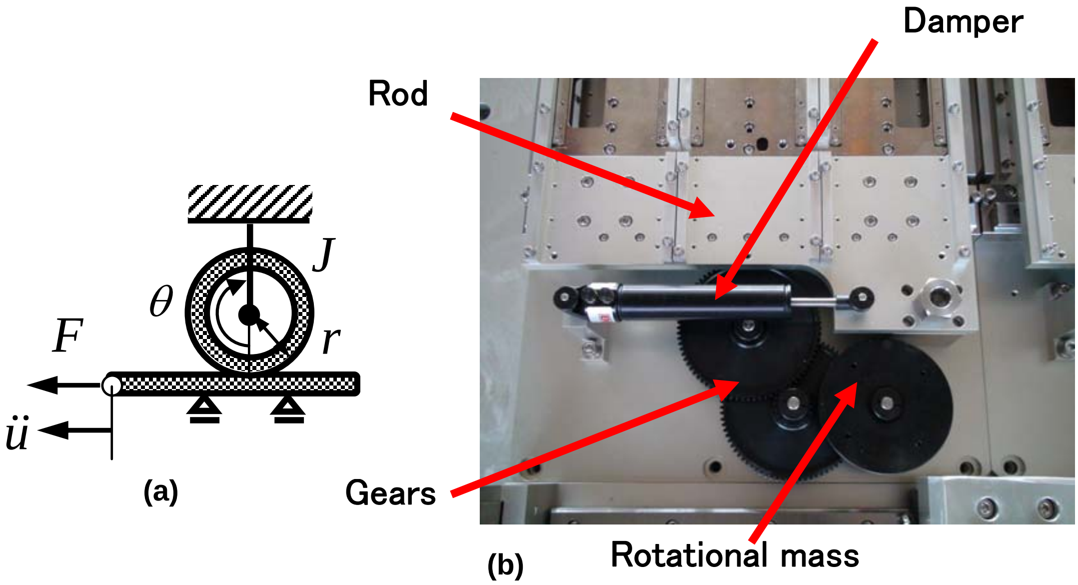

Figure 3. Mechanical analogy of gyromass element and its creation by using mechanical elements. (a) Mechanical analogy, and (b) Mechanical system of gyromass element

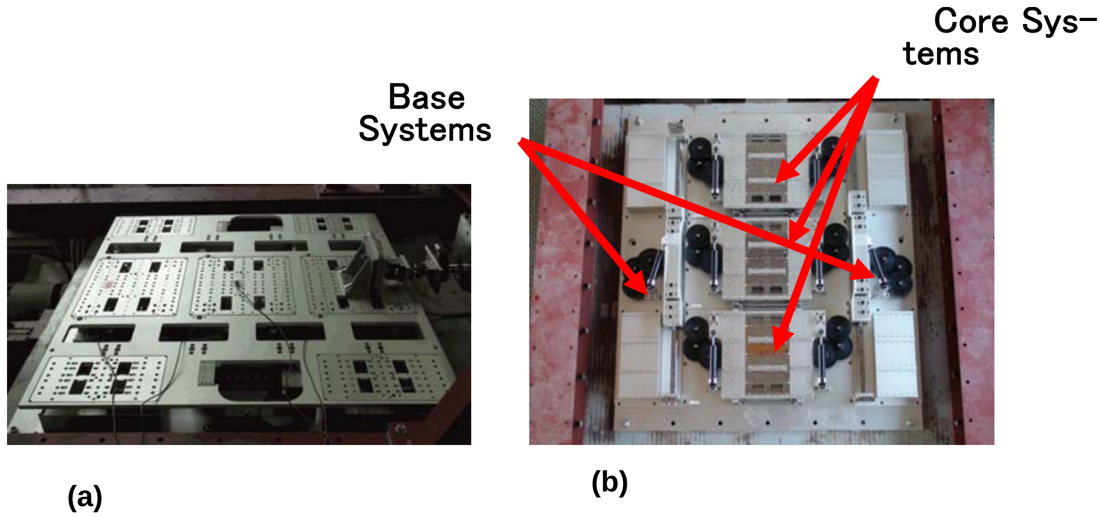

Figure 4. Constructed SFE. (a) Side view, and (b) Top view without top plate

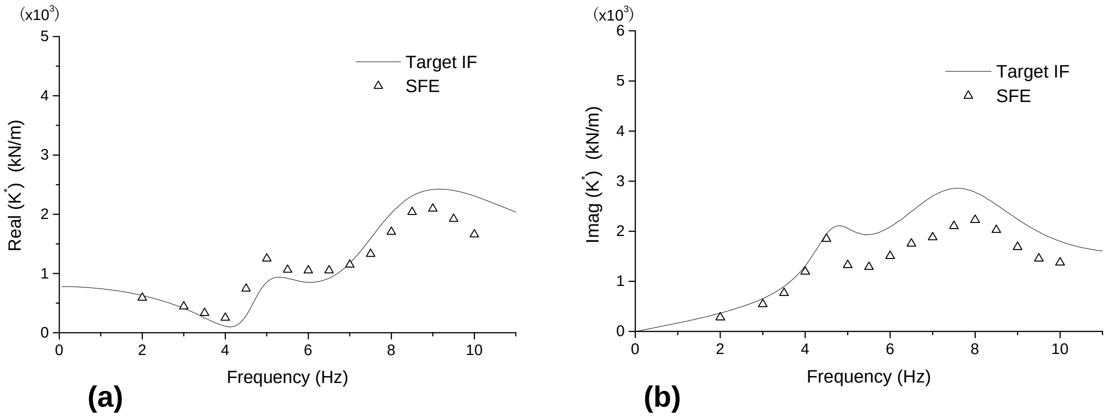

Figure 5. Impedance characteristics of SFE. (a) Real part, and (b) Imaginary part

4 CONCLUTIONS

This study presents a mechanical soil-foundation emulator (SFE) constructed based on gyro mass lumped parameter models. The experimental results show that the impedance characteristics of the SFE are in fairly good agreement with the target impedance functions.

5 REFERENCES

Meek, J. W. & Veletsos, A. S. 1974. Simple models for foundations in lateral and rocking motion. *Proc., 5th World Conf. on Earthquake Engrg.,* 2: 2610-2613.

Wolf, J. P. & Somaini, D. R. 1986. Approximate dynamic model of embedded foundation in time domain. *Earthquake Engrg. & Struct. Dyn.* 14: 83-703.

Nogami, T. & Nonagai, K. 1986. Time domain axial response of dynamically loaded single piles. *J. Engrg. Mech.*, ASCE 112(11): 1241-1252.

Nogami, T. & Konagai, K. 1988. Time domain flexural response of dynamically loaded single piles. *J. Engrg. Mech.*, ASCE 114(9): 1512-1525.

Wolf, J. P. 1994. Foundation vibration analysis using simple physical models. Eaglewood Cliffs, NJ, Prentice-Hall.

Wolf, J. P. & Song, C. 2002. Some cornerstones of dynamic soil-structure interaction. Engrg. Struct. 24: 13-28.

Saitoh, M. 2007. Simple model of frequency-dependent impedance functions in soil-structure interaction using frequency-independent elements, *Journal of Engineering Mechanics*, ASCE 133(10): 1101-1114.

Kaynia, A., & Kausel, E. 1982. Dynamic stiffness and seismic response of pile groups. *Research Report, R82-03, Dept. of Civil Engrg.,* MIT, Cambridge, Mass.

ACKNOWLEDGEMENTS

This paper is based on the work supported by the ministry of Education, Culture, Sports, Science and Technology, Japan, under Grant-in-Aid for Young Scientists (A) No. 20686031. Any opinions, findings, conclusions or recommendations expressed in this material are those of the author and do not necessarily reflect the views of the sponsors.

Demand spectra for PBD in case of improved soils, existence of basements and shallow underground cavities

K. Pitilakis, K. Trevlopoulos & G. Tsinidis
Department of Civil Engineering, Aristotle University of Thessaloniki, Greece

ABSTRACT: The main objective of this paper is to highlight the variation of the “design” input motion compared to the free field seismic motion, due to the presence of basements, soil improvement and the presence of underground cavities at shallow depth. The input motion is expressed in terms of demand spectra that are employed in performance-based methods. To this end, two – dimensional finite analyses of coupled SFS systems aroused, where the structure is simulated as a single degree-of-freedom system on a rigid foundation. For the case of soil improvement two examples are presented: reinforcement with stone columns and a new alternative approach with granular columns of sand-rubber mixture instead of pure grave. For the underground cavities case two examples are presented inspired from site conditions found in Abu Dhabi. The effect of the partial embedment of the structure on the seismic load is also presented. For all cases the “design” demand spectra are compared to the spectra for free field conditions. SFS interaction, soil improvement and the presence of cavities or basements affect the effective fundamental period of the system and the frequency content of the foundation motion which may result in a favorable or unfavorable effect on the global seismic performance of the system.

1 INTRODUCTION

It is quite common in engineering practice to ignore, for sake of simplicity, several parameters that may affect the seismic input motion. In the majority of the cases the “design” input motion is considered to be identical to the seismic input motion for free field conditions. However, it is known that parameters such as: soil improvement, presence of underground cavities or existence of basements in a structure, may cause the “design” input motion to vary in comparison to the free field input motion.

1.1 *Soil improvement*

Soil improvement is often employed in order to improve foundation ground conditions under static loads by increasing the strength of the soil and reducing its deformability. There are various techniques applied in construction practice such as dynamic compaction, deep compaction, construction of stone columns etc. The later has a beneficial effect to soil drainage as well. As mentioned, the free field motion of the original soil without any improvement is not the same with the motion of the foundation of a structure on improved ground. However this hypothesis is the basis of common engineering practice. A structure on improved soil is designed as if it was founded on the initial non-improved soil.

When a structure is founded on improved soil its seismic response may be significantly affected by the modification of soil properties. Recent studies on this subject (Kirtas & Pitilakis, 2009 and Pitilakis et al., 2010) proved that soil reinforcement combined with soil-foundation-structure interaction effects may modify significantly the foundation input motion and the structural response. The most important conclusion of Kirtas & Pitilakis, 2009 and Pitilakis et al., 2010 is that the modification of the foundation ground is not always beneficial for the seismic response of the structure and it may be in several cases on the detrimental side.

A few representative results showing the essentials of these remarks are given in Figures 1 and 2. In Figure 1, the ratio of acceleration amplitude at the foundation and superstructure level, before and after soil-stiffening is presented, for an increase of 10 times of the initial shear modulus G_0. The results are parameterized as a function of the normalized mass ratio (m_{norm}). Figure 2 presents the same results parameterized as a function of the normalized height ratio h_{norm}, (height to foundation half-width ratio). In both cases the intervention is applied in typical ground types of EC8 (soils B and C) (CEN, 2004). It is shown that for certain combination of the predominant period of the input motion and normalized height or mass of the superstructure, soil stiffening may have a clear detrimental effect on the structural response. In any case the design input motion is significantly modified compared to the original soil conditions without any intervention.

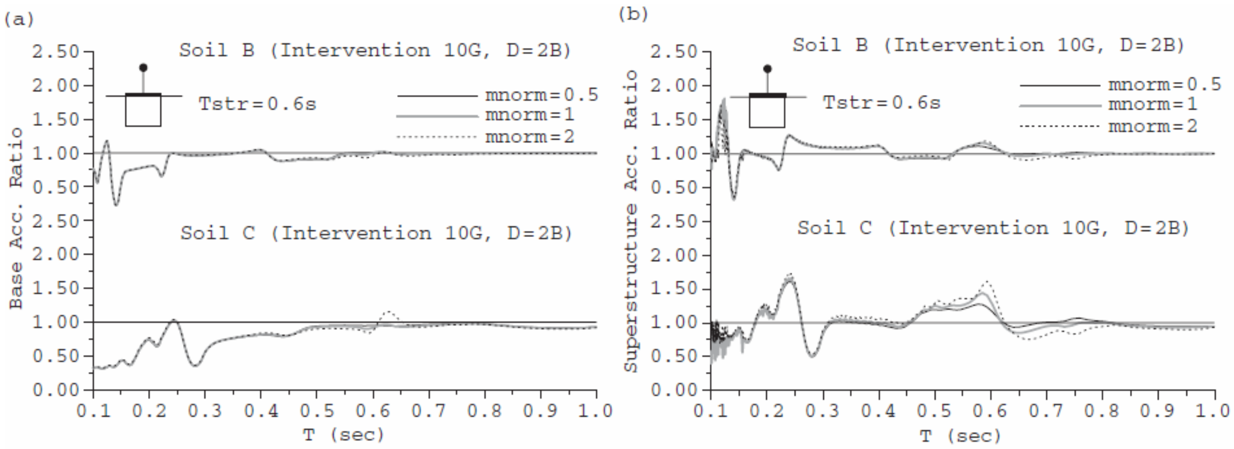

Figure 1 Ratio of the FFT amplitude of acceleration of (a) the foundation and (b) superstructure in the case of the soil-stiffening intervention to the corresponding amplitudes in the case of the system on the original soil (Kirtas & Pitilakis, 2009).

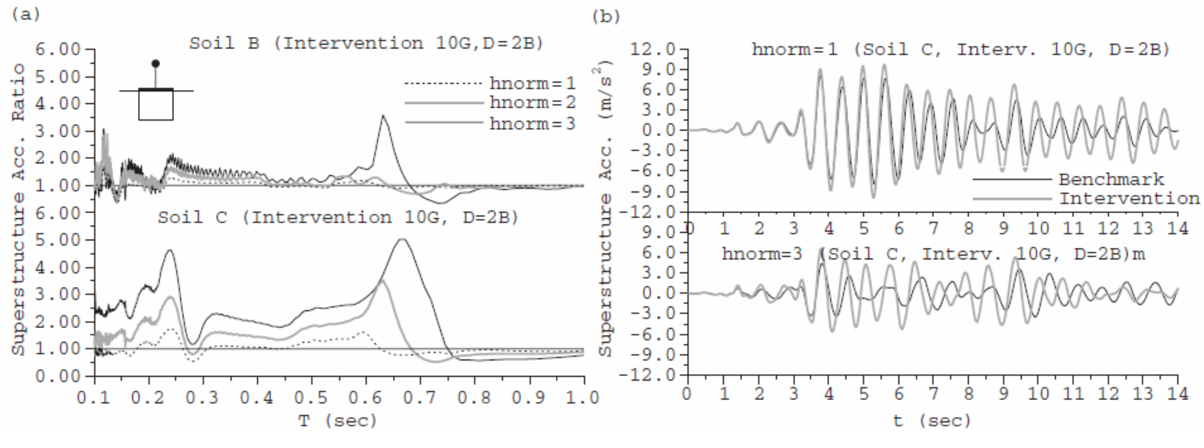

Figure 2 (a) Ratio of the FFT amplitude of acceleration of the superstructure in case of the soil-stiffening intervention to the corresponding amplitude in the case of the system on the original soil (Kirtas & Pitilakis, 2009).

Based on these introductory remarks, in this paper we elaborate further the subject in the case of two intervention techniques. The first one is the classical "stone column" method while the second one is a newly introduced method, partially by the authors, which consists of replacing the traditional stone column material with a sand-rubber-mixture (SRM). This composite material, where the rubber part is made by chips of recycled tires, may be seen as an alternative foundation isolation material, introducing additional damping in the soil-foundation-structure system, (Tsang, 2008, Senetakis et al. 2009). Of course it remains always a stone column technique appropriate for soil reinforcement and drainage. Both types of intervention have a reinforcing character and drainage effect. In the present paper it is proposed to study their effect on the dynamic response of soil-foundation-structure (SFS) systems.

For simplicity we selected a simple single degree-of-freedom (SDOF) structure for the improved-soil-foundation-structure system. By comparing the seismic performance of the coupled soil-structure system founded (i) on the original soil (type D according to EC8) and (ii) on the improved soil using the two aforementioned types of reinforcement, the effect of stone column and the alternative SRM technique on the response of the structure, is studied, representing in this case a bridge pier. SRM is considered as an alternative construction material offering probably an interesting solution to the seismic response of structures.

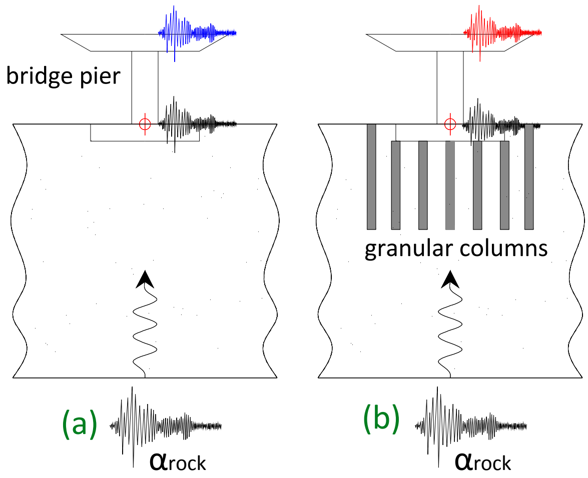

Figure 3 Typical sketch of a single degree-of-freedom structure (i.e. bridge pier) on soft soil (e.g. ground type D of EC8) with and without soil improvement with SRM or stone columns.

1.2 *Effect of underground cavities*

Large soft rock or rock cavities underlying soil deposits may affect the seismic ground motion at surface modifying amplitude and/or frequency characteristics. This potential modification of the input motion may affect the seismic response of a structure. Wave propagation theory suggests that the influence of cavities may be significant in case of large cavity dimensions in comparison to the wavelengths of interest. However, the problem studied herein refers to cases of small underground cavities that are close to the surface, which is a quite common case in some site all over the world. In a certain degree it should be seen as the effects of tunnels at relative shallow depths to the seismic response of buildings on the ground surface.

To this end, four cases are studied: (a) free field, (b) structure and free field conditions, (c) free field with the presence of cavities (d) cavities and structure (Figure 4). For each case, the effects of the parameters affecting the input motion is highlighted by comparing the demand spectra of the foundation/input motion of each case to each other, and compare them with the free field case. In all the cases for simplicity, the structure is a SDOF structure with rigid foundation.

1.3 *Existence of basements (embedded structures)*

Typically the aboveground structures are actually embedded to a certain depth through basements, which may affect the “design” input motion (Figure 5) and the dynamic behavior of the structure. These modifications, regarding on input motion and structure’s behavior are presented with two simple examples. As in the previous cases, the structure is simplified SDOF structure.

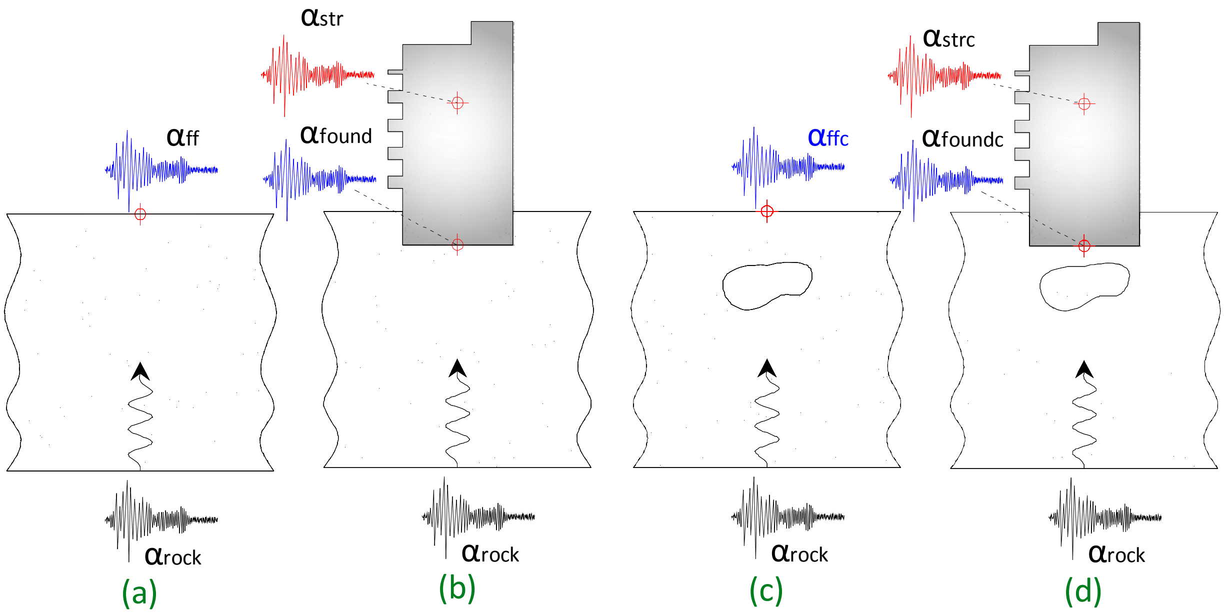

Figure 4 Effect of underground cavities on the input motion – study cases (a) free field, (b) structure, (c) cavity, (d) cavity – structure

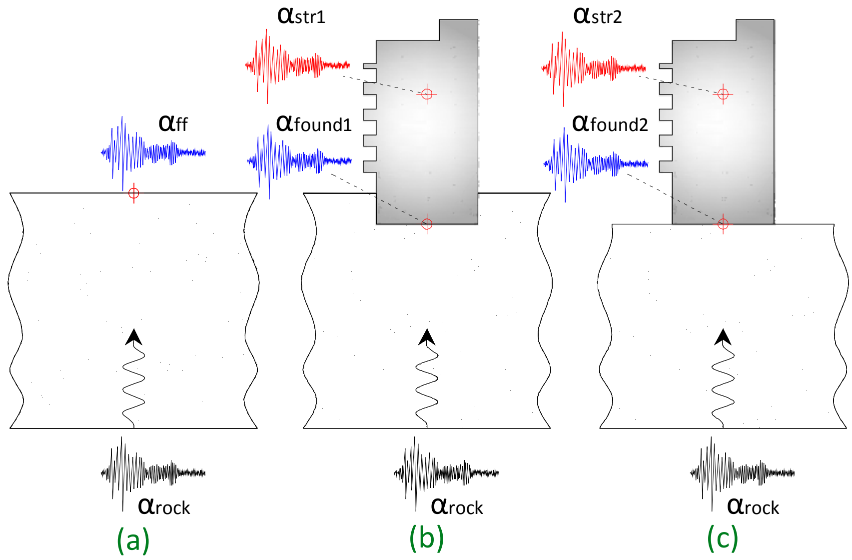

Figure 5 Effect of the basement on the input motion – study cases (a) free field, (b) partial embedded structure, (c) above ground structure

We focus on the study of potential modification of the demand spectra, and performance points in the capacity spectrum method, which are used in the performance-based design of structures. The general idea is inspired by Pitilakis, D. and Karatzetzou, A. (2011).

2 DESCRIPTION OF MODELS - CASE STUDIES

2.1 *Soil improvement*

For the study of the soil-foundation-structure system in case of soil improvement, dynamic analyses in frequency domain are performed. A set of configurations, summarized in Figure 6 is employed. The analyses are performed with the general purpose finite element code ANSYS (ANSYS, 2009) under plain strain conditions. A sketch of the models is also presented in Figure

6. The selected structure is a single degree-of-freedom system founded on a rigid foundation. The width and the depth of the improved soil with stone or SRM columns are 15m. The dynamic response of the system is studied for vertically propagating horizontally polarized shear waves emanating from the rigid bedrock at a depth of 30m. The parameters of the system considered herein are shown in Figure 6 including the normalized mass ratio (Wolf, 1985) given by Equation 1 and adapted for plane-strain conditions via Equation 2. The values for the mass of the structure ($m_{structure}$) and the natural period of the SDOF for fixed-base conditions (T_{fixed}) have been adopted from the parametric study in (Mylonakis et al., 2006). In Figure 6 d_{column} is the diameter of the stone or SRM columns, s is the distance between column centers and A_r is the replacement ratio of the initial soil.

$$m_{norm} = \frac{m_{structure}}{\rho \times \alpha^3} \quad (1)$$

$$m_{norm} = \frac{2 \times B \times m_{plstr.}}{\rho \times \alpha^3} = \frac{2 \times m_{plstr.}}{\rho \times B^2} \quad (2)$$

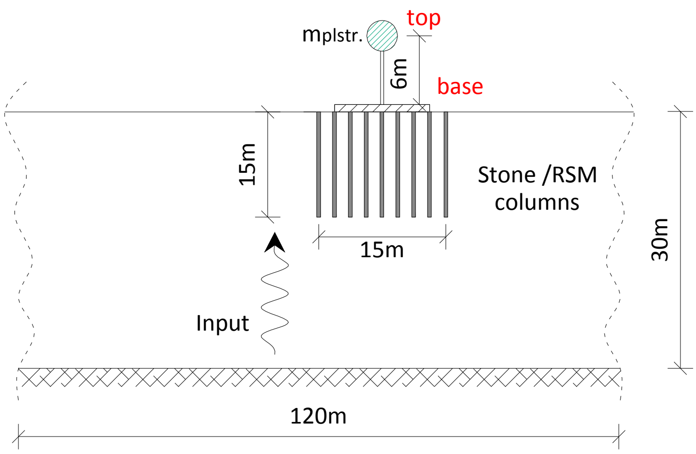

Case	SRM Col.	Stone Col.	Structure
1			
2			√
3	√		
4	√		√
5		√	
6		√	√

Parameter	Values
$m_{structure}$ (kg)	$3.5 \cdot 10^4$ kg
m_{norm}	3.0
T_{fixed} (s)	0.53
$d_{columns}$ (m)	0.9, 0.7, 0.6
s (m)	3.0, 1.5, 1.0
A_r (%)	7, 17, 31
d' (m)	0.5

Figure 6 Configurations of the plain strain model – parameters of the system

The diameter of the stone and SRM columns was modified to an equivalent diameter to account for the transition of the problem from three to two dimensions (Papadimitriou et al., 2006). The entire soil profile was modeled with 4-node plain strain finite elements, whose dimension is smaller than the 1/12 of the smallest wavelength of engineering interest. This ensured that the high end of the frequency spectrum would not be "filtered" due to sparse soil discretization according to (Kuhlemeyer & Lysmer, 1970).

The foundation and the super-structure were modeled with beam elements, which had common nodes with the 4-node soil elements (no interface elements), thus forbidding any relative movement between the structure and the soil (e.g. uplift or slide).

The nodes of the lower and side boundaries were fixed in the vertical direction while the side boundaries were placed far enough from the structure, in order to minimize their influence on the dynamic behavior of the central part of the model.

The amplitude and phase angles of the output time history result from the multiplication and addition respectively of the input with the amplification and phase difference of the transfer function (with the phase difference being the argument of the complex number at each frequency step, Figure 7). Then, the output amplitude and angle are transformed into the output time history via an inverse FFT.

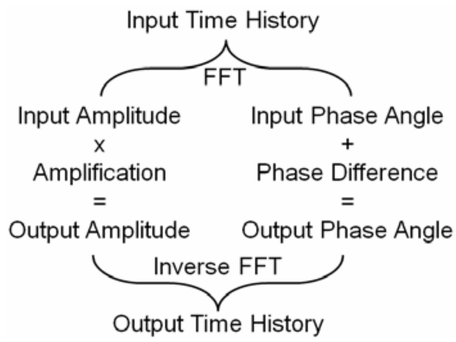

Figure 7 Diagram of the output time histories calculation procedure

The selected soil profile corresponds to soil class D according to EC8 (CEN, 2004). The G-γ-D curves of the initial soil profile were selected according to (Ishibashi & Zhang, 1993) for an average confining pressure of 200 kPa. The SRM curves correspond to a 85/15 (sand/rubber) ratio per weight mixture at a mean effective stress of 100 kPa (Senetakis, 2011).

The G-γ-D curves used for the description of shear modulus degradation and damping increase with shear strain are given in Figure 8 for the original soil (according to Ishibashi & Zhang, 1993) and sand-rubber mixture. The soil parameters (i.e. shear modulus G(γ) and material damping D(γ) used in the 2D dynamic analysis, were estimated through an 1D equivalent linear analysis with the code EERA (2000), which provides the corresponding strain levels (γ) for the selected input motion at the seismic rock basement. With an average shear strain γ equal to 0.25%, (PHGA = 0.46g at z = 0.0 m), the effective shear modulus is about the 50% of the initial one, while the effective average damping is almost equal to 13%. The shear modulus and damping ratio of the last iteration are approximately constant in the lowest 20 m of the soil profile. This makes the selection of uniform properties for the 2D model an approximation of reasonable consistency. We assumed that the SRM columns undergo equal strains with the original material as suggested by Baez & Martin (1993 in Schaefer, 1997). The SRM material for the same level of shear strain (i.e. 0.1%) presents some very interesting features: almost three times higher shear modulus and 50% higher damping. Its G-γ-D curves resulted from resonant column measurements (Senetakis, 2011) and its maximum shear modulus was adjusted to a higher value according to (Darendeli, 2001) to take into account the correlation between laboratory and field measurements.

So the SRM column system besides its contribution to the system introducing extra damping, also offers a considerable reinforcing effect. This is how we perceive SRM as an alternative material for stone column construction; a trade-off of stiffness and - to a lesser degree - of shear strength (even though we must note that the SRM columns remain stronger than the original soil) for additional damping. Further details on SRMs may be found in the literature (Edil, 2004, Zornberg et al., 2004, Lee et al., 1999).

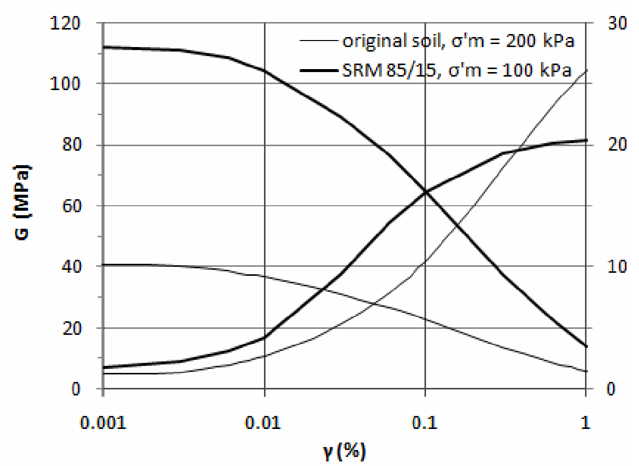

Figure 8 Shear modulus degradation and damping ratio increase with shear strain for the original soil (Ishibashi & Zhang, 1993 and the SRM material (Senetakis, 2011).

Assuming that the level of shear strain of the SRM columns is equal to that for the original soil, which was estimated with the 1D equivalent linear analysis, we selected the damping ratio to be used in the 2D models for each material from the damping curves in Figure 8.

These values are shown in Table 1 along with the shear wave velocity, the ratio of the reduced shear modulus ratio and the deformability contrast between the columns and the soil.

As input motion the N-S component of the acceleration record at the Tolmezzo-Diga Ambiesta station from the 1976 Friuli earthquake (Ambraseys et al., 2004) scaled down from 3.5 to 3.0 m/s^2 peak acceleration was used. Base-line correction and a fourth order 0.25-25.0 Hz Butterworth band pass filter were applied in Seismosignal (Seismosoft, 2011).

Table 1 Shear wave velocity, damping and moduli ratios for the materials in the 2D models

	V_S (m/s)	G/G_{max}	$G/G_{soil\ D}$	d (%)
Original soil (EC8 type D)	150	0.47	1.0	14
SRM	276	0.50	3.0	20
Stone columns	440	0.50	10.7	10

2.2 *Underground cavities*

The set of configurations of the SFS finite element models used for the study of the effect of underground cavities is presented in Figure 9 and Table 2. They are both inspired from conditions found in Abu Dhabi. The analyses are performed with the general purpose finite element code ABAQUS (2009) under plain strain conditions (Figure 9). As in the previous case, the soil was modelled with 4-nodded plain strain finite elements with sufficiently small dimension. Both the foundation and the super-structure were modeled with beam elements. No interface elements were used between soil and foundation elements. To this end, perfect bonding was considered. The same boundaries as in the previous case (soil improvement) were incorporated.

The soil properties are presented in Figure 9, while the assumed structure mass and its period ignoring the SFS interaction is tabulated in Table 3. Linear elastic behavior for the structure, the foundation and soil was assumed.

The E-W component of the acceleration record at the TRA station from the 1979 Montenegro earthquake (Ambraseys et al., 2004) scaled down from 2.0 to 0.5 m/s^2 peak acceleration was utilized as input motion. The motion introduced at the model's base.

Table 2 Cases studied herein

#	Case A	Case B	Cavity - Cavities	Structure
1	√			
2	√		√	
3	√			√
4	√		√	√
5		√		
6		√	√	
7		√		√
8		√	√	√

Table 3 Structure characteristics

Parameter	Values
$m_{structure}$ (kg)	25 x 10^4 kg
T_{fixed} (s)	0.40

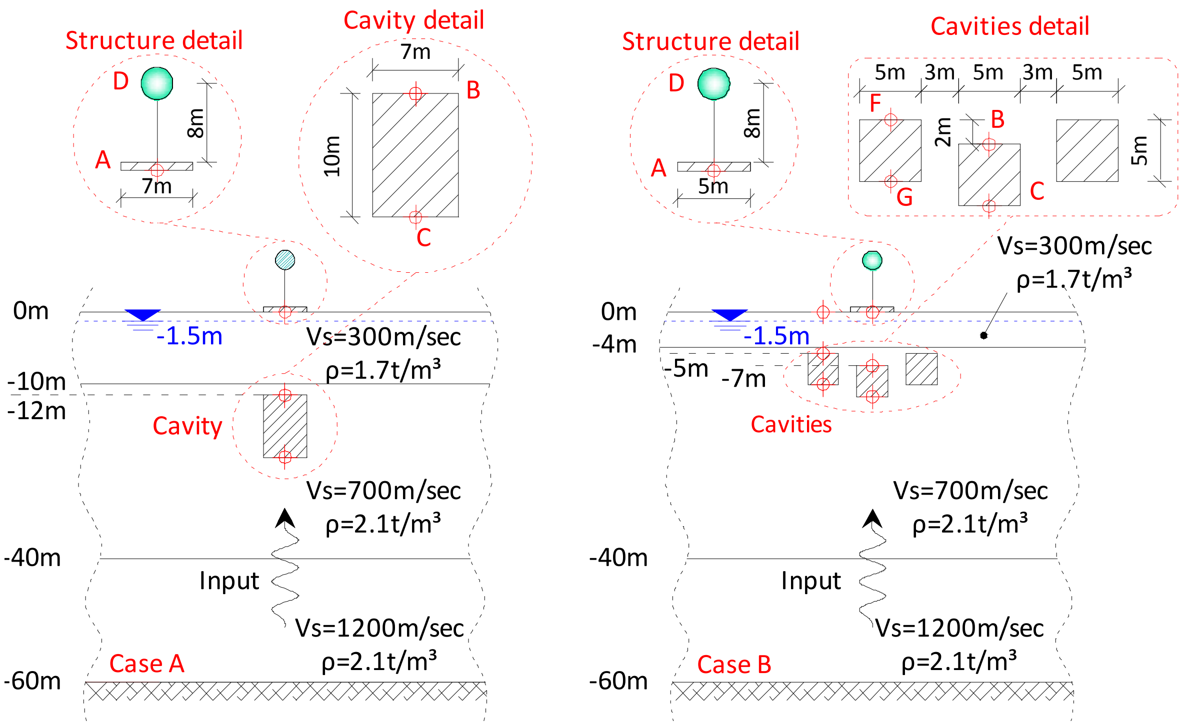

Figure 9 Configurations of the plain strain models used to study the effect of the underground cavities on the input motion, left: Case A, right: Case B.

2.3 *Basement*

For the study of the soil-foundation-structure system in the case of structures with basement, dynamic analyses in the time domain are performed. A set of configurations, summarized in Figure 10 is employed. The analyses are performed with ABAQUS under the same assumptions as in the case of cavities existence. It is noted that the beam elements simulating the underground basement, are considered as rigid. The soil properties are presented in Figure 10. Equivalent linear analyses are performed with the code CYBERQUAKE (Modaressi & Foerster, 2000) to incorporate in a simplified way the soil non – linear behavior. The procedure is analytically described in the case of studying the soil improvement.

The N-S component of the acceleration record at the Tolmezzo-Diga Ambiesta station from the 1976 Friuli earthquake (Ambraseys et al., 2004) scaled down from 3.5 to 2.0 m/s^2 peak acceleration was utilized as input motion.

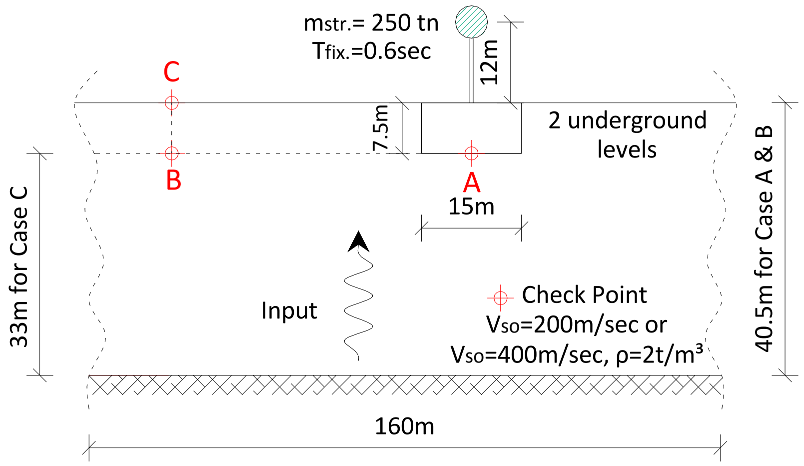

Case	Embedment	Structure
A		
B	√	√
C		√

Figure 10 Configurations of the plain strain models – study of the basement existence to the input motion.

Seismic performance of the structure, taking into account SFSI phenomena and the influence of the parameters studied herein via the coupled analyses, may be estimated with various methods; the Capacity Spectrum Method (ATC, 1996, Freeman, 1998, Fajfar, 2000) is one of the most popular.

The maximum acceleration and displacement of the superstructure, for each particular system and seismic excitation, result from the intersection of the demand spectrum of the foundation motion with the capacity curve of the SFS system. In this study the structure is assumed to be linearly elastic, therefore their capacity curves are merely lines which correspond to the effective period of the soil-foundation-structure system. Further details of this procedure may be found in (Pitilakis, D. and Karatzetzou, A. 2011). Here we present and discuss mainly the computed demand spectra and performance points of the compliant systems.

3 RESULTS

3.1 *Amplification*

- Soil improvement

Figure 11a presents the free field amplification ratio for the initial (U_{ff}) and the improved soil profiles (U_{impr}) with stone columns and SRM columns, with a replacement ratio of A_r = 31%. Figure 11b compares U_{ff} with the amplification ratio computed between the rigid bedrock and the foundation of the structure for the cases of stone and SRM columns. The first mode of the ground response under free field conditions remains practically unaffected by the ground improvement interventions. The same is observed when the model includes the structure. The amplification of the ground motion is reduced at higher frequencies, and the reduction is higher when the model includes the structure, which must be attributed to soil-structure interaction.

Figure 11c presents the U_{top}/U_{ff} ratio for the three cases studied herein, where U_{top} is the amplification ratio of the uppermost node of the structure. Note that it may be difficult discerning the effective period of SFS systems with low eigenperiods on soft soils (Kirtas et al., 2007). The effective frequency of the original SFS system is shifted from 1.46Hz to 1.56 and 1.61 Hz for the systems that include stone and SRM columns respectively.

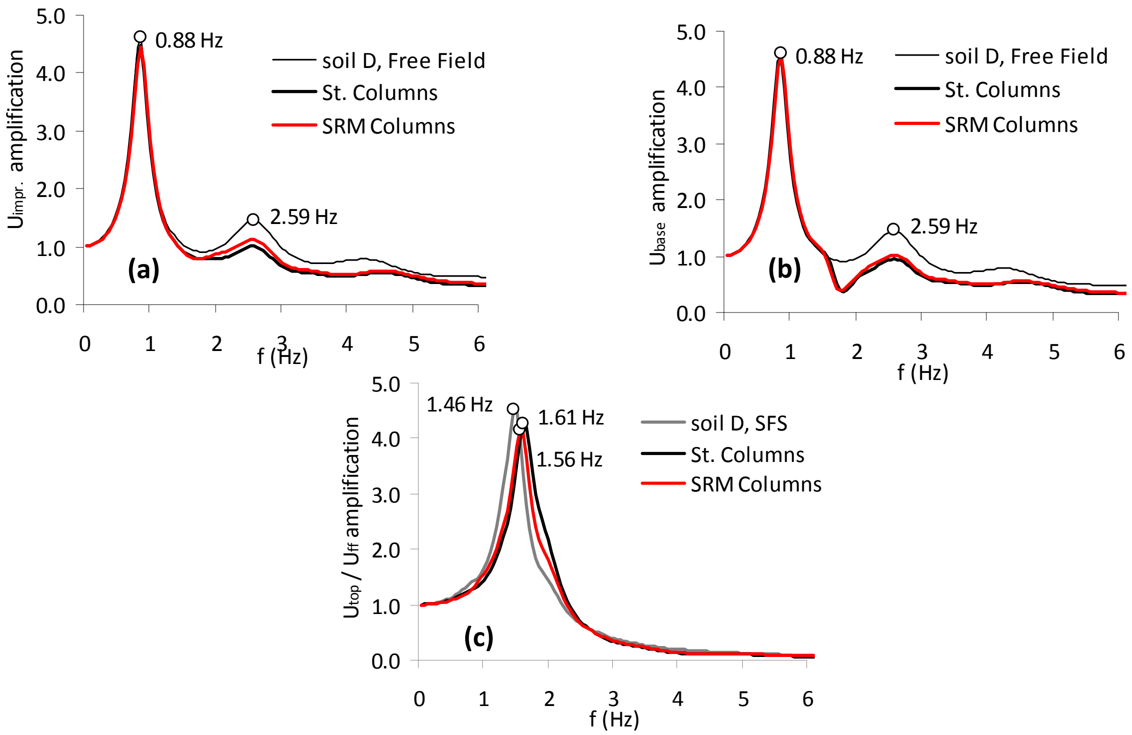

Figure 11 (a) Free field amplification ratio for the initial (U_{ff}) and improved soil profile (U_{impr}) with stone and SRM columns (A_r = 31%) (b) Amplification ratios at the middle of the foundation, U_{base} for the initial soil and the modified soil cases (c) Soil-foundation-structure system amplification ratio and effective frequencies on the original soil and on the improved soil.

- Underground cavities

Figure 12a compares the amplification ratio computed between the rigid bedrock and the foundation of the structure (Point A, Figure 9) for the all cases of the test case B (3 cavities). The first mode of the ground response under free field conditions remains practically unaffected by the existence of both the structure and the cavities. The amplification of the ground motion is increased at higher frequencies with the presence of the cavities. Finally the existence of the structure seems to slightly reduce the increase of the amplification (due to the cavities) in higher frequencies.

In Figure 12b the U_{top}/U_{ff} ratio for the cases studied is presented. The structure effective frequency is not modified.

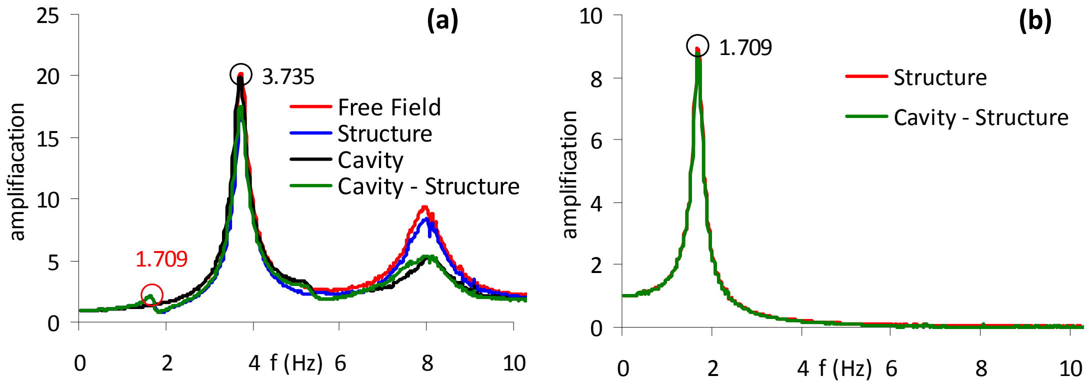

Figure 12 (a) Amplification ratios at the middle of the foundation for the cases studied (b) Soil-foundation-structure system amplification ratio.

- Basement

Figure 13 presents the amplification ratio computed between the rigid bedrock and the foundation of the structure (Point A, Figure 10). The existence of the rigid walls of the basements seems to slightly reduce the first and second resonant frequencies.

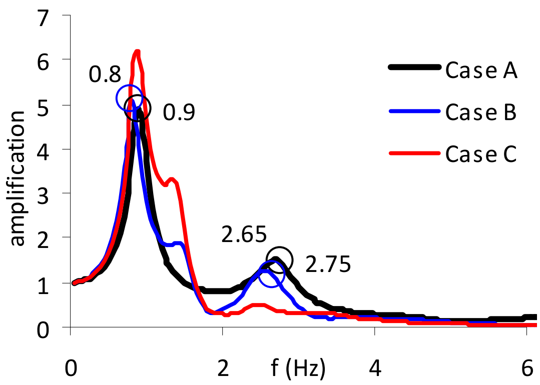

Figure 13 Amplification ratios at the middle of the foundation for the cases studied.

3.2 *Demand spectra – performance assessment*

- Soil improvement

Figure 14 presents the demand spectra calculated at the ground surface for the original soil and the two improved cases with stone column and SRM columns, under free field conditions. The improved soil presents a clearly lower seismic demand especially in short periods. In particular for the fixed base structure period (T_{fixed} = 0.53s), which should be used in the initial estimation of the seismic performance without considering SFSI effects, the acceleration is reduced from 6.0m/sec^2 to 5.0m/sec^2 and 5.3m/sec^2 respectively. The differences between the two improved soil cases are not very important, at least for the input motion used in this study.

The calculated demand spectrum of the compliant system in the case of the original soil is shown in Figure 15. It was calculated using the computed time histories of the motion at the center of the foundation. According to Pitilakis, D. and Karatzetzou, A., (2011), in the case of a compliant structure the demand spectrum has no meaning as a whole, but only for the period of the specific compliant system under study. So, only one point is of interest; the intersection of the spectrum with the line corresponding to the fundamental period of the compliant system (i.e. T = 0.68 s). The difference between that point (0.047 m, 4.0 m/s^2) and that for the fixed base structure (0.043 m, 6.0 m/s^2), which was assessed using the original demand spectrum, is 150% in terms of acceleration.

Figure 16 shows the performance points of the original compliant system studied here, and the improved cases. It is reminded that the fundamental period of the fixed base structure and the three other cases (original soil, stone columns and SRM columns with A_r=0.31%), are 0.53s, 0.68s, 0.62s and 0.64s respectively. The stone columns and the SRM columns have both a beneficial effect on the seismic performance of the compliant system. Compared to the original soil we observe a reduction of 22% and 15% respectively in acceleration and 36% and 26% in displacements. However, the differences between the two improvement cases are not so important. Further research is needed to better understand and quantify the differences between conventional stone columns and SRM columns. SRM columns having higher damping should produce a more important decrease on the seismic demand and performance.

A general remark is that soil reinforcement, with stone column or other strengthening techniques may have, under certain circumstances, a detrimental effect on the seismic performance of compliant structures. The reason is that the fundamental period will be certainly decreased, as the compliance of the system is not in this case that important as for the original soft soil case, due to the soil strengthening.

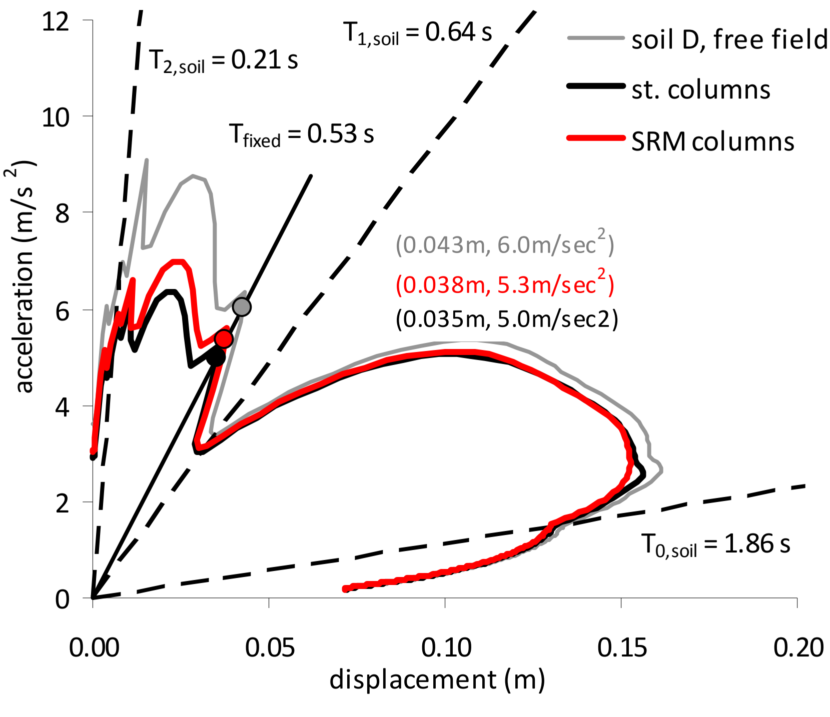

Figure 14 Calculated demand spectra at the ground surface of the initial soil and of the soil after improvement with SRM and stone columns (Ar = 31%). The first three eigen periods of the initial soil are shown for reference.

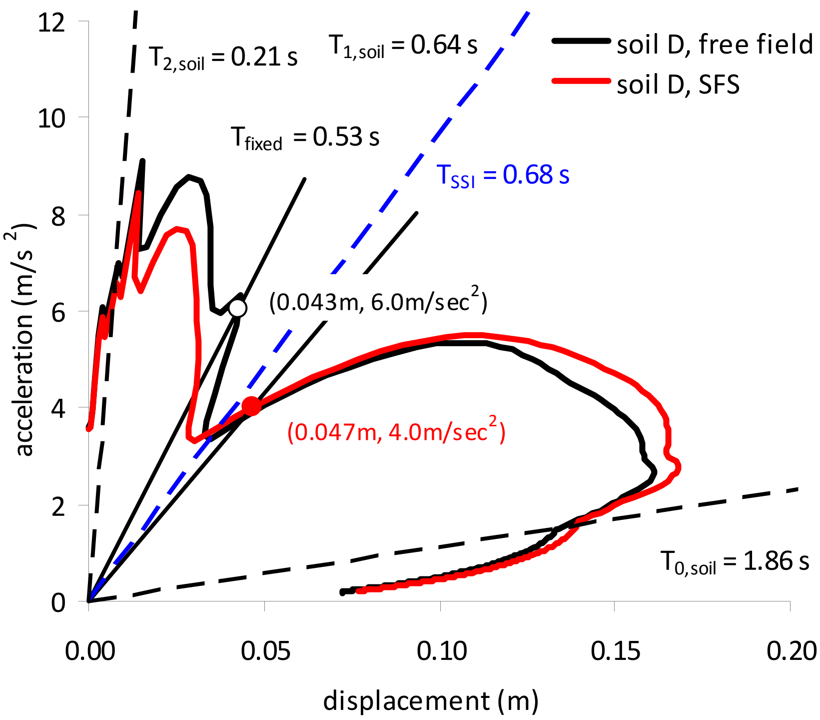

Figure 15 Demand spectra (free field conditions) of the original soil and the compliant system considering soil-foundation-structure interaction. The performance points are the intersection of the demand spectra with the corresponding capacity curves/lines for the fixed base (T=0.53s) and the compliant system (T=0.76s). The first three eigen periods of the initial soil are shown for reference.

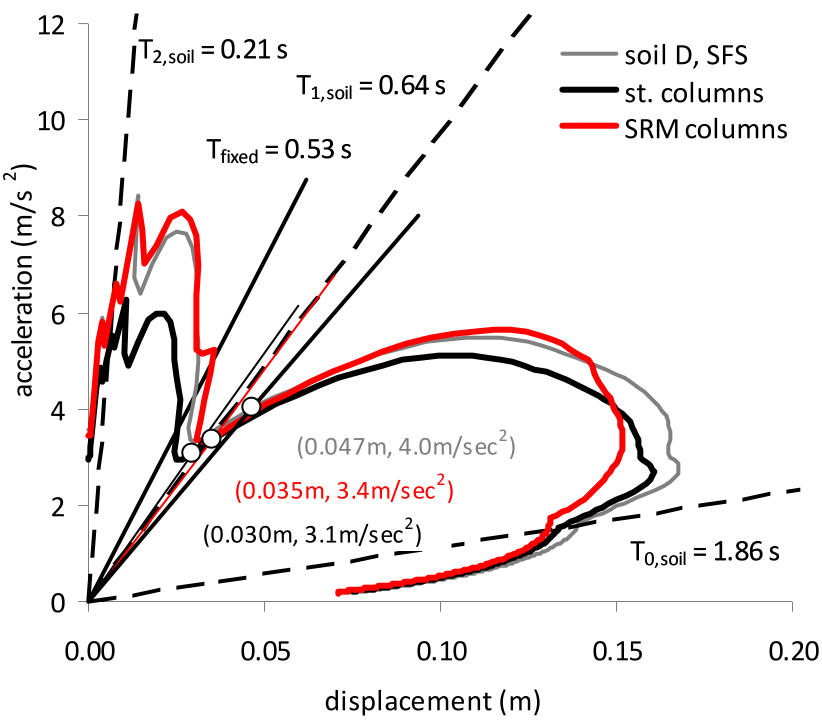

Figure 16 Performance points considering the compliant systems in the case of original soil and the two improved soil cases with SRM and stone columns (A_r = 31%). The first three eigen periods of the original are shown for reference.

• Underground cavities

Figure 17 presents the demand spectra calculated at the structure foundation (Point A), for the cases studied. The results refer to Case A (one cavity – Figure 9). For lower periods, the input motion tends to decrease in the cases where the structure or the cavity or both the structure and cavity exist, while for high periods we observe the opposite. It seems that the presence of the structure is affecting the input motion. The calculated performance points for the case of the structure studied herein, taking into account the SFSI (T_{ssi}=0.585s) are also depicted in Figure 17. The seismic load in terms of acceleration is not affected significantly, for this particular case.

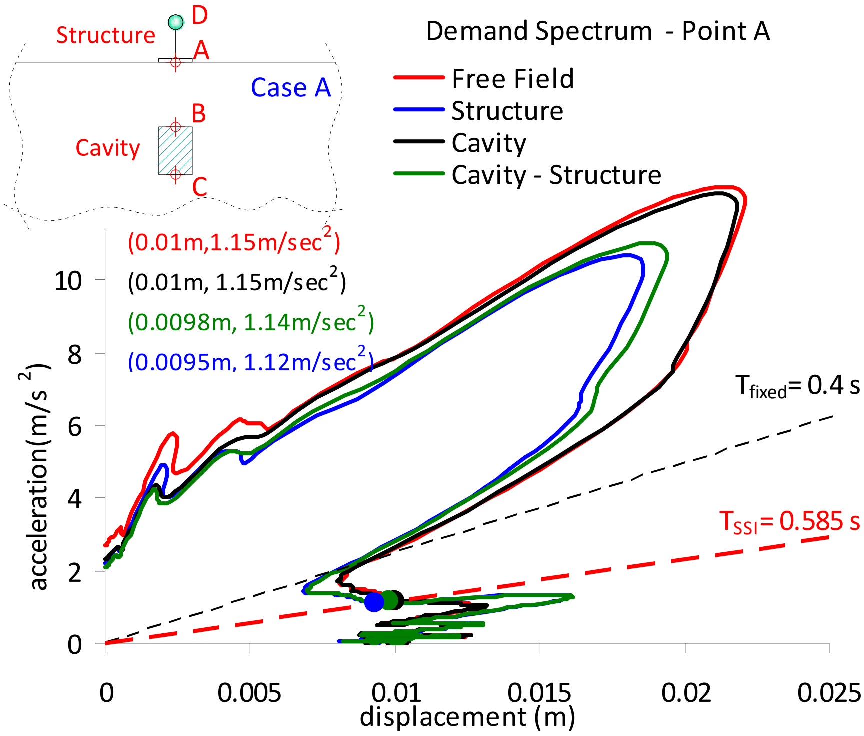

Figure 17 Demand spectra calculated for all cases of the test case A (one cavity). The performance points are the intersection of the demand spectra with the corresponding capacity curve for the structure considering the SFSI (T_{SSI}=0.585s).

Similarly, Figure 18 presents the demand spectra calculated at the structure foundation (Point A), for the cases studied, referring to Case B (three cavities – Figure 9). Again the existence of the structure is affecting the design “input” motion. It should be noted that the existence of the cavities without considering the structure amplifies the input motion, for lower periods the seismic load with respect to the free field.

• Embedment - Basement

Figure 19 presents the calculated demand spectra at structure foundation (Point A), for the three test cases studied herein. It seems that the existence of the basements reduce the seismic load of the structure in respect with the free field conditions. This reduction is attributed to the strong SFSI effects. The calculation of the performance points, for the compliant system, reveal this reduction of the seismic load, which for this case, is up to 24.7% in terms of displacement and up to 25.6% in terms of acceleration. The affection of the partially embedment of the structure is also depicted. The partial embedment seems to decrease the “design” input motion for higher periods, while for lower periods the opposite is observed.

Figure 20 presents the calculated demand spectra at the surface close to the structure (Point C) for the cases studied here. The comparison indicates that the existence of the basements of the structure can affect, as expected, the input motion of a neighbouring structure. In this case reduction of the input motion (in respect with the free field) is observed.

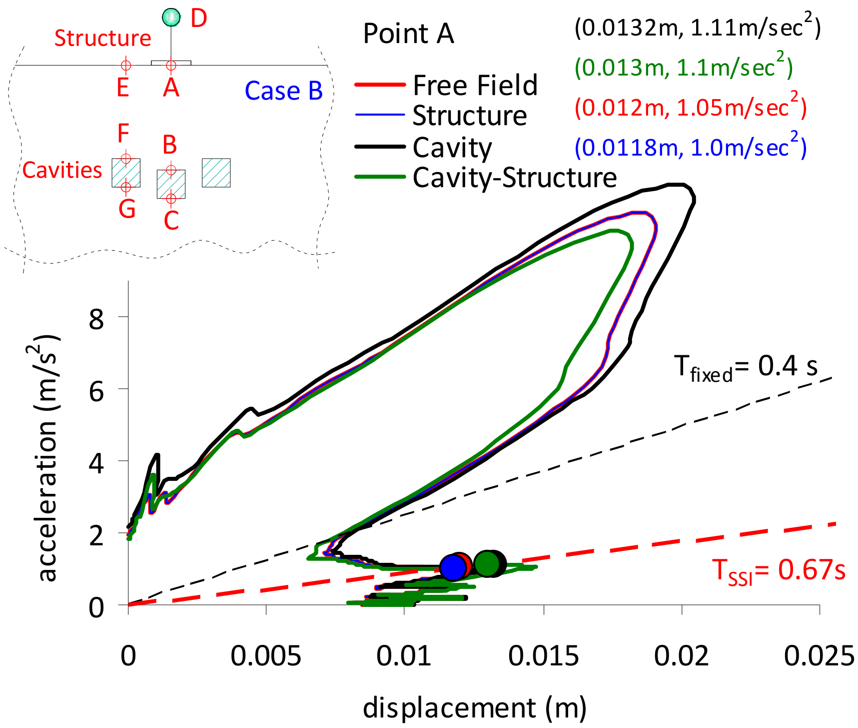

Figure 18 Demand spectra calculated for all cases of the test case B (three cavities). The performance points are the intersection of the demand spectra with the corresponding capacity curve for the structure considering the SFSI (T_{SSI}=0.67s).

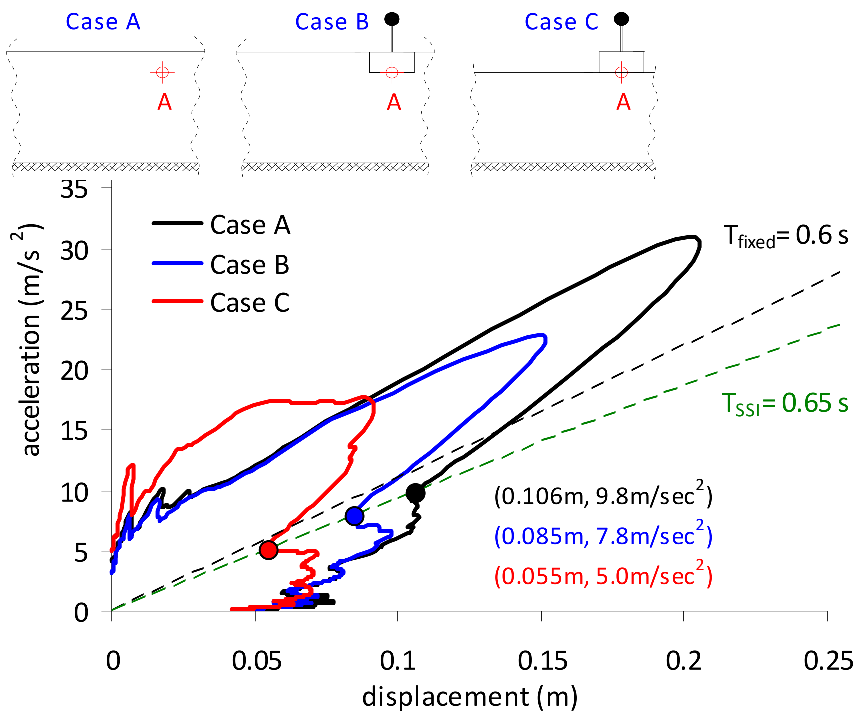

Figure 19 Demand spectra calculated at structure foundation (Point A) for the cases studied herein. The performance points are the intersection of the demand spectra with the corresponding capacity curve for structure considering the SFSI (T_{ssi}=0.65s).

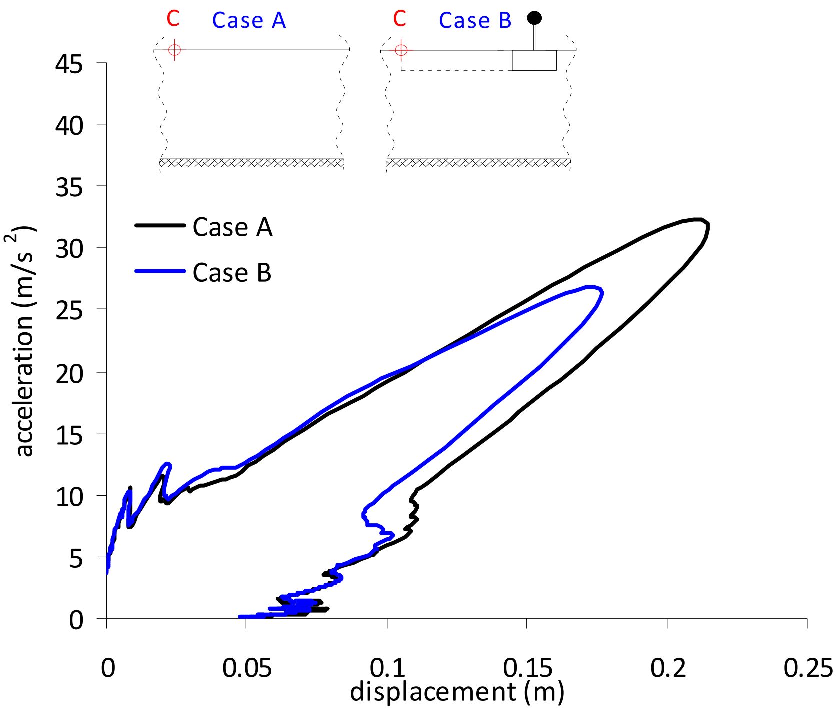

Figure 20 Demand spectra at the surface near the structure (Point C) calculated for the cases studied herein.

4 CONCLUSIONS

The effects of several aspects, such as: soil reinforcement and ground improvement, existence of underground openings and the structure's embedment (basement) on the "design" input motion has been discussed in this paper, through several examples. In all cases the structures were simplified as SDOF structures on rigid foundation, subjected to specific earthquake records.

- Soil improvement

The "design" demand spectra in the case of improved soil conditions is different from the original soil conditions, i.e., without any improvement. Moreover, SFS interaction and soil improvement affect the global response and the effective fundamental period of the coupled system, . While soil reinforcement reduces - as expected - the effective period of the SFS system, it may simultaneously have a favorable or unfavorable effect on the global seismic performance of the system. This is expected to be more important for high frequency structures.

The alternative technique presented herein with mixtures of sand-rubber stone columns instead of conventional stone columns, is a new attractive approach, which may have favorable effects on the seismic response of structures. Further research is needed to this point in order to be applied in engineering practice.

- Underground cavities

From the simplified study presented above it is concluded that the existence of small dimensions shallow cavities (or tunnels of moderate diameter i.e. 5-7m) is not affecting significantly the design input motion of the structures on the ground surface. As it was expected form the basic wave propagation theory the influence of cavities should be important in case of cavities of very large dimensions. The seismic input motion is again reduced due to soil-structure interaction effects.

- Basement

The results of the case studies presented herein indicate that the existence of basements in a structure (embedded structures) can reduce considerably the design input motion – in terms of demand spectra- with respect to the free field conditions.

It should be noted that the conclusions derived herein, especially in case of underground cavities and basements shouldn't be yet generalized, as these phenomena should further be investigated. However they indicate a clear tendency, which should be further investigated.

In conclusion, it has been demonstrated that the estimation of the design input motion need special attention. Design spectra proposed in seismic codes cannot be applied "per se". Several parameters such as: soil strengthening, existence of basements or underground cavities in relation to the compliance of the structure and the non-linear soil behavior, may have important effects on the final design values, which cannot be captured by the seismic code design spectra. Consciousness around these issues needs to increase, because as it has been shown the effects are not always favorable, regarding the seismic response of the structure, but under special conditions may be detrimental instead.

ACKNOWLEDGMENTS

Part of this work was performed in the framework of the European project "Performance-based approach to earthquake protection of cultural heritage in European and Mediterranean countries (PERPETUATE)", Grant agreement 244229.

The second author acknowledges the support by the Greek State Scholarships Foundation (www.iky.gr).

5 REFERENCES

A. Papadimitriou, A. Vytiniotis, G. Bouckovalas and Bakas (2006) Equivalence between 2D and 3D numerical analyses of the seismic response of improved sites, 6th European Conference on Numerical Methods in Geotechnical Engineering, pp 809-916, Graz, Austria, 6 - 8 September 2006

ABAQUS (2009) Analysis User's Manual – Volumes I - IV – v6.9 [Computer Program], Dassault Systèmes, SIMULIA Inc, USA

ANSYS, Inc., ANSYS (Version 11) [Computer Program] Available at: http://www.ansys.com (Accessed: March 2011).

ATC (1996) Seismic evaluation and retrofit of concrete buildings, Rep. ATC-40, Applied Technology

CEN - European Committee for Standardization (2004) Eurocode 8: Design of structures for Earthquake Resistance, Part 1: General rules, seismic actions and rules for buildings, EN 1998-1:2004, Brussels

D. Pitilakis and A. Karatzetzou (2011) Soil-foundation-structure interaction and demand spectra in the performance based design, EURODYN2011, 8th International Conference on Structural Dynamics, Leuven, Belgium, 4-6 July 2011

E. Kirtas and K. Pitilakis (2009) Subsoil interventions effect on structural seismic response. Part II: parametric investigation, Journal of Earthquake Engineering, Vol. 13, pp. 328-344

E. Kirtas, E. Rovithis and K. Pitilakis (2009) Subsoil interventions effect on structural seismic response. Part I: validation of numerical simulations, Journal of Earthquake Engineering, Vol. 13, pp. 155-169.

E. Kirtas, K. Trevlopoulos, E. Rovithis and K. Pitilakis (2007) Discussion on the fundamental period of SDOF systems including soil-structure interaction 4th International Conference on Earthquake Geotechnical Engineering, Paper No. 1692, Thessaloniki, Greece, 25-28 June 2007

EERA, Equivalent-linear Earthquake site Response Analysis (Version 2000) [Computer Program Add-in]. Available at: http://gees.usc.edu/GEES/Software/EERA2000/Default.htm (Accessed: March 2011).

G. Mylonakis, S. Nikolaou and G. Gazetas (2006) Footings under seismic loading: Analysis and design issues with emphasis on bridge foundations, Soil Dynamics and Earthquake Engineering, Vol. 26, pp. 824-853

H. Modaressi and E. Foerster (2000) CYBERQUAKE: User's manual [Computer Program], BRGM, Paris, France

H.-H. Tsang (2008) Seismic isolation by rubber-soil mixtures for developing countries, Earthquake Engineering and Structural Dynamics, Vol. 37, pp. 283-303

I. Ishibashi and X. Zhang (1993) Unified dynamic shear moduli and damping ratios of sand and clay, Soils and Foundations, Vol. 33, No. 1, pp. 182-191

J. Clinton, Geophysical Data Processing 2, ETH Zürich Department of Geophysics. Available at:

J. Lee, R. Salgado, A. Bernal and C. Lovell (1999) Shredded tires and rubber-sand as lightweight backfill, Journal of Geotechnical and Geoenvironmental Engineering, Vol.125, No.2, pp.132-141

J. P. Wolf (1985) Dynamic soil-structure interaction, Prentice-Hall, Englewood Cliffs, NJ

J. Zornberg, A. Carbal and C. Viratjandr (2004) Behaviour of tire shred-sand mixtures, Canadian Geotechnical Journal, Vol.41, pp.227-241

K. Pitilakis, A. Anastasiadis, D. Pitilakis, K. Trevlopoulos and K. Senetakis (2010) Elastic Demand Spectra, Advances in Performance-Based Earthquake Engineering, Geotechnical, Geological, and Earthquake Engineering, M. N. Fardis (ed.) Vol. 13, Pt. 1, pp. 89-99

K. Senetakis (2011) Dynamic properties of granular soils and mixtures of typical sands and gravels with recycled synthetic materials, PhD thesis, in greek, Civil Engineering Department, Aristotle University of Thessaloniki

K. Senetakis, A. Anastasiadis, K. Trevlopoulos and K. Pitilakis (2009) Dynamic response of SDOF systems on soil replaced with sand/rubber mixture, COMPDYN2009, ECCOMAS Thematic Conference on Computational Methods in Structural Dynamics and Earthquake Engineering, M. Papadrakakis, N. D. Lagaros and M. Papadrakakis (eds.), Rhodes, Greece, 22-24 June 2009

M. H. Darendeli (2001) Development of a new family of normalized modulus reduction and material damping curves, Graduate School Faculty, University of Texas at Austin

N. N. Ambraseys , J. Douglas, R. Sigbjörnsson, C. Berge-Thierry, P. Suhadolc, G. Costa and P. M. Smit (2004) Dissemination of European Strong-Motion Data, vol. 2, using Strong-Motion Datascape Navigator, CD ROM collection, Engineering and Physical Sciences Research Council, United Kingdom, Feb. 2004

P. Fajfar (2000) A nonlinear analysis method for performance based seismic design, Earthquake Spectra, Vol. 16, No. 3, pp. 573-592

R. L. Kuhlemeyer and J. Lysmer (1970) Finite element method accuracy for wave propagation problems, Canadian Geotechnical Journal, Vol. 7, pp. 106-112

S. A. Freeman (1998) The Capacity Spectrum Method as a tool for seismic design, Proceedings of the Eleventh European Conference of Earthquake Engineering, Paris, 6-11 September 1998

Seismosoft, Seismosignal (Version 4.1.2) [Computer Program]. Available at: http://www.seismosoft.com (Accessed: March 2011).

T. Edil (2004) A review of mechanical and chemical properties of shredded tires and soil mixtures, Recycled Materials in Geotechnics, Geotechnical Special Publication, No.127, pp.1-21

V. R. Schaefer (ed.) (1997) Ground improvement, ground reinforcement, ground treatment: developments 1987-1997, Geotechnical Special Publication No. 69

www.seismo2009.ethz.ch/staff/jclinton/photos/old/Exercises/10.pdf March 2011.

Normal and Reverse Fault Rupture Interaction with Caisson Foundations : Centrifuge Modeling and Numerical Simulation

M. Loli, I. Anastasopoulos

Soil Mechanics Laboratory, National Technical University, Athens, Greece

ABSTRACT: Owing to their rigidity, caisson foundations are believed to be less sensitive to fault induced loading compared to other foundation types. This paper investigates experimentally and numerically the response of a caisson foundation subjected to dip slip (normal and reverse) fault rupture. A series of centrifuge tests were conducted focusing on the effect of the caisson position with reference to the free field fault outcrop. The fault rupture was found to develop preferentially around the margins of the rigid caisson body, which acted as a kinematic constrain, altering sometimes dramatically the free field rupture pattern. Depending on the caisson position, the fault diverted towards the hanging wall or the footwall side of the caisson, or bifurcated, spreading the soil failure at a wider area on both sides. 3-D nonlinear numerical simulation of the problem was also developed and validated through comparison with the experimental results.

1 INTRODUCTION

Although being the generation source of earthquakes, faults were traditionally given little attention by the engineering community. The devastating earthquakes of 1999 in Turkey and Taiwan, however, came to prove that surface fault ruptures can be a significant hazard for structures and highlighted the need to develop design methods and guidelines against faulting-induced loading. A variety of structures were crossed by the surface fault rupture during the Kocaeli (Turkey, 1999) and Chi-Chi (Taiwan, 1999) earthquakes and a significant number of field case histories has been reported in the literature [e.g. Youd et al., 2000; Chang et al., 2000; Dong et al., 2003; Pamuk et al., 2005; Faccioli et al., 2008].

Several studies have considered the response of a structural system interacting with a propagating fault rupture, revealing that the presence of a structure may alter, sometimes dramatically, the free field rupture path. The mechanics of this phenomenon, termed Fault Rupture–Soil–Foundation–Structure Interaction (FR–SFSI), have been analyzed on the basis of : interpretation of real case histories [Anastasopoulos & Gazetas, 2007] ; centrifuge experiments [Bransby et al., 2008; Ahmed & Bransby, 2009] ; and numerical analyses [e.g. Paolucci & Yilmaz, 2008; Anastasopoulos et al., 2008; 2009].

Aiming to extend the research work on the mechanisms of FR–SFSI, which is currently (more or less) limited to the response of shallow foundations, this paper investigates the interaction of deep embedded foundations (caissons) with a rupturing normal and reverse fault. A combination of centrifuge model testing and numerical simulation of the problem was employed to this end. A series of centrifuge experiments were carried out concentrating on the effect of the caisson position relative to the fault. After validating the numerical methodology against experimental results, a parametric study was conducted identifying different interaction mechanisms, taking place for different caisson positions.

2 PROBLEM DEFINITION AND METHODOLOGY

Figure 1 illustrates schematically the main features of the studied problem for the case of normal faulting. A 5 x 5 x 10 (m) square in plan caisson foundation is considered, supported on a 15 m thick layer of dense ($D_r \approx 80\%$) dry sand. It carries a total vertical load of approximately 20 MN, which represents the weight of a superstructure of significant size (e.g., a medium span bridge). Reverse and normal (upwards and downwards) fault displacement of vertical amplitude h (throw) is applied at the bedrock. The displaced block of soil (i.e. the hanging wall) moves with a dip angle of 60°, whereas the footwall remains stationary. The fault deformation forces the caisson to move as a rigid body, experiencing both translational δ and rotational θ displacements.

The location of the caisson relative to the outcropping fault rupture is expressed through parameter s, which is defined as the distance between the caisson right corner and the point that the free-field fault rupture would cross the foundation base. In other words, s indicates the point that the fault rupture would interact with the caisson if fault rupture–caisson interaction did not take place to alter the rupture path. In the following presentation of results s is normalized by the foundation width B.

2.1 *Centrifuge Modeling*

A series of 8 in total centrifuge model tests were conducted in the beam centrifuge of the University of Dundee at an operational acceleration of 100 g. For each type of fault rupture (thrust/normal) a series of 3 fault rupture–caisson interaction tests were conducted, wherein the caisson was placed at different positions relative to the fault s/B, along with an additional free field test, which was used to determine the fault rupture trace in the free field (in absence of the foundation). Table 1 outlines the centrifuge testing program. A photograph of the centrifuge model inside the strongbox is shown in Figure 2a, as deformed after completion of test ML-05, where the caisson was placed at a position $s/B = 0.22$.

The 150 mm deep (i.e. 15 m at prototype scale) soil layer was prepared by dry air pluviation of Fontainebleau sand [Gaudin, 2002]. The sand was pluviated from a specific height with a fixed sieve aperture to control the mass flow rate, giving a uniform density $D_r \approx 80\%$ ($\gamma = 16.11$ kN/m^3). The caisson model was made of steel, having a total mass of 1.025 kg (corresponding to a prototype of 2050 Mg). Aiming to have realistically rough soil–caisson interfaces, the caisson model sides were needle-gunned. A series of direct shear tests were conducted to investigate the soil stress–strain and volumetric behavior as well as the soil–caisson interface frictional properties.

The faulting process was simulated using a split box, the moving part of which is made to translate through a hydraulic actuator. A digital camera was used to take pictures of the model from a fixed position inside the centrifuge "gondola". The photographic data were then analyzed using the Geo-PIV program, written by White et al. [2003], to calculate caisson displacements and the shear strains developed within the soil.

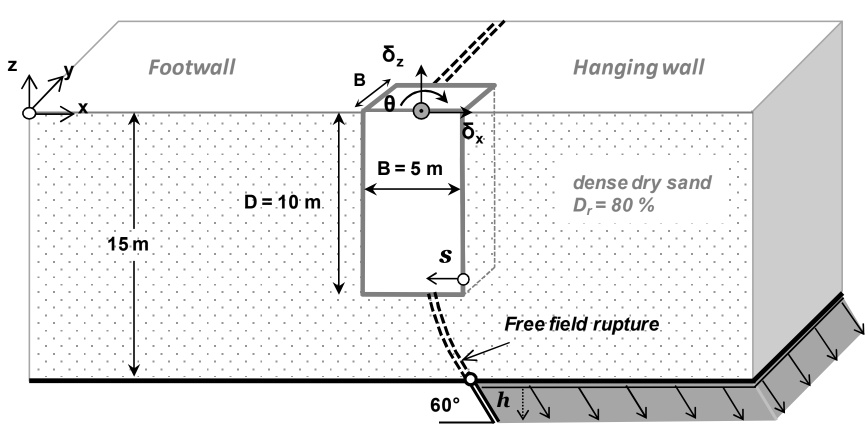

Figure 1. Problem definition : interaction of a rigid caisson with a rupturing normal fault.

Table 1. Centrifuge testing program

Reverse Faults		*Normal Faults*	
Test	*Description*	*Test*	*Description*
WA-01	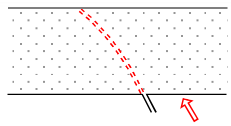	ML-06	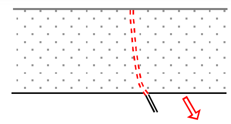
ML-04	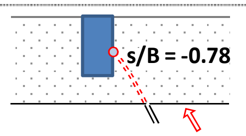	ML-08	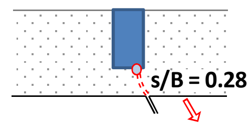
ML-05	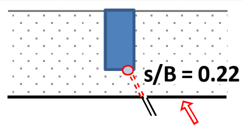	ML-10	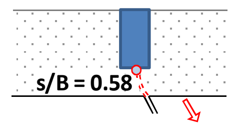
ML-03	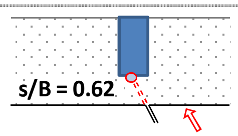	ML-07	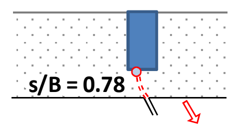

2.2 *Numerical Modeling*

Numerical simulations of the centrifuge model tests were performed employing the finite element code ABAQUS. The model dimensions were chosen to be the same as the dimensions of the physical model at prototype scale and the minimum element width (at the area surrounding the caisson) was set equal to 0.5 m. Figure 2b shows the deformed FE mesh for s/B = 0.22, for comparison with the physical model (Figure 2a). It is noted that only half of the model was simulated, taking advantage of symmetry along the centre-line of the foundation (which corresponds to the location of the Perspex front face in the centrifuge models).

Soil was modeled with hexahedral continuum finite elements. Soil modeling was based on the methodology of Anastasopoulos et al [2007]. An elasto-plastic constitutive relationship was used and encoded in ABAQUS through a user subroutine. This assumes elastic pre-yield soil behavior defined by the secant shear modulus G_s, which was in-creased linearly with soil depth. Failure was defined by the Mohr–Coulomb criterion accompanied with an isotropic strain softening law which degrades the friction (φ) and dilation (ψ) angles linearly with octahedral plastic shear strain. Calibration of the soil model parameters was performed with respect to the results of direct shear tests taking into account the scale effects associated with shear-band modeling.

3-D continuum elements were also used for the caisson, which was assumed to be linearly elastic with typical stiffness properties for steel. The soil–caisson interface was modeled using contact elements to allow sliding and/or detachment to occur. In order to simulate the centrifuge experiments, the interface properties were calibrated to match the frictional properties of the steel–sand interface as measured in the direct shear tests.

3 CHARACTERISTIC RESULTS

Due to space limitations, results are presented in detail only for two of the fault rupture–caisson interaction tests, one for each type of tectonic movement, and compared with the numerical analysis to illustrate the effectiveness of the numerical method. Yet, the mechanisms of fault rupture–caisson interaction for all the studied caisson positions (Table 1) as well as the free field response to reverse and normal fault rupture have been comprehensively reported in Loli et al. [2010 a and b].

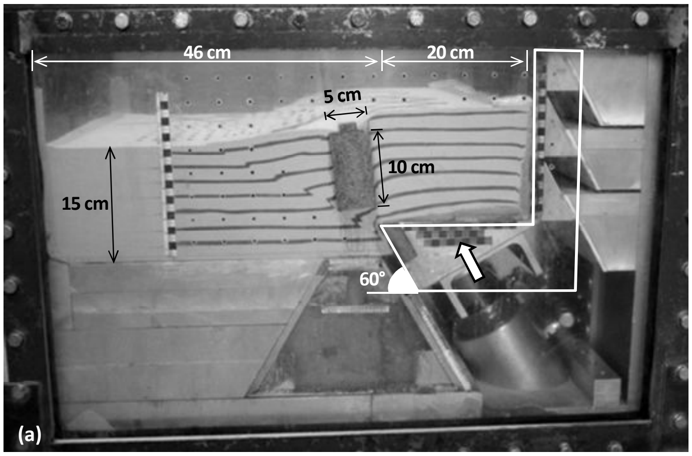

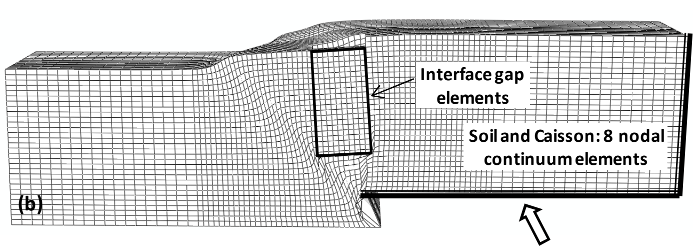

Figure 2. Combined experimental and numerical study : (a) photo of the faulting apparatus and the centrifuge model (for reverse fault rupturing at s/B = 0.22) ; (b) snapshot of deformed FE mesh.

3.1 *Reverse Fault Rupture at s/B = 0.22 (Test ML-05)*

In this test, the caisson was positioned so that the free field rupture would cross the caisson base 1.1 m to the left of its right corner (s/B = 0.22). As expected the rigid caisson mass interacts with the rupturing fault modifying significantly the failure pattern in comparison to the free field path. The mechanisms of fault–caisson interaction are highlighted in Figure 3.

Figure 3a shows a set of images captured at different time points during faulting. Significant soil deformation can be observed for h = 0.8 m propagating vertically towards the soil surface on the right (hanging wall) side of the caisson and causing significant sliding to take place along the right caisson sidewall (indicated by the dotted line), yet without evident fault plane formation (see also corresponding shear strain contours in Figure 3b). However, after 0.7 m of additional fault displacement (h = 1.5 m) a localization plane (*F1*) has clearly formed and propagated from the base dislocation point to the right corner of the foundation and all along its right sidewall. At the same time, a secondary localization (*F2*) appears. Initiating from the bedrock dislocation, *F2* intersects with the left (footwall) caisson base corner propagating with a much shallower dip angle. Thereafter, on additional fault displacement, the rupture bifurcates and fault deformation localizes upon these two distinct strands, one at each foundation side. Observe the soil heave formation next to the top right caisson corner due to *F1* and the scarp formed at the soil surface due to the emergence of *F2* for h = 3.5 m.

3.2 *Normal Fault Rupture at s/B = 0.28 (Test ML-08)*

This test, wherein the caisson was subject to normal type fault rupture at $s = 0.28B$, gave the most intriguing fault–caisson interaction mechanisms and subsequently caused the comparatively most intense caisson response (Figure 4).

Figure 4a demonstrates a progressive type of failure associated with the interplay between different failure mechanisms. First, for h = 0.6 m, the caisson acting as a kinematic constraint forces the rupture to deviate significantly from its free field path, actually changing orientation, and to propagate towards the hanging-wall (right) caisson edge. Interestingly, *F1* propagates at a dip angle greater than 90° (about 98°) contradicting the orientation of rupture in the bedrock.

Shear stresses develop along the right sidewall of the caisson and its consequent clockwise rotation causes active type stress conditions to take place on the other (left) side of the caisson. An active failure wedge forms on the footwall side of the foundation for h = 1.0 m, clearly indicated by the respective shear strain contours in Figure 4b. Soil failure on this side, as well as the soil distress underneath the foundation base due to its significant rotation, "facilitate" the diversion of the rupture to the left of the caisson and a secondary rupture plane (*F2*) is mobilized. Thereafter, a rather subtle interaction mechanism is observed, involving the formation of active and passive failure wedges on the left (footwall) and right (hangingwall) side of the caisson respectively, and fault propagation on both sides concurrently (see image for h = 2 m and the equivalent shear strain contours). Moreover, a sliding plane evidently forms along the left sidewall (highlighted in Figure 4a) and a large gap appears at the top left caisson side.

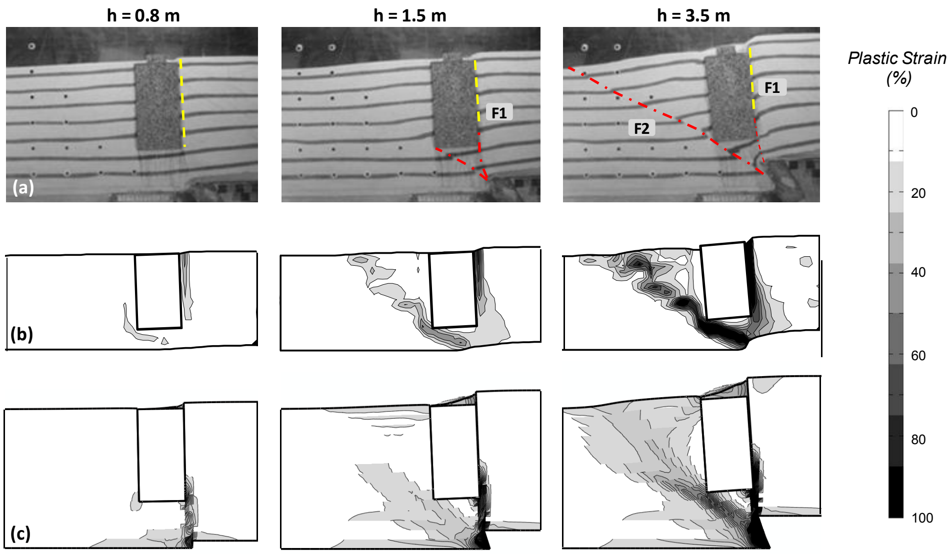

Figure 3. Reverse Fault rupture–caisson interaction at different stages of faulting for *s/B* = 0.22: (a) centrifuge test images; and contours of shear strains (b) in the centrifuge; (c) in the analysis.

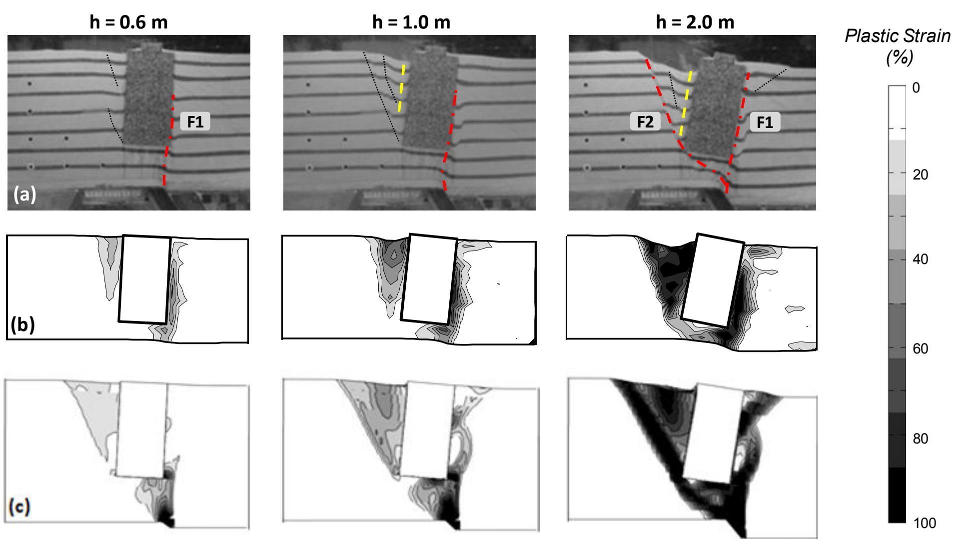

Figure 4. Normal Fault rupture–caisson interaction at different stages of faulting for *s/B* = 0.28 (Test ML_08): (a) centrifuge test model images; (b) contours of shear strains developed within the soil in the centrifuge test compared to (c) the corresponding numerical analysis.

Comparison between analytically computed and experimentally deduced shear strain contour plots (compare Figure 3b with Figure 3c for reverse faulting and Figures 4b and c for normal faulting) manifests the effectiveness of the numerical method in successfully predicting the generation and evolution of the different fault mechanisms for the whole studied range of fault displacements and for both types of dip-slip faulting. Gaining hence enough confidence in the validity of the numerical method allowed the conduction of a thorough parametric investigation of the exact caisson position effect, which is presented in the following section.

4 EFFECT OF THE RELATIVE TO THE FAULT FOUNDATION POSITION

Figures 5 and 6 summarize the results for reverse and normal faults respectively in terms of the caisson displacements (δx, δz, θ) experienced at different relative fault–caisson positions s/B for different levels of fault throw h. The different failure mechanisms taking place are also indicated by the shear strain finite element contours that correspond to different points (positions) in the graph.

For both types of tectonic movement the plane of caisson response with respect to relative position can be divided into three zones of response A,B, and C, broadly representing three different patterns of fault–caisson interaction mechanism and hence three different modes of foundation response. These are illuminated in the following. To allow comparison with the experiments and show the generally good agreement between analytical and experimental results, centrifuge test results are also indicated (with marker points) for the same fault throws.

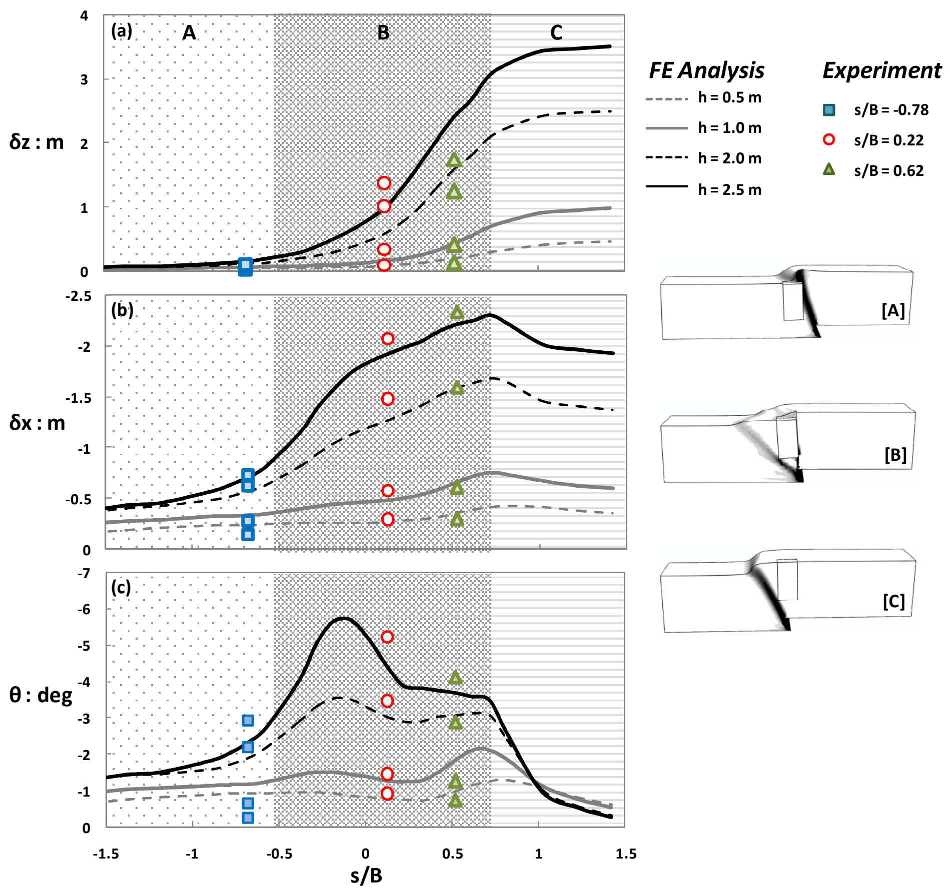

Figure 5. The effect of the exact caisson location (s) on the mechanisms of fault rupture–caisson interaction and the consequent caisson response for the case of *reverse* tectonic movement: (a) vertical displacements, (b) horizontal displacements, and (c) rotation for different levels of fault throw.

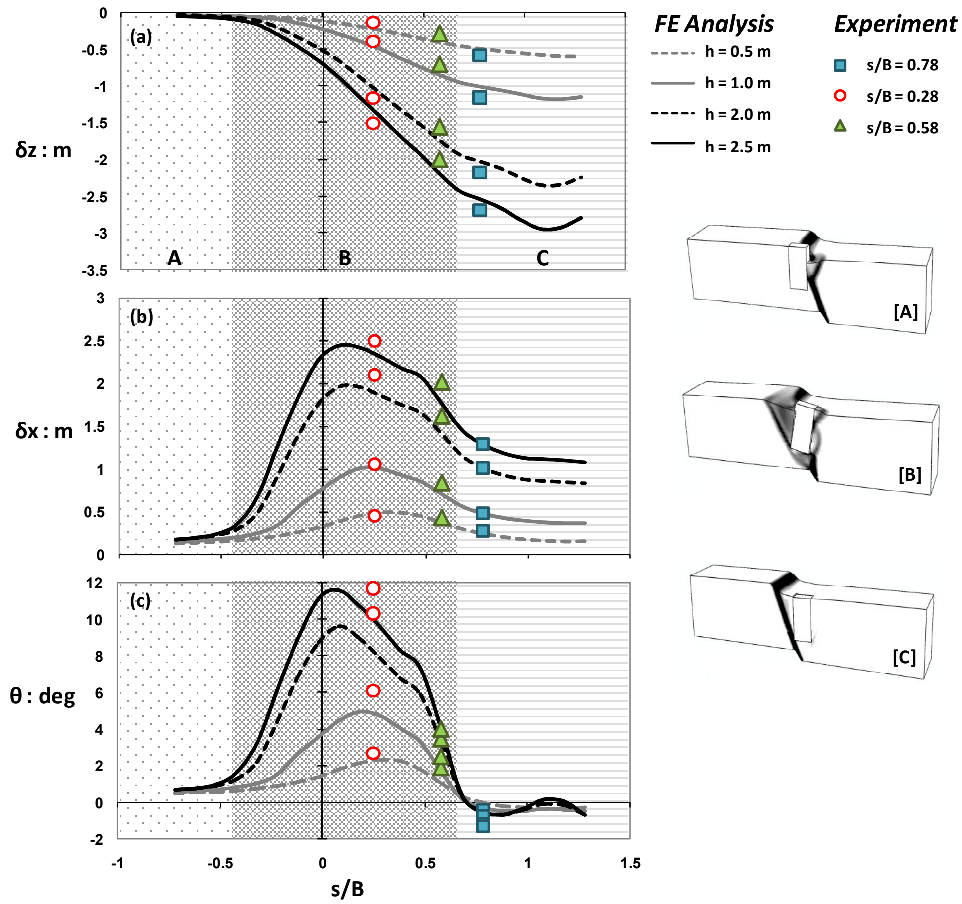

Figure 6. The effect of the exact caisson location (s) on the mechanisms of fault rupture–caisson interaction and the consequent caisson response for the case of *normal* tectonic movement: (a) vertical displacements, (b) horizontal displacements, and (c) rotation for different levels of fault throw.

4.1 *Reverse Fault Rupture–Caisson Interaction Mechanisms*

Three different interaction mechanisms can be identified, dividing the graphs of Figure 5 in three zones : (a) Mechanism A, for $s/B < -0.5$; (b) Mechanism B, for $-0.5 \leq s/B < 0.7$; and (c) Mechanism C, for $s/B \geq 0.7$. More specifically:

Mechanism A is observed when the fault rupture interacts with the upper half of the caisson right sidewall. The rupture is diverted towards the hanging wall and the caisson remains on the footwall. As a result, it experiences limited distress, being subjected to relatively small rotational and horizontal displacement, and practically zero uplift. This zone of s/B is clearly the most favorable for the performance of the supported structure.

Mechanism B occurs when the free field rupture crosses the caisson near its right base corner, as in the case of the previously discussed test ML-05 ($s/B = 0.22$). Fault bifurcation is observed and deformation occurs simultaneously upon two fault strands, one on each side of the caisson. Increased rotations, and hence horizontal displacements, are associated with this zone of response primarily due to the fault deformation spreading within a wider soil area on both sides of the foundation.

Mechanism C ($s/B \geq 0.7$; i.e. $s > 3.5$ m) the fault rupture diverts towards the caisson footwall side, intersecting at its left base corner. This leads to an abrupt decrease of θ, which is virtually eliminated for $s/B > 1.0$ (i.e. when there is practically no interaction of the fault rupture with the caisson). The caisson experiences pure translational displacement, moving along with the hanging wall.

4.2 *Normal Fault Rupture–Caisson Interaction Mechanisms*

In the same way as with reverse faults, three modes of response can be identified (Figure 6):

Mechanism A ($s/B < -0.4$) takes place when the fault rupture "grazes" the hanging-wall (right) sidewall of the caisson, missing its base by 2 m or more. The rupture path is refracted on the rigid sidewall and deviated towards the hanging-wall (to the right). The caisson remains on the footwall side of the fault, and experiences limited distress for all levels of fault throw h. This is presumably the most favorable area of possible caisson positions.

Mechanism B ($-0.4 \leq s/B < 0.6$) is prevalent when the fault rupture crosses the caisson body near its right base corner. As discussed previously for test ML-08 ($s/B = 0.28$), the interaction of the caisson with the fault rupture is in this case quite complex, involving : (i) bifurcation of the shear zone along both sides of the caisson, (ii) formation of an active failure wedge at the footwall (left) side of the caisson due to its substantial rotation, and (iii) formation of a passive-type failure wedge at the hanging-wall (right) side of the caisson (also due to the rotation). This interaction case, is probably the most detrimental for the system response.

Mechanism C ($s/B \geq 0.6$) prevails when the fault rupture crosses the caisson close to its footwall (left) corner, or misses it completely on the footwall (left) side. The rupture is diverted towards the footwall and the caisson translates downwards, following the hanging wall, with only minor rotation

5 CONCLUSIONS

Caisson foundations interact with dip-slip fault rupture (normal and reverse) and change sometimes dramatically its free field path. The rigid caisson body acts as a kinematic constraint, which forces the fault to divert. This is an important difference of caissons compared to other types of foundations (shallow footings or piles) when the fault can be partially deviated if at all.

A numerical method was developed and validated through successful comparisons with centrifuge test results, revealing its effectiveness in capturing qualitatively and quantitatively the mechanisms of fault rupture–caisson interaction. This gives confidence that the same method can be used to study other similar problems or be used as a design tool.

The validation of the numerical method allowed the conduction of a parametric study to further investigate the effect of the exact foundation position, which proved to be a determinative parameter controlling the response of the system. The different FR-SFSI mechanisms taking place at different positions *s/B* were identified and the consequent foundation performance was discussed.

6 ACKNOWLEDGMENT

The research presented in this paper was funded by the European Research Council (ERC) Program “IDEAS, Support for Frontier Research – Advanced Grant", under Contract number ERC–2008–AdG 228254–DARE.

7 REFERENCES

Ahmed, W. & Bransby, M.F. (2009). The interaction of shallow foundations with reverse faults. *Journal of Geotechnical and Environmental Engineering*, 135, No. 7, 914-924.

Anastasopoulos, I. & Gazetas G. (2007). Foundation-Structure Systems over a Rupturing Normal Fault: Part I. Observations after the Kocaeli 1999 Earthquake. *Bulletin of Earthquake Engineering*, 5, No. 3, 253–275.

Anastasopoulos, I. Gazetas, G. Bransby, M.F. Davies, M.C.R. & El Nahas, A. (2007). Fault Rupture Propagation through Sand : Finite Element Analysis and Validation through Centrifuge Experiments. *Journal of Geotechnical and Geoenvironmental Engineering*, ASCE, 133, No. 8, 943–958.

Anastasopoulos, I. Gazetas, G. Bransby, M.F. Davies, M.C.R. & El Nahas, A. (2009a). Normal Fault Rupture Interaction with Strip Foundations. *Journal of Geotechnical and Geoenvironmental Engineering*, ASCE, 135, No. 3, 359-370.

Bransby, M.F. Davies, M.C.R. El Nahas, A. & Nagaoka, S. (2008a). Centrifuge modelling of normal fault-foundation interaction. *Bulletin of Earthquake Engineering*, 6, No. 4, 585-605.

Bransby, M.F. Davies, M.C.R. El Nahas, A. & Nagaoka, S. (2008b). Centrifuge modelling of reverse fault-foundation interaction. *Bulletin of Earthquake Engineering*, 6, No. 4, 607-628.

Bray, J.D. Seed, R.B. Cluff, L.S. & Seed, H.B. (1994b). Analysis of earthquake fault rupture propagation through cohesive soil. *Journal of Geotechnical Engineering*, **120**, No. 3, 562-580.

Chang, K-C. Chang, D-W. Tsai, M-H. & Sung, Y-C. (2000). Seismic performance of highway bridges. *Earthquake Engineering and Engineering Seismology*, 2, No. 1, 55-77.

Dong, J.J. Wang, C.D. Lee, C.T. Liao, J.J. & Pan, Y.W. (2003). The influence of surface ruptures on building damage in the 1999 Chi-Chi earthquake: a case study in Fengyuan City. *Engineering Geology*, 71, 157–179.

Faccioli, E. Anastasopoulos, I. Callerio, A. & Gazetas, G. (2008). Case histories of fault–foundation interaction. *Bulletin of Earthquake Engineering*, 6, 557–583.

Gaudin, C. (2002). *Modelisation physique et numerique des ecrans de soutenement: application a l'etude de l'effet d'une surcharge sur le sol soutenu*. PhD. thesis, Universite de Nantes.

Pamuk, A. Kalkan, E. & Ling, H.I. (2005). Structural and geotechnical impacts of surface rupture on highway structures during recent earthquakes in Turkey. *Soil Dynamics & Earthquake Engineering*, 25, No. 7-10, 581-589.

Paolucci, R. & Yilmaz, M.T. (2008). Simplified theoretical approaches to earthquake fault rupture–shallow foundation interaction. *Bulletin of Earthquake Engineering*, 6, No. 4, 629-644.

Ulusay, R. Aydan, O. & Hamada, M. (2002). The behaviour of structures built on active fault zones: examples from the recent earthquakes of Turkey. *Structural Engineering & Earthquake Engineering*, JSCE, 19, No. 2, 149-167.

White, D.J. Take, W.A. & Bolton, M.D. (2003). Soil deformation measurement using particle image velocimetry (PIV) and photogrammetry. *Geotechnique*, 53, No. 7, 619-631.

Youd, T. L. Bardet, J.P. & Bray, J.D. (2000). Kocaeli, Turkey, Earthquake of August 17, 1999 Reconnaissance Report. *Earthquake Spectra*, Suppl. A to 16, 456.

1-g Experimental Investigation of the Metaplastic Rocking Response of 1-dof Oscillators on Shallow Footings

I. Anastasopoulos, R. Kourkoulis, E. Papadopoulos
Soil Mechanics Laboratory, National Technical University, Athens, Greece

ABSTRACT: This paper experimentally investigates the effect of shallow soil improvement layer on the rocking response of 1-dof systems. A series of 1-g horizontal monotonic and slow cyclic pushover tests were conducted in the laboratory of soil mechanics of the National Technical University of Athens (NTUA) with the depth of the soil improvement layer being varied parametrically. It is shown that due to the very nature of foundation rocking which mobilizes only a shallow stress bulb within the soil underneath the foundation, the presence of a shallow zone of mitigation acts very effectively towards limiting the shaking–induced settlement of the foundations.

1. INTRODUCTION

Contemporary earthquake engineering norms (e.g. EC8, FEMA 356 guidelines) while allowing ductility-controlled inelastic behavior of the superstructure -during low probability earthquake events- they dictate elastic foundation response ignoring the additional ductility that may be oferred by the soil-foundation system. Only recently, and perhaps contrary to common expectations, new studies (Paolucci 1997; Pecker, 1998, 2003; FEMA 356; Gazetas et al, 2004; Anastasopoulos et al , 2010; Gelagoti et. al., 2011) have shown that permitting non-linear soil-foundation response may overall enhance the seismic performance of the structure; nonlinearity of the soil-foundation system can act as a fuse mechanism, dissipating earthquake energy and potentially reducing demands exerted on the structural components of the building.These findings have been further verified by numerous experimental centrifuge, large scale and 1-g reduced scale tests— (Faccioli et al., 2001; Kutter et al., 2003; Gajan et al, 2005; Kawashima et al., 2007)

This paper experimentally investigates the effectiveness of non-linear foundation response in the form of rocking, for the case of 1-dof systems. It is noted that foundation rocking although desirable incorporates the peril of introducing permanent deformations (settlements and rotations) in case of low FS_v values which may possibly be unacceptable for the design. Thus, for foundation rocking to materialize through uplifting rather than settlement, the designer must ensure an adequately high safety factor against vertical loads. However, uncertainties in the exact estimation of in-situ soil properties would also hinder the exact assessment of FSv, and subsequently would practically limit the applicability of rocking-isolation in earthquake design.

In an effort to overcome this obstacle, this paper investigates the potential of *shallow* soil improvement, a concept commonly applicable in geotechnical engineering as a means to increase soil strength and reduce settlements. The competence of shallow mitigation stems from the very nature of foundation rocking which indeed mobilizes only a shallow stress bulb within the soil

(Anastasopoulos et. al., 2011b). Motivated by this behavior, a series of 1-g horizontal monotonic and slow cyclic pushover tests were conducted in the laboratory of soil mechanics of the National Technical University of Athens (NTUA) with the depth of soil improvement being varied parametrically.

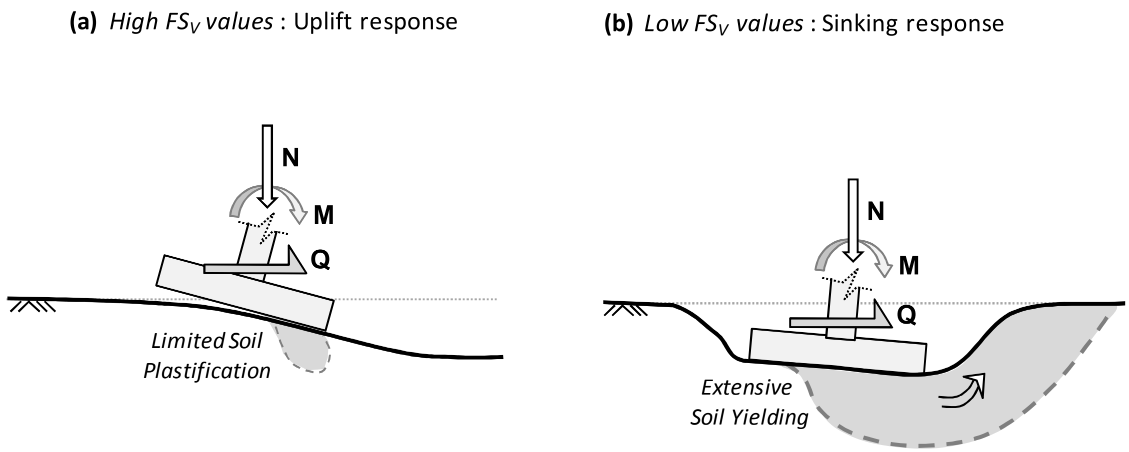

Figure 1: Rocking response of the soil–foundation systems under combined (M, Q, N) loading: (a) uplifting dominated response (high FS_v values); (b) bearing capacity failure mechanism prevails (low FS_v values).

2. PROBLEM DEFINITION AND METHODOLOGY

A single degree of freedom system has been investigated which may be considered as representative of a relatively slender bridge pier, supported on surface square foundation. Unless otherwise stated, all dimensions mentioned hereafter refer to model scale. The experimental set-up is outlined in Figure 2.

Soil Modeling

The soil used in the experiments was dry Longstone sand, an industrially produced and uniform quartz sand material. The parameters of this sand are D_{50} = 0.15mm and C_u = 1.42. The void ratios were measured to be e_{max} = 0.995 and e_{min} =0.614 and the specific solids weight G_s = 2.64. The sand was layered using dry pluviation on a rigid container with dimensions of 160 x 90 x 75 cm. Sand layering is accomplished by means of a sand raining system calibrated so as to achieve the desired soil density (Anastasopoulos et al. 2010). The height of the soil deposit ranges from 50 to 55 cm.

Superstructure Model

The foundation–superstructure model consists of a square foundation of dimensions 15 cm x 15 cm x 2 cm, two rigid columns of height 45 cm and a slab located 45 cm above the foundation level. The aspect ratio of the system yields h/B = 3. Sandpaper was placed under the foundation in order to achieve the desired friction coefficient. The 1-dof model is then placed on its position atop the soil surface by means of four jacks enabling its accurate positioning without disturbing the soil surface. Electronic spirit levels placed on the superstructure certify that the foundation is placed parallel to the soil surface, with no inclination.

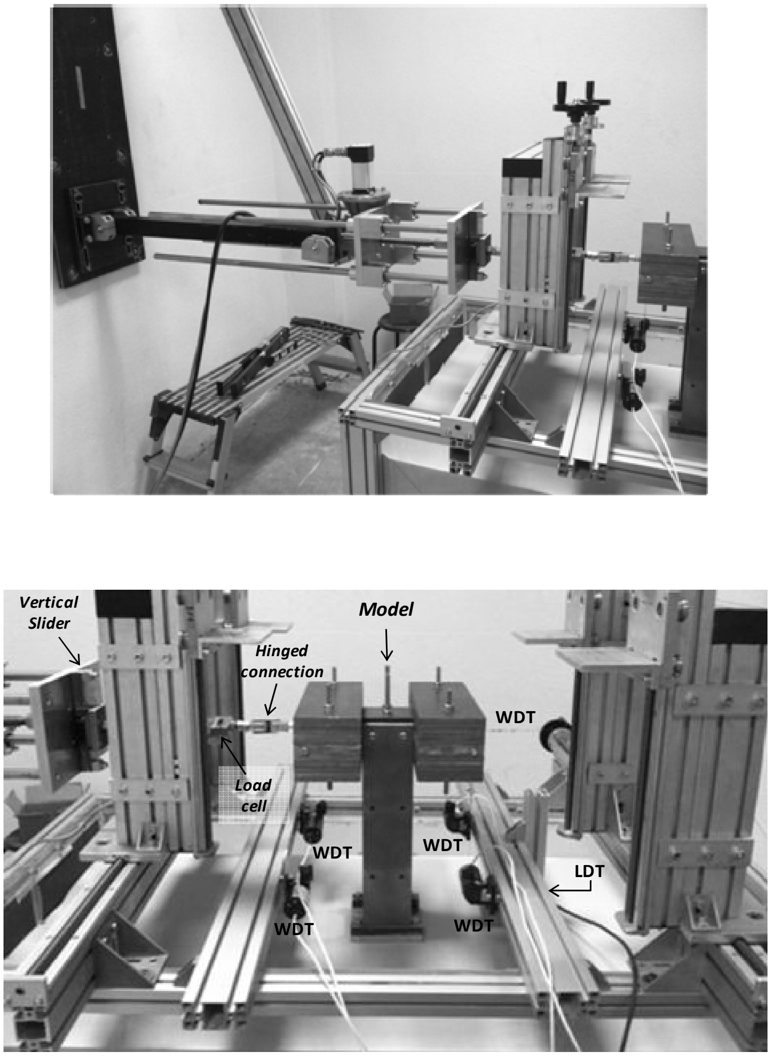

Figure 2: (a) Push over Apparatus, and (b) model instrumentation

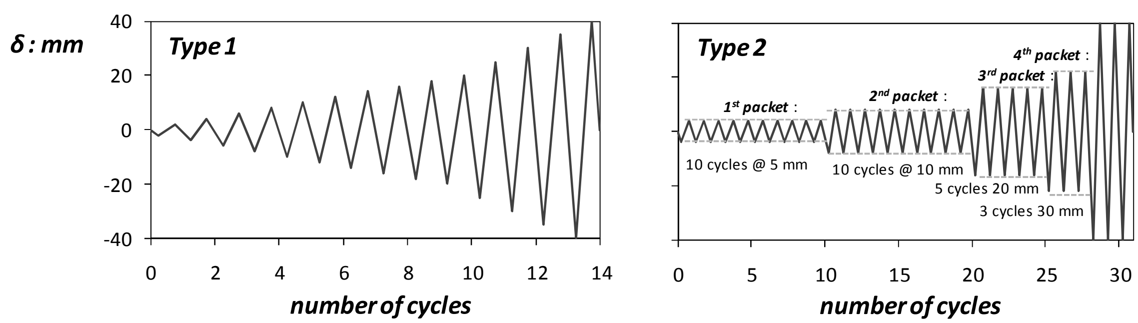

Figure 3. Two displacement protocols have been used for cyclic loading tests.

Load Application

The desired horizontal displacement is applied directly on the center of mass through a pushover apparatus consisting of a servomotor attached to a screw-jack actuator (Fig. 2a). The pushover apparatus is rigidly attached to the reaction wall while its end is connected to the foundation-superstructure model using a pin and clevis attachment (hinged connection) enabling the system to freely settle, slide and rotate as horizontal displacement is applied. The intervention of a linear guideway between the actuator and the servomotor allows the model to be subjected to exclusively horizontal loading at the mass level. Foundation and superstructure displacements were recorded through a combined system of wire and laser transducers (Fig. 2b).

Load protocol

The systems were subjected to monotonic and slow cyclic horizontal loading. Type I, the primary cyclic load protocol, consists of 14 cycles of increasing displacement, ranging from 2mm to 40mm, while Type II consists of 31 cycles, divided into 10 cycles of 4mm, 10 cycles of 8mm, 5 cycles of 16mm, 3 cycles of 24mm and 3 cycles of 40mm, in increasing order. The maximum displacement amplitude imposed is the same for both loading types (Fig. 3).

4. EFFECTIVENESS OF SHALLOW SOIL IMPROVEMENT FOR A LIGHTWEIGHT STRUCTURE

The following sections investigating the effectiveness of "shallow soil improvement" (i.e. the replacement of a shallow soil layer with soil of known properties) on the rocking response of 1-dof systems. Two different superstructure systems have been tested supported on foundation of the same width: System A refers to a lightweight (high FS_v) structure while system B represents a heavily loaded system (Figure 4). The model properties were selected so that the two systems demonstrate distinctly different behaviors, from uplift-dominated response to strictly sinking response. (Soil improvement is obviously applied on the corresponding to each system low density profiles (D_r = 45% for the lightweight system and Dr = 65% for the heavyweight one) by replacing the top sand layer with high density sand (Dr=93%), as depicted in Figure 4c. The depth (z) of soil improvement is expressed as a fraction of the foundation width (B) and has been varied parametrically in order to assess the optimum. Results are presented for the cases of z/B = 0.25, z/B = 0.25, and z/B = 1. The response of the foundation under high FS_V conditions (i.e. Dr = 93% yielding FS_v = 5 for the heavy structure and FS_v = 14 for the lightweight one) is considered to be the upper bound which should ideally be approached by the foundations on improved soil. It is noted that the FS_v values have been derived experimentally by means of vertical Push-down tests.

Monotonic Loading

Test results are displayed in Figure 5. In terms of Moment–rotation curves (Fig. 5a), it is obvious that the maximum moment rises with the increase in the depth of the soil improvement, as a result of the progressively enhanced soil strength. A similar trend may be observed for the overturning angle; the larger the depth of soil improvement, the greater its rotational capacity. [Even though experimental data have not been recorded until complete toppling of the models, the gradual increase of overturning angle θ may be derived from the slope of the descending branch of M-θ]. As expected, the increase in soil improvement depth reduces the extent of soil deformation and plastifications which are always limited only within the high density layer. Hence, the behavior of the models on the layered soil profile at large rotation angles closely resembles the response of the upper bound system (model on the homogeneous dense sand). Note that for the lightly loaded superstructure, the upper bound case (homogenous dense profile) yields a FS_V = 14, which implies almost no compliance, and thus for this limit case the rocking response almost approaches the response of a rigid block rocking on rigid base .

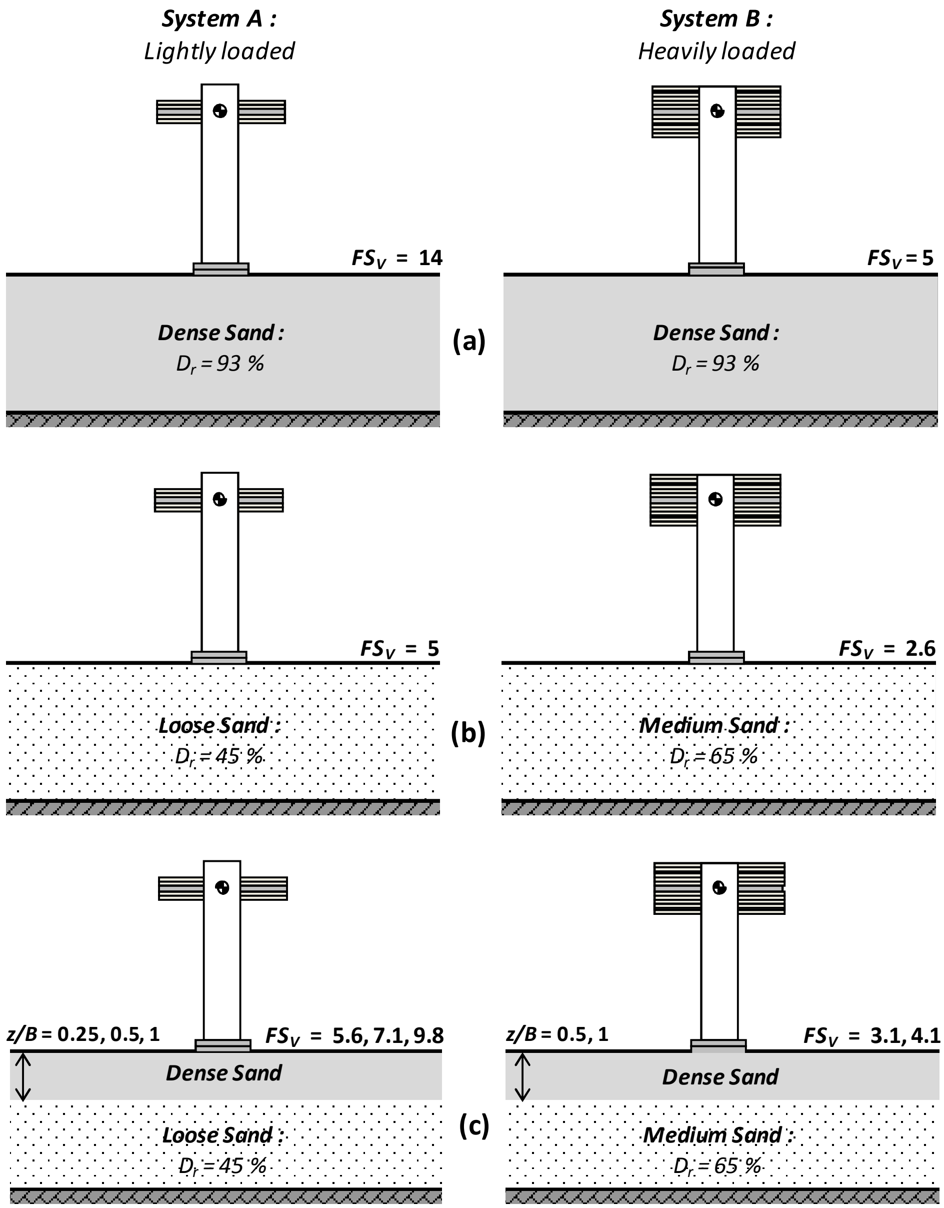

Figure 4**.** Schematic illustration of the studied soil-structure systems. a lightly loaded system (left), and a heavily loaded (right) founded on : (a) dense sand,; (b) medium and loose sand,; and (c) soil improvement with a shallow soil crust of dense sand, of varying depth (*z/B* = 0.25 to 1).

The differences between the 4 systems are more conspicuous in terms of settlement-rotation (Fig 5b). It is evident that with increasing the depth of soil improvement, foundation uplifting is promoted for a wider range of rotations. Indeed, in the unimproved soil, footing rotation would be accompanied by settlement up to an amplitude of $\theta > 0.08$; yet this value drops considerably to $\theta \approx 0.045$ when improving soil above depth z/B = 0.5 and to a mere $\theta \approx$ 0.015for z/B = 1. Moving to higher θ values (where foundation uplift dominates) the response of the models on both layered profiles almost matches the response of the upper-bound system (the three curves evolve in parallel). In fact, foundation uplift results in decrease of the effective foundation breadth in contact with the soil, which in turn reduces the size of the generated stress bulb (which is a direct function of the effective width). In effect, the rocking-induced stresses are transmitted to a smaller depth, which enhances the effectiveness of the improved soil's stiffness. In other words, for $\theta > 0.045$ the foundation on the mitigated soil profiles responds as if founded on a stiffer soil. Notice that although the z/b=1 curve practically coincides with the dense sand line it abruptly tends to override it for greater rotation values. Apparently, this behavior is attributable to some kind of flaw in the dense sand experiment and should be ignored.

The last chart (Fig. 5c) compares the experimentally derived rotational stiffness with respect to the amplitude of rotation. As calculated, K_R refers to a specific oscillator with h/B = 3 and incorporates the coupled rotational stiffness produced under simultaneous moment and shear force action on the foundation. Experimental complexities prevent the exact measurement of the initial rotational stiffness (i.e. the elastic response). At low rotation amplitude, for a given confinement stress (i.e. structural mass), the rotational stiffness K_R should be relative to the Shear Modulus G, which is affected by sand density. Thus, greater depths of soil improvement result in larger rotational stiffness. As the imposed rotation θ amplifies, foundation uplifts, K_R drastically decreases, and all profiles tend to behave identically.

Cyclic Loading

Moving from monotonic to slow cyclic loading, the results in terms of moment-rotation are displayed in Figure 6, along with the monotonic backbone curves. It is obvious that as the depth of soil improvement increases, the loops tend to transform from oval-shaped, resembling the loose sand model, to S-shaped, similar to those produced in the dense sand model. Interestingly, contrary to monotonic loading, in cyclic loading all systems seem to display the same moment capacity. While in case of the dense sand, the monotonic moment-rotation curve clearly "envelopes" the loops of the slow-cyclic tests, the latter tend to overly exceed as FS_v is reduced. This phenomenon is probably attributable to sand densification underneath the foundation due to multiple loading cycles (especially for the case of loose sand)

The foundation response in terms of settlement-rotation is portrayed in Figure 7. Even for a relatively shallow improvement depth of z/B=0.5, the foundation manifest a palpably superior behavior compared to the lower bound case of the loose soil profile, although the settlement accumulated during each cycle of loading is not as little as in the dense sand case. When the improved zone deepens to z/B = 1, the behavior quite replicates that of the model lying on dense homogenous sand, both in terms of residual displacement and tendency to uplift. These results are in full accord with the monotonic curves.

5. EFFECTIVENESS OF SHALLOW SOIL IMPROVEMENT FOR A HEAVYWEIGHT STRUCTURE

Monotonic Loading

Figure 8a shows a comparison in terms of moment-rotation. As far as ultimate moment is concerned, it is again obvious that the improvement in soil quality increases the foundation capacity, although the difference is not as large as for the lightweight model. Similarly, deepening of the mitigated zone produces larger overturning angles, although the increase does not follow that of the FS_v. This might be attributed to the fact that for such relatively low FS_v values, the overturning angle is mainly governed by soil failure rather than being a geometrical consequence.

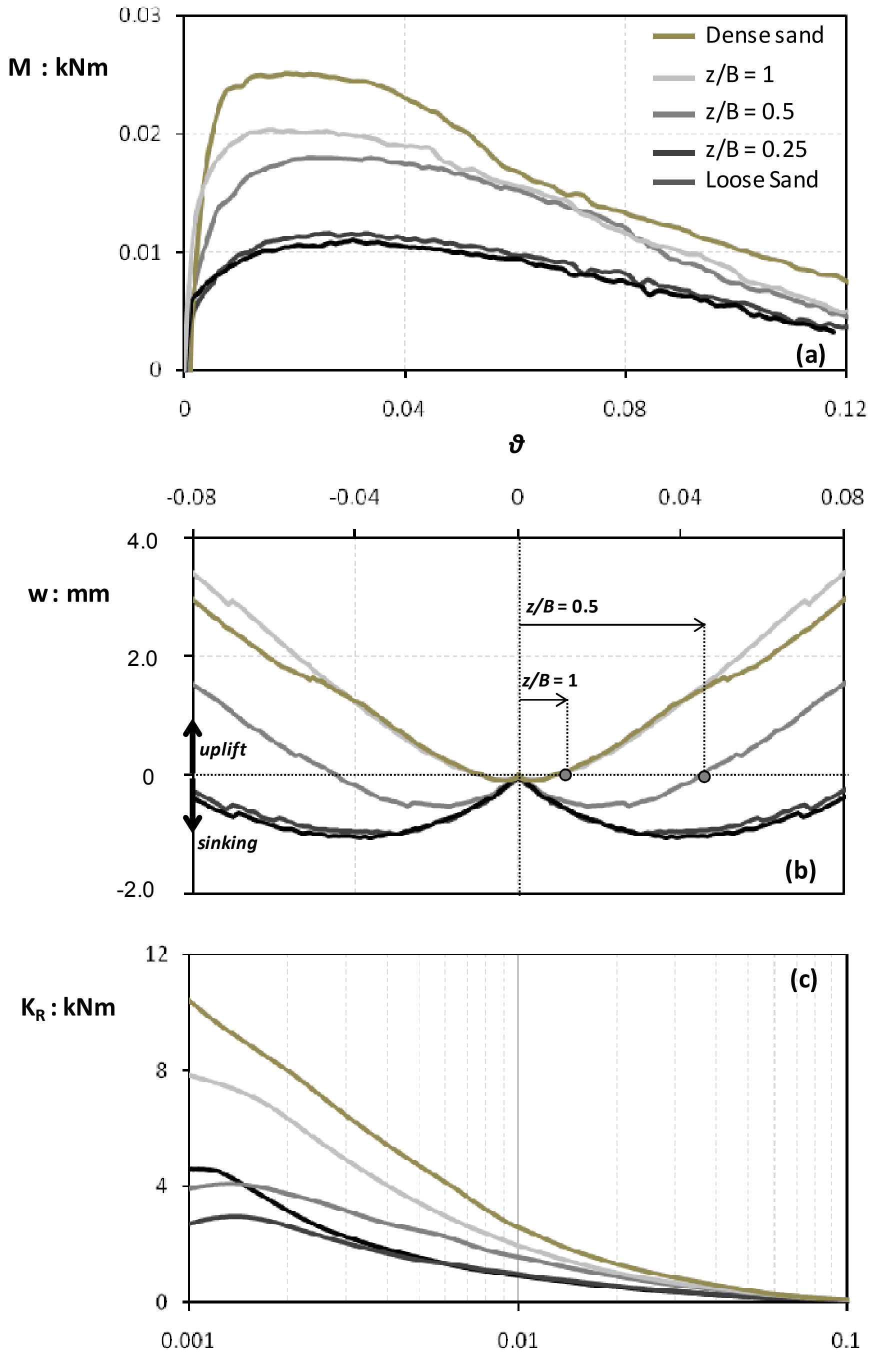

Figure 5. Effectiveness of soil improvement when the **lightly loaded system A** is subjected to monotonic loading. Comparative assessment in terms of : (a) moment–rotation, (b) settlement–rotation response ; and (c) rocking stiffness K_R

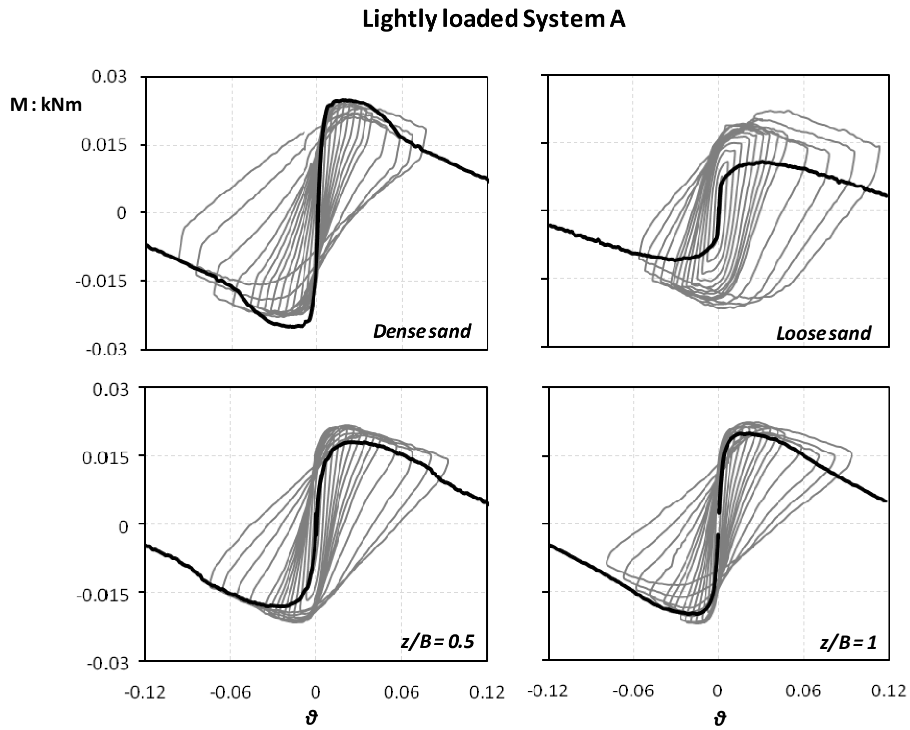

Figure 6. Effectiveness of soil improvement for the lightly loaded system A subjected to cyclic loading (Type 1 protocol). Comparative assessment in terms of moment–rotation response.

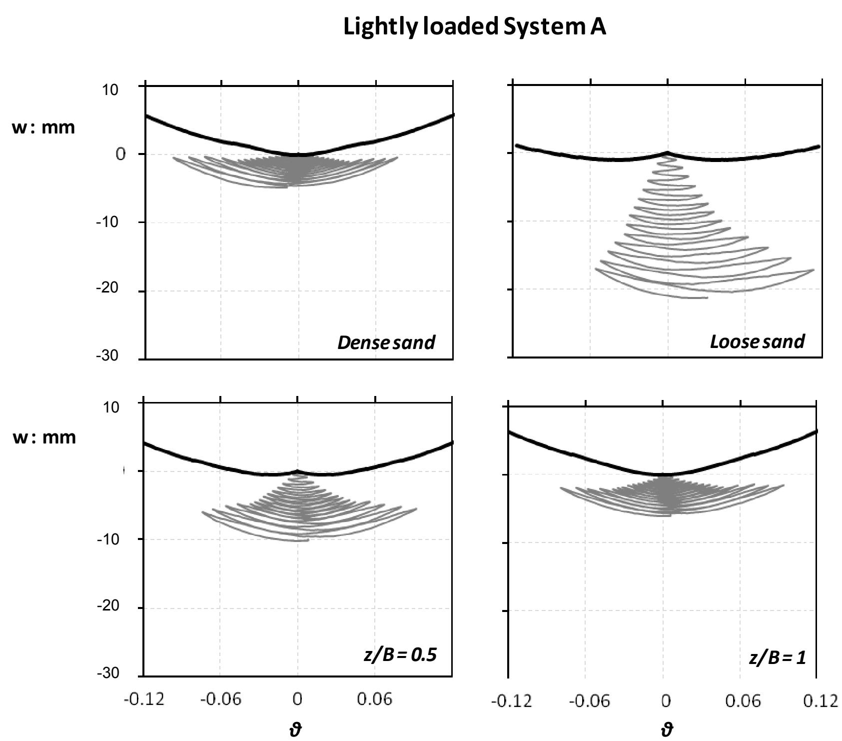

Figure 7. Effectiveness of soil improvement for the **lightly loaded system A** subjected to cyclic loading (Type 1 protocol). Comparative assessment in terms of settlement–rotation response.

In terms of settlement-rotation (Fig 8b) the main conclusions drawn in case of the lightweight system still hold true, with the main difference being the critical improvement depth (i.e. the zone thickness necessary to promote uplifting). The behavior of the models on improved sand seems to be almost identical with that on loose sand when the imposed displacement amplitude is relatively small, which reveals a negligible effect of soil improvement. Indeed, during the initial stages of loading the entire width of the footing maintains contact with the ground thus transmitting the stresses (due to the heavy superstructure) to a large depth exceeding the shallow improved zone; however as the effective contact area reduces due to foundation uplifting during subsequent stages of loading, the role of soil improvement becomes significant and disparities among the four curves are more prominent. In fact, the z/B = 1 curve demonstrates a similar pattern as the dense sand one, with the evolution of the former being parallel to that of the latter due to the (irrecoverable) settlement acquired at the initial loading stages (i.e. before uplifting). When the improvement depth is z/B = 0.5, the response of the footing remains sinking dominated for imposed rotation of up to θ = 0.12; this value reduces to 0.05 when z/B increases to 1 but it never actually reaches the dense sand uplifting threshold of θ = 0.03. Even this value however is by far higher than the corresponding threshold of the lightweight structure described earlier which is less than 0.01.

Cyclic Loading

The response of the four heavily loaded systems when subjected to slow cyclic lateral loading, are illustrated in Figures 9and 10. Quite interestingly**,** during these tests all models reached higher values of moment than the corresponding monotonic case. In fact the overstrength ratio increases rapidly as the safety factor drops resulting in an almost identical cyclic moment capacity of all footings irrespectively of the depth of the mitigation.

With respect to the settlements, all systems conspicuously reflect a sinking-dominated response (Figure 10), accumulating a considerable amount of settlement during each cycle. In this case study, contrary to the lightweight model, the improvement depth of z/B = 0.5 reduces settlements by only 30%. In order to achieve a significant reduction, the use of a deeper zone of improvement of z/B = 1 proves essential.

6. CONCLUSIONS

The primary scope of this investigation was to experimentally test and evaluate the concept of shallow soil improvement. It is concluded that under monotonic loading the ultimate moment M_u increases for higher ratios of z/B. This doesn't hold true when the systems are subjected to cyclic loading. In this case, for large amplitude cycles all models (irrespectively of the depth of the mitigation) tend to reach the same ultimate moment.

Moreover, due to the very nature of foundation rocking which mobilizes only a shallow stress bulb within the soil underneath the foundation, the presence of a shallow zone of mitigation acts very effectively towards limiting the shaking–induced settlement of the foundations. Even a shallow z/B layer ensures uplift-dominated behavior at high rotational amplitudes, while at very small rotations (when the whole foundation width is in contact with the soil) all models accumulate settlement. Yet the rate of accumulation as well as the range of rotation amplitudes where sinking prevails, is controlled by the achieved FS_V. For light systems a z/B = 0.5 was found sufficient, while for heavier systems a z/B = 1 was judged necessary in order to approach the upper bound (desired) response.

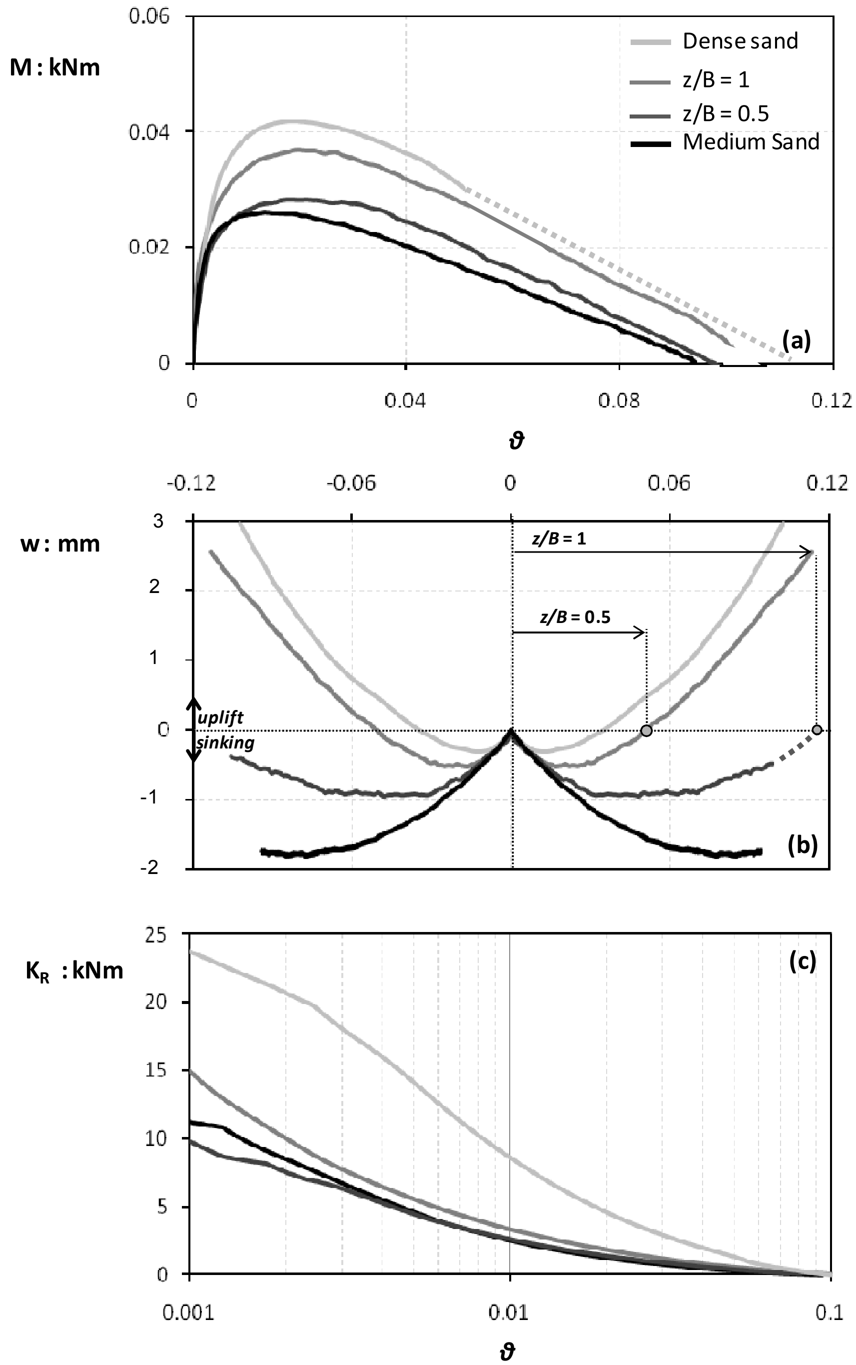

Figure 8. Effectiveness of soil improvement for the **heavily loaded system B** subjected to monotonic loading. Comparative assessment in terms of : (a) moment–rotation, (b) settlement–rotation response), and (c) rocking stiffness K_R

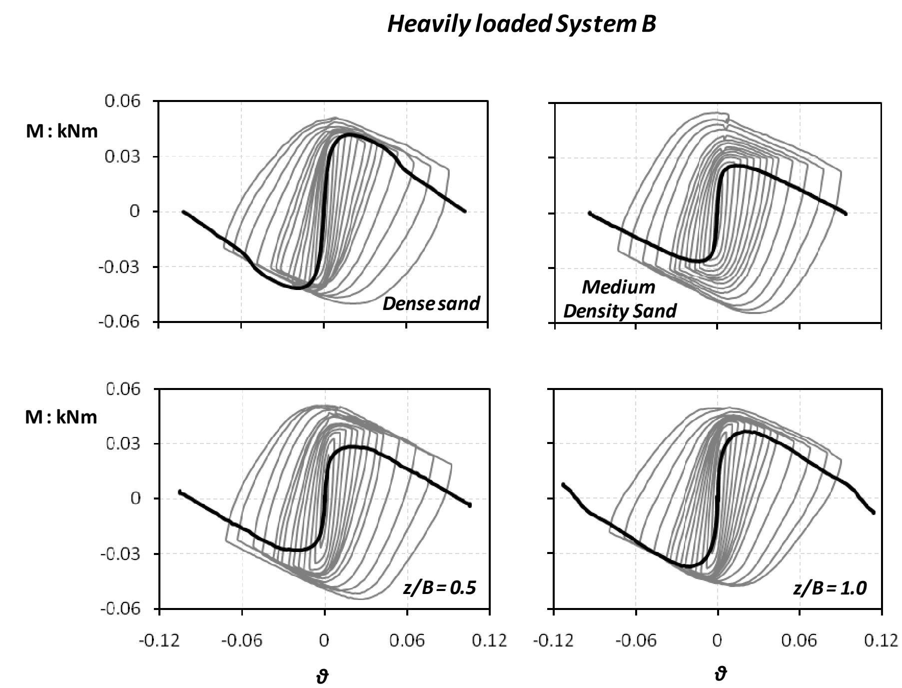

Figure 9. Effectiveness of soil improvement for the heavily loaded system B subjected to cyclic loading (Type 1 protocol). Comparative assessment in terms of moment–rotation response.

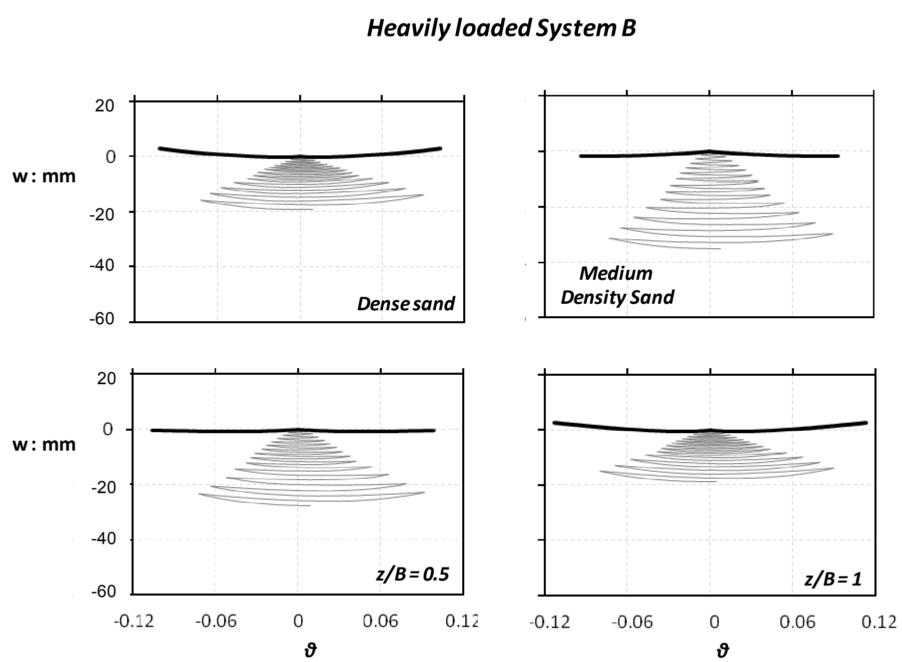

Figure 10. Effectiveness of soil improvement for the heavily loaded system B subjected to cyclic loading (Type 1 protocol). Comparative assessment in terms of settlement–rotation response.

7. ACKNOWLEDGEMENT

The financial support for this paper has been provided under the research project "DARE", which is funded through the European Research Council's (ERC) "IDEAS" Programme, in Support of Frontier Research–Advanced Grant, under contract/number ERC–2–9–AdG228254–DARE.

8. REFERENCES

Anastasopoulos I. Gelagoti F., Kourkoulis R., Gazetas G., (2011), "Simplified Constitutive Model for Simulation of Cyclic Response of Shallow Foundations : Validation against Laboratory Tests", *Journal of Geotechnical and Geoenvironmetal Engineering*, ASCE (*in print).*

Anastasopoulos I. Kourkoulis R., Gelagoti F., Papadopoulos E., (2011b), "Metaplastic Rocking Response of 1-dof Systems on Shallow-improved Sand: An Experimental Investigation", *Soil Dynamics and Earthquake Engineering*, (*Submitted for Possible Publication).*

Anastasopoulos I., Gazetas G., Loli M., Apostolou M, N. Gerolymos, (2010a), "Soil Failure can be used for Seismic Protection of Structures", *Bulletin of Earthquake Engineering*, Vol. 8, pp. 309–326.

Chatzigogos, C.T., Figini, R., & Pecker, A. and J. Salençon, (2010), "A macroelement formulation for shallow foundations on cohesive and frictional soils", *International Journal for Numerical and Analytical Methods in Geomechanics*

Chatzigogos, C.T., Pecker, A., & Salençon J., (2009), "Macroelement modeling of shallow foundations", *Soil Dynamics and Earthquake Engineering,* Vol. 29 (5), pp. 765-781

Crémer, C., Pecker, A., & Davenne, L., (2001), "Cyclic macro-element for soil–structure interaction: material and geometrical nonlinearities", *International Journal for Numerical and Analytical methods in Geomechanics*; Vol. 25(12), pp. 1257–1284.

Drosos V., Georgarakos T., Loli M., Anastasopoulos I., Zarzouras O., Gazetas G., (2010), "*Soil-Foundation-Structure Interaction with mobilization of bearing capacity : An experimental Study on Sand".*

Faccioli E, Paolucci R, G. Vivero, (2001), "Investigation of seismic soil– footing interaction by large scale cyclic tests and analytical models", *Proc. 4th International Conference on Recent Advances in Geotechnical Earthquake Engrng and Soil Dynamics*, Paper no. SPL-5, San Diego, California.

FEMA 356, (2000), *Prestandard and Commentary for the Seismic Rehabilitation of Buildings*.

Gajan, S., Kutter, B.L., Phalen, J. D.,Hutchinson, T. C., and G.R. Martin, (2005), "Centrifuge modeling of load-deformation behavior of rocking shallow foundations", *Soil Dynamics and Earthquake Engineering,* 25, pp. 773–783

Gazetas, G., Apostolou, M., and Anastasopoulos, I. (2003), "Seismic Uplifting of Foundations on Soft Soil, with Examples from Adapazari (Izmit 1999, Earthquake)", *BGA Int. Conf. on Found. Innov., Observations, Design & Practice*, Univ. of Dundee, Scotland, September 25, pp. 37–50.

Gelagoti F., Kourkoulis R., Anastasopoulos I. and G. Gazetas (2011). "*Rocking Isolation of Frames on Isolated Footings: Design Insights and Limitations".*

Kawashima K., Nagai T., and D. Sakellaraki, (2007), "Rocking Seismic Isolation of Bridges Supported by Spread Foundations", *Proc. of 2nd Japan-Greece Workshop on Seismic Design, Observation, and Retrofit of Foundations*, Tokyo, Japan, pp. 254–265.

Kutter B.L, Martin G., Hutchinson T.C., Harden C., Gajan S., and J.D. Phalen, (2003), "Status report on study of modeling of nonlinear cyclic load–deformation behavior of shallow foundations", University of California, Davis, PEER Workshop.

Paolucci, R, & Pecker, A., (1997) "Seismic bearing capacity of shallow strip foundation on dry soils", *Soils and Foundations*; Vol. 37(3), pp. 95-105.

Pecker, A, (1998), "Capacity Design Principles for Shallow Foundations in Seismic Areas", *Proc. 11th European Conference on Earthquake Engineering*, A.A. Balkema Publishing.

Pecker, A, (2003), "A seismic foundation design process, lessons learned from two major projects : the Vasco de Gama and the Rion Antirion bridges", *ACI International Conference on Seismic Bridge Design and Retrofit*, University of California at San Diego, La Jolla, USA.

Workshop History

1st workshop:	Greece (Athens),	Oct. 2005
2nd workshop:	Japan (Tokyo),	April 2007
3rd workshop:	Greece (Santorini),	Sep. 2009
4th workshop:	Japan (Kobe),	Oct. 2011

Secretariat of 4th Japan – Greece Workshop

[Japan side]
Educational Subcommittee of Earthquake Engineering
Japanese Society of Civil Engineers
Yotsuya 1-chome, Shinjuku-ku,
Tokyo 160-0004 , Japan
tel: +81-3-3355-3452
fax: +81-3-5379-2769
email: tazoh@shimz.co.jp

[Greece side]
Soil Mechanics Lab (Room 102)
Faculty of Geotechnics
School of Civil Engineering
National Technical University of Athens
9, Iroon Polytexneiou, Athens 15780, Greece
tel.: +30-210-772-3383
fax.: +30-210--772-2405
email: gazetas @ath.forthnet.gr

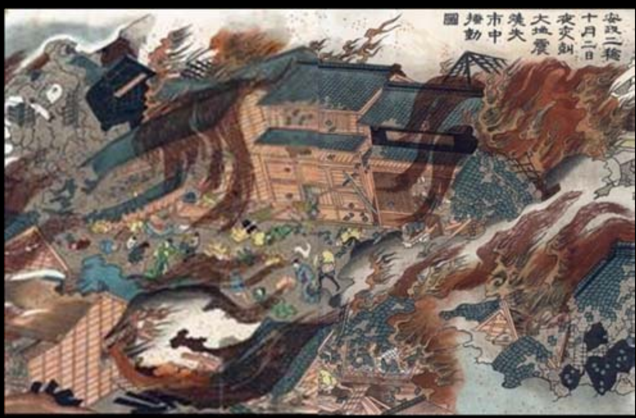
安政二稔
十月二日
夜亥刻
大地震
焼失
市中
騒動
圖